Prediction of Ash Deposition for Biomass Combustion and Coal/Biomass Co-combustion

Mohammed Umar Garba

Submitted in accordance with the requirements for the degree of
Doctor of Philosophy

Under the supervision of

Professor Mohamed Pourkashanian

Professor Alan Williams

Dr Lin Ma

The University of Leeds
School of Process, Environmental and Material Engineering

Energy Technology & Innovation Initiative (ETII)

December, 2012

The candidate confirms that the work submitted is his own, except where work which has formed part of jointly-authored publications has been included. The contribution of the candidate and the other authors to this work has been explicitly indicated below. The candidate confirms that appropriate credit has been given within the thesis where reference has been made to the work of others.

All the jointly-authored publications which form part of the thesis are derived from my PhD research. I performed all the calculations, produced all the results and draft of the papers, dealt with all the review processes and other aspects of the publications. As it was best practice, the publications process was done under the guidance of my supervisors (co-authors). To acknowledge my contribution as the lead authors of the papers, I am the first named author in all the publications. Details of all the published papers derived from my PhD work are provided in this thesis.

Acknowledgements

I would like to express my profound gratitude to God for giving me the health and ability to carry out this research. My sincere appreciation goes to the Petroleum Technology Development Fund (PTDF) for funding this research work. I also appreciate my employer, the Federal University of Technology (FUT), Minna for allowing me to embark on this research.

I am highly indebted to my supervisors, namely; Professor Mohamed Pourkashanian, Dr. Lin Ma and Professor Alan Williams, for their continued support, patience, guidance, direction and understanding during the period of this PhD research study.

I wish to acknowledge with thanks all form of support and assistance I received from Professor Derek Ingham, Dr. Richard T. J. Porter and other members of staff of the University throughout my research period. Special thanks to Dr. Houzhang Tan of the Xian Jiaotong University, China for providing valuable information on the straw-fired furnace. Also, special thanks goes to Professor Jim Williamson of Imperial College, London for his helpful information in some parts of my research findings.

I would like to thank my father (Alhaji Umaru Garba), my wife (Lami) and my children (Abubakar, Suleiman, Umar and Kamil) for their support in completing this PhD research.

Dedication

My late Mother, has always wished better things for me and this thesis has fulfilled her wishes. I therefore dedicate this Ph.D thesis to my late Mother Hajiya Aisha Wowo Gabi.

Abstract

In this thesis, a model that couples a reduced alkali kinetic mechanism for alkali sulphate formation during biomass combustion with an ash deposition model using computational fluid dynamics (CFD) techniques has been presented. Starting with a detailed gas-phase kinetic mechanism for the alkali chemistry, a systematic reduction procedure has been performed using a sensitivity analysis to reduce the reaction mechanism to a level that can be implemented into a CFD calculation. An ash deposition model that takes into consideration the ash-sticking probability and the condensation of potassium salts has been developed. The reduced mechanism and the deposition model developed are implemented into a CFD model to predict ash depositions in a 10 MW_{th} biomass grate furnace.

Also, a CFD model to predict the deposition rates for the co-combustion of coal with biomass has been developed. This deposition model is based on the combined sticking probabilities of the ash particle viscosity and the melting behaviour of the ash particles. A Numerical Slagging Index (NSI) is also employed to estimate the degree of the sintering of the deposits. Experimental data from the Entrained Flow Reactor (EFR) at Imperial College, London, have been used to validate the models. The predicted results from both the ash deposition models agreed with the experimental measurements, and the NSI has successfully ranked the investigated coal-biomass mixtures according to their degree of sintering.

Table of Contents

List of Tables

List of Figures

Nomenclature

Symbol	Units	Definition
A	—	reactant A
a	—	power of reactant A
a_n	—	NASA polynomial coefficient
A_p	$m^2\ kg^{-1}$	specific surface area of particle
c_i	$kmolm^{-3}$	gas concentration
C_i	$kgm^{-2}\ s^{-1}$	component i by condensation
C_P	$mgN^{-1}m^{-3}$	concentration of fly ash particles
$C_{t,p}$	$mgN^{-1}m^{-3}$	total concentration of fly ash particles
C_p	$Jkg^{-1}K^{-1}$	specific heat capacity
D_i	m^2/s	diffusion coefficient of the ith gaseous component through the flue gas
d_p	m	particle diameter
E	kJ/m^2s	activation energy
g_x	ms^{-2}	gravitational acceleration
H	$kJkg^{-1}$	Enthalpy
I_i	$kgm^{-2}s^{-1}$	impaction rate
J_i	$kgm^{-2}s^{-1}$	diffusion flux of species i due to concentration gradients
K	$kgm^2s^{-2}K^{-1}$	Boltzmann constant

k	$Wm^{-1}K^{-1}$	thermal fluid conductivity
K	m^2s^{-2}	turbulence kinetic energy
LHV	$kJkg^{-1}$	lower heating value
m_i	kg	mass of component i in the deposit
$\dot{m}$	$kgm^{-2}s^{-1}$	mass flux of solid particles
mc,A	$kgm^{-2}s^{-1}$	flux of ash vapors
$m_{trj,i}$	$kgm^{-2}s^{-1}$	mass flux of the particles
P	—	sticking probability
p_i	Pa	partial pressure of the ith gaseous component
$p_{s,i}$	Pa	saturation pressure of the ith gaseous component at the surface temperature
q_c	kJs^{-1}	convective heat transfer coefficient
Q_c	kJs^{-1}	heat transfer due to convection of the particles
Q_r	kJs^{-1}	heat transfer due to radiation of the particles
Q_v	kJs^{-1}	heat transfer due to vapourization of the particles
R	$mols^{-1}$	reaction rate
R_g	$8314.472Jkmol^{-1}K^{-1}$	universal gas constant
R_e	—	Reynolds number, $R_e = \frac{\rho u L}{\mu}$
S_i	$kJkg^{-1}$	internal energy source
S_m	$kJkg^{-1}$	momentum source
Sh	$kJkg^{-1}$	Sherwood number, $Sh = h_D d / D$
Stk	—	Stokes number

t	s	particle residence time
T	K	local fluid temperature
T_f	K	flue gas temperature
T_p	K	particle temperature
T_∞	K	bulk phase temperature
U	ms^{-1}	instantaneous turbulent velocity
u	ms^{-1}	fluid velocity
V	m^3	Volume
u_i	ms^{-1}	fluid phase velocity
u'	ms^{-1}	velocity fluctuating component
u	ms^{-1}	x-velocity component
v	ms^{-1}	y-velocity component
w	ms^{-1}	z-velocity component
Y_k	$kgkg^{-1}$	mass fraction of species k in the solid-gas mixture
Y_k^*	$kgkg^{-1}$	mass fraction of species k in the fine structure
We	—	Weber number, $We = \rho_p u^2 d / \delta$

Greek Characters

α	—	Absorptivity
α_s	—	swirl factor
β	—	fractional degree of burnout
Γ	—	generalized diffusion coefficient
η	—	ash sticking probability
ε	m^2s^{-3}	turbulence dissipation rate
k	m^2s^{-2}	turbulence kinetic energy
μ	$kgm^{-1}s^{-1}$	fluid molecular viscosity
μ_c	$kgm^{-1}s^{-1}$	critical (reference) viscosity
μ_p	$kgm^{-1}s^{-1}$	particle viscosity
μ_{to}	$kgm^{-1}s^{-1}$	turbulent viscosity without swell
ξ^*	—	degree of mixing
ρ	kgm^{-3}	fluid density
ρ_p	kgm^{-3}	particle density
τ	s	elapsed laboratory time
Ψ_i	$kmolkmol^{-1}$	mole fraction of species i in the gas
ϕ	—	property of transported quantity
Ω	—	characteristic swell number

Abbreviations

AFT	ash fusion test
A/B	basic to acidic oxides ratio
$B/A_{(+P)}$	fluxing to sintering oxides ratio
CPH	cone before heating
CFD	computational fluid dynamics
CPU	central processing unit
CTF	combustion test facility
CV	caloric value
daf	dry on ash free basis
DO	discrete ordinate
DNS	direct numerical simulations
DPM	discrete phase model
EDM	eddy dissipation model
EDC	eddy dissipation concept
EFR	entrained flow reactor
FBC	fluidized bed combustion
GCV	gross calorific value
HHV	higher heating value
HT	hemisphere temperature
IEA	international energy agency
IDT	initial deformation temperature
IPCC	intergovernmental panel on climatic change
LES	large eddy simulations
LHV	lower heat value

[B]	condensed form
NASA	national America space academic
NCV	net calorific value
NSI	numerical slagging index
N/A	not available
PDF	probability density function
PF	pulverized fuel
RANS	Reynolds-Averaged Navier–Stokes equations
RDF	refuse-derived-fuel
RNG	renormalized group theory
SEM	scanning electron microscopy
SH1	primary superheaters
SH2	secondary superheaters
SH3	third superheaters
SH4	fourth superheaters
SR	silica ratio
SRC	short rotation coppice
ST	softening temperature
UDF	user-defined function
VM	volatile matter
WEO	World energy organisation

List of publications

Paper Publications

1. M. U. Garba , D. B. Ingham, L. Ma, R. T. J. Porter, M. Pourkashnian, H. Z Tan and Alan Williams. *Prediction of Potassium Chloride Sulphation and Its Effect on Deposition of Biomass-Fired Boilers*. Energy & Fuels 2012; 26(11): 6501-8.
2. M. U. Garba, D. B. Ingham, L. Ma, M. Pourkashanian, M. U. Degereji and A. Williams. *Modelling of deposit formation and sintering for the co-combustion of coal with biomass*. In press, corrected proof, available online 11 January, 2013.

Conference Presentations

1. M. U. Garba , D. B. Ingham, L. Ma, R. T. J. Porter, M. Pourkashnian, H. Z Tan and Alan Williams. CareTech,. September 19-22, 2011. *Prediction of Potassium Chloride Sulphation and Its Effect on Deposition of Biomass-Fired Boilers*, 78-79.
2. M. U. Garba, D. B. Ingham, L. Ma, M. Pourkashanian, M. U. Degereji and A. Williams. ECCRIA, September, 9-12, 2012, Nottingham – UK. *Modelling of deposit formation and sintering for the co-combustion of coal with biomass*, 84.

Chapter 1

Introduction

1.1 General Background

Energy plays an important role in society, and without energy, civilization as we know it would come to an end. For this reason, energy has attracted much attention by academics, industrialists, politicians and the general public. Energy utilization and usage has increased significantly since the start of the industrial revolution. This is due to increases in human population, increased production of consumer goods, and the increasing use of energy intensive appliances, etc. When the supplies of energy are adequate then there is prosperity and development. When there is an energy supply shortfall, there is a challenge to make the best energy choices.

For more than 100 years, the energy used in generating electricity has mostly come from the burning of fossil fuels such as oil, coal and gas. These fuels are widely used because of their high energy density and world-wide availability. Coal was the first fuel that proved to be an excellent means of producing power on a large scale during the industrial revolution and remains a key fuel in the current energy blend. In 2012 (BP, 2012), more than 80% of the total worldwide energy consumption was fossil fuel based and approximately 27% of this energy was produced by burning coal (EIA, 2010). For example, in the UK the advantages of coal includes; availability, proximity to power stations, easily transportable and low cost. However, coal

produces many pollutants during combustion, such as carbon dioxide (CO_2), sulphur dioxide (SO_2) and oxides of nitrogen (NO_x). During the 1970's energy crisis, the world witnessed the rise of the oil and gas prices. In parallel to this, concerns about pollution and acid gases also arose (Bartlett, 1974).

The UK relies on imported oil and gas from abroad to meet its local needs due to its limited reserves. Its dependence on the international markets has both economical and political disadvantages. In addition, the international reserves of oil and gas are considerably less than for coal, which may lead to rises in the future price.

Coal is unequally distributed throughout the world with the largest stocks in the following order of magnitude: China>United State>India. These countries are the world's largest consumers of energy, as well as the largest emitters of CO_2. Although global primary energy consumption decreased by 1.1% in 2009, however new figures show a strong rebound of global energy consumption in 2010, following the global recession. Consumption growth has reached the highest rate of 5.6% since 1973 (BP, 2012). To meet the global energy demand, it is expected that in excess of more than 60% more energy will be needed today than in 2000 (BP, 2012). In the UK, it has been recognized that approximately one third of the total CO_2 emission is contributed by the power generation sector (Deloitte, 2000). Therefore, efforts have been made to reduced climate change by reducing emissions of CO_2 and other greenhouse gases. The UK has led the world by setting ambitious emission reduction targets. Emissions based on the 1990 baseline has been shown to be encouraging: The UK has surpassed the Kyoto target

by twice as much as the 12.5% (BP, 2012). The major concern now is to meet the 80% cut by 2050, which was made law in the Climate Change Act 2008 (European Commission, 2011).

It is evident that coal, together with other fossil fuels, such as oil and gas, are currently, and will remain for some time the main source of meeting the global energy demands. However as explained before, increased coal usage has a detrimental effect on the environment, such as the production of CO_2, SO_2 and NO_X, etc. Inevitably, coal combustion produces large amounts of CO_2. In order to meet the increasing global demands for energy, and to allow for the reduction of greenhouse gases in the coming years, alternative energy sources, which have an acceptable environmental impact, must be developed.

CO_2 emissions have significantly altered the atmosphere, particularly with regard to global warming (IPCC, 2012). The issue of climate change or global warming cannot be over-emphasised and it is one of the global problems that has remained unresolved. The planet Earth naturally supports a layer of greenhouse gases within the atmosphere that is composed of CO_2, water vapour, methane, nitrous oxide and ozone. Greenhouse gases greatly affect the temperature of the Earth; without them, the temperature of the Earth will be too cold for life to survive. The greenhouse layer prevents incoming heat from the Sun from escaping back into space and keeps the Earth warm. Carbon dioxide is part of the carbon cycle. Fossil fuel beds accumulate CO_2 over millions of years, and the CO_2 that released from the burning of the fossil fuel now outweighs the CO_2 sink from the carbon cycle. The concentration of CO_2 has increased from about 280 ppm during pre-

industrial revolution to the current level of approximately 430 ppm at a growth rate of about 2.2% per year (EIA, 2011).

Although recently surpassed by China, the US has historically been the largest producer of CO_2, however some states in the US produce much more than others. For example Texas produces approximately 700 million tons of CO_2 annually. This is more than most nations produce in the world, with the exception of China, India, Russian, Japan and Germany (EIA, 2011). As the population of the developing countries, such as China and India, keep increasing, their energy consumption per person also increases. Instead of restricting energy use and slowing development, effort must be channelled towards the development of alternative clean fuels, thus substantially reducing greenhouse gas levels in the atmosphere. Unless action is taken very soon, emissions of greenhouse gases will cause crops to fail and the sea level to rise, leading to drought and floods (EIA, 2011).

Due to its near CO_2-neurality, biomass energy utilization has received much interest in recent years with attention being focussed on reducing the environmental impact caused by the emission of greenhouse gases. The main energy utilization of biomass is combustion, pyrolysis and gasification. Combustion is the most common, and there are developed ways of converting biomass fuels to heat and/or electricity. Biomass materials are combusted for heating and power generation purposes. In power generation, the first step is biomass type selection. The biomass that arrives at the power plant is stored in the biomass yard. From this point, the incoming fuel to the different biomass piles is managed and different biomass analysis is conducted to determine its composition and properties. This analysis allows

the verification of the condition of the biomass. Biomass, as a fuel, is still not an ideal substitute for coal with respect to the ease of use and the high thermal efficiency. If a biomass presents a known problem, such as having high moisture, high alkali content or high chlorine content, it is possible to co-fire biomass with coal. The co-firing of biomass with coal provides a means of producing electricity at a relatively low cost by increasing the renewable capacity and it is an effective way of utilizing the high thermal efficiency of large coal-fired boilers. Biomass co-firing has a direct repercussion in the decrease in the amount of greenhouse emission. However, firing biomass in power generation plants produces combustion generated particles which are responsible for ash particle formation. The ash particles can be divided into several categories which depend on their size. The largest ash particles, up to several millimetres in diameter, are often called bottom ash since they are left in the combustion chamber after the combustion is complete. The fly ash particles usually leave the combustion zone with the flue gas, but some of them may be left in the furnace as wall and heat exchanger surface deposits.

Figure 1.1 shows schematically a conventional pulverized fuel boiler configuration with regions of slagging and fouling. In the boiler section, the temperature may be so high that a glassy deposit is formed - this is called slagging. In the convective section, the temperature and radiation are lower, the deposits maintain the visual aspect of the particles, and this is called fouling. Slagging and fouling reduces the heat transfer rate from the flue gas to the steam circuit and this causes a decrease in the efficiency and durability of the system (Baxter, 1993: Jenkin, 1998; Demirbas, 2004).

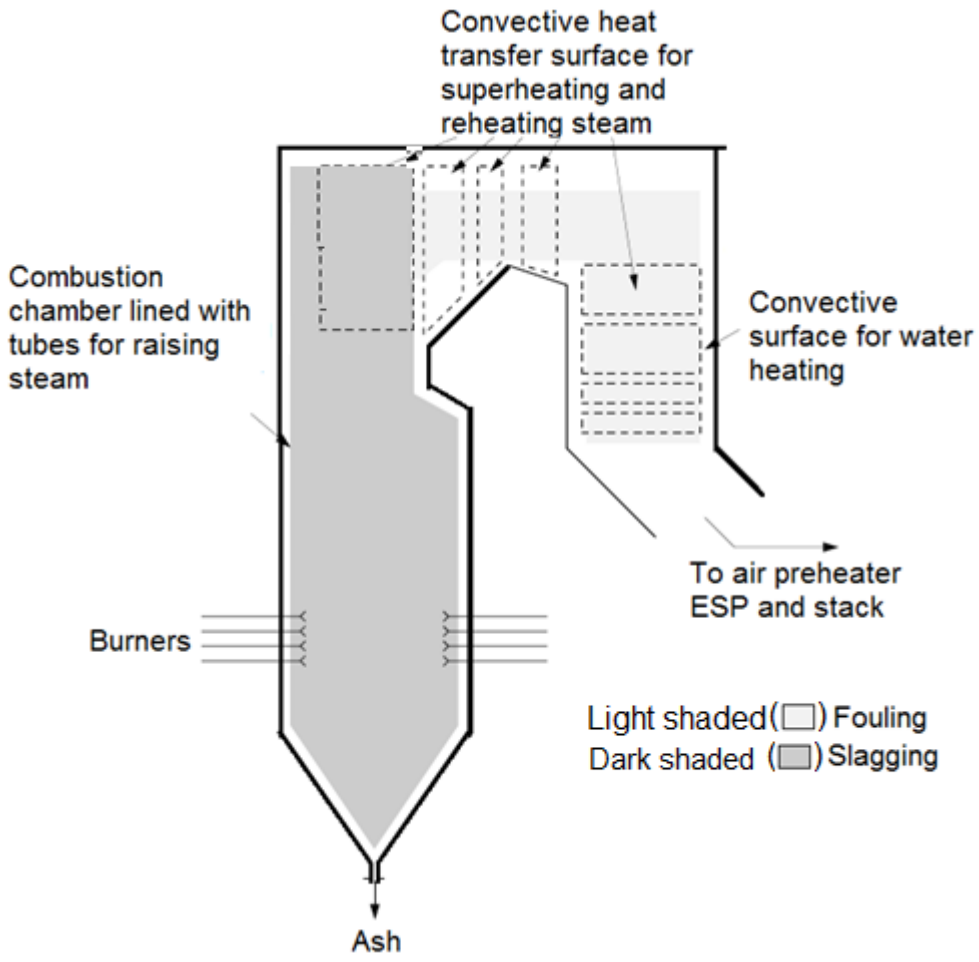

Figure 1.1: Schematic illustration of regions of slagging (dark shaded) and fouling (light shaded) in typical boilers (Couch, 1994).

Another reason that has prompted power generators to co-fire is the reduction in the fuel cost. For this reason, small savings from low cost biomass may mean a significant reduction in the power plant expenditure. However, careless co-firing of different biomass fuels can lead to a reduction of boiler efficiency, and to unscheduled plant shut-downs due to uncontrolled slagging or fouling (Kupka et al., 2008: Wigley et al., 2009: Weber et al., 2011). In addition, the boiler may be exposed to the danger of corrosion which is often considered as a further consequence of the deposits (Baxter,

1993: Kupka et al., 2008). A typical view of the deposits formed on the superheaters in a pulverized coal combustor is shown in Figure 1.2. In order for deposits to block the flow of gas through a system, or cause damage to system components, they must develop much more strength in order to hold the ash in place against gravity (see Figure 1.2). The conclusion that can easily be drawn from the figure is that the strength of the deposit may be just as important as the rate of deposition.

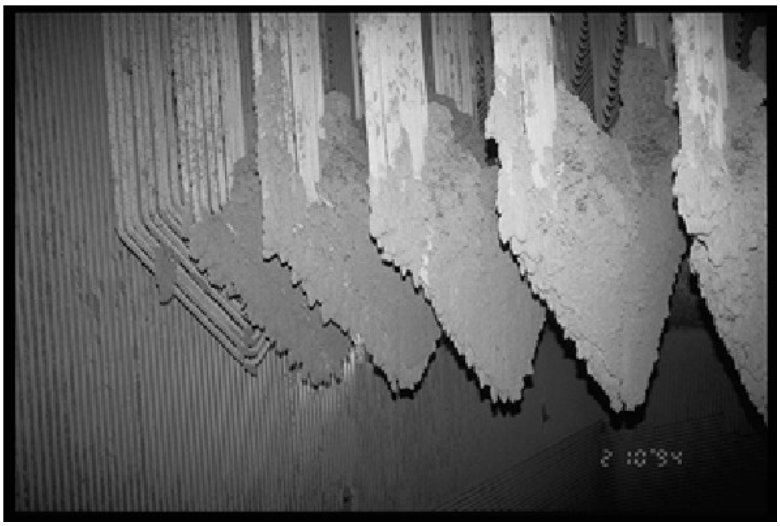

Figure 1.2: An illustration of the deposits formed on the superheater in a pulverized coal combustor (Vargas, 2001).

The ash deposition processes at operating conditions close to those that occur in real boilers is very difficult to determine effectively, but the behaviour of the ash formation and the deposition in biomass combustion has been well documented (Kaer et al., 2003; Muller et al., 2005; and Ma et al., 2006). Despite the details in these reports, the understanding of the ash deposition process is still fragmentary. Therefore, it is desirable to intensify

the studies on the individual mechanisms that are responsible for the ash deposition.

To overcome the difficulties in the experimental studies of ash deposition processes in combustion systems, several efforts have been made towards developing acceptable numerical prediction models. Several researchers have identified four main mechanisms in which the deposits are formed: inertial impaction, thermophoresis, condensation and chemical reaction (Baxter, 1993; Huang et al., 1996). Inertia and thermophoresis involve solid particles, whereas the condensation and chemical reactions affect the gas phase.

Condensation is the mechanism by which vapours in the boiler are cooled and deposited to the heat transfer surfaces. However, condensation processes mainly occur in the regions of low temperatures, especially in the downstream boiler region. Both condensation and chemical reactions are strongly dependent on the temperature, and give rise to spatial variations in the composition of the ash deposits (Baxter et al., 1993).

Baxter et al. (1993) identified three different ways that lead to condensation, namely, heterogeneous condensation of vapour on the boiler walls, homogeneous nucleation of vapours resulting in fume formation which deposits on the walls, and vapours condensing on other particles that are already deposited on the heat exchange surfaces. All the three processes require that the vapour has to transverse the boundary layer and hit the boiler walls before deposition takes place.

As far as the inertia and thermophoresis are concerned, the thermophoresis is important when the particles are very small (less than

about 1 μm in diameter) (Obernberger et al., 2011); while inertial impaction is important when the particles are larger than about 1-2 μm (Tomeczek et al., 2004; Walsh et al., 1990). Inertial impaction is typically the primary source of ash deposition on superheater boiler tubes. Inertial impaction takes place when the momentum of the particle towards the tube is large enough to overcome the drag forces produced by the fluid flow, which directs the particles around the tube. As a result, particles pass through the boundary layer and stagnation zone, and impact on the tube. The particle capture efficiency describes the propensity of these particles to stay on the surface once they impact. Both the particle and surface properties, such as the roughness of a metal surface and surface tension force, play significant roles in determining the particle capture efficiency.

Thermophoresis is the process of particle motion in a gas due to local temperature gradients. Thermophoretic forces on a particle may be induced either by the temperature gradient in the gas in which the particle is suspended. In general, these forces act in the direction opposite to that of the temperature gradient, although they can act in the direction of the gradient under certain conditions of particle surface temperature. Thermophoretic deposits are finer grained (sub-micron particles) and they are more evenly distributed around a tube surface than the deposits formed by inertial impaction. Deposit accumulation on the tube surface decreases the temperature gradient in the thermal boundary layer, and this decreases the rate of thermophoresis.

However, it should be noted that the ash deposition mechanisms are mainly responsible for the transportation of the particles to the heat

exchange surface, and therefore, there is need to numerically determine what will be the fate of the ash particles after impaction on the heat exchange surface.

Thermal conditions and the aerodynamics have been identified as some of the principal factors that can influence ash deposition characteristics in the furnace (Su et al., 2001). Also, these important features are being influenced by several factors, such as, furnace input variables, swirling motion, fuel type, burner design, etc., which also need to be investigated (Rushdi et al., 2005).

Any study on ash deposition processes that do not consider deposition characteristics due to the temperature and the operating conditions of a system is considered as a poor indicator of deposition (Nutalapati et al., 2007; Abbas et al., 1996). In addition to other deposition factors, such as fuel type, flow dynamics and reaction environment, the temperature of the ash particles and the heat exchange surface have been emphasized (Nuruse et al., 2005).

Although several attempts have been made to produce an acceptable model for the prediction of ash deposition processes (Kaer et al., 2003: Muller et al., 2005: and Ma et al., 2006), a comprehensive approach is needed to reveal the details of the individual deposition pathways.

The study of the combustion process is generally based on the laws of thermodynamics, chemical kinetics, heat and mass transfer, and fluid flow. It is considered as one of the most important processes in engineering, which involves turbulent flow, heat transfer, chemical reactions and other complicated physical and chemical processes (Versteeg et al., 2007). Most

of the processes involved in the combustion of biomass are physically immeasurable due to the high temperatures in boiler situations. This further complicates the process and suggests the need for the use of numerical techniques.

In order to solve the problems related to energy generation, experimental and numerical techniques have been developed, and some of the features of the power generation facilities and their operational conditions are modelled in order to enhance the understanding of the system. So far, tremendous achievements in the use of numerical techniques have been made (Weber et al., 2011). However, still much more needs to be done due to the increasing demand for energy and the fast depletion of some of the available energy resources.

With the advent of highly advanced modelling capabilities, several problems encountered in the combustion processes, including ash-related problems, are being investigated. More often, the ash from the combustion of solid fuels may stick to the water walls and other heat transfer surfaces in the boiler and this results in operational problems, such as slagging and fouling which results in the increased cost of maintenance (Naganuma et al., 2009; Huang et al., 1996; Rushdi et al., 2005; Mueller et al., 2003). Also, slagging and fouling affect the availability of the energy due to untimely shutdowns.

The influence of ash deposition in boilers leaves the energy engineer with the choice between coal quality and cost (Wigley et al., 1998), and to develop an effective mechanism for the removal of deposits on the boiler surfaces (Zhang et al., 2001).

However, it is very difficult to effectively determine the ash deposition processes at the operating conditions close to actual boilers in the power stations (Su et al., 2001). Benson et al. (1996) summarized the behaviour of the ash formation and deposition in coal combustion systems as being dependent on the physical transformations that are involved in a high temperature suspension, which depending on the process, may include:

i. Selective elemental vaporization and subsequent condensation to form surface coating.
ii. Coalescence of mineral grains with hot reactive char particles.
iii. Char fragmentation and partial coalescence of included mineral grains.
iv. Shedding of particles from the char surface.
v. Fragmentation or fusion of liberated mineral grains.
vi. Convective transport of the volatiles species within and between the char particle.
vii. Formation of thin-walled ash spheres.

However precise such a summary of ash behaviour can be, the understanding of the ash deposition process at high temperatures is still inadequate (Naruse et al., 2005). Therefore it is desirable to intensify studies on all the individual mechanisms responsible for ash particle deposition in boilers. This is considered as a viable means of understanding the ash deposition processes in full.

The increasing availability of user-friendly CFD software has made it possible to combine fundamental deposition models with complex flow patterns that typically occur in boilers. Several CFD models for slagging and

fouling behaviour for systems burning the solid fuels have been proposed over the last decade or so , e.g. see Huang et al. (1996), Kaer et al. (2003), Muller et al. (2005), and Ma et al. (2006). A general scheme for a deposit formation model must include three main parts:

i. Calculation of the continuous (gas flow) and discrete phase (particle tracking).
ii. Calculation of the sticking criterion of the particles.
iii. Calculation of the mass deposition for silica rich particles and particles rich in salts.

1.2 Research Motivation

The world's energy demand is continuously growing and demand figures are doubling by the decade. In addition to the release of CO_2 during coal combustion, predictions show rapid depletion of coal fuels (BP, 2012). Several researchers have focussed on the use of biomass for electricity generation. Although the use of biomass for power generation has been encouraging due to its environmental friendliness, there is not a sufficient amount of biomass available to replace coal globally. Also, biomass as a single fuel is still unable to satisfactorily replace coal as an energy resource in terms of thermal efficiency. Co-firing of biomass in existing coal-fired utility boilers is the immediate solution for reducing CO_2 emissions. However, ash deposition is a major problem to biomass-fired power generators. In the case of cofiring, it may lead to an increased danger in slagging, fouling and corrosion at higher cofiring rates of biomass.

One of the prime concerns with burning biomass fuels in boilers is the behaviour of fly ash, which often contains high concentrations of potassium. Currently there are only a limited number of experimental investigations on the biomass ash deposition and the modelling work on biomass deposition is even rarer (Ma et al., 2006). Neverthelss, continuous efforts have been made in order to prevent, or at least to reduce, these ash related problems and several research methods, ranging from slagging and fouling indices, equilibrium calculations to Computational Fluid Dynamics (CFD) models have been used. Slagging and fouling indices derived from the ash composition are simple models used to predict the ash behaviour in advance before the actual plant operation. The most commonly applied index is the basic-to-acid (B/A) ratio. Increasing the B/A of the coal decreases its fusibility and hence increases the slagging potential. The results of these indices have not been generalized for all types of coal and great care should be applied when interpreting the slagging index values for biomass. The equilibrium model is used in the field of complex chemical equilibrium simulations. One of the strengths of the equilibrium calculation is its ability to describe the melting behaviour of the slag mixture comprising liquid, solid and gas. This type of calculation has some limitations. Equilibrium calculations are based on the assumptions that all reactants are well mixed (perfect mixing) and kinetic limitations are not taken into account. The CFD model, which takes into account the physical and chemical interactions, is more suitable for general applications although it is more complex to undertake.

Recently, numerical modelling to simulate real combustion processes in conjunction with CFD has become a powerful tool and therefore it is used

in establishing the flow field, temperature, and particle aerodynamics in furnaces with high resolution and reliability. The CFD software used for the ash deposition rate calculation is FLUENT but other software such as Fire Dynamic Simulator (FDS) and STAR CD are also used. Moreover, deposition models can be incorporated into CFD codes in order to investigate deposition processes.

In conclusion, the problem of slagging and fouling in boilders firing biomass is still not fully understood and it remains a major impediment in the power generators. Mathematical and computational modelling of ash formation and deposition is generally accepted being important method of investigation and prediction of ash related problems. However, significant efforts are still required to improve the modelling capabilities relating to ash formation and deposition in biomass combustion systems.

1.3 Research Objectives

Firstly, in order to predict the effect of potassium in the biomass deposition process, this work aims at modelling two important ash related processes, one is the alkali sulphation during combustion, and the other is the effect of the alkali sulphation on the deposition in a straw grate-fired boiler. A reduced alkali kinetic model is proposed in this thesis in terms of the alkali sulphation. To the best of the author's knowledge, this is the first time that the detailed model is involved in the prediction of the deposit rate in the case of biomass combustion. Therefore models for these processes are developed. In these models, the potassium sulphate contributes to the formation of the deposit layer via the process of condensation, and the

condensable alkali has an effect on the sticking probability of the ash particles on the deposit surface. For validation purposes, two sets of experimental results are used in this thesis. One is the experiments which were performed on an entrained flow reactor by Iisa et al. (2004), and the other is the experiments which were performed on the 10 MW_{th} straw grate-fired furnace (Niu et al., 2010).

The second main objective of this thesis is to investigate the effect of biomass ash on the deposit formation, and the extent of deposit sintering (sintering is most often pointed to as being the way in which deposits develop strength). Although the interaction between two chemically different fuels (coal and biomass) is non-additive, a linear relationship between particle viscosity (Huang et al., 1996) and the melted fraction (Kaer, 2004) has been assumed. According to the concept of the melting fraction of the ash particle, if the liquid fraction of the particle is below 15%, the molten phase is not sticky. Between 15-70%, the molten phase of the ash particle is sticky. Above 70%, the molten phase of the ash particle will flow. Based on the melt fraction of the particle, the ash deposit rate was calculated for the biomass ash particle.

In parallel to the CFD model calculations, the slagging behaviour is evaluated using FactSage equilibrium calculations. In addition, slagging index based on the ash viscosity, fusibility and ash load that was developed by Degereji (2011) was modified to assess the degree of deposit sintering. The modification includes the introduction of two ash chemistry sub-models: the ratio of the basic oxides (Fe_2O_3, CaO, MgO, NaO and K_2O) to the acidic metal oxides (SiO_2 and Al_2O_3), and the ratio of the fluxing agents (Fe_2O_3,

CaO, MgO, NaO and K_2O) to the sintering oxides (SiO_2, TiO_3 and Al_2O_3) in order to account for the differing chemical compositions of the biomass fuels. For validation of both the CFD model and the slagging index, the experimental data of Wigley et al. (2007), which were performed on an entrained flow reactor, have been were used.

1.4 Scope and Limitation of the Thesis

The first part of this thesis is mainly concerned with the determination of the fate of the potassium in the ash deposition during biomass combustion. Also evaporation model best suited to high chlorine biomass since KCl is assumed to be the main evaporation species. The models are suitable to specific biomass (potassium and chlorine rich biomass, such as straw) rather than the overall biomass materials. In some crops /or biomass-derived waste with high phosphorus content, phosphorous oxide or potassium phosphate may be the key factor required in the development of the ash deposition model.

The second part of this thesis takes into account the particle viscosity and melting fraction to a developed ash deposition model for co-firing of the coal with biomass. In addition, the sintering tendency of coal with different biomass types is assessed and some of the important parameters, such as the basic to acid ratio (B/A), and the ratio of the fluxing agents to the sintering agents ($B/A_{(+P)}$) are used as options in the numerical slagging index calculation(NSI) in order to account for the chemical variabilities in the biomass.

The numerical models developed in this thesis have been tested using the available experimental data. Therefore no experimental work has been performed in this thesis in order to generate any other measurements for further validation of the proposed numerical models. However, comparison between the measured and predicted data have been analysed.

1.5 Thesis Outline

This thesis is divided into the following main chapters:

Chapter 1: This chapter provides some basic information related to the research activities undertaken in this thesis. This includes the background information on the ash deposition model, the motivation for the research, the objective of the chapter, and the scope and limitation of the research.

Chapter 2: In this chapter, a review of biomass combustion is presented. This gives a critical review on the type of the biomass materials, the biomass properties, devolatilization and char combustion processes, and the alkali formation mechanisms that are in the literature are presented. Also, the numerical techniques for investigating solid fuel combustion processes have been presented and discussed. The most representative deposition models and numerical slagging and fouling indices have been summarized and presented.

Chapter 3: In this chapter, the basic governing equations and a theoretical basis for the three-dimensional turbulent simulation for the solid fuel combustion processes are described. Some of the mathematical equations which represent the one-dimensional evaporative transport routes (excluding particle entrainment) used for alkali mechanism calculations are

also briefly described. Also, this chapter contains the ash particle deposition models that has been developed during the course of this research.

Chapter 4: In this chapter, the numerical results and discussion on the alkali kinetic model and the ash deposition model during biomass post-combustion are presented. The results of the kinetic model include the validation of the alkali mechanism, reduction of the detailed mechanism and the validation of the reduced mechanism. The dependence of the initial deposition on the interplay of the alkali kinetics (Chemkin) and the ash loading (CFD model) is described. The predictions using the ash particle deposition model are compared with all the available experimental data, and an analyses of the results and conclusions are presented.

Chapter 5: In this chapter, the numerical results are presented and discussed of an ash deposition model using CFD techniques for co-firing coal with five biomass materials, namely Miscanthus, Short Rotation Coppice (SRC), Olive residue and Palm kernel expeller cake and Sawmill residue. The predictions using the ash particle deposition model are compared with all the available experimental data, and an analyses and conclusions are presented.

Chapter 6: In this chapter, the slagging potential of two coals (Russian and South Africa coals) and Russian coal-biomass mixtures at levels of up 60 wt.% were investigated. To help determine the likelihood that liquids may form on the surfaces of ash particles, thereby increasing their stickiness, thermochemical equilibrium modelling of the ash composition has been performed using FactSage. In parallel to the equilibrium calculations, a slagging index, based on the ash viscosity, fusibility, ash load and ash

chemistry has been developed to assess the degree of deposit sintering. In order to account for the differing chemical composition of different biomass materials, the ash chemistry was further divided into two sub-models: basic-to-acidic oxides (B/A) and fluxing-to-sintering oxides ($B/A_{(+P)}$). The results of the findings have been discussed and conclusions are presented.

Chapter 7: This the final chapter contains the conclusions drawn from the implications of the modelling studies for various real world systems. It provides an insight into the findings and the general conclusions that have been made at the end of the investigation. Also, some suggestions and ideas for future work are discussed.

Chapter 2

Literature Review

This chapter discusses the properties of biomass that are relevant to combustion. The emphasis is on the release of alkali from biomass and the discussion of the deposit formation during biomass combustion and biomass co-combustion. For the sake of clarity, the properties of the biomass and its application are compared to those of coal.

2.1 Biomass Combustion

Biomass combustion, which means the burning of bio-organic material in the presence of oxygen, is one of the most important processes in engineering. It involves turbulent fluid flow, heat transfer, chemical reactions, radiative heat transfer and other complex physical and chemical processes. The chemical combination of any form of organic material and oxidizer usually produces heat and light. While wood is the most commonly used feedstock, a wide range of materials that can be burned effectively include agricultural residues and byproducts, such as straw, sawdust, olive residue, etc. Others include the so-called “energy crop”, such as switchgrass and willow that are grown specifically to create feedstock (Williams et al., 2001).

The main steps in the combustion process are the drying, devolatilization, gasification, char combustion, and gas-phase oxidation (Carpenter et al., 2007). The time for each of the combustion processes

depends on the nature of the fuel and operating conditions. The main products of these combustion processes are heat, water, carbon dioxide and ash. The combustion processes take place in boilers, most of which are divided into two main components: a burner that converts fuel to heat and a heat exchanger that transfers the heat to water or steam (carried in steel tubes). The former is used for district heating and the latter is used for electricity generation. In practice, radiant heat exchange always takes place between the flame and the heat exchanger, but for the sake of simplicity, the basic concept for the biomass combustion process reported by Quaak et al. (1999) assumes that all heat is transported to the combustion gasses (see Figure 2.1). Figure 2.1 shows the reaction between the fuel and air in the furnace and this is accompanied by the conversion of fuel into flue gas and ash, and the release of thermal energy. It is assumed that the thermal energy released by the furnace is transported to the flue gas which subsequently is used in the heating of the boiler to generate the steam that is used in steam turbines.

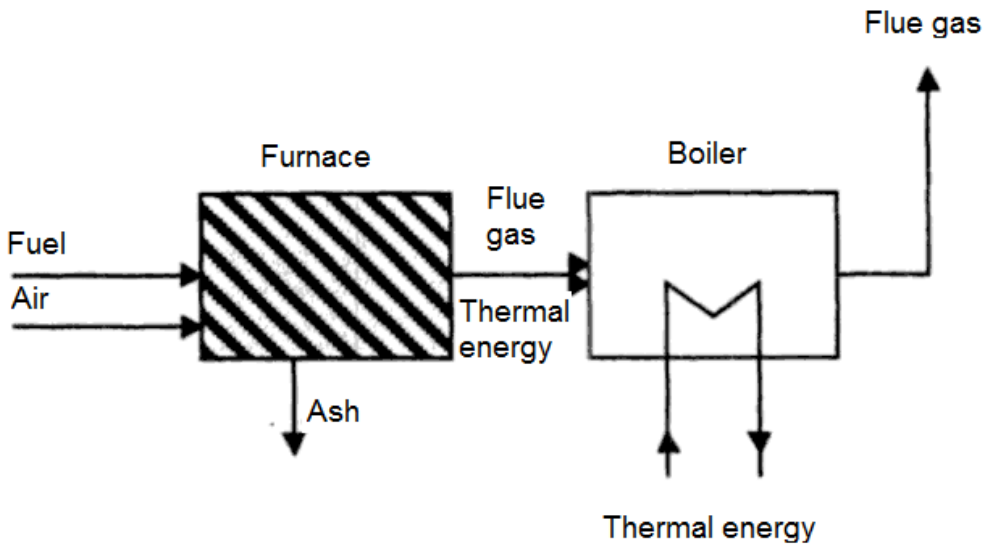

Figure 2.1: Basic process flow for biomass combustion (Quaak et al., 1999).

Farmers, and other rural homeowners, are increasingly looking towards biomass heat as an economical alternative to propane or furnace oil. This is because propane, or furnace oil (distillate and residuals oils), are expensive, polluting and are not often readily available when compared to biomass. Further, stoves and fireplaces are employed by them for domestic cooking and heating. On a large scale, biomass materials are combusted in an industrial furnace for the purpose of generating electricity or simply heat. However, biomass combustion in power generation plants produce combustion generated particles which are responsible for ash deposition in the combustion chamber as well as on the walls and the superheat tube surfaces. This causes a number of complications, such as slagging, fouling, and corrosion and reduce both system efficiency and durability. This thesis mainly concerns with the mathematical modelling of the combustion and ash deposition processes in order to improve the understanding of the underlying problems in combustors.

Combustion in grate-firing systems and fluidized bed combustors are the common types of furnaces, both of which have good fuel flexibility and can be fuelled entirely by biomass or co-fired with coal. Grate-firing is the first combustion system used for solid fuels and it is still used for domestic units (Yin et al., 2008). Larger, modern grate-fired boilers consist of four key elements: a fuel feeding system, a grate assembly, a secondary air system and an ash discharge system as shown in Figure 2.2. The grate, which is at the bottom of the combustion chamber in a grate-fired boiler, has two main functions: the lengthwise transport of the fuel, and the distribution of the primary air entering from beneath the grate.

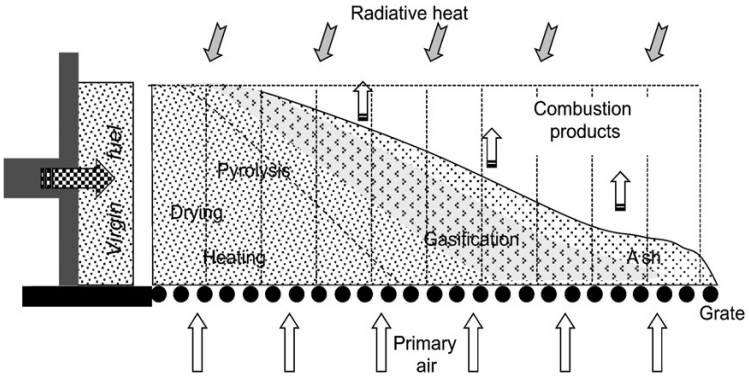

Figure 2.2: Schematic of the biomass combustion in a grate furnace (Venturini et al., 2010).

In fluidized bed combustion (FBC), solid fuels are suspended on upward-blowing jets of air into a bed (much like bubbling fluids) and this provides high combustion efficiency, low emission levels and good fuel flexibility. Two types of FBC, namely bubbling bed and circulating fluid bed, are commonly employed for medium to large industrial, commercial and utility applications because the beds enable good thermal transport inside the system and good heat transfer between the bed and its container. Figure 2.3 (Quaak et al., 1999) shows a typical fluidized bed combustion system.

At present, biomass represents only about 3 % of the primary energy consumption in industrialized countries (Bridgwater et al., 2009), see Table 2.1. However, it is important to note that there is an increasing interest in biomass utilization for energy production worldwide. Many of the population in developing countries rely on biomass, mainly in the form of wood, for fuel. Biomass accounts for 35% of the primary energy consumption in developing countries, raising the world total to about 15% of the primary energy consumption (Bridgwater et al., 2009). The use of biomass for energy consumption will therefore continue to increase because of the following advantages:

i. It provides cheap replacement for diminishing oil supplies.

ii. Many countries have agriculture surpluses and therefore it may be economical to convert these into fuel.

iii. Disposed waste is a growing problem in the developed countries, and biomass makes up a large part of that waste.

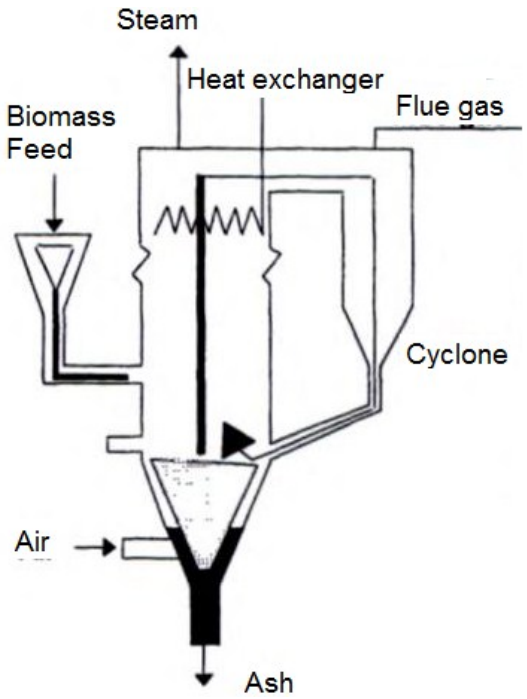

Figure 2.3: A typical fluidized bed combustion system (Quaak et al., 1999).

Figure 2.4 comprises of an historic and alternative world energy outlook scenario data for fossil, nuclear and renewable energy source (RES) starting back in 1930–2100. It is noted that between 1930 and 2010, fossil, nuclear and RES contribute to the total energy supply in the following order of magnitude: oil > coal > gas > biomass > wind. Then, this is followed by a transitional period (2030 - 2050) between today's fossil fuel based energy economy and a possible future one based on RES. The prediction of the World Energy Organisation (WEO) (indicated by red dashed line) is

significantly higher between 2006-2030. Finally, RES continues to increase, in particular biomass and solar energy.

Table 2.1: World primary energy consumption by energy (Mtoe) and by the world regions (%) (Bridgwater et al., 2009).

Energy	World (%)	Industrialized countries (%)	Developing countries (%)
Oil	34.10	38.30	25.8
Coal	24.10	24.50	23.4
Biomass	14.70	2.80	38.1
Hydro	5.50	5.70	5.10
Nuclear	4.10	5.90	0.60
Natural gas	17.40	22.70	7.10

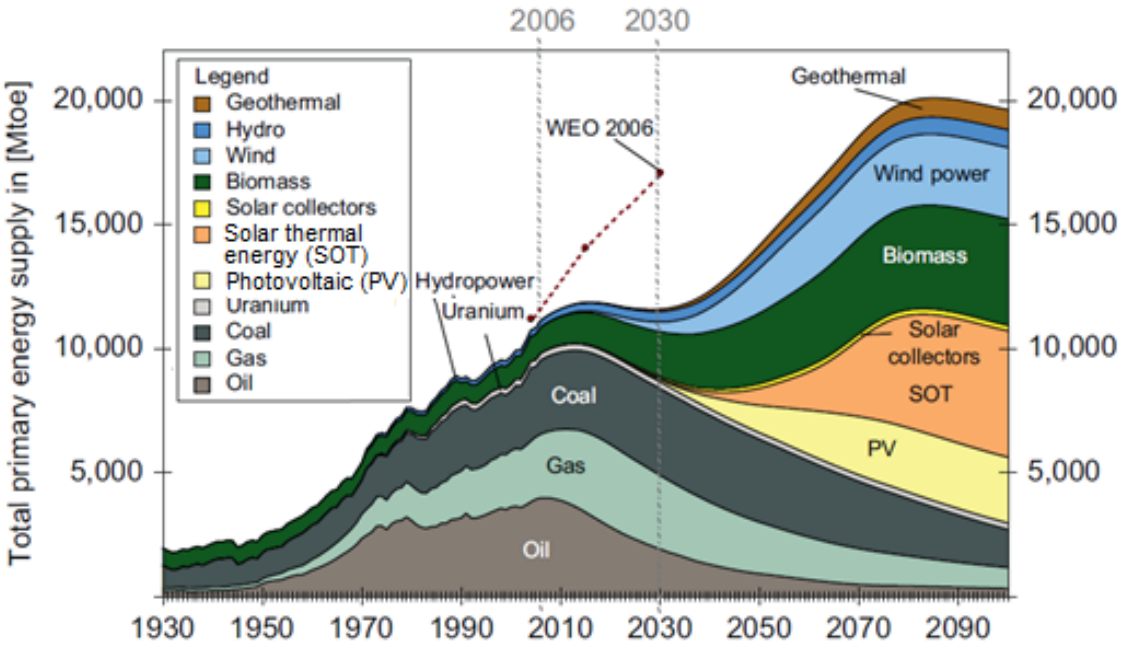

Figure 2.4: Historic and alternative world energy outlook scenario data (IEA, 2011).

2.1.1 Biomass Classification

Biomass fuels cover a large diversity of biomass feedstock that have a variety of compositions and can be divided into agricultural residues; animal manure; wood waste from forestry and industry; residues from food and paper industries; municipal green waste; sewage sludge and dedicated energy crops, such as short-rotation coppice (eucalyptus, poplar and willow) and grasses (miscanthus) (Williams et al., 2012; Kupka, 2009). Biomass combustion is a carbon-neutral process as the CO_2 emitted to the atmosphere is being absorbed with the implementation of re-planting plant. The classification techniques developed for coal, that is, proximate and ultimate analyses are also applied for the characterization of biomass fuels (Bridgewater et al., 2009).

2.1.2 Biomass Properties

In order to determine various aspects of solid fuel, such as heating value, volatile matter, ash type and particle size, it is important to analyze the fuel to find its composition. The common fuel analyses are proximate analysis and ultimate analysis. Proximate analysis involves the physical characteristics of solid and liquid fuels such as moisture, volatile matter, ash and fixed carbon contents. Proximate analysis gives insight into the behaviour of the solid fuel and the best combustion methods.

The moisture content of biomass is important during combustion; the heat absorbed by the high moisture content in the biomass tends to cool the surrounding region, thus reducing the furnace temperature and causing

problems with the flame stability. The fractional contribution by volatiles in biomass is of the order of ~70% to 90% compared to ~36% for coal (Williams, 2012). The solid combustion matter that remains after devolatilization is called fixed carbon (FC). The higher the FC content in the solid fuel, the higher is its heating value. Generally, biomass contains less carbon than coal. Moreover, parameters such as low carbon content, low heating value, and high moisture content of biomass compared with bituminous coal, makes the former difficult to ignite and can cause problems in flame stability. However, once ignited, pulverized biomass fuels burn faster than coal due to the rapid release of volatiles, and the high porosity of the biomass char particles. The proximate and ultimate analyses are illustrated in Table 2.2, along with the heating value of different solid fuels. The data from wood, grass, straw and sludge are taken from the 'Phyllis' biomass database (Phyllis, 2004). For comparison, the Table 2.2 also shows the proximate and ultimate analyses of bituminous coal taken elsewhere (Savolainen, 2003). One of the most prominent differences shown in Table 2.2 between biomass and coal is the lower heat value (LHV). While the LHV of bituminous coal is > 26 MJ/kg, it is about 17.9 MJ/kg for sludge, 18.1 MJ/kg for straw, 18.5 MJ/kg for grass, and 17.5 MJ/kg for wood.

The ultimate analysis, which is in fact the elementary analysis, gives a measure of the carbon, hydrogen, sulphur, nitrogen and oxygen content within the biomass. By knowing the amount of these elements in the fuel, the calorific content can be calculated. The sulphur and nitrogen contribute to acid rain and frequently requires removal from the stack gases of utility boilers (Demirbas, 2000). The carbon and hydrogen contents in wood are considered as the most important constituents of biomass because the

carbon content supplies most of the wood heating value. Carbon amounts for about 52% and hydrogen 6.3% by weight of the organic content of typical wood (Demirbas, 2000).

Table 2.2: Proximate and ultimate analysis of biomass and bituminous coal (Phyllis, 2004).

Component	Wood (willow)	Grass (miscanthus)	Straw (rye; wheat, rice)	Sludge (paper residue)	Russian Coal (bituminous)
Moisture wt.%	30	30.7	10.4	11.0	5.6
Ash wt.% dry	1.6	3.6	8.6	40.9	12.1
Volatiles wt.% daf	83.4	83.5	81.1	43.3	36.2
HHV MJ/kg	18.9	19.7	19.5	7.4	N/A
LHV MJ/kg	17.5	18.5	18.1	6.6	26.9
C wt.% daf	50.2	49.6	48.8	21.0	65.4
H wt.% daf	5.9	5.72	5.9	2.7	N/A
O wt.% daf	42.2	43.9	43.9	23.6	4.9
N wt.% daf	0.1	<1.5	<1.5	0.6	1.9
S wt.% daf	N/A	<0.5	<0.5	0.1	0.4
Cl wt.% daf	N/A	0.19	0.5	N/A	0.3

N/A = not available; daf = dry on ash free basis

The heat of combustion, or calorific value, also called the heating value, defines the energy content of a biomass fuel. Generally, the heating value of a fuel may be reported on two reference states of water; the higher heating value (HHV) or the gross calorific value (GCV) and the lower heating

value (LHV) or net calorific value (NCV). For the LHV, the water is in its gaseous state; for the HHV, the water is in its liquid state. The heating value of biomass fuel is about two-thirds of the heating value of coal (Quaak et al., 1999).

Biomass also contains inorganic matter, although usually the amount is small. The inorganic materials in most solid fuels, including biomass, are inherent and extraneous; the former exists as part of the organic structure of the fuel, and is commonly associated with functional groups of oxygen, sulphur and nitrogen. The latter occurs in the fuel through various processes, such as geological processes, or during harvesting, handling and processing of the fuel. Korbee et al. (2001) and Marschner (1997) provide a rough quantitative overview of the major inorganic element speciations in three useful categories, viz: water soluble or free ionic form (Na, K, Ca and Mg), organic associated (Mn and Fe) and precipitated form of pure compound, in crystalline and amorphous forms (Si). The examples listed in these categories indicate that the speciation is important in characterizing organic and inorganic constituent in biomass materials.

In the combustion process, the inorganic matter produce constituents called ash. These constituents of ash, which exist as minerals and inorganic salts, range from less than 1% in wood to 15% in herbaceous biomass and feedstock and up to 25% in some agricultural residues (Di Blasi, 1999; Williams et al., 2001). Silica, potassium, calcium, sodium and phosphorus are the main constituents in biomass ash that are responsible for the stickiness of ash particles (Raveendran, 1995).

An important property of biomass ashes is their behaviour at elevated temperatures and, in particular, their fusion behaviour. In relation to this, Bryers (1996) described three types of biomass ash; high silica/high potassium/low calcium ashes, with low fusion temperatures (e.g. agricultural residues), low silica/low potassium/high calcium ashes, with high fusion temperatures (e.g. wood) and high calcium/high phosphorus ashes, with low fusion temperatures (e.g. sewage sludge or manure). The relevant ash fusion temperatures to the behaviour of biomass fuels, to some extent depends on the type of combustors. Sintering, fusion and agglomerates of ash particles are important for both grate and fluidized bed furnaces. During biomass combustion, sintering and fusion of ash deposits may produce tenacious deposit layers that are difficult to remove by soot blowing, and often requires manual cleaning (Tobiasen et al., 2007; Bryers, 1996). Moreover, the formation of substantial agglomerates is particularly important for the fluidized bed system (Livingston, 2007). When ashes with low fusion temperature are present in the bed, they can form an adhesive layer on the surface of the sand particles. As a consequence, sand particles with a sticky surface grow towards larger agglomerates due to the formation of permanent bonds upon collisions. If this process is not observed, it will eventually lead to partial or total defluidisation of the reactor which reduces the output and efficiency of the reactor.

2.1.3 Types of Flames

Depending on how the fuel and oxidizer are brought into contact in the combustion system, three different homogeneous flame types identified are non-premixed, premixed and partially premixed types (Turns, 2006).

However, flames can also be heterogeneous if they contain particles, such as pf flames.

Non-premixed combustion: In the non-premixed (diffusion) flames, the fuel and the oxidizer diffuse into each other at an interface and flames occur. In this case, a fuel and oxidizer are introduced to the combustion zone in two or more separate streams and subsequently brought together due to diffusion and mixing prior to combustion.

The modelling of the non-premixed combustion may involve solving the transport equations for one or two conserved scalars known as mixture fractions and its variance. The mixture fraction is the local fraction of unburnt fuel stream elements in the mixture. Further, instead of solving equations for individual species, the non-premixed model often considers the species concentration from the mixture fraction fields. The thermo-chemistry calculations are pre-processed and then tabulated in a look-up table and an assumed-shape probability density function (PDF) is used to account for the interaction of the turbulence and the chemistry.

The non-premixed mixture fraction modelling approach is specific to the simulation of turbulent diffusion flames with fast chemistry (Turns, 2006). For such systems, the non-premixed model is of enormous advantage over finite reaction rate based method. It allows for possible species prediction, dissociation effects and rigorous turbulence-chemistry coupling to be considered in a computationally cost effective way without sovling a large number of species transport equations.

Premixed combustion*:* In contrast to the non-premixed flames, the fuel and oxidizer are mixed at the molecular level prior to any significant ignition.

Therefore the reactions start at the combustion zone where the unburnt reactants and the burnt combustion products are separated and subsequently brought together due to diffusion and mixing prior to combustion.

The premixed model in the commercial package FLUENT, is valid for laminar and turbulent flows, and can be used in conjunction with models for pollutant formation (e.g. soot and NOx) precidtion, and reacting discrete phase particles.

Partially premixed flames: The fuel-oxidizer mixture with non-uniform mixing is referred to as a partially premixed flame. The partially premixed flame model in FLUENT is considered as a simple combination of the two models discussed above, i.e. the non-premixed and premixed models in combination.

In addition, the following limitations apply to the non-premixed combustion model: the single-mixture-fraction approach is limited to two inlet streams, which may be pure fuel, pure oxidizer, or a mixture of fuel and oxidizer and the two-mixture- fraction approach requires three inlets streams. However, this approach requires additional computational work.

2.1.4 Devolatilization

Biomass devolatilization is the decomposition of the solid into permanent gases, condensable vapours (tar) and solid residue (char). Devolatilization of biomass starts at a temperature of about 500 K, and fast rates are attained at about 573 K and the process is practically terminated at 700-750 K (Shafizadeh, 1985; Antal and Varhegyi, 1995). Once the devolatilization species enter the gas phase, the volatile species may react

according to the input governing gas phase chemistry (Scott et al., 2007). There are two main approaches to modelling devolatilization. The first approach is where the devolatilization is modelled by a generalized expressions using predetermined rates for the release of the volatiles; a one or two stage release mechanism is commonly used which are defined based on devolatilization rates with single- or two-step Arrhenius reaction schemes (Sheng et al., 2003). The second method is to specify the solid fuel matrix and how this alters during thermal decomposition. This approach requires detailed data about the initial solid fuel matrix and the product released (Scott et al., 2007). When the solid fuel devolatilization model is based on a matrix, the chemical structure of the solid fuel is considered to be a macro-molecular network which allows the concepts of cross-linked polymers to be applied. Statistical methods are used to simulate how the network reacts under thermal decomposition via bridge-breaking and cross-linking (Solomon et al., 1993). These networks for the biomass devolatilization models are accurately described by the chemistry of the devolatilization process: the FG (functional group)-biomass model (Backreedy et al., 2005) and bio-FLASHCHAIN (Niksa, 1999) are examples of these network models.

In FLUENT, the default vaporization temperature of coal is about 773 K, but in order to start the reactions, it is lowered to about 343 K and once the flame shape is obtained, this temperature is changed back to its required value in order to achieve flame stability.

2.1.5 Char Combustion

The char combustion process commence during or after devolatilization. This process is slower and it takes much more time than that

for devolatilization. In coal combustion, the char oxidation process, which depends on the physical structure of the coal, is very important. At temperatures near 900 ^{o}C, most of the volatile matter has been evolved and with the supply of a sufficient amount of air being mixed into the jet, then the fuel is ignited.

The rate of char combustion can be affected by its mineral matter content. It is characterized by wide variations in its properties and composition, and its successful combustion operation depends on a proper application of much fundamental knowledge and skills (Eghlimi et al., 1999).

The use of CFD models to describe the combustion processes, including the char combustion process, has become an important aid in the optimization of biomass combustion (Williams et al., 2002; Ma et al., 2007; Weber et al., 2011). The burning rate of a particle, that is assumed to be spherical and homogeneous, is determined from its size, velocity and temperature (Murphy et al., 2002). However, sometimes it is appropriate to assume that the burning of all particles take place at the same rate (Field, 1969; Lee et al., 1999). Mathematical models are available to model the combustion of char includes diffusion limited rate, kinetic diffusion limited rate, intrinsic rate and multiple surface reaction rate models (Lee et al., 1999).

The diffusion-limited model assumes that the overall reaction rate of char to be limited by the diffusion of oxygen to the char particle (Dhumai et al., 2007). However, the model ignores the kinetic contribution to the surface reaction and also assumes that the diameter of the particle may remain constant or vary (Eghlimi et al., 1999).

The kinetic/diffusion-limited model assumes that the reaction may be limited by either the diffusion of the oxygen or the kinetic reaction of the char. This model is widely used for coal combustion and it has been applied to biomass successfully (Xu, et al., 2003), and it is assumed to be a simple model (Sheng et al., 2004).

The intrinsic char combustion model also includes the effects of the diffusion and kinetics on the limiting char combustion. However, the kinetic reaction rate is expressed in terms of the intrinsic reactivity of the char particle. The intrinsic chemical activity takes into account the porosity and the surface area of the particles (Smith, 1982). Therefore on using this model, the heterogeneous char combustion is predicted by a first-order ordinary differential equation, with a combined rate coefficient that accounts for the global diffusion of oxygen to the char surface and the reaction rate of the char oxidation (Lee 1999; Backreedy et al., 2005).

With the multiple surface reaction models, the chemical state of the surface can be described by a set of surface coverages which specify the fraction of the surface that is covered by a particular species (Miessen et al., 2001). However, the multiple surface reaction models have some limitations. For example, in the FLUENT software, the model is only available with the steady sticking and species transport options, and therefore it is not applicable with the premixed and partially combustion models (FLUENT Inc., 2009).

2.2 Biomass Co-combustion

Biomass co-firing is a cost-effective technology that has been considered as an important step for the development of biomass-to-energy capacity. Biomass fuel has the thermal potential to replace coal despite its low heat of combustion and low bulk density. In general, the combustion efficiency of biomass can be 10% lower than that of coal at the same installation, but the co-firing efficiency in a coal fired plant is on the average between 35-40% higher than the efficiency of biomass-dedicated plants (IEA, 2011). In the case of less than 10% partial replacement of coal by biomass material, only minor changes in the handling equipment are required and the boiler output is not noticeably reduced. However, for biomass greater than 10%, or if coal and biomass are burned separately, then changes in the components such as mills, burners and dryers are required. Over 100 co-firing installations have been demonstrated in Northern Europe, United States and Australia using different feedstocks (wood, residues and crops) (Heinzel et al., 1998). Coal is cheaper than biomass at present because of its high thermal efficiency and output – co-firing is only used at present in most countries if it is subsidised by the Government. However, by using biomass, the payback can be obtained in a short period of time (2 years) (Demirbas, 2000), but care must be exercised because biomass is usually associated with slagging and fouling and this affects the reliability of the plant and may raise costs.

However, the implementation of co-firing in existing coal-fired facilities is still under investigation. So far, the feasibility of different combustion systems has pointed out that the management of ash-related problems is a

major issue that requires a much better understanding (Khodier, 2012). The different types of biomass sources intended for co-firing include wood residue, agricultural residues, energy crops and sewage sludge.

Although each form of biomass has its different composition and properties, typical biomass fuel has a lower inorganic content than coal. However the alkalis in biomass could change the properties of the fuel when co-fired with coal, thus resulting in higher deposition rates (Wigley et al., 2007). Ma et al. (2006) are of the opinion that the presence of inorganic species in biomass, particularly potassium, can increase its deposition tendencies by significantly lowering its fusibility.

Therefore, it is suggested that the use of biomass fuel in combustion systems comes with the added operational difficulties related to ash deposition (Lokare et al., 2006) and the implementation of co-combustion in existing coal power plants and its engineering consequences are some of the problems being investigated (Heinzel et al., 1998). The results of these investigations can be used to minimize the deposit formations.

The different mineral matter composition of biomass may result in an increased slagging and fouling tendency in the boilers. Also, biomass has a higher content of moisture, volatile matter and oxygen, and it has a lower density, ash content and heating value than that of coal (Molcan et al., 2009). Although there is no available index that predicts the slagging and fouling of biomass, unequivocally, some of the coal slagging indices are used for biomass (Munir et al., 2010a).

2.3 Deposit Formation

2.3.1 Release of Alkali in Biomass

According to the current understanding, a portion of the alkalis in biomass is released into the gas phase as chloride vapours (KCl, NaCl) and hydroxide vapours (KOH, NaOH) (Dayton et al., 1996; Baxter, 2000; Jensen et al., 2000; Knudsen et al., 2004). However, these species transform in the flue gas through reactions with other species and this causes the formation of molten salt mixtures on accessible surfaces of boiler parts, and on the fly ash particles. Alkali plays a central role in the deposition of molten salt on the surfaces of boiler parts, and on the fly ash particles. In biomass combustion, the potassium content is relatively high compared to sodium and therefore the effect of potassium on the deposition is considered to be very likely to occur. This thesis focuses on potassium as the main component of biomass that is responsible for the deposition in the downstream region of the boiler.

Olsson et al. (1977) studied the alkali release during the pyrolysis of wheat straw using a surface ionization technique. A small fraction of the alkali metal content (0.1-0.2%) was found to be released below a temperature of about 500 ^{o}C while a significant amount was released above 500 ^{o}C. The release of potassium above 500 ^{o}C was found to correlate with the chlorine content in the fuel, while the alkali metal released in the low-temperature region was thought to be due to the decomposition of the organic matrix.

Dayton et al. (1996) investigated the released vapour species from the combustion of switch grass samples in a laboratory reactor using a molecular-beam mass spectroscopy. The studies revealed that HCl, SO_2 and minor amounts of K were volatilized during the devolatilization, whereas alkali was mainly volatilized during the char burnout. The amount of alkali released was independent of the feedstock composition and combustion conditions. Potassium was found to be predominantly in the form of KCl, but the addition of steam also yields some KOH. Similar to the findings of Olsson et al. (1977) and Dayton et al. (1996), Miettinen-Westberg et al. (2003) showed that the K released as KOH was stabilized by the presence of moisture.

Davisson et al. (2002) studied the release of alkali species during the rapid pyrolysis of birch wood. They observed that a minor part of the total alkali was emitted in the temperature range 200-400 ^{o}C, during the decomposition of the organic matrix of wood, whereas a large proportion of alkali is released from the ash fraction at temperatures in excess of 600 ^{o}C. The general conclusion of Olsson et al. (1977) and Davidsson et al. (2002) was that on increasing the temperature causes an increase in the amount of alkali released.

Jensen et al. (2000) investigated the release of K and Cl during the pyrolysis of straw at relatively low heating rates. They found that Cl was released primary as HCl, and afterwards KCl and KOH are released during the char combustion. They also found that the release of K was not significant below about 700 °C, whereas above 700 °C, the volatilization of K increased progressively with increasing temperature and approximately 25%

was volatilized at a temperature of 1050 °C. Knudsen et al. (2004) investigated the release of K, Cl and S during the combustion of annual biomass fuels at grate-combustion conditions. Further, they found that the release of these elements is strongly dependent on both the temperature and inorganic composition of the fuel. The release of K to the gas phase starts at about 700 ^{o}C and the percentage of K increases to 50-90%, depending on the fuel type. It is further reported from this experiment that the chlorine content in the biomass dictates the amount of potassium released during combustion. This is because the major fraction of the fuel-Cl was released as KCl at a temperature of about 700-800 ^{o}C and a higher fraction of K is released from fuel with higher Cl content. In contrast, Si was found to reduce the devolatilization of K due to the incorporation of K into the silica matrix. Up to 55% of fuel sulphur was released at 500 ^{o}C as a result of the release of organic S-compounds.

After vaporization, alkali encounters the complex chemical environment that affects the conversion of the alkali in the gas phase. Thus, alkali may exist in the gas phase in the form of sulphate (K_2SO_4), hydroxide (KOH) or chloride (KCl). KCl dominates when the Cl content in the fuel mix is high. Chlorine in biomass is mainly released as HCl, or as metal chlorides such as KCl. The chlorine content in the biomass often dictates the amount of potassium released during the combustion and it also strongly influences the transport of the alkali from the fuel to the heating tube surfaces, where the alkali often forms sulphates. The presence of KOH in the gas phase is favoured by increasing the temperature, and the high content of the water vapour (H_2O) and low content of HCl.

Christensen et al. (1998) has developed a model for the particle formation during the cooling of a flue gas from the combustion of fuels rich in volatile alkali species. According to that model, suphate seeds are formed by the homogeneous nucleation of K_2SO_4 vapours at approximately 1073 K. When the flue gas cools down, KCl condenses on these nuclei. This interpretation has been validated by experimental observations on the aerosol formation from alkali chloride in the flow reactors (Christensen et al. 1998). Moreover, Iisa et al. (1999) provide detailed measurements on the rate of sulphation of KCl in gas and condensed phases and they have demonstrated that the rate of sulphation is considerably slower in the condensed phase.

Jensen et al. (2000) studied the formation of alkali sulphates during the cooling of a synthetic flue gas ($O_2/H_2O/N_2$) with alkali vapours in a laboratory flow reactor. In order to suppress the alkali chloride nucleation, SO_2 is added to the feed gas. This led to a significant increase in the concentration of effluent particles and this causes the inclusion of sulphate into the chloride composition.

Christensen and Livbjerg (2000) and Christensen et al. (1998) have studied the formation of potassium sulphate (K_2SO_4) in the flue gases of boilers fired with straw. They have measured the concentrations of sulphation dioxide (SO_2) and HCl in the flue gases, as well as the amounts of KCl and K_2SO_4 in fine particles. Further, the fraction of potassium in the fine particles was assessed as the sulphate varied from 7 to 100%. A theoretical model for the aerosol formation was used to predict the fine particle compositions and SO_2 and HCl concentrations from the known K, S

and Cl contents of the straw and the temperature profile in the boiler. The experimentally observed alkali sulphate has been found to be limited by the reaction kinetics. Their model suggested that K_2SO_4 condensed homogeneously and that the condensed K_2SO_4 served as condensation nuclei for the KCl condensation.

Several authors have reported that KCl and K_2SO_4 are able to condense directly from the gas phase and as a result an appreciable vapour pressure of KCl and K_2SO_4 are produced (Backman et al., 1985). In the light of this, Tomeczek et al. (2004) developed rate and equilibrium constants for NaCl and KCl sulphation. An equilibrium $Na_2SO_4(l) \leftrightarrow Na_2SO_4(g)$ and $K_2SO_4(l) \leftrightarrow K_2SO_4(g)$ between the liquid and gaseous phases was also assumed. They concluded that the reactions within the gaseous phase enabled the determination of partial pressures of the condensing vapours in the vicinity of the boiler tubes. Further investigations have revealed that the saturated vapour pressure of the alkali salt plays a larger role in the formation of the inner layer of the deposit on the super heaters (Akbar et al., 2010). The data from Valmari et al. (1998) suggests that it is virtually impossible for the alkali metals to form a sticking layer without transformation into alkali salts. At the moment, the transformation of alkali species in the gas phase has been modelled under the equilibrium assumption between the gaseous and liquid phases (Tomeczek et al., 2004). In a proposed chemical kinetic model, Glarborg et al. (2005) have described the conversion of gaseous (AOH) alkali hydroxide and (ACl) alkali chloride to K_2SO_4 (see Figure 2.5). The detailed formation of K_2SO_4 involves H_2/O_2, chlorine, sulphur, potassium chemistry and the interactions between them. The sulphation is initiated by the oxidation of SO_2 to SO_3, SO_3

subsequently reacts with *A*OH or *A*Cl to form an alkali hydrogen sulphate ($KHSO_4$) or an alkali oxysulphation chloride (ASO_3Cl), and they, in turn, form K_2SO_4 under sufficiently stable conditions in the gas phase. In Hindiyarti et al. (2008), sulphate aerosol formation was analyzed based on calculations with a detailed gas phase mechanism. The rate-limiting step was thought to be the oxidation of sulphite to sulphate, rather than the oxidation of SO_2 to SO_3 as proposed previously.

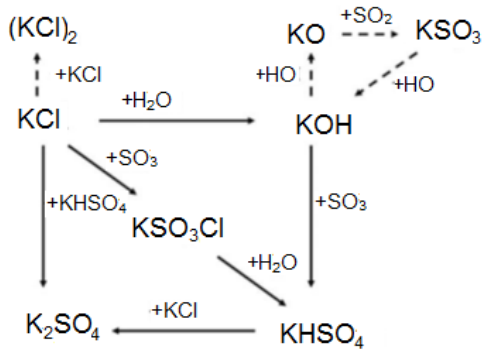

Figure 2.5: Pathway diagram for potassium transformations (Glarborg et al., 2005).

2.3.2 Fly Ash Particles

Fly ash is a by-product of the solid fuel combustion which becomes entrained within the flue gas flow. Ash, which is not entrained into the flue gas flow, is called bottom ash. The particles of fly ash usually leave the combustion zone along with the flue gas but some are left on the furnace wall and the heat exchange surface as deposits. Further, the particles in the flue gas contribute to the ambient air pollution. These airborne particles are removed by a mechanical collector, electrostatic precipitator or a wet scrubber.

Obernberger et al. (2001) gave a detailed description of how ash materials are generated, particularly fly ash and aerosol particles, from the grate firing of biomass materials. The authors characterized the particles of different sizes which includes fine particles that consist of aerosols with diameters between 0.1 and 1 µm and coarse particles which mainly consist of non-volatilized ash residuals with diameters of 1 µm and 100 µm. The sub-micron aerosols are formed by the condensation from the vapour phase of alkali metals and some heavy metal compounds, principally as chlorides and sulphates. During the combustion of wood on a grate furnace, the fly ash and aerosols released are transported by inertial impaction (entrainment of ash in the gas flow), nucleation, coagulation, condensation and gas phase reactions (KCl, K_2SO_4) as shown in Figure 2.6.

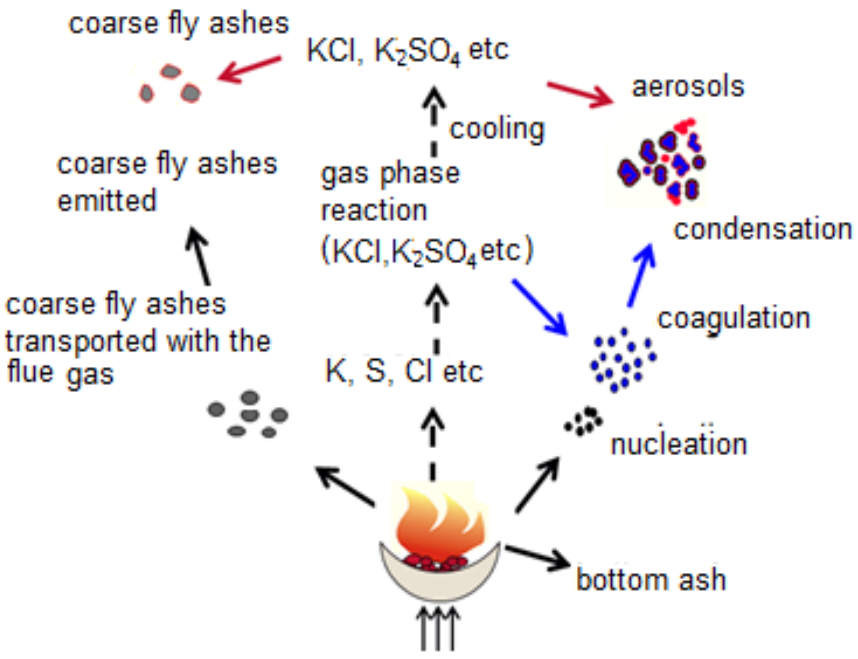

Figure 2.6: A schematic diagram of the fly ash and aerosol release from the combustion of wood on a grate (Obernberger et al., 2001).

During the combustion of bark, Obernberger et al. (2001) found higher contents of Ca and Mg which they predicted to originate from mineral particles entrained from the bed of the grate furnace. The size of the biomass fuel particles is about 10 times larger than that of the pulverized coal particles (Ma et al., 2006) and the transportation of fly ash depends on the fluid dynamics and size of the ash particles. The delivery mechanism of particles with a size smaller than about 10 μm is thermophoresis, which could cause the deposition to take place at the side and the rear of the tube space (Tomeczek et al., 2004). This implies that the deposition on the front side of the tube is mainly as a result of inertial impaction.

2.3.3 Deposit Formation

Deposit formation can be considered as a sequence of events which consist of the arrival and the adherence of particles to the tube or boiler wall surface. The inorganic constituents in the biomass are incorporated into the fly the ash particles which may deposit on the heat transfer surfaces. Deposits found can be divided into two types: slagging and fouling. Slagging occurs in the boiler regions where heat transfer is predominantly by radiation, whereas fouling deposits are formed in the colder sections of the boiler. A process that is common to both slagging and fouling is sintering which is the fluxing together of the deposit particles to a more hardened form. Depending on the composition of the ash, ash deposits may be subjected to distinctive visual differences ranging from lightly sintered deposits to completely fused deposits (Hutchings et al., 1996).

The reaction mechanism based on condensation and heterogeneous reactions occur during the initial stages of the deposit formation, and then at

a later stage matured deposits are formed by inertial impaction. In the first stages of the initial deposit, the tube surface is assumed to be clean and relatively cool; only cool unsintered deposits (condensed or partially molten particles) can adhere to the surface. The initial deposit is thought to have a very low thermal conductivity (0.1 $Wm^{-1}K^{-1}$) and as a result of which the ash build-up on the tubes and this produces a decrease in the net heat transfer through the ash layer. This affects the surface temperature, and thereby increasing the deposit thickness. With an increase in the surface temperature, the deposit melts and slags, and then moves from a weak deposit layer towards a strong deposit and eventually to a completely molten slag (Van Dyk et al., 2005).

Jensen et al. (2004) investigated the layers of mature deposit in 33 and 100 MW straw-fired boilers. Their results revealed that the thick deposit (2-15 cm) consisted of three layers. The innermost layer is made up of KCl and K_2SO_4, the intermediate layer is depleted of Cl but enriched in Si, K and Ca, the outermost layer consistes mainly of Si and Ca, glued together by KCl and K_2SO_4. Although the thickness of the deposit has been attributed to three layers by Jensen et al. (2004), Cundick et al. (2007) further classified the deposits thickness into four layers which includes the particulate layer (initial deposit), sintered layer, solidified slag layer (frozen) and slag layer (molten liquid) as shown in Figure 2.7. The authors suggested that at high temperatures, when the slag layer becomes thick enough, the slag may insulate itself to the point that part of the slag may freeze. The formation of each of these four layers from the same ash may vary widely in density and thermal conductivity. To this end, Cundick et al. (2007) developed a model to

describe the changes that a deposit experiences as it grows and implemented this into a 2-D boiler model.

Several authors have reported that different locations of the heating surface have different formation mechanisms of the deposition (Niu et al., 2010; Tomeczek et al., 2004; Forstner et al., 2006). A study performed on matured deposits in a 12 MW biomass fired grate furnace on three superheaters (i.e. fourth, secondary and first superheaters) shows that 1-20 cm thick deposits are formed. The fourth superheater shows high concentrations of aluminium and silicon that have trapped the alkali species to form alumino-silicate. While the secondary superheater contains high concentrations of K, Na and Cl, which form a sticky layer on the tube surface, and as a consequence traps the large particles (Si and Al). Initial deposits, comprising of K, Na and Cl, were observed on the primary superheater (Niu et al., 2010). Furthermore, the authors reported the presence of a loose and porous layer that has good insulating properties. This reduces the heat transfer on the heating surfaces and raises the temperature of the deposit on the outer surface.

In a related work by Niu et al. (2010b), deposits were collected on the surface and upstream of the bag filters in a 12 MW biomass-fired grate furnace. Deposits on the surface consist of K, Cl, S and Na as major elements, whereas high concentrations of Si, Al and Ca were obtained in the upstream region of the boiler. The presence of layers of K, Cl and S (as KCl and K_2SO_4) adjacent to the surface of the tube have been confirmed by many studies involving various kinds of biomass fuel (Jimenez et al., 2005; Valmari et al., 1998). Experimental work on the combustion of biomass

shows that K_2SO_4 nucleates when the gas temperature decreases (Valmari et al., 1998) while KCl condenses at low temperatures on the nucleon of K_2SO_4 (Jimenez et al., 2005).

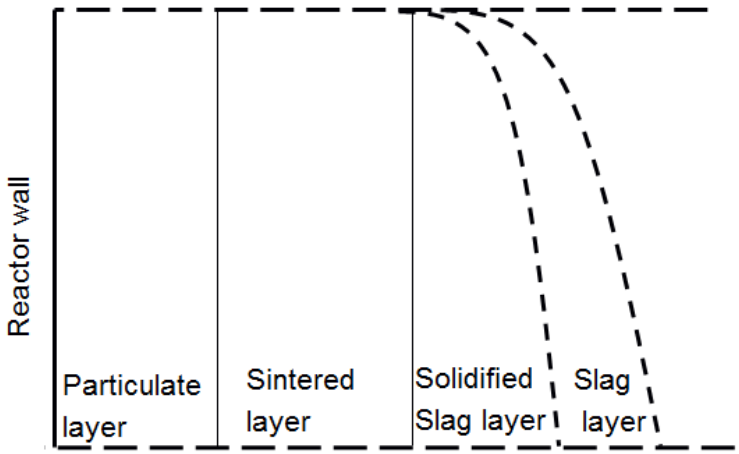

Figure 2.7: Schematic deposit formation layers (Cundick et al., 2007).

Robinson et al. (2002) investigated the influence of coal-biomass co-firing on the ash deposition on a pilot scale. The pilot scale experiments were performed under conditions representative of those found in the superheater region of pulverized-coal boilers. The fuels used in the blends include three types of bituminous coal, sub-bituminous coal, two types of straw, switch grass and wood. A reference test of unblended fuel was established as a baseline for comparing the results from the co-firing tests for each fuel. They found that the ash deposition rates for the coal-biomass blends fall within the range of the observed behaviour of the that of unblended fuels. Furthermore, the deposition rate of co-firing coal-straw was higher than unblended coal, but lower than for unblended straw. Similarly, the deposition rate of co-firing coal-wood is slightly lower than that of unblended coal. Figure 2.8 shows the general schematic of the fuel

interaction during the co-firing of coal with biomass. While coal releases silicate into gas flow, biomass release alkali. The interaction between coal and biomass during co-firing produces Ca/Si based aerosols and condensates in the form of KCl and K_2SO_4. The conclusion is that the primary interaction between the biomass and coal during co-firing is the reaction of the sulphur from the coal with the alkali species from the biomass. It is therefore demonstrated that co-firing of coal with biomass can serve as a mitigation factor for some of the fouling difficulties associated with the combustion of high-fouling biofuels.

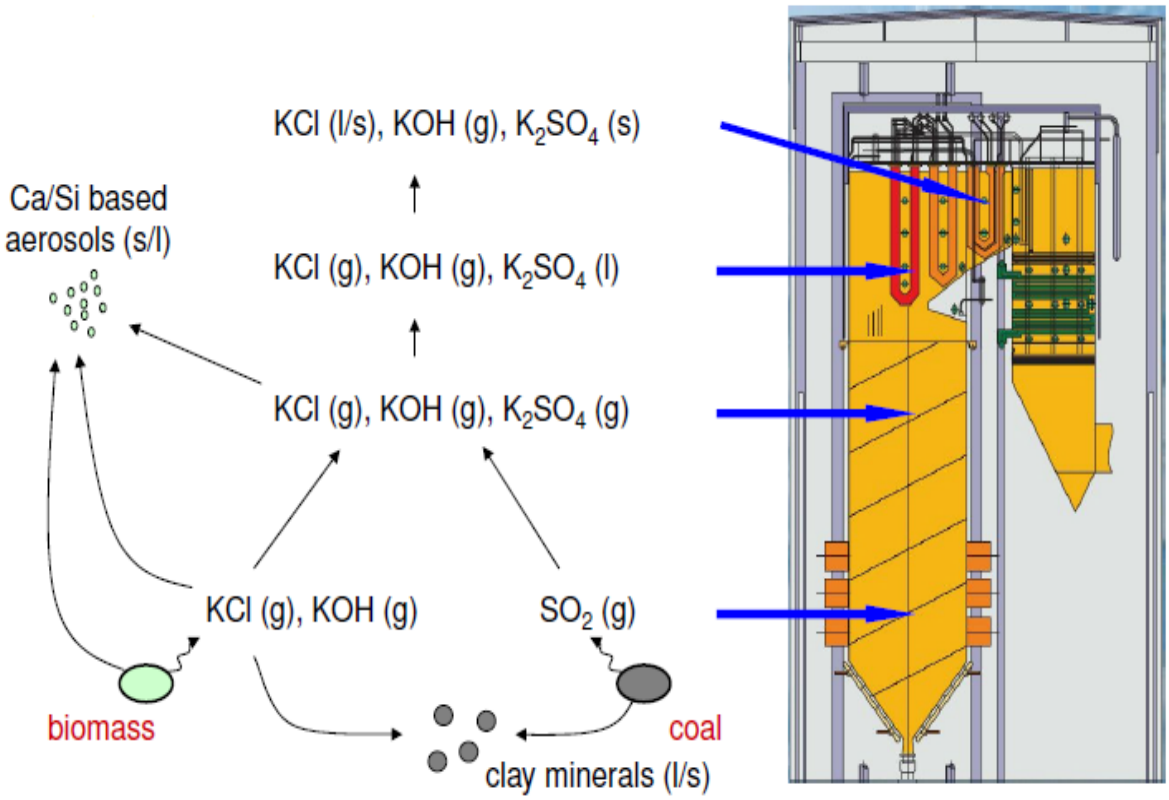

Figure 2.8: General schematic of fuel interactions (Kiel, 2008).

Pronobis (2006) investigated the boiler fouling and efficiency for co-combustion of biomass with bituminous coal in a pulverized fuel steam

boiler. Biomass with different chemical properties has been taken into consideration: straw, wood and dried sewage sludge. It was concluded that the properties of the additional fuels aggravate deposition. In this regard, the sewage shows a deterioration when 20% sludge was co-fired with coal. In terms of the boiler efficiency, the reduction in the fuel consumption is higher than the boiler efficiency loss. Therefore, biomass co-firing was agreed by Pronobis (2006) to be advantageous.

It has often been stressed that ash deposition cannot be properly understood without considering the coal minerals and biomass salts interaction (Zheng et al., 2007). Figure 2.9 shows a general schematic of fuel interaction between biomass and coal. As a product of these interactions, ash particles with a low fusion temperature are generated and this leads to partial melting. When such partially molten ash particles hit the tube surfaces, they become sticky on the surfaces. Zheng et al. (2007) investigated the interaction between coal and straw ash and the effect of the coal quality on the fly ash as well as the deposit properties in an entrained flow reactor. The coal used includes two bituminous coals and one lignite coal. Their results revealed that there is a competition for potassium capture between sulphation and silicate. The chlorine concentration in the ash may be decreased through an increment in SO_2 concentration in the gas. Furthermore, potassium sulphate can react with silica and alumina to form more stable potassium aluminosilicates. Also, in the high flame temperature region (>1300) KCl, can directly react with alumina and silica to form potassium aluminosilicates and release chlorine to the gas phase. In addition to some of the guidelines for practical co-firing of straw with coal in pulverized fuel systems which this finding provides, the ash content

produced as a by-product meets the requirements of the fly ash used in concrete and cement. In conclusion, the deposition can be estimated to some extent by the fuel composition.

In a detailed review of co-firing technology, Leckner (2007) presented several options: co-firing coal in pulverized or fluidised bed boilers, combustion on additional grates inserted in coal fired boilers and combustors for added fuel coupled in parallel to the steam circuit of a power plant. In addition, biomass can be used for the reburning in order to reduce NO emissions, or for after burning, to reduce N_2O emissions in fluidised bed boilers. The combination of fuels can aggravate or mitigate synergy effects of the interactions between S, Cl, K, Al and Si. With a better understanding of fuel interactions, the positive effects can be utilised and the negative ones can be avoided.

Molcan et al. (2009) investigated the co-firing of pulverised coal directly co-milled with 5–20% biomass on a 3 MW_{th} combustion test facility. Their results suggest that the biomass replacement to coal would improve the combustion output because of the lower carbon monoxide concentrations and higher char burnout level in co-firing. Furthermore, flame stability has been found to be closely linked to the NOx emissions and the reduction in SOx emissions have been found in general for all co-firing cases. The authors suggest that, due to the variability in the physical and chemical properties of the biomass fuels, the replacement of coal with biomass may have a significant impact on the combustion characteristics in a very complex manner.

Munir et al. (2010b) have studied the energy potential of shea meal coal, cotton stalk/coal, sugar cane bagasse/coal, and wood chip/ coal blends in a 20 kW pulverized coal fired combustor. The experiments were set up for biomass blending with 5, 10, and 15% thermal input. The results revealed that agricultural residues have larger fractions of cellulose and acid cellulose hydrocarbons, which indicates less aromaticity as opposed to coal. It was also revealed that co-firing agricultural residues with coal has a positive impact on NOx, SO_2 reduction, and carbon burnout. However, slagging and fouling indices for coal ash fusibility displayed mixed results when applied to pure agricultural residue ash. Biomass fuel nitrogen is known to form NH_3 in contrast to coal nitrogen which tends to form HCN. It is suggested that co-firing agricultural residues with coal may have larger effects on NOx reduction when operated under air and fuel staging conditions.

2.3.4 Deposit Sintering

Deposit sintering can be considered as a process that takes place when ash is transformed into a compact or hardened material. The data from Kupka (2009) suggests that the ash deposits on the heat transfer surfaces can be sintered and difficult to remove by sootblowers after just a few hours of deposition time. The problems of deposit sintering in the combustion plants includes the formation of the sintered ash deposits on the heat transfer surfaces that reduces the heat through the boilers, resistance in the cleaning of the deposited ash, and, occasionally, this may cause mechanical damage to the heat transfer surfaces. The deposit characteristics throughout the radiative section can change in character, varying from dusty accumulations, sintered and subsequently become completely molten

(Kupka, 2009). In general, deposit formations can be described in terms of two interacting mechanisms, the deposit growth and the strength development. As the deposit grows, the temperature profile throughout the deposit changes, which affects the strength development. Finally, the strength development is generally due to one of two sintering mechanisms, namely, silicate and salt-based.

Silicate-based sintering: Silicate-based sintering is controlled by the transport and stickiness of highly viscous melts which may occur when silica is present in the ash. The capability of silica to form a glassy melt phase, which does not recrystallize when the temperature decreases below their first melting point, is a problem (Skrifvars el al., 1998). Kamiya et al. (2002) have analysed the cohesion behaviour of the ash particles using two ash powders. The two ash powders, which includes ash collected in pulverized coal combustion and model ash powders prepared from fine pure amorphous silica powder coated and heat-treated on the surface with 0.5 wt % sodium and/or potassium. The results show that a small amount of low melting- point eutectic materials, consisting of amorphous silica and alkali metal, for example, $K_2O.4SiO_2$, whose melting point was about 770 °C formed a liquid phase and that this was responsible for the majority of the increase in the adhesive force mechanism of the ash powders at high temperatures.

Salt-based sintering: Salt-based sintering is attributed to low viscous melts, such as mixtures of sulphates, chlorides and carbonates of sodium, potassium, calcium and magnesium which may subsequently fill the pores in the deposit (Backman et al., 1999). The fraction of the melt phase is crucial

for the deposit growth. It has been found that the melt phase between 10-20 wt.% in the ash is enough to cause deposit formation, while the melt phase between 60-80 wt.% can cause the ash to be so wet that instead of causing further deposit growth, they flow down a vertical tube (Skrifvars et al., 1998).

The sintering of ash can be predicted using several types of methods which are based on the different ash properties, such as compressive strength test, viscosity measurement, ash fusibility test and empirical correlation based on composition of ash or fuel.

Ash Fusibility Test (AFT): An ash fusion temperature (AFT) is one of the most important parameters used in order to predict the melting behaviour of coal ash in power generation reactors. AFT predictions are functions of the oxide composition of the solid fuel, which means that estimations are only as good as the characterization of the ash. Thus industrial practice shows that at temperatures much lower than the ash softening temperature, hard or sintered deposits are formed.

When heat is applied to an ash sample with a temperature ranging between of 1000-1600°C, particles fuse and sinter and this can form a molten slag. These changes serve as a basis for ash fusibility test (AFT) (see Figure 2.9). The AFT test implies the controlled heat-up of an ash specimen of a well-defined shape and the simultaneously determination of temperatures corresponding to specified geometrical shapes as shown in Figure 2.9. In this way, the progress in melting is described by four characteristic temperatures (corresponding to three or four specified geometrical metrical shapes). The cone before fusion (CBF) is an ash cone with a tip apex. The initial deformation temperature (IDF) of the ash cone is

the temperature at which the rounding of the tip of an ash cone is observed, and this is the temperature where the ash first softens and may become sticky (Wall, 1998). The softening temperature (ST) of the ash cone is considered to be the equality between the height of the cone and the base of the cone. The hemisphere temperature (HT) of the ash cone is taken to be when the height of the cone is half the cone width (Wall, 1998). The flow temperature is considered to be when the sample height is about 1.5 mm. Also, the ash fusibility temperatures can be related to the ash chemical composition. It has been emphasized that the temperature at which the initial deformation is observed is not the temperature at which ash melting begins, and many coal ashes have been found to start melting at temperatures far below the initial deformation temperatures.

Figure 2.10 shows the ash fusibility as a function of basic oxides (Couch, 1995; Bryers, 1996). The curves presented in Figure 2.10 indicate that severe slagging occurs when the sum of the basic ash elements (Fe_2O_3 + CaO + MgO + NaO + K_2O) is within the range of about 0.7–2 % and moving away from this range, in either direction, decreases the slagging severity.

The correlations between the chemical composition of coals and coal ashes from a wide variety of deposits and AFTs have been reported in Vassilev et al. (1995). In their study, X-ray diffractometry, differential-thermal, thermogravimetric and chemical analyses have been used for the characterization of ash samples. The results revealed a reliable explanation and prediction for the characterizing of the fusion of the coal-ash minerals, their quantities as well as their fluxing behaviour. Van Dyk (2005) showed

that Fe, Na, and K are responsible for significant changes in the AFTs. Their work confirmed the suspicions of other researchers, e.g. that AFT analysis alone does not indicate exactly at what temperature the first melt occurs.

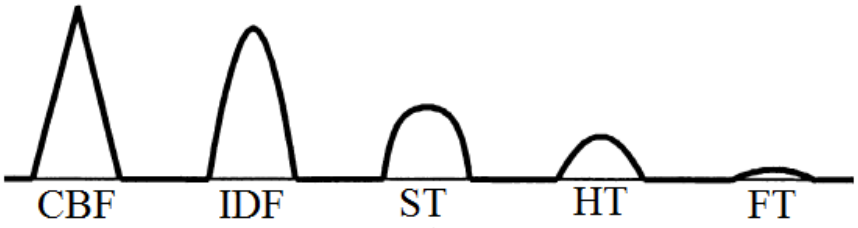

Figure 2.9: Schematic of the US standard of ash fusion cone behaviour as it is heating at different fusion temperatures (Evgueni et al., 2002).

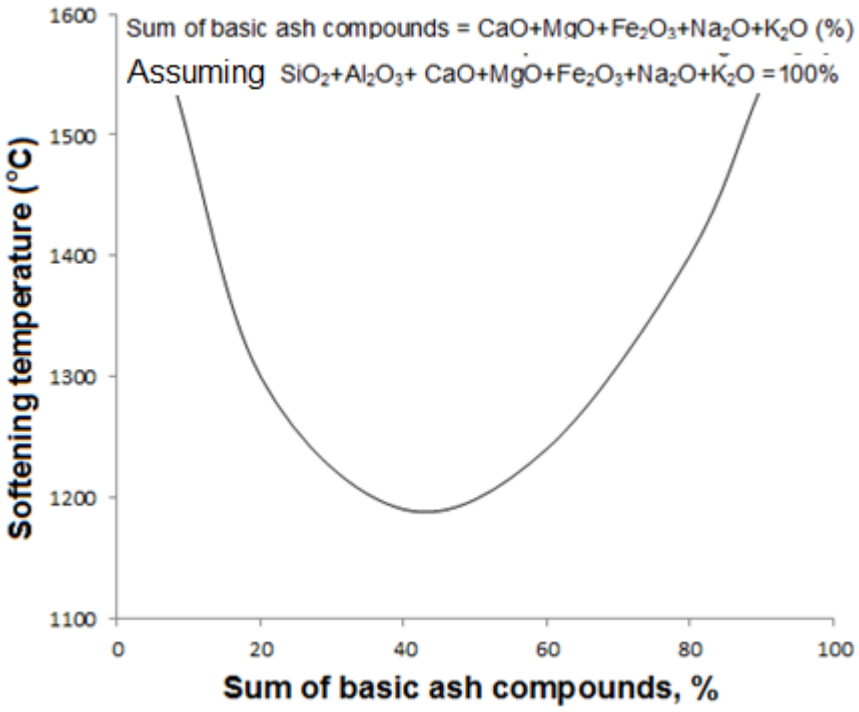

Figure 2.10: Ash fusibility as a function of basic ash elements (Couch, 1995; Bryers, 1996).

Compressive strength test: To determine the sintering behaviour, an ash pellet is heated in a laboratory furnace for 16 hours in air or flue gas at a pre-determined temperature. Two types of ash can be used – those

generated by solid fuel burning in a laboratory muffle furnace at a temperature 815^{o} C and fly ash and slag deposits collected directly from the industrial furnace. In this case, ash pellets are prepared from slag by milling. Using this method, the sintering tendency at different temperatures, deposition times and gas compositions can be determined (Kupka, 2009). Kupka (2009) used this method to study the ash effect in the co-firing of coal with three biomass fuels (saw dust, sewage sludge and refused derived fuel - RDF). He observed significant differences in the strength development with temperature between the ash pellets of the parent fuels and concluded that the differences in the ash chemistry between the parent fuels is responsible for the strength development. Higher content of phosphorus, iron and calcium (P_2O_5+Fe_2O_3+CaO) in sewage sludge shows strong compressive strength, while woody fuel (saw dust) has only a marginal effect on the compressive strength. Also the influence of the particle size on the comprehensive strength was tested for three different Middleburg coal ashes: an ash produced in the laboratory muffle furnace at a temperature 815^{o}C (6μm), cyclone ash (diameter, 10 μm) and drum ash (diameter, 18 μm) (Kupka, 2009). The results revealed an inverse relationship between the compressive strength and particle size – while the particle size increases, the compressive strength decreases and the effect is stronger at higher temperatures.

Viscosity: Viscosity reflects the extent to which fluid opposes the flow and it can be thought of as a measure of the internal friction of the fluid. The relationship between the viscosity of ash slag and the temperature provides a useful insight regarding the melting behaviour and flow characteristics of ash slags. The melting behaviour of ash materials is linked to the stage of

deformation obtained by heating cone-shaped ash samples at different temperatures (Van Dyk et al., 2005).

Table 2.3: Viscosity scale for bituminous coal ashes (Raask, 1985).

Event	Viscosity range (Ns/m^2)	Temperature (^oC)
Flame region		
Silicate particles deformation	10^3-10^7	1270 – 1400
On boiler tubes		
Onset of sintering	10^9-10^{11}	930 – 1030
Medium sintering	10^7-10^9	1030 – 1130
Rapid sintering	10^5-10^7	1130 – 1280
Formation of nonflowing slag	10^3-10^5	1280 – 1380
Slow movement of slag due to gravity	10^2-10^3	1380 – 1430
Satisfactory flow from cyclone-fired boilers	<25	>1430

Viscosity in the case of coal-rich silica which possesses strong covalent bonds is extremely high. With the successive addition of biomass, rich alkali oxide which exhibits a high ionic behaviour, the silica covalent bond breaks down and, consequently, the viscosity decreases gradually with increasing alkali oxides (Richardson, 1974). It has been demonstrated that the viscosity of the liquid phases present in the ash deposits is inversely proportional to the sintering of them (Raask, 1985). Table 2.3 illustrates the viscosity scale for bituminous coal ashes injected into a flame including ash

deformation, sintering and slagging. This demonstrate that the viscosity present in the ash deposit is inversely proportional to the rate of sintering them and it decreases rapidly at elevated temperatures.

2.4 Prediction of Ash Deposition

Numerical prediction of ash deposition is used to advance the understanding of the underlying processes that lead to deposit formation, and it is considered as a powerful tool for the design and optimization of the operating parameters. Several attempts have been made to accurately predict the slagging and fouling behaviour of solid fuels in boiler situations. Slagging and fouling indices derived from the ash composition are simple models used to predict the ash behaviour in advance before the actual plant operation. Thermodynamic calculations used to assess the melting behaviour of fly ash particles and slags are another class of models. The most popular models of ash deposition are CFD-based ash deposition models which combine the complex aerodynamics of a boiler with the basic mechanisms of ash transport in the boiler.

2.4.1 Slagging Indices

A number of indices have been development for the assessment of the propensity of coal and other solid fuels, ash to slag or foul. Over the years, many mathematical indices have been developed and a detailed description of the working principles of the indices is presented in Raask (1985), Wigley et al. (1990) & Kupka (2009). In general, these indices take into account either the fuel ash content and the ash chemical composition, or experimental data from experiments that have been performed on small

samples of fuels. Table 2.4 shows some of the frequently used slagging indices. For the most part, these indices have been developed originally for the assessment of coals, and are applied to biomass materials and biomass/coal ashes with appropriate modification. For example, the basic to acid ratio has been modified by adding a phosphorus component to the basic oxides in order for the indices take into account of biomass materials that are rich in phosphorus oxides.

The majority of coal slagging indices relate the chemical composition of the ash with the slagging tendency. For example, the ratio of the basic metal oxides (Fe_2O_3, CaO, MgO, NaO and K_2O) to the acidic metal oxides (SiO_2 and Al_2O_3). This index is important for the melting behavior of alumino-silicate coal ash and the application to biomass ash systems, which have different chemical properties, and therefore this can be misleading.

For co-firing biomass with coal, the interaction between the coal and biomass salt are the key components of the ash deposition model. Therefore, it is expected that the alkali metal in most biomass fuels and in some crops that the phosphorus metal may act as a strong flux for alumino-silicate systems. As a consequence, the fusion temperature of the co-firing biomass will reduce. At relatively low levels of co-firing biomass, alumino-silicate is predominant and the coal slagging index remains valid. However, at higher co-firing ratios, the fluxing agents in the biomass ash become very important and the coal slagging index cannot be applied to biomass with confidence.

Since fouling is initiated by a thin layer of material of condensed vapour, the composition of the fouling indices are the alkali content of the

fuel. Most fouling indices are therefore based on the sodium and potassium contents of the fuel (Miles et al., 1995). Moreover, in vapour condensation of alkali species, the metal surface temperature of the heat transfer surface plays a key role. The importance of the surface phenomena has been utilized in previous research, e.g Xu et al. (2007). Xu et al. (2007) have developed a fouling index based on the gas temperature, probe surface temperature, coal melting temperature and mineral percentage and they have found that the results obtained from the fouling index calculation replicate the experimental data on fouling.

Table 2.4: A summary of the indices for the determination of the slagging and fouling propensity (Wigley et al., 1990; McLennen et al., 2000 & Vamvuka et al., 2004).

Index		Slagging range			
		Very high	High	Medium	Little
Base/Acid ratio	$R_{B/A} = \frac{Fe_2O_3 + CaO + MgO + K_2O + NaO}{SiO_2 + Al_2O_3 + TiO_2}$	>0.5 – slagging danger			
Flux/Sinter ratio	$R_{B/A(+P)} = \frac{Fe_2O_3 + CaO + MgO + K_2O + NaO + (P_2O_5)}{SiO_2 + Al_2O_3 + TiO_2}$	0.72-2			0.3-0.4
Fouling index	$Fu = R_S \cdot \frac{Na_2O + K_2O}{S_{dry}}$	>40	0.6-0.4	<0.6 – no fouling	
Iron index	$Fi = Fe_2O_3 \cdot R_{B/A}$	>2.0 – high		<0.6 – low	

2.4.2 Thermodynamic Equilibrium Calculations

The inherent problems that are generally encountered with equilibrium calculations have been demonstrated in the early works on the prediction of combustion behaviour (Wibberley et al., 1982; Michal et al., 2005). One such problem is the lack of a thermodynamic database on some of the ash species and their reactions which may be important. Another problem is the attainment of an equilibrium state under the assumption that all the reactants are well mixed (homogeneous), and that the reactions are able to reach equilibrium. In reality, neither of these assumptions is completely true. Nevertheless, thermodynamic equilibrium calculations may be used to quantify the composition and the amount of the gas phase, liquid phase and solid phase during the complex combustion processes. The principles behind the algorithms in the commercial software is the minimization of the Gibbs free energy. One popular software is FactSage, which is a merged product from Fact – Win and ChemSage programs (Bale et al., 2002).

Wibberley et al. (1982) have investigated the behaviour of alkalis in the furnace gases of pulverised-coal-fired boilers by using a thermodynamic calculation tool. Their findings imply that a large portion of the volatile sodium in the coal reacts with the silica fly ash and forms a low viscosity surface layer of sodium silicate on the ash. Another practical example of the formation of silicates is suggested by the equilibrium calculations with Si originating from coal ash (Michal et al., 2005). Some influence of sulphur on the alkali capture and the formation of alkali sulphates was also observed in

equilibrium calculations in the case of straw with a high sulphur content (Hansen et al., 2000). Thermodynamic calculations should be applied with great care since information on accurate equilibrium constants for many species involved in the reactions are not available. Caution should be exercised in investigating very complex systems that are kinetically controlled, such as the formation of sulphates (K_2SO_4 and Na_2SO_4). The main difficulty in the determination of alkali vapours is in knowing the speciation (quantitative distribution of an element) of the alkali species during devolatilization and char combustion and often measurements are needed for the fuel under investigation. The thermodynamic data base needed for such calculations is far from being complete and requires upgrading and maintenance.

2.4.3 Chemical Kinetics

After vaporisation in biomass combustion, the alkali released may react with the sulphur in the flue gas and other elements in the ash compounds that form deposits on accessible parts of the boiler, particularly on the heat exchanger surfaces. The reaction rates are slower than the reactant mixing rates and therefore the thermodynamics equilibrium calculation is not applicable. For example, the thermodynamic data base needed for sulphation can be misleading (Weber et al., 2011). Such reactions may be kinetically controlled and therefore should be treated only with the kinetic data.

A recent study on the kinetically controlled conversion of SO_2 to SO_3 is provided by Jorgensen et al. (2007). In this study the conversion of SO_2 to SO_3 experimentally with an inlet flow consisting of 500 ppm SO_2, 60% O_2 0-

1% H_2O, and the remaining balance was N_2. The SO_2 conversion has been performed under a trace amount of water condition in a temperature range of 1000-1400 K. Parallel to the experimental investigation, numerical calculations were performed using the chemical kinetic model of Hindiyarti et al. (2007) and also chemical equilibrium calculations were also performed. Their results, see Figure 2.11, revealed that while the chemical kinetic predictions (solid lines) are in quite good agreement with the experimental data (Δ), but the equilibrium calculation (dashed lines) shows a significant deviation in the temperature range 1250-1323 K and the detectable conversion of SO_2 was not obtained in the temperature range 1023-1250 K. These findings suggest a strong dependence of the kinetic rates on the temperature.

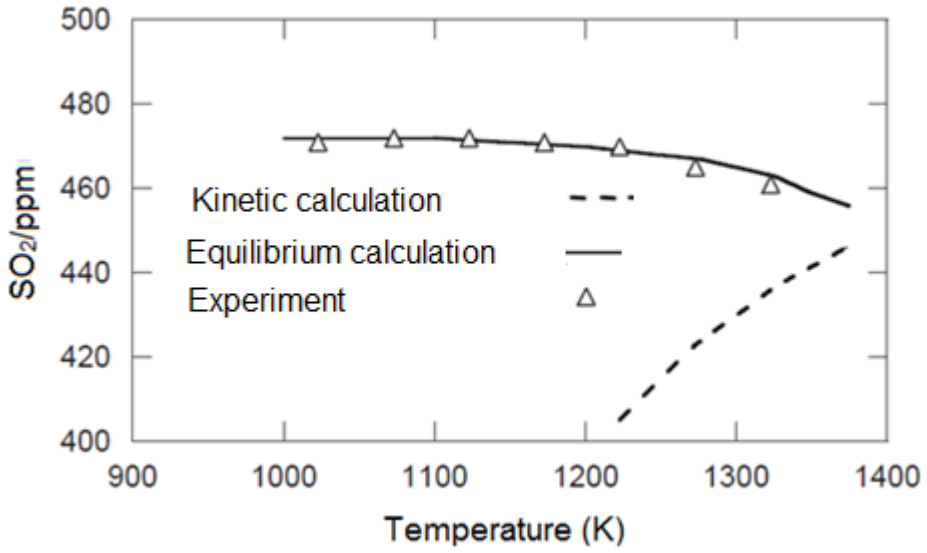

Figure 2.11: Comparison of the experimental data and the prediction of the oxidation of the SO_2-SO_3 in the temperature range of 1023-1323 K (Jorgensen et al., 2007).

2.4.4 CFD-Based Ash Deposition Models

Nowadays, the advance in the computing resources in terms of memory usage and central processing unit (CPU) time has brought CFD-based models close to reality. Consequently, CFD has a wide range of acceptability as a design tool and the publications in the open literature are now broadly categorized as being either experimental or computational. The increasing availability of user-friendly CFD software has made it possible to combine fundamental deposition models with complex flow patterns that are typical of those that occur in a boiler.

One of the earliest studies on 3-D ash deposition modelling has been performed on a straw-fired grate boiler situated at the Masnodo CHP plant, Denmark (Kaer et al., 2003). Commercial CFD software has been used to model the deposit on the furnace walls and the superheater tubes in the boiler using the commercial FLUENT software. The deposition model was implemented through the User Defined Functions (UDF) and a Graphical User Interface was included in the standard FLUENT interface to ensure ease of use. This allows the user to choose any of the standard FLUENT models to solve for the fluid dynamics and combustion processes while at the same time being able to include the deposition model. The turbulence model chosen was the Renormalized Group (RNG) k-ε model and the radiative heat transfer used was modeled using the Discrete Ordinates Model (DOM) which is available in FLUENT. A two-step reaction mechanism was used for the gas combustion with CO as the intermediate species. The input size distribution and potassium content data and the furnace temperature were obtained through the gas phase calculations. The melt

fraction was used to predict the sticking probability based on the assumption that the sticking probability is proportional to the melt fraction (Nielsen, 1998). The results obtained showed the inertial impaction, vapour and boundary layer controlled deposition fluxes around the secondary superheater. It was concluded that the poor mixing in the furnace is a key issue leading to the high emission levels and the relatively high amount of unburnt carbon in the fly ash. The model was found to accurately predict the operational trends to be the same as in to the boiler experimental investigation (Kaer at al., 2006). However, a significant effort should be put into further improvements and validation of the modelling concept, especially with respect to the deposition on the tube bank model. In a related study, Mueller et al. (2005) developed a CFD sub-model for the molten alkali-rich fly ash biomass deposition near the furnace walls and the heat exchanger surfaces in an electrically heated entrained flow reactor. A sticking criterion adopted assumed that all particles with a melt fraction between 15% and 70% stick to the surface, according to Backman et al. (1999). The results of their finding show the effects of ash viscosity, species condensation and chemical reaction on the deposit build-up.

The viscosity of the liquid phase present in ash deposit is inversely proportional to the rate of sintering and will decrease rapidly at elevated temperature. In the work of Raask et al. (1985) viscosities in the range of 10^7-10^{11} Pa*s resulted in the formation of significant sintered deposits in coal-fired boilers.

Condensation of vapours that are produced in the flame during mineral matter decomposition and subsequent homogeneous reactions

within the combustion chamber, contributes to the deposition mass rate. Condensation occurs either heterogeneously on the tube surface, or homogeneously leading to a fume that deposits by thermophoresis on the tube surface. The condensed deposits influence the ash particles capture on the surface. Chemical heterogeneous reactions of gases with the deposit matter can also contribute to deposit mass. Among the most important reactions are: sulphation, alkalies absorption and oxidation. Silica absorbs alkali material to form silicates in deposits thus induces sintering and changes of deposit properties (Akbar et al., 2010; Tomeczek et al., 2004).

Ma et al. (2006) examined the biomass particle depositions in a 1MW pulverized fuel Combustion Test Facility (CTF) that is situated at the Power Technology Centre, E.ON UK plc. The P1 radiation model and the RNG k- ε model were adopted for the combustion calculations and about 300,000 computational cells were employed in the computational domain. The size of the wood particles that enter the furnace are 150 μm, 320 μm and 640 μm (the percentage of each size fraction cannot be found in the literature where this information was extracted). The turbulent gas phase selected was the eddy-dissipation model, whereas a global one-step reaction was considered in the two-step reaction mechanism. Further, the biomass burning was assumed to have occurred in two global steps: first, a homogeneous combustion and second, a heterogeneous combustion. In the homogeneous combustion, devolatilisation of the biomass particles occurred and the combustion in the gaseous phase took place whereas in the heterogeneous combustion, burning of solid char occurred. A combination of particle melting temperature and particle melt fractions has been used to estimate the stickiness of the particle and both are related to the potassium content within

the particle. The result of the model reproduces a genuine environment for the deposition of ash in the furnace, especially the release of the potassium species and the stickiness of the biomass particles. However the work did not consider the downstream location where the temperature drop permits the condensation of the alkali species to take place. The deposition of the vapour, as well as the particles on the furnace walls and boiler surfaces, has been covered by the deposition model of Forstner et al. (2006) in a pilot scale low NOx biomass furnace. The build-up of the deposit layer depends on the wall temperature and, the deposit porosity and the chemical composition is also taken into account in their deposition model. The results obtained for the modelling of the deposit formation for the furnace and grate-fired combustion were found to be plausible, although the results were not quantitatively validated. In another study, Venturini et al. (2010) reported the modelling of multiphase combustion and deposit formation in a biomass-fired furnace. The work underlines the capability of predicting the combustion conditions and, in particular, the growth rates of the deposits of different particle sizes over the furnace walls, as well as the radiative and convective sections for the particle deposition. These kinds of ash deposition serve as a basis for for application in coal/biomass co-combustion.

Plaza et al. (2009) investigated the effects of slagging and fouling when co-firing coal/biomass blends using a predictive model for large utility boilers. This model is based on the coupling of physical and chemical methods. For the physical model (Kouznetsov et al., 1973; Hesselmann, 1998), the Russian standard zone method to determine the midsection temperature distribution throughout a boiler was adopted while the thermo-chemical module, which utilizes the FactSage chemical database, was

adopted for the chemical method. The results obtained for the equilibrium calculations indicate the proportion of the ash in the solid or molten phase. Alongside the standard zone and equilibrium calculations, a complementary chemical fractionation approach (based on laboratory investigations for coal/biomass combustion) was investigated. The results indicate that the interaction between the alkali and silica give rise to low-melting temperature alkali silicates which, as a consequence, contributes to the melt phase that occurs in the boilers. All the ash particles are assumed to be 10 μm diameter spheres and, the application of this prediction is made for a 618 MW_{th} wall-fired pulverized coal boiler, co-fired with a typical medium volatile bituminous coal and two substitute fuels, sewage sludge and sawdust, for different co-firing ratios. The modelling results revealed that, for increased co-firing of sewage sludge, an increase in the danger of slagging and high-temperature fouling occurred. It is important to note that this contrasts with the effects which occur with the utilization of sawdust.

Doshi et al. (2009) developed a co-firing advisory tool to predict the ash release behaviour and chemical composition of inorganics during the co-firing of coal with biomass. Biomass samples considered for the study include wood chips, wood bark and straw. The advisory tool has been divided into four: (i) the determination of the speciation of biomass using pH extraction analysis, (ii) the classification of inorganic (ionic form and organically associated) within the coal and biomass during ash formation, (iii) the interaction of inorganics with those of the coal during combustion, and (iv) the condensation of inorganics during the cooling in the boiler tubes. The preliminary investigation of the interaction between the coal and biomass showed that the Al, Si and S elements in the coal may act as a

'buffer' on the biomass metals, and thus reduce the alkali gases that are being formed.

2.5 Conclusions

This chapter has discussed the properties of coal and biomass that are relevant to combustion. The emphasises has been placed on the three phases of the slagging process – initiation, ash deposition and sintering.

In the initial stages of slag formation, when the metal surfaces are clean and relatively cold (about 1000^{o}C or less), only the molten or partly molten particles can adhere to the surface, and the deposition rate is low. The dominant deposition processes are often the condensation of volatile alkali species. The released alkali species from the combustion bed to the gas phase and the subsequent condensation of alkali species with emphasis on potassium species has been reviewed.

In the ash deposition stages of slag formation, when the deposit on the metal surface is relatively thick and the temperature of the ash material at the outside surface of the deposit is about 1000^{o}C or more. The deposit surface becomes receptive to the fly ash particles which arrive by inertial impaction. The transport mechanism and the adhesion of the ash particles to the deposit surface have been reviewed extensively with an emphasis on the ash viscosity and the abundance of melted ash particles.

As the deposition proceeds for a short period of deposition time, the deposit gradually becomes sintered and harder. The general ash deposits are mainly composed of aluminosilicate glass with some proportion of basic

oxides (fluxing agents). It is the presence of basic oxides (fluxing agents) that determines the viscosity and rate of sintering.

There are not many publications where numerical predictions of ash deposition have been used to predict the slagging and fouling propensity in industrial boilers. Most of the publications have been concerned with coal ash deposition. At present, there are only a few published papers on numerical predictions on biomass ash deposition and the modelling work on co-combustion of coal and biomass is even rarer in the literature probably due to the fact that co-firing is a developing technology still in the testing phase.

Almost every publication on slagging and fouling underlines the primary importance of inertial impaction as the dominant mechanism of ash deposition compared to thermophoresis, chemical reaction or condensation. Condensation of alkali salts on the tube surface has been reported in the literature only to a limited extend for biomass ash deposition.

A number of attempts have been made to accurately predict ash deposition rates in boiler situation. Results of such research works continue to improve with the introduction of better prediction techniques/tools and mathematic models. Ash predictive tools such as slagging and fouling indices, equilibrium calculations and CFD models are commonly used. Slagging and fouling indices derived from the ash composition are simple and restrictive and therefore cannot be used for all kinds of coals and biomasses. Another class of model is based on thermodynamic calculations which only predict the evaporative transport routes for the element and species in the slag, but does not take into consideration the effects of particle entrainment, which are significant in combustion. The most popular

models of ash deposition are CFD-based ash deposition models which provide insight into the flow dynamics of a boiler where it is experimentally costly, difficult to achieve and time consuming. But at the present CFD models suffer from a lack in accuracy since the numerical methods rely on modelling assumptions that have not been validated to a satisfactory level. However, CFD models often can predict the trend correctly. In the case of coal-biomass co-combustion, additional complexities are introduced because of the behaviour of the ash. In this thesis, slagging index and equilibrium calculation were used to complement CFD calculation. While equilibrium calculation are used to provide insight into some of the observations made during the CFD calculation, the slagging index has been used to account for the effect of melting behaviour of biomass rich phosphorus contents that were absent in the proposed ash deposition model used in the CFD calculation.

Most of the papers on ash deposition model do not consider the contribution of the detailed alkali mechanism to the formation of deposition layer via condensation process, which are significant in biomass combustion. Also, ash viscosity and melting fraction methods are the sticking criteria widely reported in the literature for coal ash and biomass ash respectively. But, there is no modelling investigations that have taken advantage of combining the effects of ash viscosity and melting fraction methods in determining the ash stickiness for co-firing system.

Condensation occurs either heterogeneously on fly ash which is transported to the tube surface by inertial impaction or directly on the tube surface. Condensation on fly ash has not been address in the state-of-the-art literature. In this thesis, a mathematical model based on condensation on

fly ash and inertial impaction of ash particles have been developed. Another weakness of the state-of-the-art literature is absence of detail kinetic model to account for the gas phase reactions that occur during biomass combustion. In this respect, a reduced alkali kinetic model is proposed for alkali mechanism and the proposed kinetic model has been implemented in the prediction of deposition rate on the straw-fired grate furnace.

For the case of co-firing, a mathematical model have been develop that take into consideration of combining ash viscosity and melting fraction key components in calculating the stickiness of ash particles.

This Chapter has helped formulated of the direction of the thesis by reviewing the fundamental and frontier knowledges on the ash formation that occur in a typical solid fuel boiler. The slagging behaviour with regard to the deposit growth and sintering has been reviewed. The phenomenon of ash particle behaviour during the deposit formation discussed in Chapter 2 are the underlying principles used for the development of the mathematical models for ash particle deposition presented in Chapter 3. This chapter has critically reviewed the deposition behaviour of ash particles in boilers and this will help to provide guidelines for the deposition model that will be developed in the subsequent chapter.

Chapter 3

Mathematical Modelling

The purpose of this Chapter is to outline the basic governing mathematical equations and the numerical methods which are necessary for the work presented on this thesis. Firstly, the numerical steps required for any given reaction mechanism is covered. Secondly, the principles underlying the existing models that have been adopted and/or developed, including the ash particle deposition rates model, are presented.

3.1 Thermochemistry

Thermodynamic data are used in the calculation of the equilibrium chemistry. These data provide the enthalpy, entropy and specific heat of a given species at a specific temperature. The thermodynamic properties are calculated from 14 National American Space Academic (NASA) polynomial coefficients (Burcat, 1984; McBride et al., 1993; Griffiths et al., 1995) and for each species, seven are for the low temperature range (300-1000 K) and seven are for the high temperature range (1000-5000 K). Polynomial coefficients can be evaluated at a given temperature (T) to obtain the specific heat capacity (C_p^o), enthalpy (H^o) and entropy (S^o), as follows:

$$\frac{C_p^o}{R} = a_1 + a_2 T + a_3 T^2 + a_4 T^3 + a_5 T^4 \tag{3.1}$$

$$\frac{H^o}{RT} = a_1 + \frac{a_2}{2} T + \frac{a_3}{3} T^2 + \frac{a_4}{4} T^3 + \frac{a_5}{5} T^4 + \frac{a_6}{T} \tag{3.2}$$

$$\frac{S^o}{R} = a_1 \ln T + a_2 T + \frac{a_3}{2} T^2 + \frac{a_4}{3} T^3 + \frac{a_5}{4} T^4 + a_7 \tag{3.3}$$

where a_1, a_2, a_3, a_4, a_5, a_6 and a_7 are the NASA polynomial coefficients (Burcat, 1984; McBride et al., 1993; Griffiths et al., 1995) and R is the universal gas constant. The change of enthalpy (ΔH_j^o) and entropy (ΔS_j^o) that occur in passing completely from reactants to products in the jth reaction are defined as follows:

$$\frac{\Delta S_j^o}{R} = \sum_{i=1}^{I} v_{ij} \frac{S_i^o}{R} \tag{3.4}$$

$$\frac{\Delta H_j^o}{RT} = \sum_{i=1}^{I} v_{ij} \frac{H_i^o}{RT} \tag{3.5}$$

where v_{ij} is the Stoichiometric coefficient of species i in reaction j. The magnitude of heat release during ΔH_j^o and ΔS_j^o is dependent on the reaction rate, which in turn depends on the temperature. The interrelationship between the R, T, v_{ij} and H_i^o in equation (3.5) is described by what is known as the thermokinetic effect in which the chemical reaction rates and enthalpy change are computed simultaneously (Lignola et al., 1987).

3.1.1 Elementary Chemical Reaction Rate Equations

The rate of the change in the concentration of any species involved in a chemical reaction can be described in terms of the product of the concentration terms and a temperature dependent rate constant (or coefficient). This is often referred to as the rate law. In the present context, such descriptions refer to the series of the elementary reactions which make

up a kinetic mechanism, but also may refer to the single step reaction. The stoichiometric description of a chemical reaction may be represented by the simple generic form:

$$v_a A + v_b B + ... \rightarrow v_c P + v_q Q + ... \tag{3.6}$$

where v_i are the stoichiometric coefficients and are normally integer values for the elementary reactions and A and B are the reactants while P and Q are the products, respectively. The rate law with respect to the components A, B, P and Q take the following form:

$$\frac{-1}{v_a}\frac{d[A]}{dt} = \frac{-1}{v_b}\frac{d[B]}{dt} = \frac{1}{v_p}\frac{d[P]}{dt} = \frac{1}{v_q}\frac{d[Q]}{dt} = k_f [A]^a [B]^b \tag{3.7}$$

where k is the rate coefficient and [] represents the concentration of the quantities within the brackets. The orders of the reactions for the reactants A and B are represented by the powers a and b, respectively, and the overall order is given by the coefficient of the reactant, i.e. $(a+b)$ (Griffiths and Barnard, 1995).

An important description of the rate coefficient (A) for the temperature dependent reactions is the Arrhenius equation which is defined as follows (Kee, 1996):

$$k_f = AT^n \exp(\frac{E}{RT}) \tag{3.8}$$

where A is the pre-exponential factor, n is a dimensionless exponent of the temperature and E is the activation energy and these are the three Arrhenius rate parameters expressed in a mechanism. The sign '=' in equation (3.8) denotes reversible reactions. The forward rate equation (3.9)

is given by: the rate which is calculated using equation (3.8). The reverse rate (k_f) must be calculated through the equilibrium constant in the concentration units (k_c) as follows (Kee, 1996):

$$k_f = \frac{k_f}{K_c} \tag{3.9}$$

The equilibrium constant, k_c, is more easily calculated from the thermodynamic properties in terms of the pressure for each reaction. k_c is related to the equilibrium constant in the pressure units (k_p) using the following expression:

$$k_p = K(RT)^{\Delta v} \tag{3.10}$$

where Δv is the sum of stoichiometric coefficients products minus those of reactants, i.e. $(v_p + v_q + ...) - (v_a + v_b + ...)$. and k_p is obtained from (Kee, 1996)

$$k_p = \exp\left(\frac{\Delta S^o}{R} - \frac{\Delta H^o}{RT}\right) \tag{3.11}$$

3.1.2 Third Body and Reaction Fall-Off

Extensive analysis of the combustion systems has revealed that all the reactions cannot be represented by the rate parameter which may be fitted via the basic Arrhenius definition of the equation (3.8) (Kee, 1996). Therefore further explanations are necessary to enable the satisfactory fitting of the combustion data. To this end, a third body reaction which does not participate in the chemical interactions of a reaction, but are necessary for it to proceed, has to be introduced (Kee, 1996). For example, the reaction

$$H + O + M \rightarrow OH + M \tag{3.12}$$

obeys this criteria by producing a third body which does not participate in the chemical reactions of the reaction, and it has a rate that is defined as follows (Kee, 1996):

$$rate = k[H][O][M] \tag{3.13}$$

The symbol M is used to represent any molecule present in the system and it is known as a third body species, while [M] represents the total concentration of the molecular species present in the system. From equations (3.12) and (3.13), it can be seen that M remains unchanged but the rate at which the reaction proceeds is affected. In the literature, e.g. Griffiths et al. (1995), it has been shown that the third body is required to absorb some of the energy released by the reaction through the molecular collisions.

3.2 CFD Governing Equations

In modelling combustion systems, the fluid motion is described by a set of the partial differential equations. The main equations which determine the motion of the conserved quantities are called conservation equations. When compressible flow is assumed, the equations for the conservation of mass and the momentum can be used to establish the flow field. However, for reactive flows, additional transport equations for the enthalpy and species concentrations must be considered.

Turbulent flows are characterized by fluctuating velocity fields which are primarily due to the complex geometries and/or high flow rates.

Turbulence affects the heat and mass transfer and plays an essential role in some processes, such as biomass combustion in furnaces. The major efforts in the area of the turbulence modelling have been directed towards closely simulating the real behaviour of the turbulence with reasonable demands on the computational resources. As a consequence, a large number of the models have been developed over the last three decades or so. These modelling approaches can be grouped into three categories according to the accuracy of the predictions; the first is the Reynolds-Averaged Navier–Stokes equations (RANS) followed by the large eddy simulations (LES) and then the direct numerical simulations (DNS). As one progresses from RANS to DNS, more and more of the turbulent motions are included into the physics and, therefore, the computations become more complex. RANS resolves the time-averaged equations for fluid flow whereas in DNS all the motion contained in the flow are directly resolved while in the LES, the larger eddies are resolved but the smaller eddies are modelled through sub-grid models.

3.2.1 Fluid Flow Equations

In generally, the governing equations for fluid flow (representing the continuity, equation (3.14); momentum, equations (3.15)-(3.17); and energy equation (3.18), are given as follows (Versteeg et al., 2007):

$$\frac{\partial \rho}{\partial t} + div(\rho \bar{u}) = 0 \tag{3.14}$$

$$\frac{\partial \rho u}{\partial t} + div(\rho u \bar{u}) = -\frac{\partial p}{\partial x} + div(\mu grad\, u) + S_{mx} \tag{3.15}$$

$$\frac{\partial \rho v}{\partial t} + div(\rho v \bar{u}) = -\frac{\partial p}{\partial y} + div(\mu grad\, v) + S_{my} \tag{3.16}$$

$$\frac{\partial \rho w}{\partial t} + div(\rho w \bar{u}) = -\frac{\partial p}{\partial z} + div(\mu grad\, w) + S_{mz} \tag{3.17}$$

$$\frac{\partial \rho i}{\partial t} + div(\rho i \bar{u}) = -p div\, \bar{u} + div(k\, grad\, T) + \Phi + S_I \tag{3.18}$$

where S_m, S_i and Φ are the momentum sources, internal energy source and dissipation function, respectively, k is the Boltzmann constant, ρ is the fluid density, $\bar{u}$ is the velocity vector, u, v and w are the velocity components, p is the fluid pressure, T is the temperature of the fluid, and i is the specific internal energy. For a transported quantity with property ϕ, its transport process is represented as follows:

$$\frac{\partial(\rho\phi)}{\partial t} + div(\rho\phi \bar{u}) = div(\Gamma \mu grad\, \phi) + S_\phi \tag{3.19}$$

The rate of change of the property ϕ and the convective terms are presented on the left hand side of equation (3.19), while the diffusive and the source terms are on the right hand side of the equation, and Γ is the diffusion coefficient. The difference between the convective term and the diffusion term describes the nature of the transport. For the convective term, the transport of the materials are due to the velocity of the fluid, whereas for the diffusive term, the transport results from diffusion. Although the rate of the transport of the species or particles is derived from the single fluid flow field, the local concentration of the species, or particles, may affect the flow field itself. The source term describes the destruction or formation of the

species due to the chemical reactions or any other phenomena the user wishes to implement in the model.

3.2.2 Modelling of Coal Combustion

In general, the thermo-conversion of coal and biomass described in the next section is assumed to follow the main reaction steps: drying and heating, pyrolysis, volatiles combustion and char burnout. The drying process is modelled as a heat transfer controlled process between the particles and the surrounding gas. Many studies have been made and many models have been built to describe the combustion process (Williams et al., 2002).

Drying and heating up: The process of drying involves the evaporation of the surface moisture and the loss of the inherent moisture. The heat transfer can be described by the following general conduction equation (Tillman, 1991):

$$q = k_c A_p [(T_1 - T_2) / r_p] \tag{3.20}$$

where q is the flow of heat, k_c is the thermal conductivity of the fuel, A_p is the surface area of the fuel particle, T_1 is the temperature at the particle, T_2 is the temperature at the centre of the particle, and r_p is the radius of the particle.

After the drying process is accomplished, the particle is further heated to the pyrolysis reaction temperature in order to give off volatiles (devolitilization). The heating of a particle is governed by the following heat balance equation (Williams et al., 2001):

$$C_{p,p}\frac{dT_P}{dt} = Q_c + Q_r - Q_v \tag{3.21}$$

where T_p refers to the temperature of the particle, $C_{p,p}$ is the specific heat of the particle, Q_c, Q_r and Q_v are the heat transfer due to convection, radiation and vapourization, respectively, of the particles.

Devolatilization model: At a critical pyrolysis reaction temperature, biomass starts to give off volatiles. Basically, two mechanisms can be distinguished, namely one-step global and semi-global multi-step. Further, devolatilization rates for the two mechanisms are defined from the Arrhenius reaction schemes. In the former, only one set of the parameters describes the reaction (Olsson et al., 1997; Jensen et al., 2000):

$$Biomass \xrightarrow{k_1} Xvolatiles + (1-X)char \tag{3.22}$$

where X is the volatile fraction and k_1 is given by: $k_1 = A_1 \exp(-E_1/RT)$.

In contrast, two-step models take into account the effect of the heating rate in the prediction of the volatile fraction. Therefore, the heating rate is represented by a set of the competing reactions (Olsson et al., 1997; Jensen et al., 2000):

$$Coal \begin{cases} \nearrow Volatile_1 + \mathrm{Re}sidue_1 \\ \searrow Volatile_2 + \mathrm{Re}sidue_2 \end{cases} \tag{3.23}$$

The rate constants are given by : $k_2 = A_2 \exp(-E_2/RT)$ and $k_1 = A_1 \exp(-E_1/RT)$, where A_1 and A_2 are the pre-exponential factors, and E_1 and E_2 are the activation energies whose relative magnitudes determine the extent of the overall volatile formation as a function of the heating rate.

Volatile Combustion Model: A single-step reaction mechanism was used for volatile combustion and the eddy dissipation model used to couple turbulence and chemical reactions. Typical rate constants employed for coal and biomass are the same as have been reported in Backreedy et al. (2006) and Ma et al. (2009), respectively.

Char Combustion model: The char combustion sub-model is based on Smith's intrinsic model (Yu et al., 2001). For coal chars this model was modified by including a variable char surface area sub-model together with char annealing effects based on the Suuberg (Westberg et al., 2003) annealing model. The overall char reaction is a function of particle temperature, surface area, chemical reaction rate, and oxygen concentration and diffusivity. It is assumed that the oxygen order of the surface reaction is unity under the conditions studied. The effective surface reaction rate includes the effects of both bulk diffusion and chemical reaction rates. Coefficients can be used to modify the reaction rate for the effect of annealing and maceral content (f_{ann} and f_{mac} , respectively).

$$(dm_p / dt) = f_{ann} f_{mac} A_{p,i} [(\rho_p R T_\infty Y_{ox}) / M_{w,ox}][D_o R / (D_o + R)] \tag{3.24}$$

$$D_o = C_1([T_P + T_\infty)/2]^{0.75} / d_p) \tag{3.25}$$

where T_∞ is the temperature in the medium, Y_{ox} is the species concentration of oxidizer, D_o (3.25) is the bulk diffusion coefficient, $M_{w,ox}$ is the molecular weight of oxidant species and $A_{p,i}$ is the specific internal area of the char particle. The chemical rate R, is explicitly expressed in terms of the intrinsic chemical and pore diffusion rate. Details regarding the calculation of the

chemical rate (including swelling caused by vitrinite components) are given in (Backreedy et al., 2006). For biomass, an intrinsic char combustion model was used in a similar way to that for coal combustion. The rate of biomass char combustion is slighter higher because the carbon has a less ordered structure. The other corrections used for coal char were not applied to biomass (Ma et al. 2009).

3.2.3 Modelling Co-combustion of Coal and Biomass

For co-firing there are additional factors relating to the nature of the biomass particles, including issues surrounding the choice of heat capacity and emissivity for biomass. Large biomass particles do not generally follow the same combustion laws assumed for small coal particles due to large thermal thickness, but for the EFR experiments larger particles were excluded in order to achieve a high degree of burnout at the outlet of the EFR for all co-firing coal with biomasses (Borroso et al. (2006).

During the investigation into biomass ignition, it was found that the amount of moisture within the biomass can have a large effect on the time to ignition. Moisture in the coal or biomass can be accounted for within CFD models by including evaporation of water from the fuel particle. For a 1 mm biomass particle heated at 2200 K, the time to ignition increased from 0.0076s for moisture content of 5%, to 0.0264s for a moisture content of 25% thus taking 3.5 times longer to reach ignition temperature than for a low moisture particle; due to heating of water within the particle prior to ignition (Ma et al., 2006). The dimension of the particle is also important with respect to heating up times, doubling the size appears to double the time to ignition

and obviously for all particle sizes, the higher the temperature of the environment during heating the faster the time to ignition. A decrease in temperature from 2200 to 1500 K causes a threefold increase in time to ignition.

The straw particles investigated were assumed to be cylindrical, with lengths ranging from 1 μm to 111 μm. In order to account for the non sphericity, a shape factor, Θ, was used, defined as the ratio of surface area of an equivalent volume sphere to the surface area of a cylindrical particle. When calculating heat transfer to and from the straw particles, the surface area of the equivalent spheres were modified according to the particle shape factor, $A_p = 4\pi r_p^2 / \Theta$, where A_p and r_p are the area and spherical radius of the equivalent volume particle, respectively. In the case of coal combustion in EFR, the pulverised coal particles were assumed to be spherical in shape, and the size distribution ranged between 1 μm to 95 μm, with a mean diameter of 85 μm.

In the combustion of coals, the values for devolatilisation rate constants A and E, for the overall first order step obtained from previous studies (Williams et al., 2002) on devolatilisation network codes were used. The devolatilisation rate constant parameters for the release of tar, gas and total volatiles for the Russian and South African coals were calculated by FG-DVC (Williams et al., 2002; Backreedy et al 2006). Average values for the coals, leads to an activation energy E of 230 kJmol^{-1} and a pre-exponential factor A of 4.2 $\times$ 10^{14}s^{-1}. The test coals used in this study are similar (Williams et al., 2007) in nature to those discussed in (Backreedy et

al., 2006) and consequently the above values were used for all the coals in this study.

The reaction rates of biomass have been widely studied using TGA or drop tube reactors, but there is little direct experimental information on their behaviour in furnace flames where the heating-up rate is important. A first order kinetic rate model has been widely used for all biomass materials. Values of A = $6\times10^{13}s^{-1}$ and E = $2.5\times10^{8}Jkgmol^{-1}$ have been used and are based on values previously used for the pf wood (Backreedy et al., 2005). Small variations in the pre-exponential factor had only a small effect. In the devolatilisation model, particles are assumed to be spherical and thermally thin and the kinetic expression rate for the biomass (and the coals) is only applicable in this case.

Prior to their co-combustion of coal with biomass in the EFR, the samples were dried, milled and sieved under 100 μm. Larger particles were excluded in order to achieve a high degree of burnout at the outlet of the EFR for all coals, obtaining a stream of particles with a low carbon content, representative of fly ashes at the furnace exit of real boilers (Borroso et al. (2006); Wigley et al., 2007). Based on this report (Wigley et al., 2007), we consider the particles to be spherical and identical in size for the co-firing case investigated. The particle sizes were distributed between 1 and 95 μm in 10 injection groups, with a mean particle size of 85 μm and a spread parameter 1.3 has been used.

3.2.4 Radiation Models

The radiative heat transfer is always considered when the radiative heat flux is large compared to the heat transfer due to conduction and convection. The P-1 Radiation model and the Discrete Ordinates (DO) model are commonly used in coal combustion (Lee et al., 1996). The P-1 model is not Central Processing Unit (CPU) intensive and it is mostly applicable for combustion models with large optical thickness (typically greater than 1). On the other hand, the DO model is more intensive in terms of its CPU demand, but it has the advantage of spanning the entire range of optical thicknesses. Optical depth, or optical thickness, is a measure of transparency. Optical depth is defined as the negative natural logarithm of the fraction of radiation (e.g., light) that is not scattered or absorbed on a path. Hence optical depth is dimensionless, and in particular is not a length, though it is a monotonically increasing function of path length, and approaches zero as the path length approaches zero. In the DO modelling, the energy transfer due to radiation as a function of position, r, and direction, s, is governed by the Radiative Transfer Equations given as follows (Chui et al., 1993):

$$\frac{dI(r,s)}{ds} = -(K_a + \sigma_s)(r,s) + K_a I_b(r) + \sigma_s \bar{I}(r,s) \tag{3.26}$$

where K_a and σ_s are the absorption and scattering coefficients, I_b and $\bar{I}$ are the black body and in-scattering coefficients, respectively. The terms on the right hand side of the equation (3.27) represent the absorption, out-scattering, emission and in-scattering coefficients, respectively.

3.3 Turbulent Chemistry Models

Generally based on the CFD techniques, the continuous phase, which is referred to the gaseous phase in the furnace, is modelled in an Eulerian reference frame whereas the second phase, which is referred to as the discrete solid particles, is modelled a the Lagrangian approach. In turbulent fluid flows, the continuity equation, along with the Navier-Stokes equations, is characterized by a dimensionless parameter, called the Reynolds number is defined as follows (Turns, 2006):

$$R_e = \frac{\rho u L}{\mu} \tag{3.27}$$

where u and L are the velocity and length scales, respectively, while ρ and μ are the density and viscosity, respectively.

Most of the combustion processes are turbulent. This means that the flow is dominated by fluctuations in the fluid velocity and the species concentrations with a wide range of length and time scales that add to the complexity of the problem. One method of dealing with the complexity of the turbulent flows is through an averaging technique called the Reynolds decomposition. All variables in the flow field can be split into a basic state and a turbulent part. For example, the instantaneous turbulent velocity is decomposed into its steady basic state (mean value), u with a turbulent part (fluctuating component), u', (Versteeg et al., 2007), namely

$$U(t) = u + u'(t), \tag{3.28}$$

In addition to the turbulent flow, variable-density flow and turbulence-chemistry interaction models are required for the turbulent combustion

simulations. The variable density flow is handled by the averaging methods as described by Favre (1965).

3.3.1 Averaging Methods

Reynolds averaging: As explained in Section 3.3 , the Reynolds average comprises of the time-averaged mean value, ϕ, and the turbulent fluctuation, ϕ''. Therefore, the Reynolds decomposition of ϕ is defined as follows:

$$\phi = \bar{\phi} + \phi'' \tag{3.29}$$

where $\bar{\phi}$ is the time-average mean value, ϕ'' is the turbulent fluctuation and ϕ represents any quality of the turbulent flow, such as *u, v, w*.

Favre averaging: The term containing the correlation involving the density fluctuations is suppressed and this leads to significant simplifications in the averaged equations. Here we average as follows:

$$\tilde{\varphi} = \overline{\rho\varphi} / \rho \tag{3.30}$$

$$\phi = \tilde{\phi} + \phi'' \tag{3.31}$$

3.3.2 RANS Equations

In averaging equations (3.28)-(3.29), unknown terms appear due to the interactions between the various turbulent fluctuations. These unknown terms are modelled using the k-ε model and the Reynolds stress model. Averaging the density and velocity, leads to averaged forms of the general equations. Representing the momentum conservation, continuity and scalar, for high Reynolds number, we obtain the following (Versteeg et al., 2007):

$$\frac{\partial}{\partial t}(\rho u_i) + \frac{\partial}{\partial x_j}(u_i u_j) = \frac{\partial}{\partial x_j}\sigma_{ij} + F_i \tag{3.32}$$

$$\sigma_{ij} = -p\delta_{ij} = \mu(\frac{\partial u_i}{\partial x_j} + \frac{\partial u_j}{\partial x_i}) \tag{3.33}$$

$$\frac{\partial \rho}{\partial t} + \frac{\partial}{\partial x_i}(\rho u_i) = 0 \tag{3.34}$$

where

$$\delta_{ij} = \begin{cases} 0 & for\, i \neq j \\ 1 & for\, i = j \end{cases} \tag{3.35}$$

$$\frac{\partial}{\partial t}(\rho\phi) + \frac{\partial}{\partial x_i}(\rho u_i \phi - \Gamma \frac{\partial \phi}{\partial x_i}) = S \tag{3.36}$$

The equations (3.32), (3.34) and (3.36) represent the momentum, continuity and scalar transport, respectively. Equation (3.34) is part of the momentum equation, representing the Newtonian fluid. Further, u_i represents the fluid velocity, σ_{ij} represents the stress, and F_i represents the body forces.

3.3.3 k-ε Model

The k-ε model considers the physics of the production and destruction by introducing two extra entities - k and ε. The k and ε models are semi-empirical and are based on the transport equations for the turbulence kinetic energy (k) and its dissipation rate (ε). Thus, they require two additional equations to be solved. The first is for the variable, k, which is the energy of the turbulence, whereas the second is ε, the scale of the turbulence.

The k-ε models include the standard, the Renormalization Group (RNG) and the realizable models of turbulence. The assumption in the standard k-ε model is that the flow is fully turbulent and the effect of the molecular viscosity is negligible. This method is based on modelling the transport for the turbulence kinetic energy (k) and its dissipation rate (ε). The turbulent viscosity in the high Re limit is calculated as follows:

$$u_t = \rho C_\mu \frac{\mathrm{K}^2}{\varepsilon} \tag{3.37}$$

and the default value of the constant C_μ, is 0.0845, in the standard k-ε model (Launder et al., 1972).

From the time that the standard k-ε model was introduced by Launder et al. (1972), its strengths and weakness have been identified. Thus further elaboration has been made to improve its performance. This has lead to the creation of the RNG and realizable models. The RNG techniques includes the effects of the swirling flows and it also accounts for the low values of the Reynolds number (Re). Modifying equation (3.37) to account for the swirling effects, gives the RNG k-ε model as follows:

$$u_t = u_{t0} f(\alpha_s, \Omega, \tfrac{\kappa}{\varepsilon}) \tag{3.39}$$

where u_{t0} is the turbulent viscosity without swirl, Ω is the characteristic swirl number, α_s is the swirl factor, κ is the turbulent kinetic energy and ε is the dissipation rate. The turbulent viscosity without swirl and the characteristic swirl number are represented by u_{t0} and Ω, respectively, while the swirl factor α_s takes the default value 0.07. However, for strong swirling flows, the swirl factor can assumed to take a higher value. Numerically, the striking

difference between the standard and RNG k-ε models is the RNG model has an additional term in the ε equation (Orszag, 1993 quoted in Fluent inc., 2009).

3.3.4 Turbulent-Chemistry Interaction

In term of the turbulent chemistry interactions, the heat release by the turbulent reacting flow causes variations in the density. The main challenges in modelling turbulent combustion are the handling of the mean rate of reaction and the adequate representation of the chemistry in the model. Combustion models for predicting mild flames can be assessed by conserved scalar based models and volumetric reaction-based models. For the volumetric reaction approach, the eddy dissipation model (EDM) and the eddy dissipation concept (EDC) were used. In the EDM and EDC models, the transport equations for the mass fraction for each species in the chemical mechanism are modelled as follows:

$$\frac{\partial}{\partial t}(\rho Y_i) + \nabla.(\rho v Y_i) = -\nabla.J_i + R_i \tag{3.41}$$

where ρ is the mixture density, $Y_i = \frac{m_i}{m_{total}}$ is the mass fraction of the species i, v is the velocity vector, J_i is the diffusion flux of species i due to concentration gradients, and R_i is the net rate of production of the species i by equation (3.38). In FLUENT, the species transport provides an option for choosing various turbulent-chemistry interactions.

Eddy Dissipation Model: The model assumes that the chemical reactions are infinitely fast and are not governed by reaction rates but by turbulent mixing.

Due to the simplicity of the model, this approach is commonly used in coal combustion and other fuel combustion simulations when the flow is fully turbulent.

In the EDM model, the turbulence–chemistry interactions are accounted for through the representation of the chemistry source term R_i in equation (3.33). Two rate terms are computed: an Arrhenius rate based on the global chemistry mechanism, and a turbulent mixing rate based on the Magnussen–Hjertager expression. The smaller of the two rates is then used as the chemical source term in the species transport equations. In cases where the chemical reaction rate is not fast enough then the Arrhenius rate is used. In this approach, once ignition has occurred, the turbulent mixing rate is generally smaller than the Arrhenius rate and the reactions become dominantly mixing-limited.

Eddy Dissipation Concept: However, the EDC, an extension of the EDM, allows the full chemical kinetics to be accounted for in the calculations. The EDC model assumes that the chemical reactions occur in small turbulent structures, called fine scales. The evolution of the species concentrations is then computed by integrating the chemistry within these fine scales. The turbulence–chemistry interaction in the EDC model is tackled using the turbulence quantities *k* and *ε* to determine the size of the fine scales (ξ^*) in which the chemical reactions occur and the chemical residence time (τ^*) over which time the integration is performed. Combustion is assumed to occur within the fine scales as a constant pressure reactor and the size of the fine scales is modelled as follows:

$$\xi = C_{\xi}(\frac{\nu\varepsilon}{\kappa^2})^{2/3} \tag{3.40}$$

where the asterisk denotes fine-scale quantities, ν is the kinematic viscosity, and the constant C_{ξ} = 2.1377. The species are then assumed to react within the fine structures over a residence time scale τ^*, given by (Versteeg et al., 2007):

$$\tau^* = C_{\tau}(\frac{\nu}{\varepsilon})^{1/2} \tag{3.41}$$

where C_i is a time scale constant equal to 0.4082. The chemistry source term (R_i in equation (3.35) is computed for each mean species i as follows (Versteeg et al., 2007):

$$R_i = \frac{\rho(\xi^*)^2}{\tau^*[1-(\xi^*)^3]}(Y_i^* - Y_i) \tag{3.42}$$

where Y_i is the fine-scale species mass fraction after reacting over the time τ^*. Y_i^* is the mass fraction occupied by fine structure and the evolution of Y_i^* depends on the chemical kinetic mechanism.

3.4 Deposition Model

In this section, a numerical model to predict the deposition rates for the biomass and biomass-coal ashes has been developed. For the biomass fuel ash, the investigation presents a simplified ash deposition model taking into account the inertia and condensation of the vapour and particles in the flue gas stream. The ash particle stickiness is computed based on the product of the coarse fly ash particle and the difference between the vapour

pressure and saturation pressure of the potassium salts. The probability of the solid particle remaining on the surface is proportional to the flux of the vapours condensing on tube surface and forming a sticky layer. For the biomass-coal deposits, the deposition model takes into account the combination of the melting fraction and the particle viscosity methods. The combustion codes in the new FLUENT 12.1 and ANSYS FLUENT 13.0.0 have been used to implement the ash deposition models.

3.4.1 Particle Transport

In addition to solving the transport equations for the gaseous phase (Eulerian frame of reference), a discrete second phase (spherical particles) is simulated in a Lagrangian frame of reference. In this framework, the force balance equation in the x–direction can be written as follows:

$$\frac{dU_p}{dt} = F_D + F_g + F_t \tag{3.43}$$

where U_p is the velocity of the particle, F_D, Fg, and F_t are the x-components of the drag, gravitational, and therrmophoretic forces, respectively, that are acted on a unit mass of the particle.

The drag that acts on the particle by the carrying the gas phase is usually expressed as follows:

$$F_D^i = C_D \frac{18\mu}{\rho_p d_p^2}(u^i - u_p^i) \tag{3.44}$$

where, ρ_p, d_p, and u_p, are the density, diameter and velocity of the particle, respectively. C_D is the drag coefficient that often has to be obtained

experimentally and it may be expressed as a function of the particle Reynolds number, R_e as follows:

$$C_D = \frac{a_1}{\mathrm{R}_e} + \frac{a_2}{R_e^2} + a_3 \tag{3.45}$$

where a_1, a_2 and a_3 are constants that apply to smooth spherical particles (Morsi et al., 1972). For example, when R_e is greater than about 10000, the constants a_1, a_2 and a_3 take the following values $a_1 = -1662.5,\ a_2 = 5.4167 \times 10^6$ and $a_3 = 0.5191$.

The thermophoretic force due to the temperature gradient in the gas flow is calculated as follows, see, for example, Talbot et al. (1980) and Huang et al. (1996):

$$F_t = -\frac{6\pi d_p \mu^2 C_s (K + C_t K_n)}{\rho(1 + 3C_m K_n)(1 + 2K + 2C_t Kn)} \frac{1}{m_p T} \frac{\partial T}{\partial x} \tag{3.46}$$

where the Knudsen number is defined as $Kn = 2\lambda / d_p$ and the mean free path is given by

$$\lambda = \sqrt{\frac{\pi}{2}\frac{\mu}{p}}\sqrt{RT} \tag{3.47}$$

$$K = k / k_p \tag{3.48}$$

where k is the fluid thermal conductivity, k_p is the particle thermal conductivity, $C_s = 1.17, C_t = 2.18, C_m = 1.14$, m_p is the particle mass, T is the bulk phase temperature.

The energy balance equation of a fly-ash particle, which is solved along its trajectory to obtain the corresponding temperature at the point of the impact, is given as follows (Lee et al., 1999):

$$m_p C_p \frac{dT_p}{dt} = hA_p(T_\infty - T_p) \tag{3.49}$$

where C_p is the particle specific heat, T_p is the particle temperature, h is the convective heat transfer coefficient and T_∞ is the bulk phase temperature.

Having subscribed to the popular opinion that inertial impaction (I_i), thermophoretic effect (T_i), condensation (C_i) and heterogeneous reaction (R_i) are the major processes of the particle deposition, the rate of the deposition of an ash particle at its residence time, t, relative to the injection time is determined as follows (Baxter et al., 1993):

$$\frac{dm}{dt} = I \cdot G + T + C + R \tag{3.50}$$

where I is the inertial impaction rate taking into consideration the dust loading, G is the capture efficiency, T is the thermophoretic deposition rate, C is the condensation rate and R is the chemical reaction rate.

3.4.2 Capture Efficiency

The captures efficiency which determines the particle capture extent is specifically developed against two separate validation cases considered in this thesis. Firstly, in order to predict the initial deposition formation that occurs during biomass combustion, the effect of condensable alkali on the sticking probability of the ash particles has been considered. Secondly, in

order to predict deposit formation during co-firing of coal with biomass, the contribution of the coal ash viscosity and the biomass ash melt have been combined. For low co-firing ratio (≤20 wt.%), coal ash deposition is the dominant factor, however, with a higher biomass co-firing ratio, the melting behaviour of the biomass becomes important. It should be noted that if the ash deposits were collected at a heating surface of about 1250^{o}C or more, condensation is no longer a key player in the deposition.

Dust loading play important role in the capture efficiency. For example, woody biomass is generally of the lowest in ash, alkali and Cl contents among solid biomass fuel groups and the capture efficiency is the lowest. Grasses usually have slightly larger ash, alkali and Cl contents than that of woody biomass and the capture efficiency is high. Coals are comparable to grasses or woody biomass in terms of alkali and Cl contents, but the ash content is often considerably larger and varies significantly and the capture efficiency is often highest. The ash and alkali content in RDFs (refuse derived fuels) is generally within the range of coals, but the Cl content is significantly larger. Finally the straws are comparable to RDFs in terms of Cl and ash content, but have a significantly larger alkali content than that of other fuel groups.

Ash deposition for biomass: During the post-combustion of the biomass, when the flue gas meets with the superheaters then and it cools, and when KCl and K_2SO_4 saturation pressures are reached, KCl and K_2SO_4 condense and deposit on the cool surfaces. This can occur either by direct vapour condensation on the tube surface or by vapour condensation on the fly ash or aerosols formed in the free gas stream within the thermal boundary layer

close to the surface as depicted in Figure 3.1, which is based on a figure by Kaer (2001). According to Kaer (2001) there are at least three mechanisms by which these salts may arrive at the heat transfer surfaces (Fig. 3.1):

- Vapour diffusion followed by condensation on the cooled surface.
- Condensation on existing sub-micron fly ash particles followed by transport to the surface by e.g. turbulent impaction or thermophoresis.
- Homogeneous nucleation of the vapour followed by transport by particle diffusion, eddy impact or thermophoresis to the surface (the predominant mechanism (Nielsen 1998)).

The figure shows the dominant mechanism of the transport of salts to the heat transfer surface, i.e. the inertial impaction of large particles, condensation of liquid, and thermophoresis micron particles.

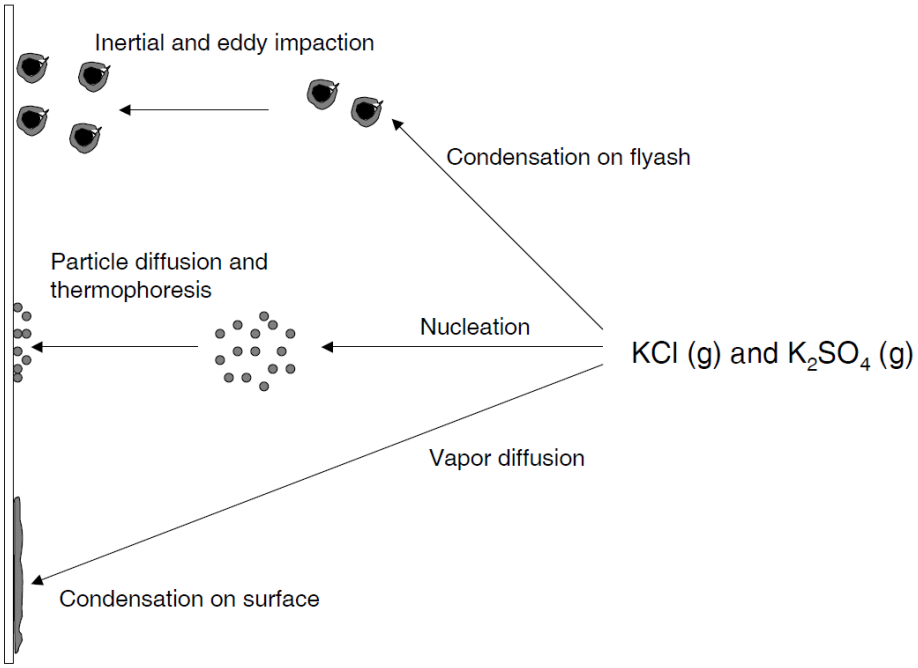

Figure 3.1: Systematic presentation of vapour deposition mechanisms (adopted from Kaer 2001).

Tomeczek et al. (2004) and (2009) proposed the concept of particle size dependence of the ash sticking probability and assumed it to be equal

to the product of the estimated final deposit size formed on the superheater, S, and the flux of vapours condensing on its unit surface area and forming a sticky layer, $m_{c,A}$. Therefore the particle sticking probability, P, can be expressed as follows:

$$P = Sm_{c,A} \tag{3.51}$$

with the value of $S(kg/m^2s)^{-1}$ estimated on the basis of the final deposit size formed on the superheater tube during uninterrupted industrial boiler behaviour (Tomeczek et al. 2004; Tomeczek et al., 2009).

The flux of the ash vapours condensing on the fly ash within the tube boundary layer, diffusing towards the unit surface area of the tube surface and condensing later on it can be calculated as follows:

$$m_{c,A} = Sh\pi d_p^2 \frac{C_p}{C_{t,p}} D_i \left(\frac{p_i - p_{i,s}}{kT_p}\right)\rho_g \tag{3.52}$$

where C_p is the concentration of the fly ash particles, $d_p > 10\mu m$, within the boundary layer where the ash forming vapour condenses on the fly ash particle, $C_{t,p}$ is the total concentration of the fly ash particles, (Hansen, 1998), p_i is the partial pressure of $_i$th gaseous component (Pa), $p_{s,i}$ is the saturation pressure of the $_i$th gaseous component (Pa), Sh is the Sherwood number, T_p is the particle temperature (K), k, Boltzmann's (kgm^2/s^2K) and ρ_g is the flue gas density (kg/m^3). The diffusion coefficient of KCl and K_2SO_4 condensing on the fly ash particle are defined as a function of the flue gas temperature (T_f): $D_{KCl} = 2.67\times10^{-9}\times T_f^{2/3}$ (m^2/s) and $D_{K_2SO_4} = 1.78\times10^{-9}\times T_f^{2/3}$

(m^2/s) (Zhou et al., 2007). The particles are assumed to take a spherical shape and d_p is the diameter of the particle. Following Tomeczek et al. (2009), the saturation pressure for the potassium salts considered in this thesis is calculated as follows:

$$p_{i,s} = p_n \exp(A_i - B_i / (T + C_i)) \tag{3.53}$$

where the A_i, B_i, C_i are constants given in Table 3.1, p_n =10 Pa (a reference partial pressure of the gaseous component taken from Tomeczek et al. (2009)) and T_f is the local gas temperature.

Table 3.1: Values of the constants A_i, B_i and C_i (Tomeczek et al. 2009).

Component	A_i	B_i	$C_i\,(K)$	Temperature, range (K)
K_2SO_4	18.08	39449	0	1150-1800
KCl	11.01	17132	-122.7	1094-1680

The deposition flux of a single particle that hits the tube can be evaluated from the mass flux of the particles denoted by their trajectories, $m_{trj,i}$ and the sticking probability of the impacting particle, P. The total deposition flux on a unit area of the tube can be determined by (Forstner et al., 2006):

$$\dot{M} = \sum_{i=0}^{n} (m_{trj,i}.\eta) \tag{3.54}$$

where $m_{trj,i}$ is the trajectories of ith particle, η is the sticking probability of impacting particle and $\dot{M}$ is the total deposition flux on the wall surface.

Particle ash deposition for co-firing of coal with biomass: The key ash effects of the co-firing of coal with biomass are severe deposition problems. These deposits depend on the chemistries of the coal and the biomass ashes and the biomass co-firing ratio. While the composition of the coal ash is mainly silica and alumina, the composition of the biomass ash is relatively high in alkali content. In terms of the ash chemistries, alkalis are known to act as effective fluxes for the alumina-silicate system (Picco et al., 2010). At low co-firing ratios, less than about 20 wt.% on a mass basis, power generators get away with a modest effect on the ash deposition. At higher levels of co-firing ratios, greater than about 20 wt.% on a mass basis, power generators experience severe effects on the ash deposition (Wigley et al., 2007).

In coal/biomass blend combustion, both surface phenomenon and the bulk property of the fuel are known to contribute to the deposit formation on the heat transfer surfaces (Heinzel et al., 1998; Akbar et al., 2010) and the overall deposition rate is described as follows:

$$\frac{dm}{dt} = I.\eta + C \tag{3.55}$$

where I , η and C are the particle impaction rate, the sticking probability and the condensation rate, respectively.

During the first stages of the deposits formation, alkali salts condense on the surface. In this case, the metal surface controls the deposition. However, at certain flue gas temperatures (>1000^{o}C), higher than the saturation temperature of the condensable species, the condensation

process stops as the deposit surface temperature increases and the slagging mechanism becomes more of a bulk property of the mixed fuel than a surface issue (Picco et al., 2010). Therefore equation (3.54) reduced to

$$\frac{dm}{dt} = I.\eta \tag{3.56}$$

In comparison with coal ash, biomass ash shows a lower ash content and lower fusion temperatures. According Heinzel et al. (1998), whether deposit or parts of them either show the behaviour two single ashes or behaves like a mixture of ash is one of the most important questions for co-combustion.

The stickiness of the coal ash is determined from the viscosity-based models, while the stickiness of the biomass ash is determined from its melt fraction and the particle softening temperatures. Since a particle and deposit layer consists of a mixture of salt and silica rich material, the sticking probabilities of the coal ash viscosity and the melting components of the biomass may be combined as follows:

$$\eta = x\eta_c + y\eta_b \tag{3.57}$$

where x, y, η_c and η_b are the ratios of the coal in the blend, the ratio of the biomass in the blend, the coal ash sticking probability and the biomass ash sticking probability, respectively.

For the coal ash sticking model, the sticking probability is primarily concerned with the viscosity of the fly-ash. The fly ash viscosity is linked to the configuration of the oxide melt, and it is very sensitive to the changes in the temperature and composition. In this case, the sticking probability is

defined as the ratio of the critical (reference) viscosity, μ_f, and the particle viscosity, μ_p, at a certain temperature. The assumption is that any impact that involves any viscosity below a critical value results in the particle sticking to the heat transfer surface. Therefore, the particle stickiness can be expressed (Huang et al., 1996) as follows:

$$\eta_{c_i} = \frac{\mu_f}{\mu_p}, \text{ where } \mu_p > \mu_f \text{ and } \eta_{p_i} = 1, \text{ where } \mu_p \le \mu_f \tag{3.58}$$

A number of different values have been suggested for the critical viscosity, as discussed by Huang et al. (1996). We have adopted the value of 10^5 Pa s following the suggestion of Degereji et al. (2011). The particle viscosity (Pa s), as a function of the particle temperature, can be calculated from the Watt–Fereday model (Watt et al., 1969) as follows:

$$\mu_p = 10^{y-1} \tag{3.59}$$

where

$$y = 10^7 m / (T - 150)^2 + c$$

$$m = 0.00835(SiO_2) + 0.00601(Al_2O_3) - 0.109$$

$$c = 0.0415(SiO_2) + 0.0192(Al_2O_3) + 0.0276(Fe_2O_3) + 0.016(CaO) - 3.92$$

and the values for the two parameters, namely the slope, m, and the intercept, c, are computed from the species concentration in weight percentages of the ash with the following assumption (Vargas et al., 2001):

$$(SiO_2) + (Al_2O_3) + (Equiv.Fe_2O_3) + (CaO) + MgO = 100wt\% \tag{3.60}$$

For biomass ash with high content of alkali suchas Miscanthus, Straw, SRC, and Olive, a combination of the particle softening temperature and the melting fraction has been used to estimate the stickiness of the particle. According to Ma et al. (2006), a particle would be perfectly sticky when it has been completely melted and the softening temperature of the biomass can be estimated using the following empirical equation:

$$T_b = 1.81(CaO) + 4.20(Al_2O_3) - 2.41(K_2O) + 5.31(P_2O_5) + 1017^0 C \tag{3.61}$$

where CaO, Al_2O_3, K_2O and P_2O_5 are the relative mass concentrations of these species in the biomass ash and they are normalized so that they sum to 100%.

However, when a particle has not burnt out completely, only a fraction of the melt will be sticky. Thus, if the temperature of the particle has reached the melting temperature of the potassium species (about 700°C), but has not yet reached the particle softening temperature estimated by equation (3.61), the potassium species will be melted and the following expression is used to calculate the sticking probability of the biomass ash:

$$\eta_{b_i} = \frac{m_{silicate}}{m_{salt} + m_{silicate}} \cdot f_{melt,silicate} + \frac{m_{potassium}}{m_{salt} + m_{silicate}} \cdot f_{melt,salt} \tag{3.62}$$

where $m_{potassium}$, $m_{silicate}$, $f_{melt,potassium}$ and $f_{melt,silicate}$ are the mass of the potassium, the mass of the silica, the melt fraction of the potassium and the melt fraction of the silica, respectively. In the case of the biomass ash, two types of ash are considered, potassium and silica particles. The melting behaviour of these ashes are found in Kaer et al. (2001). While $m_{silicate}$ and m_{salt} are estimated from the equilibrium calculation, $f_{melt,silicate}$ and $f_{melt,salt}$

are obtained from the melting curves (see Figure 3.2) of the potassium and silica particles, respectively. This model is developed for biomass with high potassium content such as straw, miscanthus, olive and SRC. The melting behaviour of such biomass material is given in Figure 3.2 (Kaer et al., 2001).

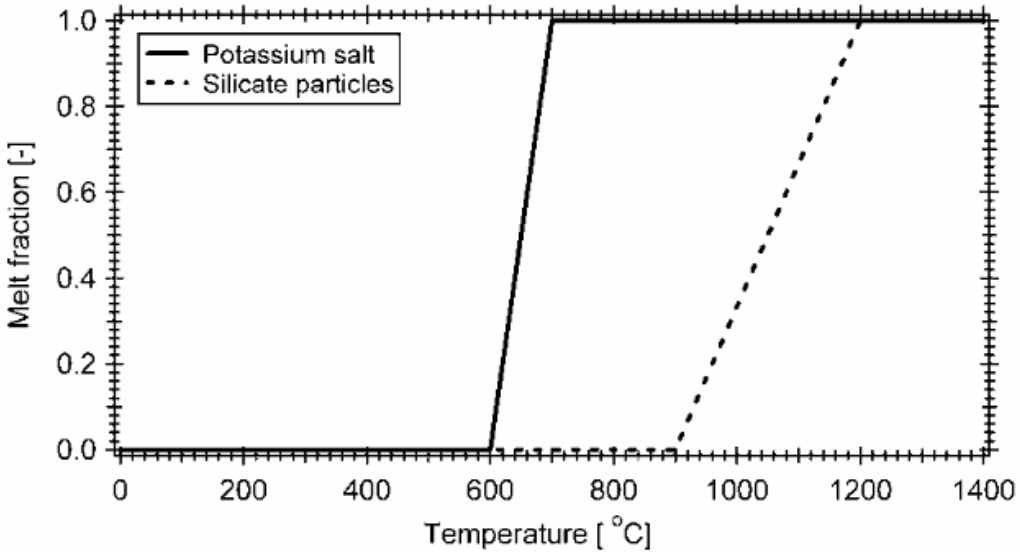

Figure 3.2: Approximated melting curves of the potassium salt and silica-rich particles (Kaer et al., 2001).

In the modelling work of Kaer et al. (2001), it has been assumed that the mass of the molten phase is non-sticky if the mass of the molten phase is below about 15 %. Between 15 and 70 %, the mass of the molten phase is assumed to be sticky and above this percentage, the mass of the molten phase is assumed to be flowing. The thermodynamic equilibrium calculations are used to calculate the amount of the melt fraction considering the possible phases of the liquid slag and solid solution.

Deposition Efficiency: The deposition efficiency has been calculated for the co-combustion of coal and different masses of the biomass materials in the

EFR (Wigley et al., 2000). The deposition efficiency was calculated for each EFR run and it is calculated as follows (Wigley et al., 2000):

$$Deposition\ efficiency = \frac{Incident\ ash\ retained\ on\ the\ probe}{Total\ ash} \times 100 \tag{3.63}$$

Rebound Criterion: Establishing whether a colliding particle actually sticks or rebounds from the heat transfer tube begins with the calculation of the excess energy. This is in addition to the sticky probability of the particle on the deposit surface. To represent this numerically, a rebound criterion, as derived by Mueller et al. (2005) was employed. The rebound tendency has previously been assumed to be a function of the viscosity, impact velocity and static angle of the particle (Mao et al., 1997). If a particle possesses the necessary excess energy, E_x, (> 0), the particle is judged to bounce off the surface, otherwise it sticks. The particle excess energy is calculated using the following empirical formula (Ma et al., 2006, Degereji et al., 2011):

$$E_x = \frac{D^2}{4}(1-\cos\alpha) - \frac{3D^{2.3}}{25}(1-co\alpha)^{0.63} + \frac{2}{3D} - 1 \tag{3.64}$$

where D is the ratio of the maximum deformation of the particle diameter to the actual particle diameter and this ratio is related to the particle Weber number and the Reynolds number as follows:

$$D = (12+We)^{1/2}[3(1-\cos\alpha) + 4(We/\mathrm{Re}^{1/2})]^{1/2} \tag{3.65}$$

Table 3.2: Summary of the coal existing and new biomass deposition models.

Existing coal deposition model		
Work	Sticking criterion	Deposition model
Huang et al., 1995	Coal ash viscosity (Watt Feraday model)	$\log\eta = A\frac{m}{(T-B)^2}+C,$ where m = f(composition)
Forstner et al., (2006)	Coal ash viscosity (Urbain model)	$\eta = a.T.e^{Ab/T}$, where a, b = f(composition)
Muller et al., (2005)	Deposit layer thickness melting fraction	$s_{\max} = \frac{\lambda(T_{70}-T_W)}{\alpha(T_{FG}-T_{70})+\sigma\varepsilon\cdot(T_{FG}^4-T_{70}^4)}\cdot 10^3$
Ma et al., (2006)	Biomass softening temperature	$T_{sof} = 1.81CaO+4.20Al_2O_3-2.41K_2O+5.31P_2O_5+1017^oC$
Akbar et al., (2010)	Biomass condensation	$N_{c,i} = \frac{p.K_D}{R\Omega_D}\cdot y_{i,bulk}\cdot\frac{\Delta T}{2\delta}\cdot\frac{1}{T_{bulk}^{1/2}-(T_{bulk}-\Delta T)^{1/2}}$
Tomeczek et al., (2009)	Biomass condensation	$m_{c,A,i} = \beta_i\frac{p_i-p_{i,s}}{p}\rho_g$
New biomass and coal/biomass models proposed in this thesis		
Garba et al., 2012	Biomass heterogeneous condensation	$m_{c,A} = Sh\pi d_p^2\frac{C_p}{C_{t,p}}D_i(\frac{p_i-p_{i,s}}{kT_p})\rho_g$
Garba et al., 2013	Combined ash viscosity (coal) and melting fraction (biomass)	$\eta = x\eta_c+y\eta_b$

The Weber number is defined as follows:

$$We = \frac{\rho_p u^2 d}{\delta}, \tag{3.66}$$

and α is the static contact angle and δ is the particle surface energy.

In order to highlight the difference between some of the existing coal and biomass ash particle deposition model and the one that has been proposed in this thesis, a summary of the reviewed deposition models and the one been proposed are presented in Table 3.2. The various approaches used in determining the particle stickiness are also presented in the Table 3.2. In this thesis, the mathematical equation in the last two rows in Table 3.2 have been implemented using the FLUENT 12.1 software in order to determine the fate of ash particles that hit the heat transfer surfaces of a boiler.

3.5 Numerical Methodology

In an attempt to improve the combustion efficiency, modelling and numerical simulation of the PF combustion processes are considered as an important tool for the diagnostics and predictions of the operations and boiler situations (Yin et al., 2008). In order to predict the deposition mechanism of the ash particles, some important steps have to be followed. Therefore, this thesis is guided by the following steps:

- Generating a computational grid to represent the combustion furnace that has been used in the calculations, and identifying the furnace operational conditions.

- Setting up simulations using the available and suitable CFD codes in the FLUENT 12.1 software, by selecting suitable models for the fluid flow and its various characteristics, such as, turbulence, heat transfer, chemical kinetics, etc., in an Eulerian frame of reference in order to establish the gas phase of the combustion processes.
- The identification of the appropriate detailed alkali mechanisms that are used in exploring the biomass combustion. Because it is costly to implement detailed gas-phase kinetics in FLUENT, Chemkin – a software used for solving problems involving detailed gas phase kinetics was employed. Chemkin is a solver that is linked to FLUENT to enable it perform calculations involving large number of species. The detailed mechanism prediction was subsequently validated against the experimental data.
- The reduced alkali mechanism imported into the FLUENT solver. FLUENT is a solver based on the finite volume method. In the finite volume method, the appropriate geometry is first created and then the computational grid is generated with the suitable meshing techniques.
- Two theoretical models to predict the biomass and coal/biomass ash deposition rates in boilers has been developed. The model has been hooked into the FLUENT 12.1 software, as a UDF boundary condition in order to determine the fate of the ash particles that may impact on the surfaces of the heat exchanger. This stage is of major concern to this thesis, being a test point for the effectiveness or otherwise of the proposed model.
- The results of the predictions using the developed deposition codes are compared with the available data in order to validate the proposed

codes. This step was followed by the post-processing analyses and a discussion on the results of the predictions using the proposed deposition model. In order to determine how well the UDFs is able to predict FLUENT 12.1 combustion and deposition behaviour, the results were compared with experimental data.

Figure 3.3 depicts a flow chart illustrating an overview of the necessary computational steps for the prediction of the ash deposition rates in boilers which are based on the salient steps mentioned above . Figure 3.3 shows that the required input into the commercial software for the initial set of calculations include a completed computational grid representing the various sections of the test boiler, the physical and chemical properties of the fuel, and the operational conditions of the boiler. These input data will be discussed in detail in the next sections. When a converged solution of the first set of computational iterations is obtained, the temperature and velocity fields, and the heat fluxes, are recorded and analysed.

The second phase of the calculations, as shown in Figure 3.3, is basically on the particle trajectories and the determination of the fate of the particles when they are transported to the boiler walls. The particle trajectories are calculated under the influence of turbulence, particle dispersion effects, high temperature and pressure gradients, etc.

For the ash particle that possess sufficient energy and velocity to transverse the boundary layer and hit the boiler walls, the viscosity, surface energy and excess energy of the particle are computed in order to determine whether the particles stick to the walls or rebound.

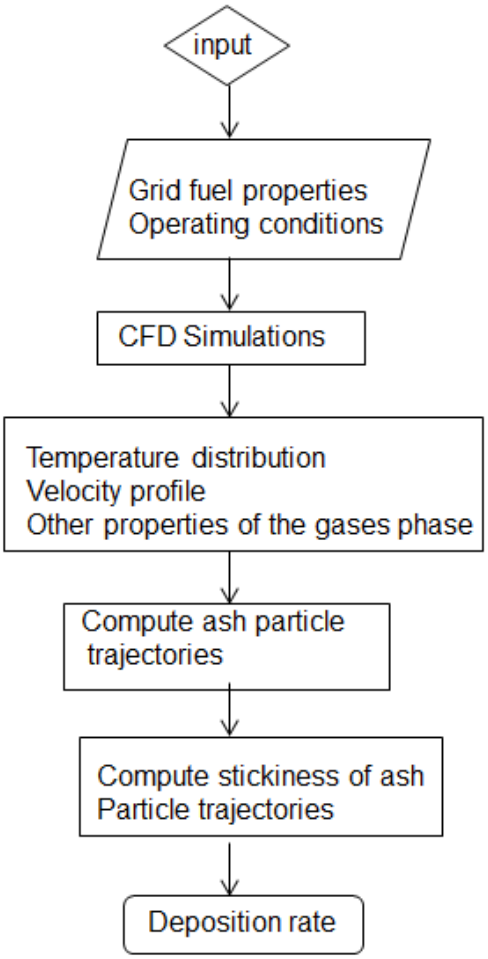

Figure 3.3. Flow chart for the prediction of the ash particle deposition rate.

3.5.1 Chemkin Family of Codes

The Chemkin family of codes, which includes Chemkin, KINALC, Kintech, etc. are known worldwide in the combustion modelling of a number of reactions (Kee, et al., 2000). They have had a very large impact on the research community because they provide a common framework for communicating reaction mechanisms. The combustion modelling is achieved via a Chemkin format (Westbrook et al., 2005; Kee, et al., 2000). A Chemkin format mechanism usually consists of chemical elements, chemical species,

NASA polynomial coefficients for each species (from which the temperature dependent thermodynamic properties are calculated) and elementary reactions and the associated Arrhenius parameters.

3.5.2 CFD Codes

CFD is a design tool that has been developed for over 40 years and it is continually being developed as the understanding of the physical and chemical phenomena governing the CFD theory advances (Versteeg et al., 2007).

Pre-processor: This is mainly the input of the flow problem to a CFD program. The pre-processor stage is dominated by the user activities, such as:

- Defining the computational domain.
- Generating meshes for the domain.
- Selecting the physical and chemical processes to be modelled.
- Defining the fluid properties.
- Specifying the boundary conditions.

Solver: Based on the control-volume technique, the numerical algorithm consists of three basic steps: integrating the governing equations of the fluid flow over the finite control volume of the domain, discretizing the resulting integral equations into sets of algebraic equations and solving the algebraic equations iteratively.

In the FLUENT software, the choice of the solver is limited to pressure-based or density-based and segregated or coupled types. The pressure-based solver was originally developed for low-speed

incompressible flows. In this approach, the pressure field is extracted by solving the pressure equation which is obtained by manipulating the continuity and the momentum equations.

Post-processor: The CFD post-processing packages provide complete insight into the fluid dynamics, such as image generation to communicate the results visually, quantitative displays of data, animations of the dynamic results, etc. With the increased popularity of engineering workstations, a large amount of development work has recently taken place in the post-processing field.

The CFD models are usually developed based on several variables and assumptions, all in an attempt to investigate if the codes can closely model the actual situations in the engineering field. The CFD codes are expected to provide reasonable engineering/scientific conclusions.

User-Defined Functions: The UDF developed by a user is compiled and linked to the main code. This is done in order to further enhance the features of any of the existing codes. Most codes incorporate user defined macro and additional tools, such as erosion rates and scalar values along the particle trajectories to facilitates its use.

The deposition model has been compiled and linked to the main code in the FLUENT 12.1 software using the UDF. The main code in FLUENT calculates the particle trajectories while the role of the deposition code (UDF) is to add stickiness to the particle as it is being transported from the combustion zone to the furnace wall, or the heat transfer surface.

Also, the numerical slagging indices for the coal and biomass blends have been implemented as a ‘define-on-demand’ UDF. The slagging model

are considered as user-defined programs which are executable in the FLUENT software using the execute-on-demand' command.

3.5.3 CFD Simulation

The CFD solver type, the solver settings and the solution procedures adopted in these calculations are discussed in this section. Also, in this section, the CFD codes employed for different combustion processes have been discussed and summarized.

Single rate devolatization: In modelling deposition rates, an accurate calculation of the temperature field is a key issue and this largely depends on the combustion models. The combustion model follows the approach previously used by some of the present authors (Backreedy et al., 2006; Ma et al., 2009). The model uses a first-order devolatization step for the biomass followed by a global one-step reaction for the combustion of the volatiles. The values of A and E were already given in Section 3.2.3.

Kinetics/diffusion-limited model: The char combustion begins when most of the volatiles are released and it is assumed that the reaction rate is dependent on either the chemical reactions or on the bulk diffusion (Backreedy et al., 2005). The particle size was assumed to remain constant, while the particle density decreases. The values of A and E already were given in Section 3.2.3.

The RNG k-ε model: This turbulence model is said to be more suitable than the standard k-ε model in similar calculations that have been reported, especially, considering the furnace size. This is because the model takes into accounts the effect of both small scales and swirl motions (Ma et al., 2006; Fluent Inc., 2009). The RNG is an anisotropic k-ε model that includes

the effects of strained flows, and this greatly enhances the accuracy of the prediction (Eaton et al., 1999).

Radiation model: Heat transfer between the particle and the heat transfer surfaces due to radiation is implemented using the Discrete Ordinate (DO) model (Ma et al., 2009). The default values were increase for the angular discretization in order to refine the computational steps for better results, but with additional computational cost (Fluent Inc., 2009).

Tabe 3.3: Summary of the combustion models employed in the calculation.

Activity	Model Used
Turbulence	RNG k-epsilon
Absorption coefficient	WSGGM
Radiation	Discrete ordinates
Combustion	Species transport
Particle diameter distribution	Rosin-Rammler
Particle dispersion	Stochastic DRW
Devolatilization	Single rate
Char burnout	Kinetics/diffusion – limited

Particle trajectories: the trajectories of the ash particles have been calculated with the Langragian approach. The simplified equation of motion for a particle moving in a viscous environment, equation (3.43) has been employed. Complete steady-state calculations were performed and the results of the predictions obtained, using the proposed deposition model,

have been compared with the available experimental data. A summary of some of the mathematical models used for various aspect of coal and biomass combustion in these calculations are shown in Table 3.4

3.5.4 CFD Procedure

The steady state RANS calculations have been performed using the CFD model. As gas aerodynamics is solved using an Eulerian approach, while the ash particle trajectories and tracking were calculated separately in a Lagrangian frame of reference. An overview of the solution procedure is shown in Figure 3.10.

The PRESTO pressure scheme, which accounts for the effect of the large pressure gradient involved in swirling flows, with first-order discretization, was initially used in the simulation. After obtaining a converged solution, the second-order upwind scheme was applied for more precise conditions. Using the pressure-based solver, the equations were solved iteratively in the natural variables of pressure and velocity using the SIMPLE method which caters for instabilities due to mesh skewness.

The choice of the under relaxation factors, which are used to stabilize the iterative pressure, is better made through experience. Therefore, the under relaxation factors for the pressure, momentum, species, turbulence, radiation and discrete phase sources were maintain less than unity. For example, the default under relaxation value 0.3 was maintained for the pressure, and 0.4, 0.95 and 0.1 have been set for the momentum, radiation and discrete phase source calculations, respectively (Degereji et al., 2010).

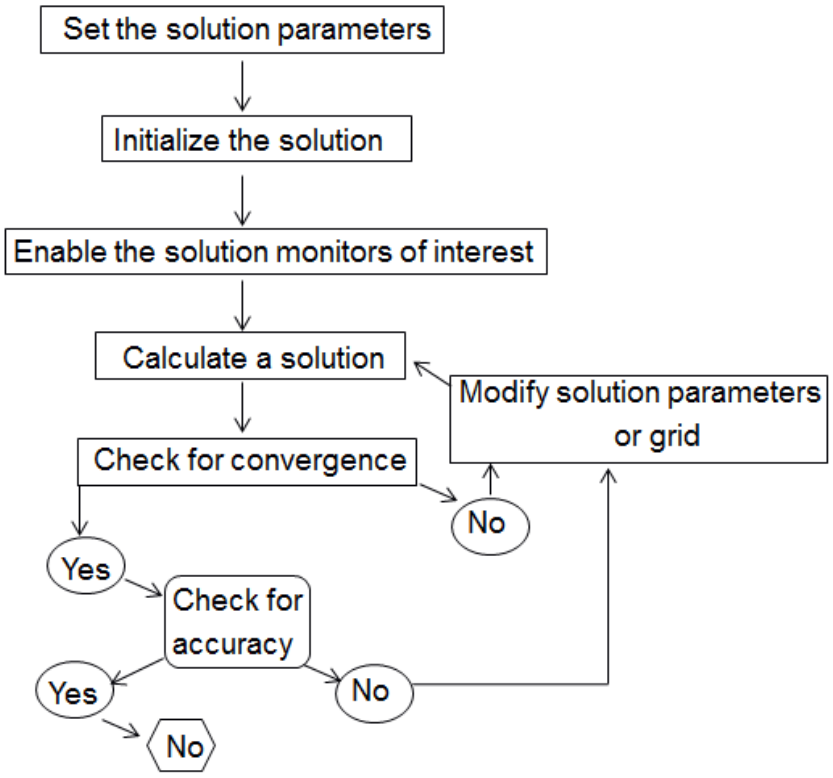

Figure 3.4: Algorithm of numerical approach used by simulation software's (Rubini, 2007).

After setting all the boundary conditions, especially, for the inlets, walls, outlet, etc., the solution was initialized. The iterative procedure, illustrated in Figure 4.8, requires the initialization of all the variables before calculating a solution, and a realistic guess of the initial values improves the solution stability and convergence.

While performing the calculations, the solution convergence was determined both quantitatively and qualitatively. Monitoring the magnitude of the scaled residuals of all the species has been used in order to assess the solution convergence in qualitative terms. The scale of the residuals for the major flow fields were established, such as the velocity components and continuity equation have decreased by 3 orders of magnitude from the initial value of a single order, while the scaled energy and radiation residuals

decreased to 10^{-6} before convergence was achieved. The scaled residuals for the species have decreased to 10^{-5}, and this is necessary in order to have species balance. The converged solution has also been monitored quantitatively by ensuring that the property conservations were satisfied. Some convergence difficulties have been experienced after switching to the second-order discretization. However, when under relaxation factors were reset to the values given above, fall convergence was achieved.

3.5.5 FactSage Calculation Method

An equilibrium analysis of the biomass and biomass/coal blend combustion was undertaken in an attempt to explain some of the observations made during the CFD predictions in Chapter 5. This is because the equilibrium calculations offer a convenient explanation into the complex phase chemistry for the multi-component ashes from the combustion zone. For the equilibrium calculations, the FactSage 6.2 software was employed.

In order to predict the melting behaviour of slag from FactSage 6.2, some important steps (Figure 3.5) which have to be followed are summarize below:

- The selection of the Equilib. The Equilib module is the Gibbs energy minimization workhorse of FactSage. It calculates the concentrations of chemical species when specified elements or compounds react or partially react to reach a state of chemical equilibrium.
- This is followed by the selection of the FACT and FToxid. The FACT databases are the largest set of evaluated and optimized thermodynamic databases for inorganic systems in the world while

FToxid is a oxide database for slag, glass, mineral, ceramic and refractory. FToxid also contain data for stoichiometric oxide and oxide solution including all the solid fuel components employed in this thesis.

- Then the fuel elemental components and the components of the ash under investigation were entered.
- At this stage, an appropriate slag type “A” is selected from the different available options. Different slag types have different composition of oxides in the slag system.
- In a sequel to the proceeding stage, the temperature and pressure is specify and then follow by a click on the calculate button to commence computation.
- Phases from the compound and solution databases are retrieved and offered as products in the Menu Window. The products include pure substances (liquid, solid) and solutions (gas, liquid, solid, aqueous) retrieved as mineral output.

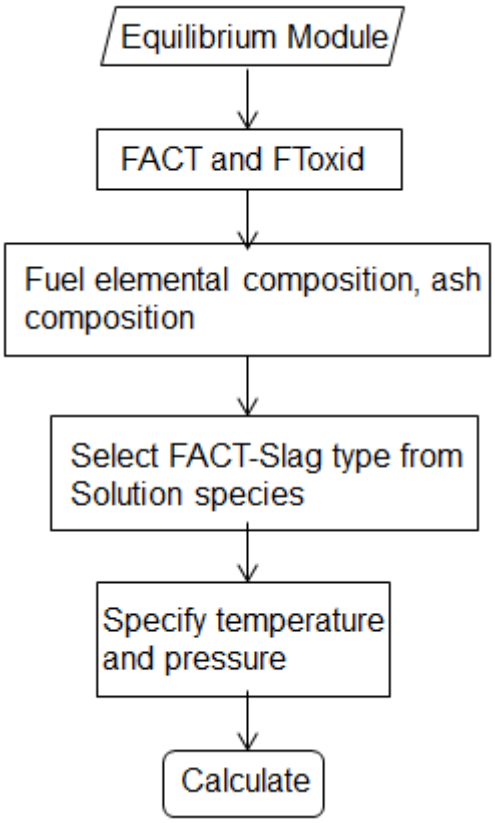

Figure 3.5: Flow chart for the prediction of the melting behaviour of slag system from FactSage.

One of the predictive tools used successfully in coal ash applications is the computer package FactSage^{TM} (Bale et al., 2002). FactSage is used worldwide in various industries to predict the chemical equilibria, the proportions of liquid and solid phases as a function of temperature, and the composition and atmospheric conditions. One of the strengths of FactSage is its ability to describe the melting behaviour of the oxide systems, commonly referred to as slags. FactSage is a combination of two linked models in the area of computational thermochemistry, namely Fact-Win and ChemSage, that consist of a series of information, database, calculation and manipulation modules that enable the users to access and operate pure substances and solution databases in relation to a variety of thermochemical

calculations. This calculation is based upon the concept of the Gibbs free energy minimization (Bale et al., 2002). The model calculates the concentrations of the chemical species when specified compounds react, to reach a state of chemical equilibrium (Jak et al., 2007).

When the elementary compositions of the fuel and air, pressure and temperature have been introduced and a slag type is selected from the default list of slags, FactSage searches the thermodynamic database for the species including all the elements in the slag type selected. The behaviour of the mineral matter from the combustion process can be subsequently extracted at the various temperatures (van Dyke et al., 2009). It is thus possible to determine the quantity, as well as quality, of the gas phase, liquid phase and solid phase. In this investigation, FactSlage A is selected (containing 1144 species - 278 gas, 173 liquid, and 693 solid species) to conduct the thermodynamic calculation for the system including the elements C, H, O, N, S, Cl, Si, P, Ca, K, Na, Mg, Al, Fe, Ti and Mn. The physical and chemical properties of the coal and biomass composition are presented in Table 5.3. The temperature range considered was from 1200–1600 °C with a step of 100 °C. The thermodynamic equilibrium was therefore calculated for a range of temperatures between 1200°C and 1600 °C, corresponding to the widest range of the temperatures anticipated on the EFR (Wigley et al., 2007). Calculations were performed assuming a pressure of 1.0 atmosphere, a reasonable approximation to the furnace pressure which was usually kept at a slight negative value. 1000 g fuel is used as a basis for the equilibrium calculation. The FactSage database contains more than 300 gaseous, liquid and solid phases, including salt melt

and silicate melt. However, this investigation only looked at the slag liquid, slag liquid composition and solid phase that are stable at the designated temperature range.

The stable chemical species and physical phases of the elements included in the equilibrium calculation are determined as a function of temperature, pressure and total composition of the system considered. The possible phases are as follows: liquid slag and several solid-solution phases: mullite ($Al_6Si_2O_{13}$), tridymite (SiO_2), leucite ($KAlSi_2O_6$), cordierite ($Mg_2Al_4Si5O_{18}$), hematite (Fe_2O_3), anorthite ($CaAl_2Si2O_8$), forsterite (Mg_2SiO_4) and spinel ($MgAl_2O_4$). This type of calculation has some limitations. In particular, the equilibrium calculations are based on the assumptions that all reactants are well mixed (homogeneous) and kinetic limitations are not taken into account. It must be stressed that FactSage only predicts the evaporative transport routes for the element and species, and it does not take into consideration the effects of particle entrainment, which are significant in combustion (van Dyke et al., 2009).

3.6 Summary

In this chapter, the major theoretical mathematical models used in this investigation have been presented. The assumptions of both the adopted and the developed codes are also stated. The law of conversation of mass and the fundamental laws of thermodynamics are the governing equations for the fluid flow and the enthalpy calculations, while the effect of radiation is obtained using the DO model.

Turbulence is calculated according to the RNG k-ε model, and the species transport is computed using the eddy dissipation model and the eddy dissipation concept, which are found suitable for turbulent diffusion flames with fast and finite chemistry, respectively. The rate of release of the volatile matter (VM) is assumed to be first-order dependent on the amount of volatiles remaining in the particle, while the kinetic/diffusion-limited model, which includes the effects of the bulk diffusion and the chemical reactions, has been employed for the char combustion calculations.

The overall sticking tendency of the particle is determine on the basis of its calculated condensate, viscosity and melting fraction at impaction on the boiler walls and its tendency to rebound after impaction.

The ash deposition model developed in Chapter 3 has been implemented on the grate-fired furnace and the EFR. The combustion code available in the FLUENT 12.1 software have been used in order to generate the required gas phase temperature and velocity fields. The calculations have been performed in time-averaged gas aerodynamics and have been solved using an Eulerian approach, while the particle trajectories and tracking were determined using a Lagrangian approach.

The approach to the deposition model has been linked to the FLUENT 12.1 commercial software as a UDF boundary condition which determines the fate of the ash particles that may impact on the furnace walls. A computational grid that represents one half of the furnace has been employed for the calculations. The grid generation, the fuel properties and the furnace operating conditions have been used as simulation input for the commercial software.

Chapter 4

Application of Biomass Deposition Model: Results and Discussion

The ash deposition model has been set out in Chapter 3. In this Chapter, the results of the reduced alkali model are verified quantitatively, and the results of the predictions using the CFD-based ash deposition model are verified only qualitatively. Further, the CFD-based modelling of the straw-fired grate furnace is inherently more difficult due to the complex biomass conversion in the fuel bed on the grate which is not a part of this thesis. Finally a comparison and discussion of the deposition patterns are presented in this chapter and, some conclusions are drawn from these discussions.

4.1 Introduction

Cotton straw is a readily available agriculture waste product, and it is widely used as a renewable energy source. About 600 million tons of straws and stalks are produced annually (Junfeng, 1997) in China, and 17.8 million tons are produced annually in the UK (Palz et al., 1985). Direct combustion of straw in grate furnaces is mainly used but there are great difficulties with slagging and fouling. This is because cotton straw contains large amounts of potassium, chlorine and silicon, which often lead to a rapid buildup of unmanageable amounts of deposits. This results in reduced boiler efficiency and unscheduled plant shutdown. In biomass combustion, in general, the

main part of the deposit is formed by particle inertial impaction, but other deposition phenomena, such as chemical reactions and condensation, are also of great importance with regard to the deposition of potassium, chlorine and sulphur. Sulphation of potassium hydroxide and potassium chloride are important chemical reactions that lead to ash deposition in both coal and biomass combustion. Alkali compounds contained in the fuel may be released during combustion and form alkali species, including salts and particulate matter (fly ash particles and aerosols). Under grate-firing conditions, particles of different sizes are characterized into two main groups: fine particles that usually consist of aerosols with diameters between 30 and 300 nm and coarse particles that mainly consist of nonvolatilized ash residuals with diameters between 1 and 100 μm, depending upon the fuel and furnace (Venturini et al., 2010). The deposition of the sub-micrometer class of particles is mainly influenced by the thermophoresis and turbulent diffusion within the turbulent boundary layer. Further, the deposition of larger fly ash particles is more likely to be dictated by the inertial impaction. In this thesis, the particle sizes up to approximately 110 μm have been considered on the basis of experimental data from the combustion of waste wood and wood chips (Venturini et al., 2010).

There is still a lack of knowledge on the exact mechanism of potassium release during biomass combustion, particularly when the particles are being heated at a high rate and to a high temperature, as found in grate-fired furnaces. It is generally accepted that the release of potassium from biomass particles is usually in the form of KCl and/or KOH, depending upon the biomass composition. The former, in particular, is among the most stable high-temperature, gas-phase, alkali-containing species. The chlorine

content in the biomass often dictates the amount of potassium release during combustion, and it also strongly influences the transport of alkali from the fuel to the heating tube surfaces, where the alkali often form sulphates. The potassium that is released into the gas flow undergoes complex transformations and forms KOH, KCl and K_2SO_4 in different temperature regimes. Further, they are expected to nucleate as well as form aerosols in the flue gas. KCl and K_2SO_4 can condense on the surfaces of the fly ash/aerosols and on the superheater system, thus providing a sticking layer for the arriving particles to deposit (Kaer, 2001).

The reactions between the alkali and sulphate have only been investigated to a certain extent (Hindiyarti et al., 2008; Jiménez et al., 2007; Jensen et al., 2000; Christensen et al., 1998; Kassman et al., 2010). Several authors have reported the properties of fine alkali particles emitted from biomass-fired furnaces (Jensen et al., 2000; Christensen et al., 1998; Kassman et al., 2010; Christensen et al., 2000; Boonsongsup et al., 1997). These particles are found to consist of alkali chlorides and sulphates in relative amounts that depend upon not only the properties of the fuels burned but also the characteristics of the boiler (Christensen et al., 1998; Kassman et al., 2010). Christensen et al. (Christensen et al., 1998) developed a model for the formation of fine particles during the combustion of straw. They deduced that the oxidation of SO_2 to SO_3 was the rate-limiting reaction in the formation of alkali sulphate. Further investigations by these authors in laboratory experiments with different biomasses confirmed this limiting step (Christensen et al., 2000). Recently, Glarborg and Marshal (2005) proposed a detailed reaction mechanism for gaseous alkali formation in combustion conditions, and the model adequately reproduced some

experimental results on the suphation of gaseous KCl. According to the detailed mechanism (Glarborg et al., 2005), the modelling of the formation of alkali sulphates from alkali chlorides, found in deposits or ash particles, is based on the assumption that potassium species first transform in the gas phase (homogeneous reactions) and then react in condensed or solid phases (heterogeneous reactions). In the proposed heterogeneous mechanism, a gas-phase alkali containing a precursor is transported to a surface where it is then sulphated by reactions in condensed or solid phases. Concerning the homogeneous reaction, alkali sulphate aerosol seeds are formed in a series of steps that occur in the gas phase by homogeneous nucleation. The seeds also act as condensation nuclei for further condensation of alkali sulphate vapours and other supersaturated vapours, e.g. alkali chlorides, as the flue gas cools (Glarborg et al., 2005; Hindiyarti et al., 2008; Boonsongsup et al., 1997). Iisa et al. (Iisa et al., 1999) provide detailed measurements of the rate of sulphation of KCl in gas and condensed phases and demonstrated that the rate of sulphation is considerably slower in the condensed phase.

Previous numerical studies have addressed the deposition on heat-exchange surfaces as a function of tube arrangements (Tomeczek et al., 2004), locations within the boiler (Forstner et al., 2006; Baxter, 1973), and deposition probe location (Akbar et al., 2010). Most of these studies have focused on the modelling of particle sticking behaviour, such as ash particle viscosity and melting fraction, to determine the particle collection efficiency (Ma et al., 2006; Huang et al., 1976; Degereji et al., 2011). The size of fly ash adhered together by alkali salts is also essential in determining the sticking probability. The effects of this factor have been investigated in coal

combustion (Tomeczek et al., 2009), but in biomass combustion, which has a higher content of inorganic components and more interactions and association of these elements, little has been reported. The ash-forming vapor is involved in a complex system. Because of the strong dependence of the kinetic rates upon the temperature (Christensen et al., 1998), it is expected that the composition of ash-forming vapors will be near equilibrium conditions at typical flame temperatures, with increasing deviation from equilibrium at lower temperatures, as the flue gas cools and condenses on the heat-transfer surfaces. As a result of this condensation, high concentrations of K, Cl and S constitute the initial deposit. The aim of this investigation is to reduce a comprehensive alkali mechanism for the sulphation of KCl to a level that may be practically implemented into CFD simulations of alkali species transformation in a combustion system and to implement the reduced mechanism in a test furnace to determine its effect on the initial deposit formation incorporating an ash deposition model.

4.2 Overview of the Biomass Deposition Scheme

To successfully validate a numerical model for ash deposition, the species concentration, temperature profile and velocity distribution of the gas phase are first established. The interaction between the carbon, H_2/O_2, chlorine, sulphur and potassium within the turbulent reactive flow, condensation, nucleation and deposition of fly ash particles is very complex (Bryers, 1996). The predominant stable alkali-bearing species released from the fuel grate bed at the prevailing combustion temperatures (<1000^{o}C) is potassium chloride (Baxter, 1998a). For straw, with a high content of

chlorine in the fuel mix, such as the straw that is being investigated in this thesis, sulphation of KCl is the dominant pathway (Jensen et al., 2000). The presence of KOH in the gas phase is stable under an increasing temperature, and a high content of water vapour (H_2O) and low content of Cl (Kassman et al., 2010). In the post-combustion region, the flue gas meets with the superheaters and it cools. When the saturation pressure of KCl and K_2SO_4 is reached, it condenses and deposits on the cooled surfaces. This can occur either by direct vapour condensation on the tube surface or by vapour condensation on the fly ash, or aerosols being formed in the free gas stream within the thermal boundary layer close to the surface, as depicted in Figure 4.1 (see for example, Kaer, 2001).

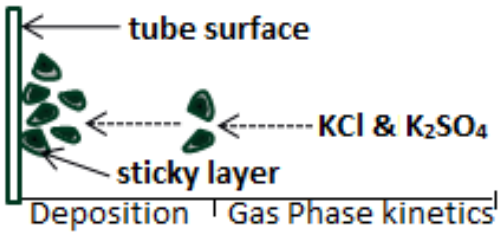

Figure 4.1: Systematic presentation of the vapour deposition (Kaer, 2001).

The formation of KCl and K_2SO_4 involves H_2/O_2, chlorine, sulphur, potassium chemistry and the interactions between them (Glarborg and Marshall, 2005; Hindiyarti et al., 2008). The implementation of a detailed alkali reaction mechanism in a multi-dimensional and large-scale CFD calculation is computationally expensive, often even prohibitive, and therefore, developing a reduced alkali mechanism is a necessary precondition. The approach taken in this investigation was to remove redundant species and reactions from the detailed reaction mechanism using a sensitivity analysis at specified reaction conditions that are pertinent

to the grate furnace combustion investigated. Once the reduced mechanism has been developed, it is validated against both experimental data and the detailed reaction mechanism from which it was reduced to ensure that any performance error incurred as a result of the reduction is within an acceptable level. The reduced mechanism is then imported into the CFD model in the CHEMKIN format and is used to calculate the production and destruction of the species participating in the chemical reactions (Kee et al., 1996). FactsSage calculation provides an inlet boundary condition of the gas phase composition to the CFD model which is then used to calculate the sulphations and other species transformations and condensations across the computational domain, incorporating the reduced alkali mechanism. Figure 4.2 shows the connection between CHEMKIN, FactSage and the CFD model. The condensation of alkali salts in the flue gas is addressed as a reaction step that is added to the reaction mechanism with the rate constant suggested by Glarborg and Marshal (2005).

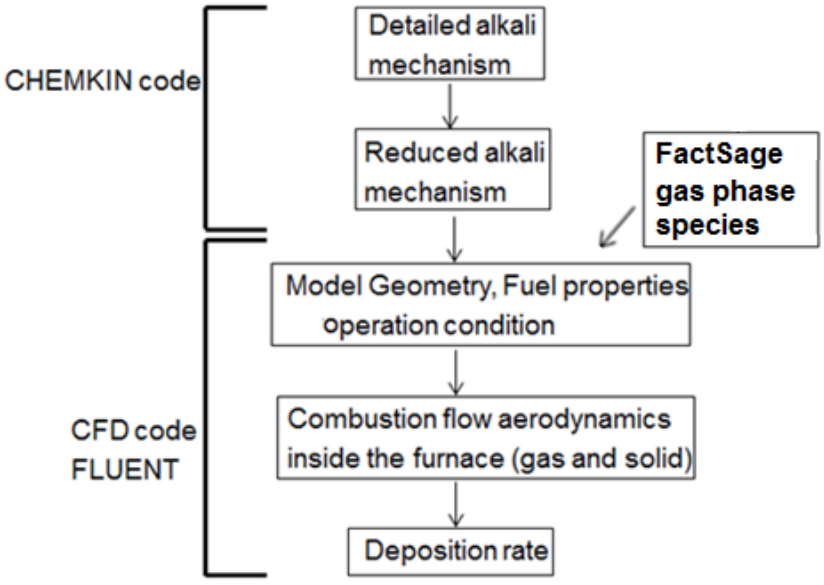

Figure 4.2: Schematic of the connection routes between CHEMKIN, FactSage and the CFD model.

4.2.1 Reduction of the Detailed Alkali Mechanism

A complex chemical process, such as combustion, can be modelled with a number of individual reactions called a mechanism. A mechanism study proposes a set of reactions, runs a numerical calculation, and compares the result with experiment. For example, biomass combustion mechanisms dealing with the alkali transformation involve tens to thousands of chemical reactions occurring simultaneously within a complex flow field. Currently, the direct use of detailed chemical mechanisms in Computational Fluid Dynamics (CFD) calculations of reactive flows is computationally expensive principally due to the large number of species involved and the wide range of chemical time scales present. Therefore, there is a well-recognized need to develop reduced mechanism that reproduced the primary features of the detailed mechanism with highly simplified kinetics in order to obtain a quick solution.

To produce a reduced alkali mechanism that retains the essential features of the detailed chemistry, but with a much improved computational efficiency in terms of computer memory usage and central processing unit (CPU) time, we start with the detailed chemical kinetic model by Hindiyarti et al. (2008) that includes 54 chemical species and 220 elementary steps. A systematic reduction procedure, based on a sensitivity analysis, was performed to remove the redundant chemical species and reactions from the detailed mechanism using the KINALC software code (1989). The code is a post-processor to the CHEMKIN family of codes that are used to integrate the governing coupled differential equations that describe the rate of change of the gas concentration for each chemical species in a given reactor with

highly simplified physics. The rate of change of concentration in a closed vessel is given by:

$$\frac{d[c_i]}{dt} = \sum_j v_{ij} R_j \qquad (4.1)$$

where c_i is the concentration of species i, v_{ij} is the stoichiometric coefficient of the species i in the reaction j and R_j is the jth reaction rate. The Jacobian system is used to reduce mechanism by first identifying the necessary species (Turanyi, 1989). In order to reproduce the concentrations of important species, the concentration of selected species were defined by the user. The sensitivity of the rate of production of an important species to a change in concentration of species i, is given by:

$$B_i = \sum_{n=1}^{N} (\partial \ln f_n / \partial \ln c)^2 \qquad 4.2$$

where f_n is the rate of production of species n. B_i is set to different threshold values for the species sensitivities at several reaction conditions. The higher the B_i value, the greater is the direct effect of species i on the rate of production of important species. Necessary species are taken into account by an iterative procedure, whereby the B_i values are calculated for all species and the species with the highest B_i value is incorporated into the necessary species after each calculation. The procedure is repeated again and again until a large gap appears between the ranked B_i values of necessary and redundant species as they form definite groups. The union of necessary species over these conditions was taken. As a result, a reduced

mechanism comprising 36 species, i.e. SO_2, SO_3, K, KO, KO_2, KOH, $K_2O_2H_2$, KCl, K_2Cl_2, $KHSO_3$, KSO_4, KSO_2, KSO_3, $KHSO_4$, K_2SO_4, KSO_3Cl, $K_2SO_4(B)$, CO, CO_2, H, O, OH, H_2, O_2, HO_2, H_2O, H_2O_2, HOSO, $HOSO_2$, HCl, Cl_2, Cl, ClO, HOCl, ClOO and N_2, and 137 reversible reactions was created, see Appendix A.

4.2.2 Inclusion of the Alkali Mechanism into the CFD model

The commercially available CFD software package FLUENT 12.1 (Zhou et al., 2007) was used in this thesis. FLUENT can model the mixing and transport of species by solving conservation equations describing convection, diffusion and reaction sources for each component species. Multiple simultaneous chemical reactions occurring in reduced alkali mechanism can be modelled. The reduced alkali mechanism developed, together with all of the thermodynamic properties that are required, is imported into the CFD model in a typical CHEMKIN format, where it is used to calculate the production and destruction term in the transport equations for the chemical species. Typical solutions from a CFD code include temperature, pressure, velocity and species concentration of the fluid in the computational domain. The gaseous phase in the furnace was modelled in an Eulerian frame of reference, whereas the discrete solid biomass particles was modelled using the Lagrangian approach. The transport equations for the gaseous phase were solved as well as the discrete phase equations formulated in Lagrangian form where the coupling between phases were introduced via particle sources in the Eulerian continuum phase equations. With solid fuel combustion, the transport of fuel/ash particles in the computational domain is typically calculated using the Lagrangian frame of

reference. Therefore, the tracking of the particles through the furnace and the angle at which the particles hit a wall surface is calculated using CFD. The ash deposition model is integrated into the CFD model using a user-defined function (UDF) DEFINE_DPM_EROSION. The variables required in the deposition model include the partial pressure, saturation pressure, diffusion coefficient of K_2SO_4, and information on the ash particles. They are all part of the solution of the CFD solver and are used as input to the ash deposition model. The ash deposition calculation may be performed as a post-process after the reacting flow simulation is complete if the impact of the ash build-up on the heat transfer and fluid flow is ignored, as may be the case in the initial stages of ash deposition.

4.3 Validation of the Alkali Reaction Mechanism

4.3.1 Detailed Mechanism Validation

To investigate and later validate both the detailed and reduced alkali mechanisms, the experimental data by Iisa et al. (1999) was chosen for model evaluation. This is because this was conducted under well-controlled conditions that are within the temperature regime of a typical biomass combustion flue gas. The experiments employed a laminar entrained flow reactor, where small, solid particles (65− 125 μm in diameter) of KCl are fed at a rate of 0.24 g/min, together with a gaseous mixture containing 2% SO_2, 5% O_2, 10% H_2O and (remaining balance) N_2%. In laminar flow the motion of the particles of fluid is very orderly with all particles moving in straight lines parallel to the reactor walls. The particles were rapidly heated to a temperature of 1173−1373 K by hot reactor walls and the hot secondary gas

with a residence time of up to 1.5 s. The heated KCl particles became molten, partially vaporized, and then became sulphated in the presence of SO_2, O_2 and H_2O. The products of the reaction between the vapour phase (i.e. SO_2, O_2 and H_2O) and molten KCl were collected separately and analyzed for ions of K, SO_4 and Cl using a capillary electrophoresis analysis to determine the extent of the alkali sulphation.

It should be noted that these solid KCl particles are employed purely for the purpose of producing gas-phase KCl in the entrained flow reactor in order to investigate the alkali sulphation. They are not used for the particle deposition experiments. The conversion of KCl(s) to KCl(g) is first transformed into three unstable reactive intermediates before it is converted to KCl(g). The order of reactivity of the intermediates are given as followed: KCl***> KCl**> KCl* where KCl*** is the most highly reactive intermediate and KCl* is the least reactive intermediate. The evaporation of the solid potassium chloride was modelled with three pseudo-first-order reactions taken from Hindiyarti et al. (2008) with rate constants fitted to match the experimental data in the detailed mechanism.. These pseudo-first-order reactions for the evaporation of KCl at different kinetic rate is shown in Table 4.1. The composition of the KCl(g) and the gaseous mixture fed plug flow reactor in Chemkin used for the kinetic calculations is shown in Table 4.2. The pseudo-first-order reactions are the reactions where the concentration of one of the species is in large excess. The concentration of the species in excess will not change appreciably and can be considered constant and therefore the reaction behaves like a first-order reaction and is designated as a pseudo-first-order reaction.

Table 4.1: The vaporization model for the KCl at different kinetic rates (Glarborg et al. 2005).

Input	k (s^{-1}) 1373 K	k (s^{-1}) 1173 K
KCl***=>KCl**	2.4	0.72
KCl**=>KCl*	2.4	0.72
KCl*=>KCl(g)	2.4	0.72

where asterisk (*) is the unstable reactive intermediate.

Table 4.2: Composition of the KCl(g) and the gaseous mixture fed plug flow reactor in Chemkin used for the kinetic calculations at 1373K and1173K.

Input	Mol %
KCl	4.78E-1
SO_2	1.99
O_2	4.98
H_2O	9.95
N_2	82.6

Figures 4.3 and 4.4 show a comparison between the predicted and experiment data for the KCl vaporization and the sulphation as a function of the residence time from the full alkali mechanism at 1373 K. It is observed that the prediction of KCl vaporization and sulphation by the detailed mechanism are in good agreement, although the theoretical simulation of the sulphation of KCl slightly underpredicts the experimental data. Similar

observations with respect to the underprediction were also reported for the detailed mechanism in the work by Hindiyarti et al. (2008).

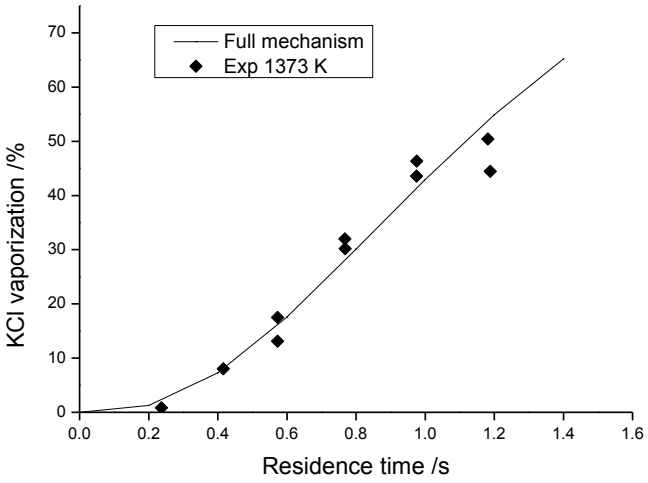

Figure 4.3: Full mechanism vaporization of KCl as a function of the residence time.

Figures 4.5 and 4.6 show the vaporization and sulphation of the KCl as a function of the residence time at 1173 K and 1373 K for full mechanism. The prediction for the vaporization and the sulphation are reasonably consistent with the measurement data, particulary at a temperature of 1373 K. The underprediction for the sulphation of the KCl at 1173 K has been observed in Figure 4.5 for the vaporization and sulphation at 1173 K, especially for the sulphation. This is because of the strong dependence of the kinetic rates on the temperature and it is expected that the combustion gases will be near equilibrium at typical flame temperatures, with an increasing deviation from the equilibrium at the lower temperatures as the flue gas cools down in the boiler back-pass.

Figures 4.7 and 4.8 show the vaporization and sulphation of the KCl as a function of the residence time at 1173 K and 1373 K for reduced

mechanism. The prediction for the vaporization and the sulphation are also reasonably consistent with the measurement data, particulary at a temperature of 1373 K. The significant underprediction for the sulphation of the KCl at 1173 K has been observed in Figure 4.8.

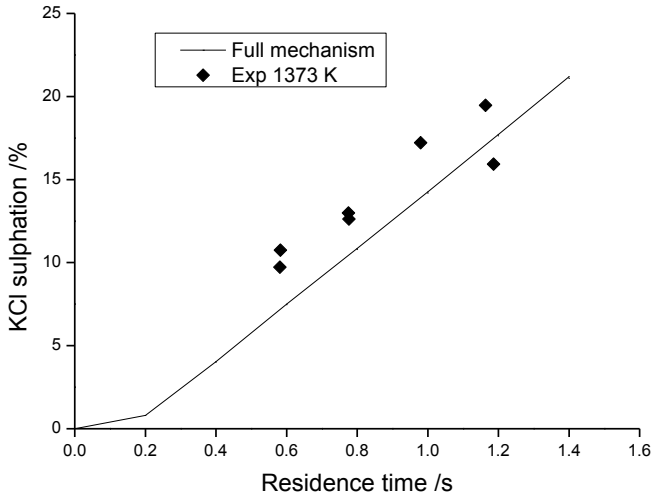

Figure 4.4: Full mechanism of the sulphation of KCl as a function of the residence time.

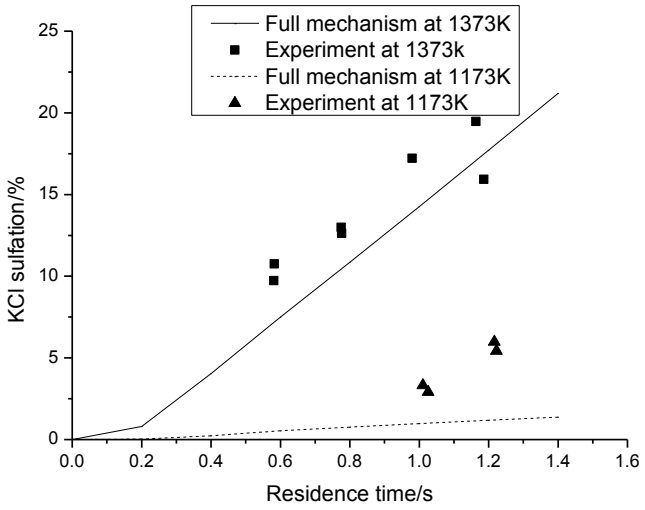

Figure 4.5: Full mechanism sulphation of the KCl as a function of the residence time at 1173 K and 1373 K.

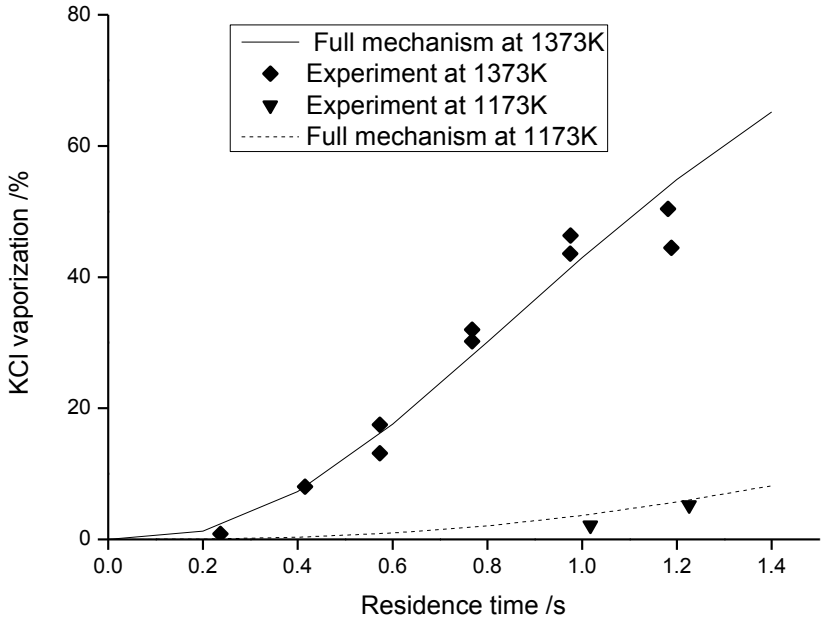

Figure 4.6: Full mechanism vaporization of the KCl as a function of the residence time at 1173 K and 1373 K.

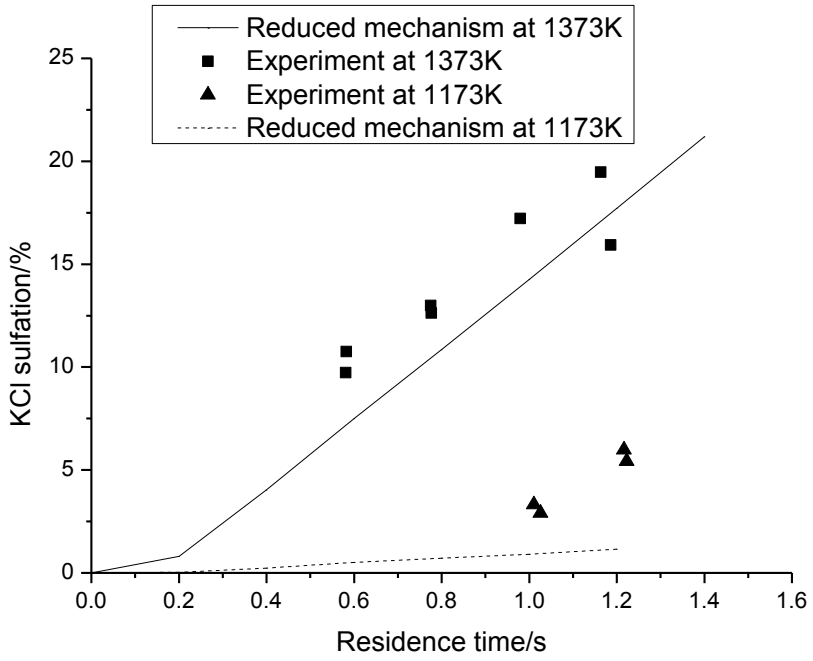

Figure 4.7: Reduced mechanism sulphation of the KCl as a function of the residence time at 1173 K and 1373 K.

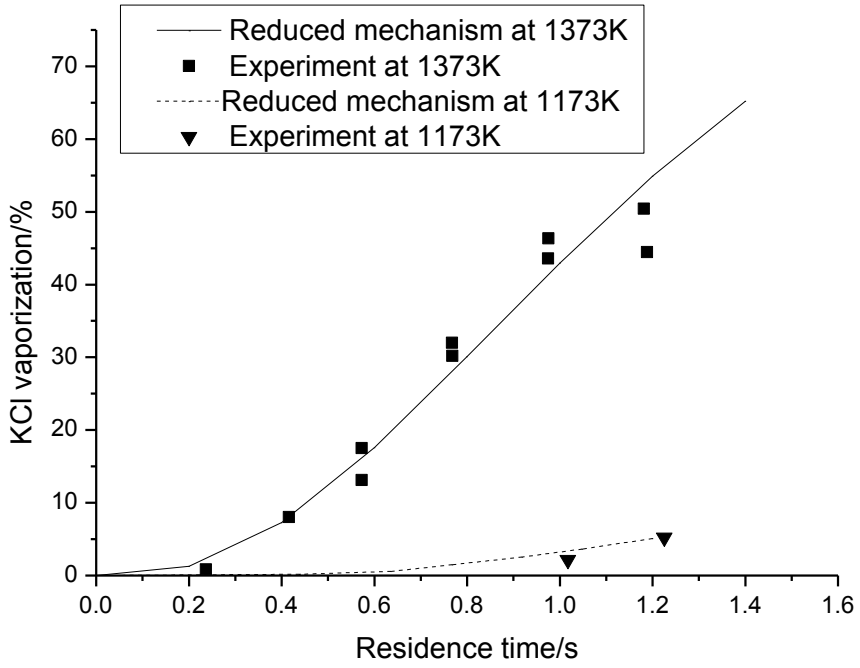

Figure 4.8: Reduced mechanism vaporization of the KCl as a function of the residence time at 1173 K and 1373 K.

4.3.2 Reduced Mechanism

The reduced mechanism was developed through an iterative analysis of the Jacobian matrix (Turanyi, 1989) of the system of kinetic differentials that investigates the effect of species concentration changes on the rates of production of important and necessary species. The aim of the reduction is to produce a reduced subset of the species and reactions that can reproduce the concentrations of important species, or important reaction features that are represented in the detailed mechanism. Thresholds for ranked species sensitivities were applied at several predicted biomass post combustion reaction conditions, and the union of the necessary species over these conditions was taken.

The validation of the reduced mechanism is performed by first comparing the results from the reduced alkali mechanism with the experimental data as shown in Figures 4.9 and 4.10. Figures 4.9 and 4.10 show a comparison of the reduced mechanism to the benchmark performance of the full mechanism and the experimental data.

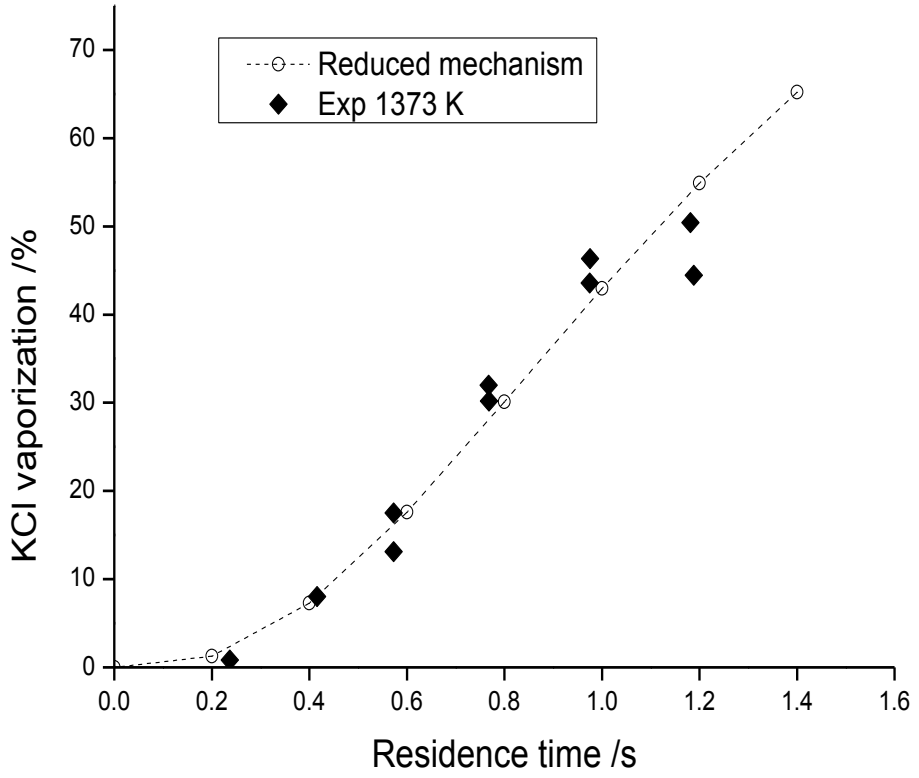

Figure 4.9: Reduced mechanism vapourization of KCl as a function of the residence time.

Examination of the features of the reduced mechanism reveals that the potassium vaporization process is well-predicted by the reduced scheme, see Figure 4.11, where the two theoretical predictions overlap each other. In terms of the KCl sulphation predictions shown in Figure 4.12, the predictions obtained using the reduced mechanism are shown to reproduce the primary

features of the detailed mechanism and they almost overlap each other. It may be concluded that the reduced alkali mechanism with 36 species and 137 reactions can reproduce the predictions from the full detailed reaction mechanism under the conditions investigated with reasonable accuracy and can therefore be used with confidence . This corresponds to a computational cost reduction of at least 50%. It is possible to reduce the numbers of species and reactions even further. However, the increased error induced by the reduction below the 36 necessary species and 137 reversible reactions was considered to be unsatisfactory, and it gave little extra computational saving.

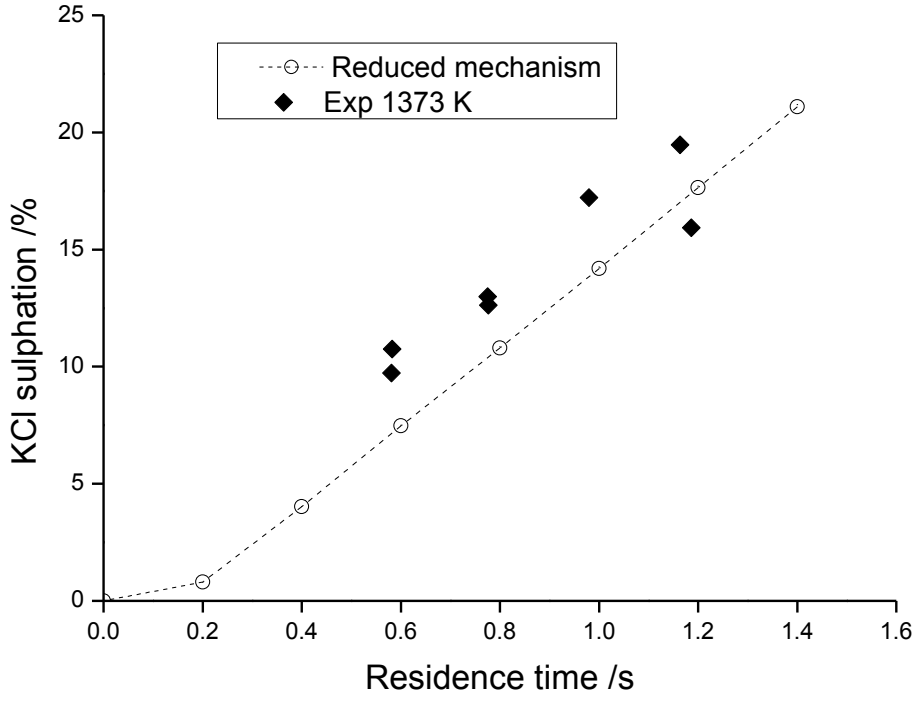

Figure 4.10: Reduced mechanism of the sulphation of KCl as a function of the residence time.

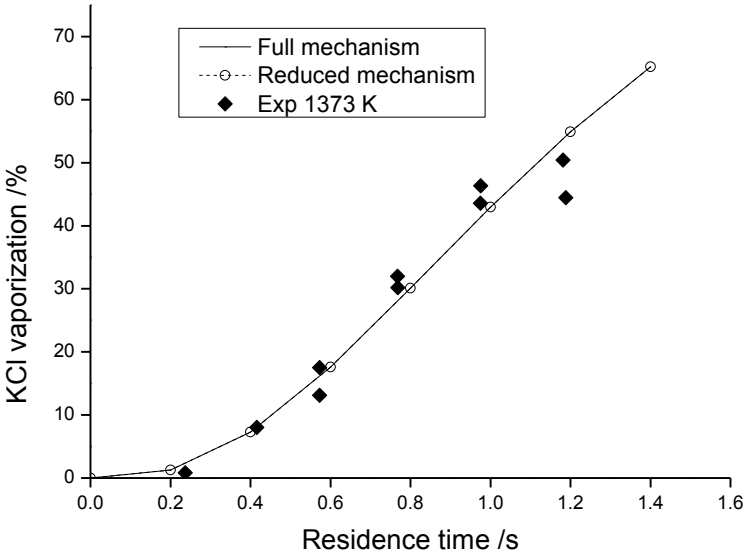

Figure 4.11: Full and reduced mechanism vaporization of KCl as a function of residence time.

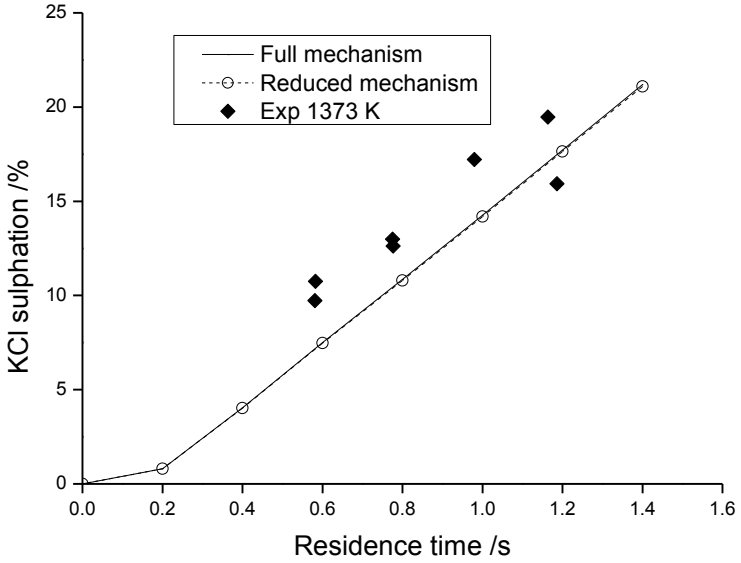

Figure 4.12: Full and reduced mechanism of the sulphation of KCl as a function of the residence time.

4.4 Straw-fired Grate Furnace

During biomass combustion, ash forming vapours are released from the fuel bed into the gas phase. The compositions of the chemical species released as gas phase have been determined using equilibrium calculations which are shown in Table 4.3. According to equilibrium calculation 80% of the potassium were assumed to remain in the solid phase. Gaseous and condensed components estimated are shown in Table 4.3. When the gases are cooled down in the convection section of the boilers, more condense and form a large part of the ash particle fraction. The mass flux and the composition of these ash particles depend on the temperature in the fuel bed as well as the composition of the fuel. A complete modelling of a biomass-fired grate boiler involves the modelling of the biomass combustion inside the fuel bed on the grate and gas-phase reaction above the grate-bed (freeboard). A more detailed model that treats the ash fuel bed on the grate using a two-dimensional discretization has been described by Zakaria et al. (2000) and Kaer et al. (2001).

In the burner region of the furnace, there may be a residual carbon content in the deposited particles which are oxidized at the furnace wall. This can potentially change the local conditions from an oxidizing condition to a reducing condition, thereby increasing the temperature of the local deposit. In coal-fired boilers, this changes the sticking propensity significantly if the ash contains iron. However, in biomass combustion systems this effect is not significant (Baxter et al., 1996) because of the low content of the iron present in biomass fuel.

In a grate fired boiler, a fraction of the ash particles is entrained in the gas flow due to the following: (i) the flow of primary air through the grate, (ii) the interaction with air from the injection nozzles above the fuel layer, and (iii) because of grate vibrations. From full scale measurements, Michelsen et al. (1998) estimate that approximately 20% of the ash is entrained.

Inertial impaction and condensation of the ash forming vapours were considered as the mechanisms of matter transport to the boiler surfaces. Inertial impaction is governed by the motion of the particles caused by the mean gas velocity field. Further, the inertia of the larger particles is sufficient to allow their trajectories to deviate from the gas streamlines and impact on the walls.

Table 4.3: Composition of the input for the CFD model – all values in mol% at 1274K.

SO_2	SO_3	K	KO	KO_2	KOH	$K_2O_2H_2$	KCl	K_2Cl_2
3.59E-04	9.66E-07	4.39E-09	2.30E-10	6.50E-10	6.11E-05	2.41E-10	3.51E-04	3.39E-06
$KHSO_3$	KSO_4	KSO_2	KSO_3	$KHSO_4$	K_2SO_4	KSO_3Cl	K_2SO_4[B]	CO
4.79E-10	1.55E-06	7.19E-11	3.40E-11	1.16E-11	1.55E-06	9.49E-11	2.57E-09	3.68E-08
CO_2	H	O	OH	H_2	O_2	HO_2	H_2O	H_2O_2
0.153	6.99E-09	9.95E-09	3.39E-06	1.76E-08	3.10E-02	7.49E-12	0.11	8.49E-12
HOSO	$HOSO_2$	HCl	Cl_2	Cl	ClO	HOCl	ClOO	N_2
1.55E-13	9.88E-12	2.00E-06	7.79E-12	5.23E-09	5.59E-13	1.42E-13	4.60E-11	0.706

Condensation is governed either by the cooling of the flue gas within itself or the contact of the flue gas with the cooled wall. As a consequence, the vapour pressure of the flue gas components decreases. If the vapour pressure of the ash vapour becomes lower than the saturated pressure of the ash vapour, the aggregate state changes to liquid or solid phases. Consequently, particles which are entrained in the gas flow are deposited on

the walls, or are emitted from the furnace exit as the condition of the gas phase changes.

Table 4.4: Temperatures of the different heating surface and parameters used as input to the CFD modelling of the straw boiler.

Parameters	Average superheater tube temperature
Fourth superheater (K)	764
Secondary superheater (K)	731
Primary superheater (K)	663
Superheat outlet temperature (K)	612
Mass flow rate (kg/s)	10
Inlet temperature	1274
Ash content (%)	3.38
Particle size distribution (μm)	1-110 (see Table 4.6 for the details of the particle size distribution)

Prior to CFD calculation, the combustion process was modelled by Factsage calculation to provide insight into the phases (gas, liquid and solid) that occur during potassium vaporization and transformation. FactSage gives the gas phase composition (Table 4.3) and this is used as an input into the CFD model and then linked to the reduced chemical mechanism embedded in the CFD model. Solid potassium is first vaporization to KCl and subsequently KCl is transformed to K_2SO_4 in the gas phase. The estimated results of the potassium species in form of KCl, K_2SO_4 and other species are

given in Table 4.3. During deposition formation, KCl and K_2SO_4 in the gas phase is first condense to form liquid K_2SO_4 (see result of the condensed K_2SO_4 Figure 4.12) which the subsequently provide a sticky layer for ash solid particles (such as Si, Al, Ca, K, etc) to be deposited on the heat transfer surface**.**

In order to investigate the capabilities of the model developed to predict the effect of condensable alkali salts on ash deposition rates, simulations were performed for a 10 MW_{th} biomass-fired industrial grate furnace. A complete modelling of a biomass-fired grate boiler involves the modelling of the biomass combustion inside the fuel bed on the grate and gas-phase reaction above the grate-bed (freeboard). The coupling of the two processes has been modelled by several investigators taking into consideration the combustion gas released from the fuel bed into the freeboard and the radiative heat flux emitted by the flame and furnace walls onto the fuel bed (Shin et al., 2000). However, for the purpose of investigating ash depositions on the superheaters downstream of the boiler, in this chapter only the second half of the entire boiler was simulated with the boundary conditions to the model obtained from the onsite measurements.

The boiler uses an M-type arrangement and four grade superheaters, as is schematically shown in Figure 4.13. The flue gas leaves the furnace through the third (SH3), fourth (SH4), secondary (SH2), then the primary superheaters (SH1) one after the other, and then goes through the economizer and the air pre-heater. Heavy slag formed on the furnace is found in the cooler section of the boiler where the fourth, secondary and

primary superheaters are located. The locations correspond to the section where the combustion gases deviate from being in equilibrium and the kinetic dependence on temperature becomes significant. Cotton straw is used as the fuel in the experimental investigations and its typical chemical and thermo-physical properties, as found experimentally and used as input to the simulation, is shown in Table 4.1. As expected, a high level of K and Cl is present in the fuel analytic data. A more detailed description of the furnace and the experiments performed can be found in Niu et al. (2010).

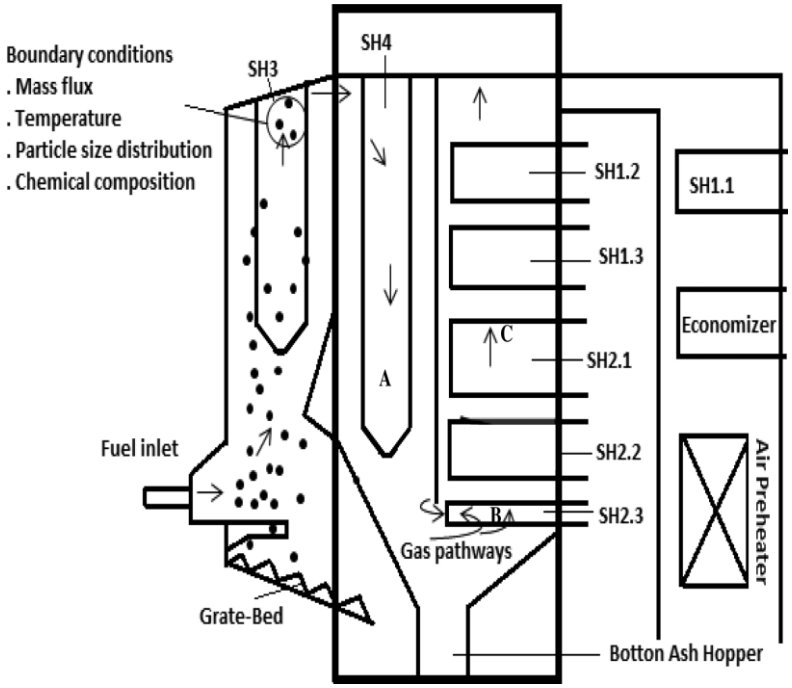

Figure 4.13: Schematic diagram of the Shenyang power plant furnace (Niu et al., 2010).

CFD model**:** The section of the boiler considered for the deposit formation simulations are indicated as enclosed in the thick box in Figure 4.2. Due to computational complexities, only half of the boiler is considered in the CFD model which covers all the locations where deposits are formed on the superheaters. The present computational capabilities do not permit detailed resolution of each and every tube in the boiler, even when a structured grid

is used for the grid generation. The presence of tube banks in the geometrical model of the test case must be simplified in order to sufficiently account for the super heaters. In typical biomass fired boilers, superheaters are designed with spacing between the tubes for the ash to build up. For simplicity, Figure 4.14 illustrates how the superheaters are taken into account in the CFD model. Each tube is assumed to be a rectangular block and the vertical array of tubes are taken as a single tube (A-A, B-B, C-C and D-D). The number of the rectangular block that has been resolved in this investigation can be view from View A-A, View B-B, View C-C and View D-D The resolution of the geometrical details was relaxed so as to achieve reasonable computational effort.

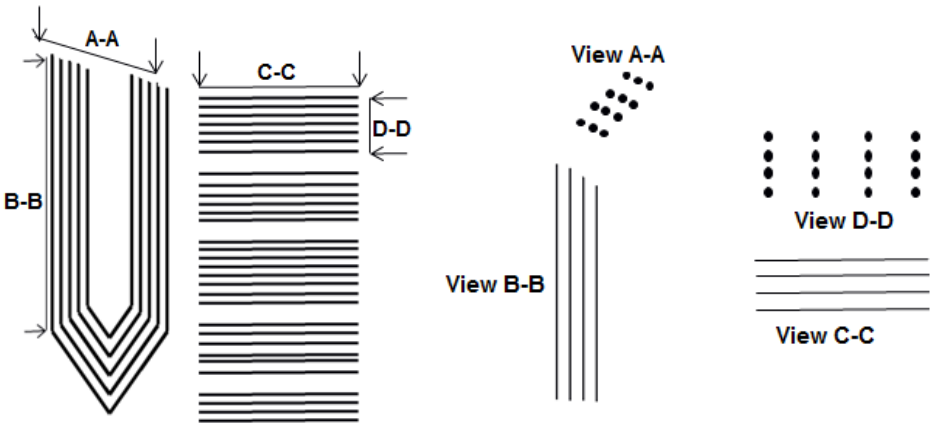

Figure 4.14: Geometrical representation of the CFD model.

The main dimensions used in the CFD model are indicated in Figure 4.15. The diameter of the tube used in the superheaters is 38 mm and the computational domain is meshed with the GAMBIT mesh generator. The mesh employed consists initially of about 1 million cells. The grid was later continuously refined to ensure a grid-independent solution which ended with 1.9 million cells. No significant changes in the gas temperature and the

velocity distributions with a further increase in the number of computational cells was observed. A typical computational mesh is shown in Figure 4.16.

Fuel properties and operating conditions: The chemical and physical properties of the cotton straw that have been used in these calculations are shown in Table 4.5.

Table 4.5: Chemical and thermo-physical properties of the cotton straw (wt.%).

Proximate analysis (% wt as received)		Physical property of the fuel	
Moisture	2.63	Density, kgm^{-3}	570
Ash	4.22	Specific heat, $Jkg^{-1}K^{-1}$	1670
Volatiles	72.61	Heat conductivity $Wm^{-1}K^{-1}$	0.12
Fixed carbon	20.54		
Ultimate analysis (% wt as received)		Ash (% wt as received)	
C	45.86	SiO_2	13.74
H	5.53	Al_2O_3	4.03
O	40.96	Fe_2O_3	1.16
N	0.61	CaO	25.15
S	0.19	MgO	10.99
Cl	0.44	TiO_2	0.21
K	1.03	SO_3	5.75
		P_2O_5	6.98
		K_2O	25.40
		Na_2O	6.58

All the boundary conditions used for the CFD model are taken from the experimental data and/or theoretical estimations. Table 4.4 shows the some of the boundary condition used for the straw-fired furnace. The ash content of about 80% (4.22%) were assumed at the top of the bed and used as inlet boundary conditions for the CFD model (see Table 4.4). The details of the particle size distribution is given in Table 4.6. The gas temperature along the flue gas flow has been measured under the 10 MW_{th} load (Table 4.4). Averaged gas temperatures at the fourth, primary and secondary superheater are 764, 731 and 663 ^{o}C, respectively. For simplicity, a mean flow rate at the inlet of the computational domain of 10 kgs^{-1} of flue gas is applied over the entire boiler inlet area with a temperature of 1274 K. In the absence of experimental data, the ash particle size distribution obtained from the combustion of waste wood and wood chips has been used, ranging from approximately 1 to 110 μm as shown in Table 4.6. Immediately downstream from the combustion zone, it is likely that the gas-phase quickly reaches and maintains equilibrium due to the high temperature at the exit of the upstream section of the furnace. Therefore, chemical equilibrium is assumed at the inlet of the computational domain. Average superheater tube temperatures of 764, 731 and 663 K were used based on the steam temperature of the fourth, secondary and primary superheaters, respectively (Niu et al., 2010). A steam temperature of 613 K is used at the exit of the boiler. The furnace wall temperature of the CFD domain is specified between 800 – 1000 K based on the estimated local water tube surface temperature (Niu et al., 2010).

To model two-phase flow in the boiler, the gaseous phase was modelled in an Eulerian reference frame whereas the discrete phase

particles were modelled using the Lagrangian approach. The realizable version of the k–ε model has been used for the turbulence modelling because it takes into account the effects of the swirling in the furnace. The eddy dissipation concept (EDC) model is used for the turbulence-chemistry interaction because it accounts for the fine-scale turbulence structures. The stochastic tracking model (Discrete Random Walk) was applied to take into account the randomness of the turbulence during the dispersion of the ash particles in the furnace.

Table 4.6: Size class for the fly ash distribution (Venturi et al., 2010).

Size class	Particle concentration ($mgN^{-1}m^{-3}$)	Average diameter (m)	Particle mass flux (kgh^{-1})
1	87.00	1.10e-6	0.017545
2	145.44	1.10e-5	0.029263
3	153.60	3.10e-5	0.030904
3	146.24	5.10e-5	0.029423
4	100.16	7.10e-5	0.020152
5	87.20	9.10e-5	0.017545
6	13.28	1.11e-4	0.002672

The radiation heat transfer between the particles and the furnace has been modelled with the Discrete Ordinates (DO) model because it has the advantage of spanning the entire range of optical thicknesses. The procedure was modified by adding the deposition code that has been developed. The deposition calculation is performed as a post processing process with all the contributing factors obtained from the CFD calculations.

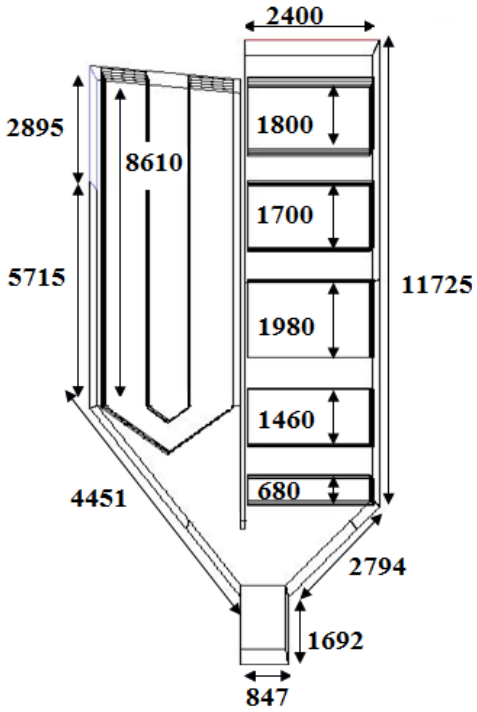

Figure 4.15: A schematic diagram of the CFD model geometry with the dimensions (mm).

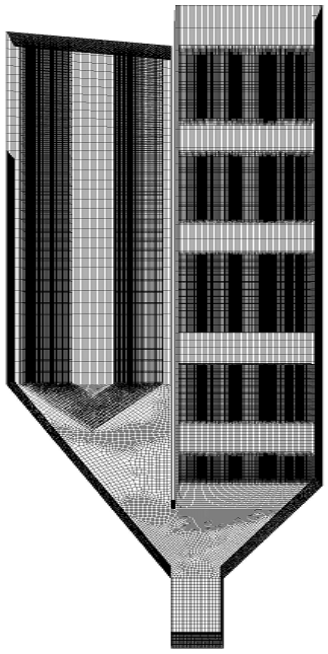

Figure 4.16: A typical computation grid employed in the calculations.

4.4.1 Gas Phase Temperature and Condensation

The predicted gas temperature profile on the plane of symmetry of the computational domain is shown in Figure 4.17. The CFD simulations show a recirculation zone, which causes a very uneven distribution of the flue gas temperature. The initial drop in the temperature is due to the high heat transfer to the water cooled walls, particularly on the front wall just below the inlet, see Figure 4.17. The subsequent fall in the temperature over the height of the boiler is caused by the heat transfer to the secondary and primary superheaters.

Concerning the homogeneous reactions, which involves the gas phase, nucleation and condensation, only two steps are taken into account, i.e. the formation of an alkali sulphate in the gas phase and its subsequent condensation. For the purpose of computational modelling, the detailed mechanism of deposit formation had to be simplified so that the nucleation and condensation processes are not included in the present work. This is because of the complex physical and chemical transformations of the inorganic components during the biomass combustion process. The condensation model approximation is described by second-order reactions and the rate constant (set to 10^{14} cm^3 mol^{-1} s^{-1}) for the pseudo-reaction [K_2SO_4] are taken from the work of Glarborg et al. (2008) has been adopted. If the temperature is below about 1240 K, condensed K_2SO_4[B] is formed quickly (Hindiyarti et al., 2008): However, we follow the suggestion of the authors by setting the rate constants for the pseudo-reaction to be 10^{13} cm^3 mol^{-1} s^{-1} and the maximum K_2SO_4 [B] concentration can be found in the ash

hopper, as shown in Figure 4.18 and also further upstream over the height of the boiler.

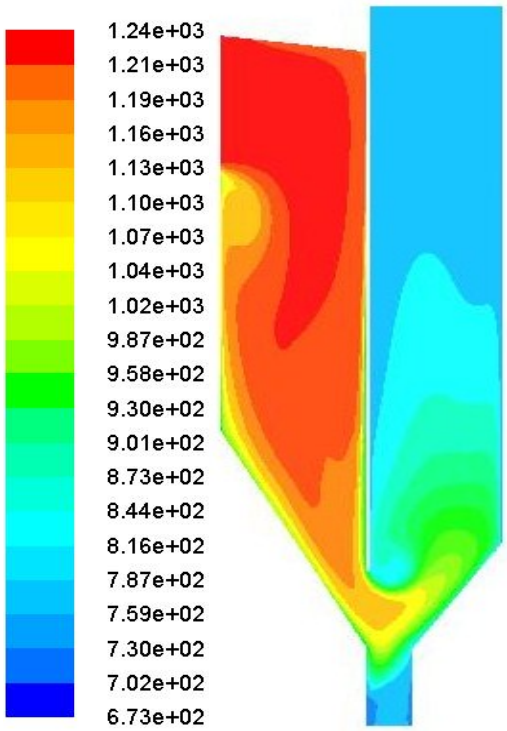

Figure 4.17: Contour of the static gas temperature (K) on the symmetry plane of the boiler.

Quantitatively, the predicted gas temperatures in the region of the three superheaters are in agreement with the measured data, see Figure 4.19. The discrepancies between the predicted temperature in Figure 4.19 and the measurement are believed to be mainly due to the boundary conditions used in the CFD model. This is because some of the boundary conditions are difficult to determine for a biomass-fired grate boiler in operation and could be very different from the real conditions for a number of reasons, for instance, non-uniform mass flow rate in the real boiler.

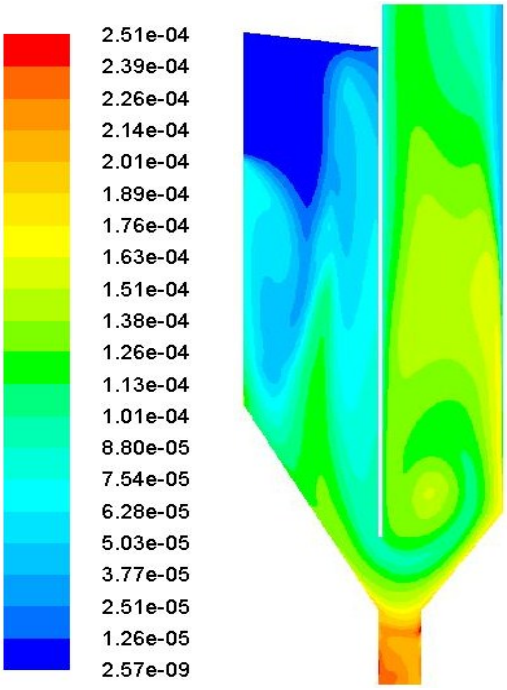

Figure 4.18: Concentration field of K_2SO_4 [B] on the symmetry plane of the domain of the boiler.

Further, the mass flow rate is far from being uniform, while the modelling is based on the mean flow rate over the entire boiler inlet area. This may explain why the predicted temperatures are higher than the measurement data. Another reason is the initial deposit formed on the superheaters; the surface temperature of the initial deposit that forms on the superheater causes the real surface temperature to be significantly higher than the measured temperature. Kaer et al. (2001) and Huang et al. (1996) reported that the initial fly ash lowers the surface temperature due to the very low thermal conductivity (0.1 $Wm^{-1}K^{-1}$) of the ash which thus affects the surface temperature.

4.4.2 Gas and Particle Velocities

As explained in Chapter 3, a mean flow rate at the inlet of the computational domain of 10 kgs^{-1} of the flue gas is applied over the entire

boiler inlet area. Figure 4.20 shows the gas velocity in the vertical plane of the freeboard. It is observed that the gas entering the freeboard undergoes an abrupt enlargement, leading to a decrease in the flue gas speed. This is partly mitigated by the drop in the density due to the combustion between the secondary air and the left over species (the gas inlet is adjacent to the secondary air inlet). Further, the geometry of the combustor creates a wide recirculation zone in the central region of the freeboard, as inferred by the low velocity values in that region. The recirculation vortex reduces the apparent cross-section available to the main flow, which accordingly speeds up the flue gas near the walls. As the flow path narrows down in the freeboard, the flows are accelerated and as the flows turn into the second chamber of the domain, a maximum velocity of 20ms^{-1} is recorded.

The motion of the particles caused by the mean gas velocity field can significantly influence the slagging pattern. According to the literature (Tomeczek et al., 2004; Walsh et al., 1990), it is assumed that 10 μm diameter particles would be expected to make the largest contribution to the deposit formation on the dry surface of the convective heat surface. Based on this assumption, and considering the large size of the biomass particles, deposition is calculated only on the front part of the probe. The inertia of the larger particles is sufficient to allow their trajectories to deviate from the gas streamlines as indicated in Fig. 4.21, where the predicted particle velocity is higher than the predicted gas velocity. In this region of the boiler, the gas velocity which lies between 3.5 and 4.7 ms^{-1}, causes a stagnation of the condensable species within the boundary layer of the tube, thus providing a sticking layer for the arriving particles. It is observed that the predicted gas velocities on the vertical plane of the boiler are in good agreement with the

measurement results. For the measurement points 1 and 2, where the velocities are high, predictions are within an accuracy of about 5% and this is considered to be good.

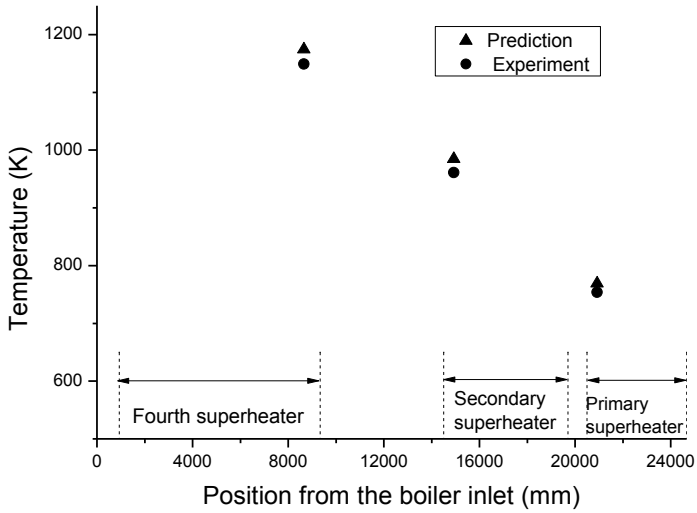

Figure 4.19: Measured gas and predicted gas temperature (^{o}C) in the boiler.

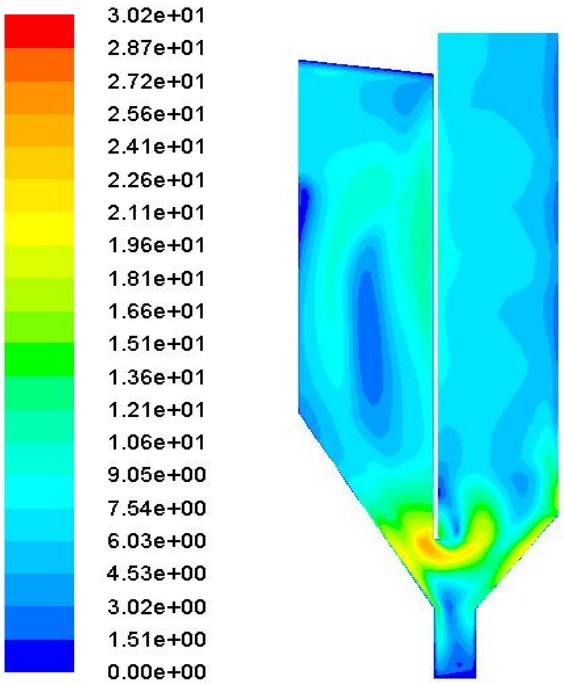

Figure 4.20: Contours of the gas velocity in a vertical plane of the freeboard.

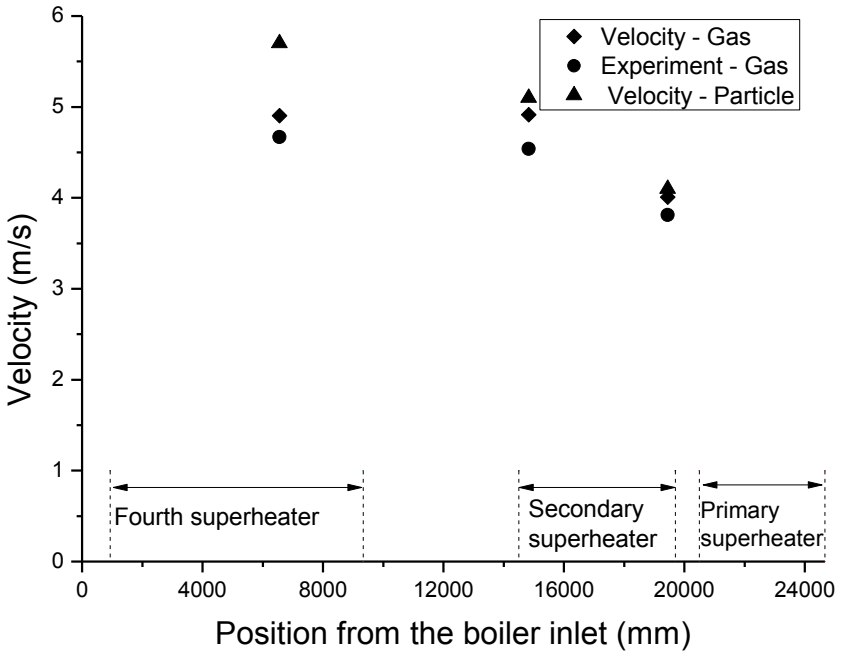

Figure 4.21: Measured gas and predicted gas and particle velocities of the boiler.

4.4.3 Deposition Rates on the Boiler Superheaters

The deposition rates of the ash particles have been calculated using the particle size dependence on the ash sticking probability. The particles are assumed to be sticky if the size of the particles captured by the sticky layers is greater than unity.

Figure 4.22 shows the contours of the predicted deposition rates on the fourth, second and first superheaters. As shown in Figure 4.13, the fourth, second and first super heaters are located at 8610, 1521, and 2210 mm away from the boiler inlet, respectively.

Due to the effect of the swirling flow in the downstream region of the fourth superheaters, particles are driven towards the second and first superheaters by the centrifugal force. Figure 4.22 shows that the rate of

deposition drops significantly near to the exit of the furnace where the particles are almost fully combusted and become light in weight. This means they easily follow the carrying gas stream and have less chance to deposit and the deposition rate is therefore expected to fall. In the boundary layer on these superheaters, the temperatures are low and the impaction particles are captured by condensed potassium sulphates and potassium chlorides on the tube surface. However, some particles are only partially able to reach the primary superheaters located further upstream of the secondary superheaters, so the deposit on it develop slowly, as shown in Figure 4.22. Detailed predictions of the deposit formation on the rows of the tubes have shown that the deposition rate on the first row of the tubes exceeds that on the subsequent rows in the tubes bank (Boonsongsup et al., 1997). This slowing down in the rate of deposit formation on the row of tubes can be clearly seen on the front side of the first and the subsequent tubes. The position of the deposits in Figure 4.22 has been guided by the contour map of K_2SO_4[B] formation as shown in Fig. 4.18, particularly around SH2 where the severity of the deposits have been reported experimentally by Niu et al. (2010) and now validated by the biomass deposition model. In addition, the deposit shape on the secondary superheaters (SH2.2) is illustrated in Figure 4.23, and it is observed that it is adequately captured and easily noticeable on the secondary superheaters (SH2.2) in Figure 4.22 This offers some evidence that the model has reproduced important information regarding the deposition of fly ash on the superheater.

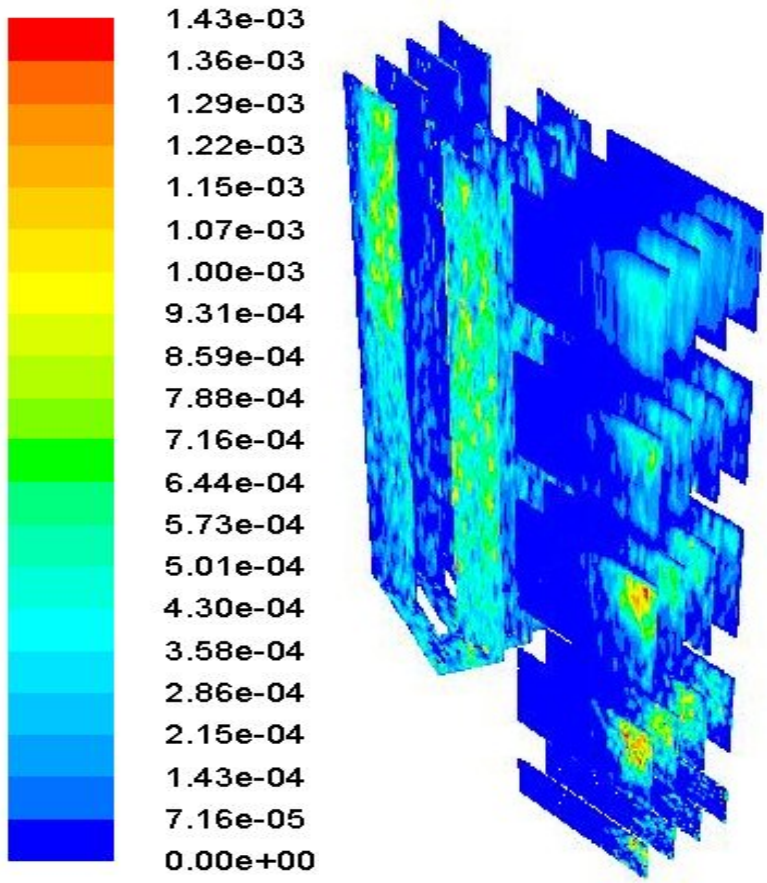

Figure 4.22: Contours of the deposition rates on the vertical surface of the boiler super heaters.

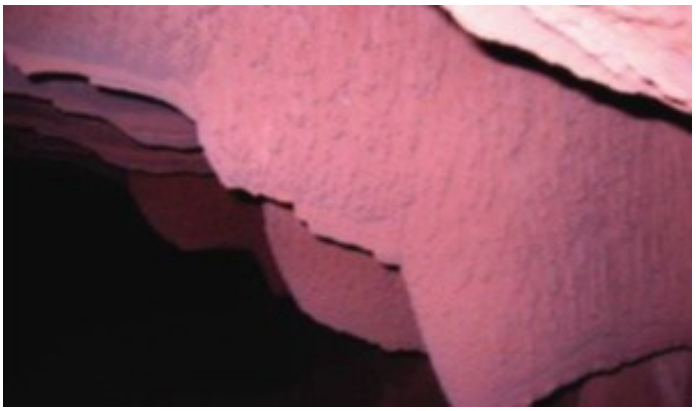

Figure 4.23: A photograph of the deposition formed on the vertical section of the secondary superheater (SH2) (Niu et al., 2010).

In order to test the sensitivity of the model, a calculation using the sticking probability coefficient of 0.9 rather than 1 has been performed and

the results of the prediction is shown in Figure 4.18. The behaviour of the deposits formed in Figures 4.22 and 4.24 shows a similar deposition pattern in terms of the location of the superheater regions where intensified deposits occur. However, the rates of the deposits change, as indicated by the colour code. This shows that when the sticking probability is reduced by 10%, the deposition rates decrease by about 15%. This means that a higher potassium content increases the condensates on the tube wall and on the particle and as a consequence this makes it more likely to stick on the tube surface. Therefore, accurate predictions of the condensate is of predominate importance in the low temperature environment close to the tube surface.

Typical model output data from straw-fired furnace include distributions of gas temperature, velocity, pressure, species concentrations and ash deposition distribution and rates. Typical values of calculated gas temperature, velocity and deposition rates are presented in Table 4.7. The output data from FactSage calculation at 1274K have already been presented in Table 4.3. The output data were taken at the exit of the straw-furnace.

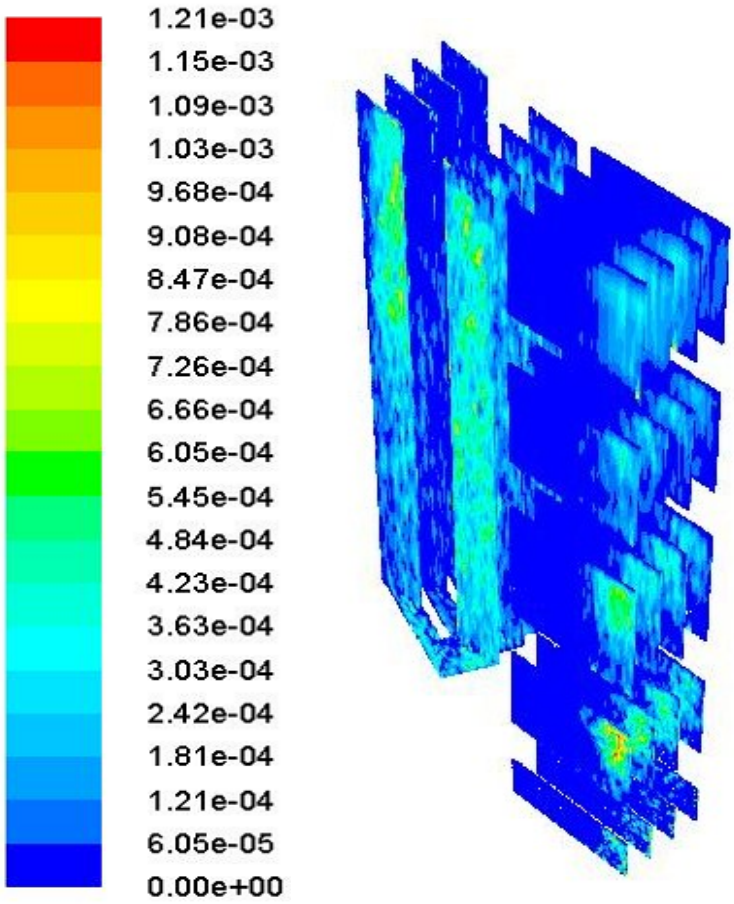

Figure 4.24: Contours of the deposition rates on the vertical surface of the boiler super heaters.

Table 4.7: Table of output data from straw-fired boiler.

Output data from FactSage	See Table 4.3 , page 146
Output data from CFD	
Average gas temperature at the exit of the furnace	673 K
Average velocity at the exit of the furnace	151 m/s
Average deposition rate at the exit of the furnace	716 kg/m^{2}s^1

4.5 Conclusions

The calculations on the section of Shayang boiler considered for the deposit formation have been performed in order to test the ash particle

deposition model. Advance CFD techniques are used in the implementation of the model in the FLUENT 12.1 commercial software. Although solution convergence difficulties have been experienced, the predicted results obtained are reasonable within the available boundary conditions. Therefore, the following conclusions are made:

- A reduced alkali kinetic model for alkali sulphates formation during the biomass combustion has been developed. The reduced kinetic model accurately reproduces the alkali phenomena observed in the experiments at 1173K and 1373K.
- The generated reduced kinetic model was implemented into multi-dimensional and turbulent reactive flow and the temperature profiles computed for cotton straw using CFD code. The qualitative agreement between the experiment data and computational results is good for the temperature profile and velocity distribution.
- A deposition model, based on the size of the particle coated with a sticky layer (potassium salts), vapour pressure and saturation pressure of the potassium salts has been developed. The predicted results of the deposition contour in the Shayang furnace have been compared qualitatively and the predicted location and the shape of the deposits match with the experimental observations.

Chapter 5

Application of the Ash Deposition Model to Co-firing in the EFR: Results and Discussion

The co-firing ash deposition model that has been proposed in Chapter 3 has been implemented according to the procedures explained in Chapter 4. The work draws upon the experimental results from the EFR at Imperial College, London, for the deposition efficiencies of the coal and biomass blends (Wigley et al., 2007). A comparison is made between these results and the computed data and the validity of the deposition model discussed. Also, some conclusions are drawn from the discussions and these are presented at the end of the chapter. Therefore, this chapter is mainly concerned with the discussion of the results obtained for the predictions using the co-firing deposition model which was described in the preceding chapter.

5.1 Introduction

This section discusses deposition issues associated with co-firing biomass and coal in the EFR. The primary motivation for such co-firing is the effective reduction in CO_2 emissions, as biomass feedstock are essentially CO_2 neutral. Carbon neutral means that the CO_2 generated during the combustion of the biomass is utilized for the growth of the biological material.

In addition to organic matter, the inorganic matter in pulverised coal constitutes between 5 and 30 wt.%. During combustion, the volatile matter is first vaporised with the gas phase and this is followed by the burning of char. The inorganic matter in the coal consists of discrete minerals and organically associated inorganic matter that are transformed into ash after combustion. There are no fewer than 100 types of mineral grains in coal and those that are common are quartz, clay minerals such as kaolinite, carbonates such as calcites and sulphides such as pyrites (Gupta et al., 1998). The minerals exist in different forms, such as discrete mineral grains, flakes or a combination of the two shapes (Bryers, 1996). The mineral matter present in coal can be classified as either included mineral matter or excluded mineral matter. Included mineral matter is intimately associated with the combustible material in coal while the excluded mineral matter is that portion of the mineral matter which is separated from the carbonaceous portion of the coal during pulverisation. The main organically bound inorganic matters are alkali and alkaline matter bonded with the oxygen functional groups in coal (Gupta et al., 1998). However, these alkalis constitute a very small fraction in high rank coals and are often ignored in the study of the ash prediction models (Benson et al., 1996; Sarofim et al., 1977).

The ash formation during the combustion of different biomass fuels can be predicted from the composition of the inorganic matter in the fuel. Although the ash content of the biomass is generally lower than that of the coal, the composition of the biomass ash is very different. Coal ash mainly comprises of alumino-silicates with clay and quartz, whilst biomass ash mainly consists of quartz and inorganic salts of chlorides, sulphates and phosphates (Van Loo, 2002). According to Korbee et al. (2003), biomass

ash mainly contains elements from alkali metals (Na and K), and alkaline earth metals (Mg and Ca), in addition to smaller amounts of Si, P, S, Cl, Mn and Fe. The high content of alkali and alkaline earth metals (K, Na, and Ca) in the biomass can lower the ash fusion temperatures and increase the potential for the melting of a large amount of ash particles from the inorganic constituents during combustion (Korbee et al. 2003). In addition to the high content of alkalis, the oxygen and organic volatile matter content which are present largely in the biomass make it more reactive than coal. This is because devolatilisation will occur at lower temperatures, thus increasing the tendency for releasing larger amounts of the vapours from inorganic constituents during combustion.

Ash related issues such as slagging, fouling and corrosion are of significant concerns in the co-firing of coal with biomass. This is mainly because the biomass materials applied in co-firing, such as energy crops and agricultural residues, usually contain large amounts of alkali metals, alkali earth metals, phosphorus, chlorides and sulphates. The interaction of these species with one another and/or with other compounds can lower the melting temperature of the ash particles and lead to partial melting. When such partially molten ash particles become entrained in the flue gas flow and collide with the heat transfer surfaces, they form deposits (Bryers, 1996; Skrifvars et al., 2005; Shao et al., 2010).

Therefore, it is critical to understand and address the ash related problems in the co-firing of coal with biomass. With this objective, the fundamentals on ash formation and deposition in solid fuel combustion have been reviewed in Chapter 2. It should be noted that the present section uses

the Entrained Flow Reactor (EFR) at Imperial College, London as the source of experimental data.

The furnace used for this study was the Imperial College Entrained Flow Reactor (EFR) which is schematically shown in Figure 5.1. The measurement techniques employed and the data obtained were reported in Manton et al. (1997); Wigley et al. (2007) and these are summarized as follows. The reactor consists of an assembly of four electrically heated furnaces, which are approximately 5 m long vertical tube with a diameter 100 mm. These furnaces comprise of three heating elements; molybdenum disilicide ($MoSi_2$), silicon carbide (SiC) and two kanthal AF wire (FeCrAl alloy) that heat the reactor body, providing a temperature gradient from 1650 ^oC at the top to 1200 ^oC at the bottom. A series of joints between each furnace accommodates the probes which allows the ash and char samples to be withdrawn from the combustion atmosphere. The gas temperatures at the ports 1 and 2 are at temperatures of approximately 1400 ^oC and 1250 ^oC, respectively. Uncooled ceramic probes have been used to collect the ash deposits. The burner section consists of the primary inlet through which the primary air and the pulverized coal are fed, and the secondary air inlet, for the hot swirling air. The coal flow rate of 0.014 gs^{-1} was used, the primary air flow rate was 0.067 kgs^{-1} at 70 ^oC, and the secondary air flow was 1.167 kgs^{-1} at 300 ^oC, see Table 5.1.

The effects of the five types of biomass have been studied: miscanthus, short rotation coppice (SRC), olive residue, palm kernel expeller cake and sawmill residue. The two coals used, Russian and South African, are typical bituminous UK power station coals with higher and lower slagging potentials, respectively. The results using Russian coal were chosen for this

investigation because they are slightly more slagging than the other set of data using South African coal (Wigley et al., 2007).

Coal was blended with 0, 20, 40 and 60 wt.% of each of the biomasses. The fuel samples studied were dried, milled and sieved so that their diameters were less than 100 μm. The samples were then blended and dried at 120 °C in nitrogen gas prior to use. 100 g of fuel mixture was run for a duration of 30 min, and the deposit sample was collected on probe 2 which is located in the midsection of the EFR. The probe has thermocouples that register the surface temperature of the deposits.

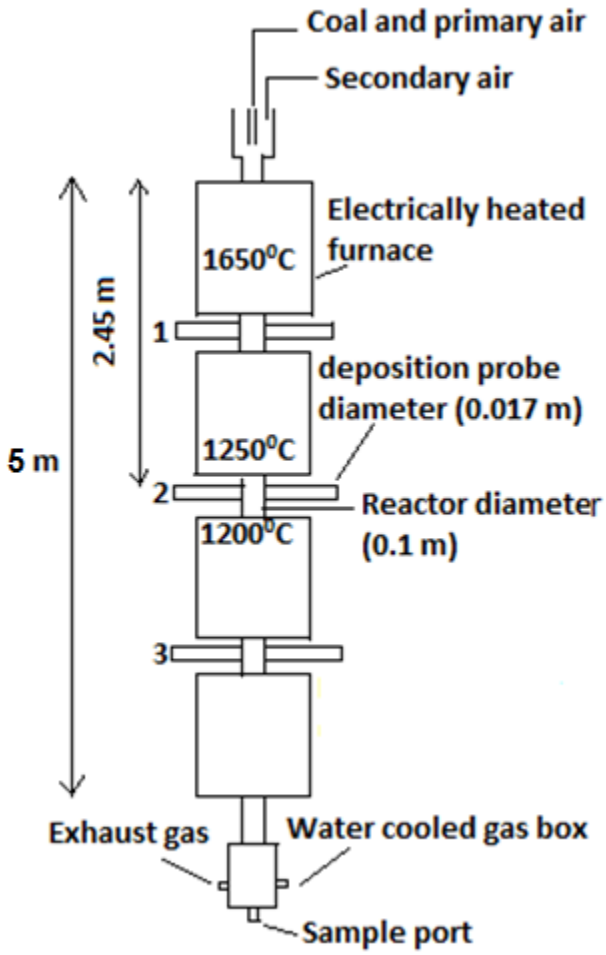

Figure 5.1: Schematic diagram of the Imperial College EFR (Hutchings et al., 1996).

Naturally, fouling is formed on the convective heat surfaces, while the slagging is formed on the furnace wall, or on the partially fouled wall (convective surfaces exposed to radiant heat). In many research papers using an EFR (Hutchings et al., 1995; Manton et al., 1997; Barroso et al., 2006; Wigley et al., 2007), a mullite probe is used for the deposit collection rather than a metallic probe since it (i) provides a porous ceramic surface, which is very similar to a partially fouled wall in comparison to the polished surface of the metallic probe, and (ii) the long exposure time that occurs during the formation of the initial deposit layer on the metallic surfaces is avoided. The deposits collected from Russian coal with palm kernel at different levels of addition (top — 0 wt.%, 10 wt.%, 20 wt.%, 40 wt.% — bottom) on mullite tubes is shown in Figure 5.2.

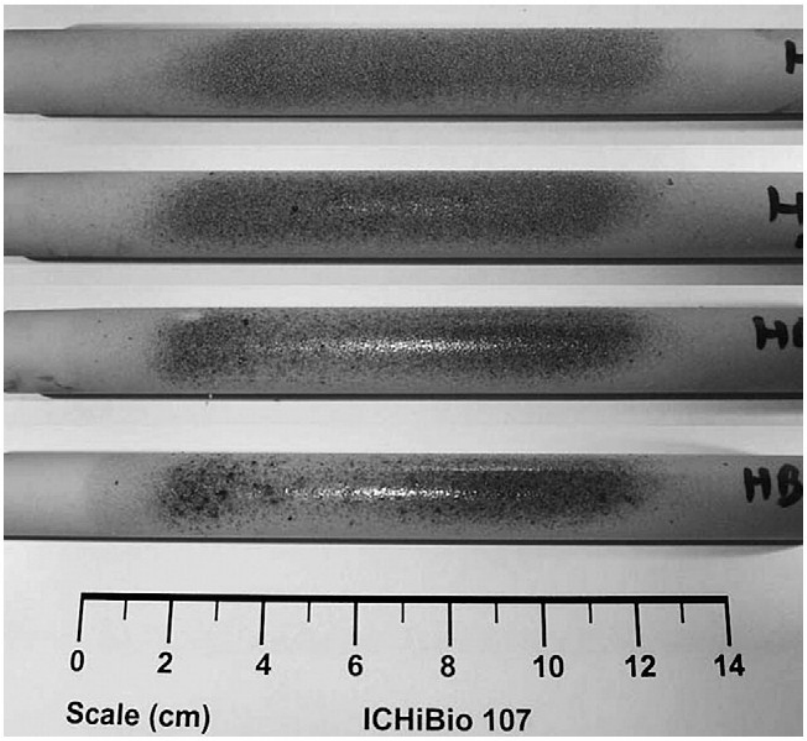

Figure 5.2: EFR deposits from Russian coal with palm kernel at different levels of addition (top — 0 wt.%, 10 wt.%, 20 wt.%, 40 wt.% — bottom) on mullite tubes (Wigley et al., 2007).

The ash deposits collected on the probe 2 were then coated in a low viscosity epoxy resin, which penetrates the open porosity of the sample, and this gives stability to the deposits. Sections through the deposits were then cut to reveal a cross section. Two cross-sections were mounted in resin blocks and the samples were ground and polished for sintering analysis in a Scanning Electron Microscope (SEM). The comparison of the microstructures of the deposit from Russian coal – biomass mixture is shown in Figure 5.3.

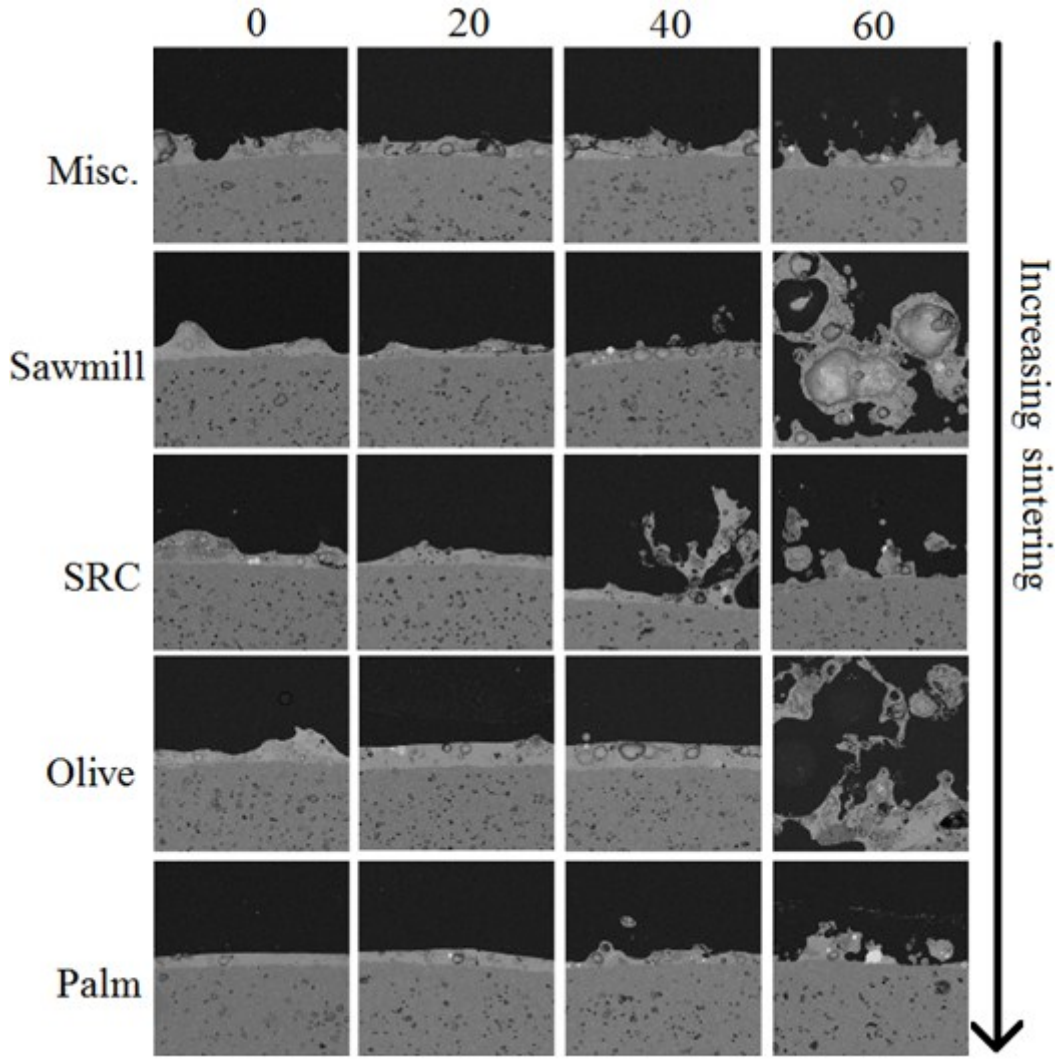

Figure 5.3: Cross-sections through the EFR deposits from Russian coal with biomass fuels at different levels of addition (wt.%) (Wigley et al., 2007).

CFD Model: In the present study, the computational simulations of the EFR has been performed using the commercial CFD code FLUENT, version 13.0.0 (Fluent, 2009). To reduce the computational complexity, symmetrical conditions were assumed. This resulted in a model of one half of the EFR and then the use of the symmetry to predict the full domain. In the experimental work in Hutchings et al. (1995), the deposits were collected at the probe position, where the gas temperature is about 1400 ^{o}C on an uncooled ceramic probe of the EFR are generally of highly fused nature. This deposits give little indication of the likely slagging propensity of the coal. However, when deposits are collected at the probe position, where the gas temperature is about 1250 ^{o}C on an uncooled ceramic probe, the deposits range from a thin dusty covering of lightly sintered ash particles to well-bonded and coherent deposits, the type of the deposit, depending on the nature and proportions of the mineral matter present in the coal. The deposits collected under these conditions closely resemble those sintered deposits that are formed from the bulk ash on the furnace walls and the superheaters of large furnaces and therefore are suitable for characterization. For this reason, the samples of the fly ash particles inside the EFR considered in the experimental work of Wigley et al. (2007) were collected on a mullite tube 2 set at a temperature 1250 ^{o}C. As a consequence, mullite probe 1 (port 1) was not considered in the CFD build-up of the present calculations.

Prior to their testing in the EFR, coal and biomass fuels were dried, milled and sieved under 100 μm. Larger particles were excluded in order to achieve a high degree of burnout at the outlet of the EFR for all the fuels in order to obtain a stream of particles with a low carbon content,

representative of fly ashes at the furnace exit of real boilers. (Barroso et al., 2006). Based on this information, both coal and biomass particles were assumed to be spherical and equal sizes. The particle sizes were distributed between 1 and 95 μm in 10 injection groups, with a mean particle size of 85 μm and a spread parameter 1.3 has been used. The burner region is shown in Figure 5.4. The mesh was refined to yield about 1.2 million cells, and it was found that the gas temperature and the velocity profiles show no significant difference between using 1.0 and 1.2 million cells. Therefore, the predicted results have been obtained using 1.2 million computational cells. The deposition code, equations (3.56)-(3.62) in Chapter 3, has been developed and was compiled and linked to the main code in FLUENT via DEFINE_DPM_EROSION. The main code in FLUENT calculates the particle trajectories while the role of the deposition code is to add stickiness to the particle as it is being transported from the combustion zone to the furnace wall or the heat transfer surface.

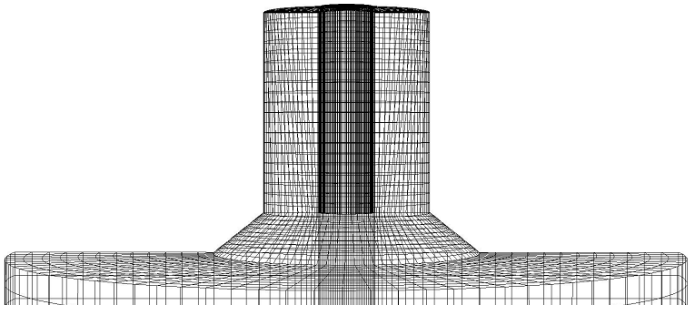

Figure 5.4: Close-up view of the grid in the near burner region.

Since the particle trajectory of the DPM (Discrete Phase Model) is sensitive to the flow field, such as the fluid velocity and turbulence fields, the cold flow solution (non-reacting solution) was first started as a necessary

step in order to guarantee a convergence of the solution. The non-reacting solution was set-up by disabling the energy, radiation, and DPM from the governing equations. Once the flow field of the cold flow solution is established, the coal particles are released by enabling the energy, DO and DPM model equations. When heat is release suddenly, the flow fields may change very quickly and this causes divergence in the iterative procedure. To control this, under-relaxation factors have been introduced into for the second-order solution procedure. The Discrete Phase Sources under-relaxation factor is set to 0.1, which is more stable than the default value of 0.5 (Degereji et al., 2010).

Fuel properties and operating conditions: The properties of the coal and biomass are given in Table 5.2. With differing chemical properties in the ash content between the five biomass investigated, their slagging tendencies vary with the level of the biomass addition (Wigley et al., 2007). The deposition model is limited to only SRC, Olive and Miscanthus that are fairly rich in alkali contents. Palm was not modelled because of the complexity of the ash content. However, all the five biomass materials were employed in the numerical slagging index (NSI) calculations. Data for Miscanthus, Olive, Palm, SRC and Sawmill were taken from the 'Phyllis' biomass database (Phyllis, 2004) while the ash content and its composition was taken from Wigley et al., (2007). Because of the relatively narrow range of coals used here, single values were used for the coal properties, including the coal density of 1400 kg m^{-3} and specific heat of 1.68 J kg^{-1} K^{-1}.

Table 5.1: Coal and biomass ash content (wt %) and chemical composition (wt %) (Wigley et al., 2007; Phyllis, 2004).

Component	R. coal	S. coal	Misc.	Olive	Palm	SRC	Sawmill
Proximate analysis	Wt % on dry basis						
Volatiles	30	36	83.5	79.0	77.1	80.5	81.2
Fixed carbon	76	73	29.3	33.1	34.0	32.1	31.6
Moisture	5.56	5.47	30.7	24.0	23.0	18.5	19.0
Ash	12.6	12.1	2.3	5.7	4.2	2.4	2.5
CV(MJ/kg)	27	26.7	18.5	22.0	22.2	17.5	19.1
Ultimate analysis	Wt % on dry basis						
C	76.5	68.67	48.1	42.2	4.31	50.2	50.1
H	4.5	4.66	5.8	5.1	5.1	5.9	6.2
O	4.9	26.54	41.9	45.6	45.2	42.2	42.4
N	1.9	1.78	0.3	1.62	1.51	0.1	0.5
S	0.4	0.83	0.1	N/A	N/A	N/A	0.05
Cl	0.25	0.00	0.16	N/A	N/A	N/A	0.013
Ash composition	Wt % on dry basis						
SiO_2	60.1	54.1	57.0	32.1	15.1	17.3	40.7
Al_2O_3	24.0	33.5	2.4	6.6	3.2	4.4	8.1
Fe_2O_3	6.0	3.1	3.4	4.9	5.3	3.8	3.8
CaO	4.1	4.1	10.0	12.4	10.7	33.3	28.6
MgO	1.1	1.3	3.1	12.2	12.0	8.6	4.1
K_2O	3.0	0.7	18.2	18.9	9.7	13.8	6.8
Na_2O	0.4	0.1	1.1	0.4	0.3	1.0	1.1
TiO_2	1.2	1.7	0.2	0.2	0.1	0.3	1.1
MnO	0.1	0.0	0.4	0.0	1.0	0.4	3.6
P_2O_5	0.0	1.4	4.2	12.2	42.7	17.0	2.1

N/A = not available.

Ash Deposition: The second part of the calculations, which is part of the original work in this investigation, is mainly to predict the behaviour of the ash particles in the furnace using the established gas phase temperature and velocity fields. The ash particles deposition process includes the following: the transportation of the particles to the heat exchange surface; the tendency of each particle to stick to the surface upon impaction.

The propensity of the particle to stay on the surface once they impact. Condensation, viscosity and melting fraction have been employed to determine the stickiness of the particles. For the coal ash, the viscosity stickiness is determined by comparing the particle's viscosity to a reference viscosity. The sticking probability of particles having a viscosity less than or equal to the reference viscosity has been assigned the value of unity. While for the particles with a viscosity greater than the reference viscosity, the sticking probabilities are determined between the reference viscosity and their actual viscosity, and such particles are assumed to be non-sticky.

For biomass, the sticky propensities of the surface are function of melt fraction. Below a melt fraction of 0.15, the sticking probability is set to zero. Between the melt fractions of 0.15-0.7, the sticking probability is assumed to be sticky and above 0.7, the sticking probability is assumed to be flowing.

Complete steady-state calculations are performed and the results of predictions obtained, using the proposed deposition model, have been compared with the available experimental data (Wigley et al., 2007).

5.2 Results and Discussion

5.2.1 Gas Phase and Particles Temperatures

The furnace temperature is of importance since it is closely related to the deposition potential on the heat transfer surface. Figures 5.5 and 5.6 show the predicted gas and particle temperature for pure coal. The combustion of the injected particles starts immediately after the particles have mixed with the oxidizing air at the exit of the burner. This is promoted by the recirculation zone observed in the vicinity of the burner. Further, the particles are rapidly heated by radiation from the hot reactor walls.

It can be observed that the majority of the particles within the vicinity of the burner reach a temperature of about 1500-1600 ^{o}C, where large numbers of the particles melt (Hutchings et al., 1996). According to Hutchings et al. (1996), these particles are completely fused and potentially flow around the mullite probe or the furnace wall when they impact on a surface or wall. For this reason, as previously explained in Chapter 4, the deposition probe 1 was not considered in this calculation. In a particle temperature range of about 1250-1400 ^{o}C, which corresponds to the position where probe 2 is located, the particles have been reported to display a semi-molten, more compact aspect and potentially remain sticky on the mullites upon impaction (Hutchings et al., 1995; Manton et al., 1997). However, particles that emerge from the burner, and those in the lower section of the EFR, experience lower particle temperatures. A temperature range of about 1250-1800 ^{o}C has been obtained in the vertical plane of the furnace and this is in good agreement with the measurement data which is in the region 1200-1700 ^{o}C, although slightly over predicted by about 6%.

Figure 5.7 shows the predicted gas temperatures (^{o}C) as a function of the distance from the burner for coal combustion. The predicted peak temperature is located about 0.25 m from the burner. The predicted gas temperatures for co-firing coal with SRC for up to 60% co-firing ratio are presented in Figure 5.8. For the co-firing ratio of 20 wt.%, the temperature profile does not differ significantly from that of pure coal. However, for a co-firing ratio greater than 20 wt.%, a significant difference is observed. The results show that the temperature of the gas at the exit of the furnace decreases when the proportion of the SRC blended with coal increases.

The peak gas temperature achieved during the coal devolatilization illustrated in Figure 5.9 and it is observed that it decreases with a commensurate increase in the thermal ratio of miscanthus. The prediction of co-firing with 20 wt.% Miscanthus shows about 5 ^{o}C reduction in the peak temperature, while co-firing with 40 wt.% and 60 wt.% shows about 40-70 ^{o}C reduction. Therefore this means that by replacing coal with biomass, the heat transfer from coal devolitilization to the surrounding region reduces, and thereby the combustion of the biomass particles in the vicinity of the burner region is not favoured. Research has shown that at relatively low levels of biomass replacement with coal, say less than 10-20 wt.% (Pronobis et al., 2006; Plaza et al., 2009), the temperature profile has been found to be little affected (virtually no affected) as highlighted in Figure 5.9.

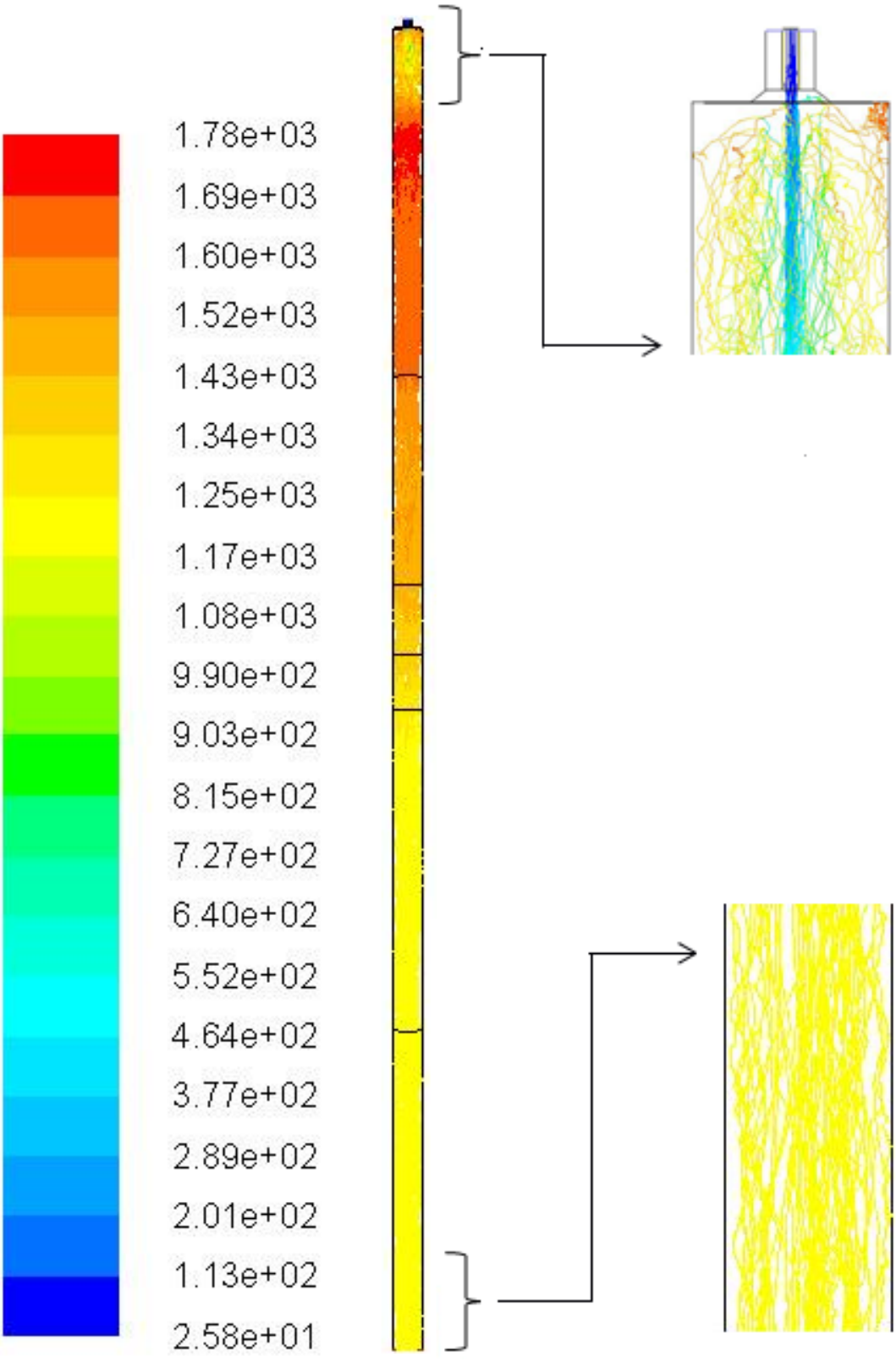

Figure 5.5: Contours of the particle temperature (^{o}C) in the vertical plane of the furnace.

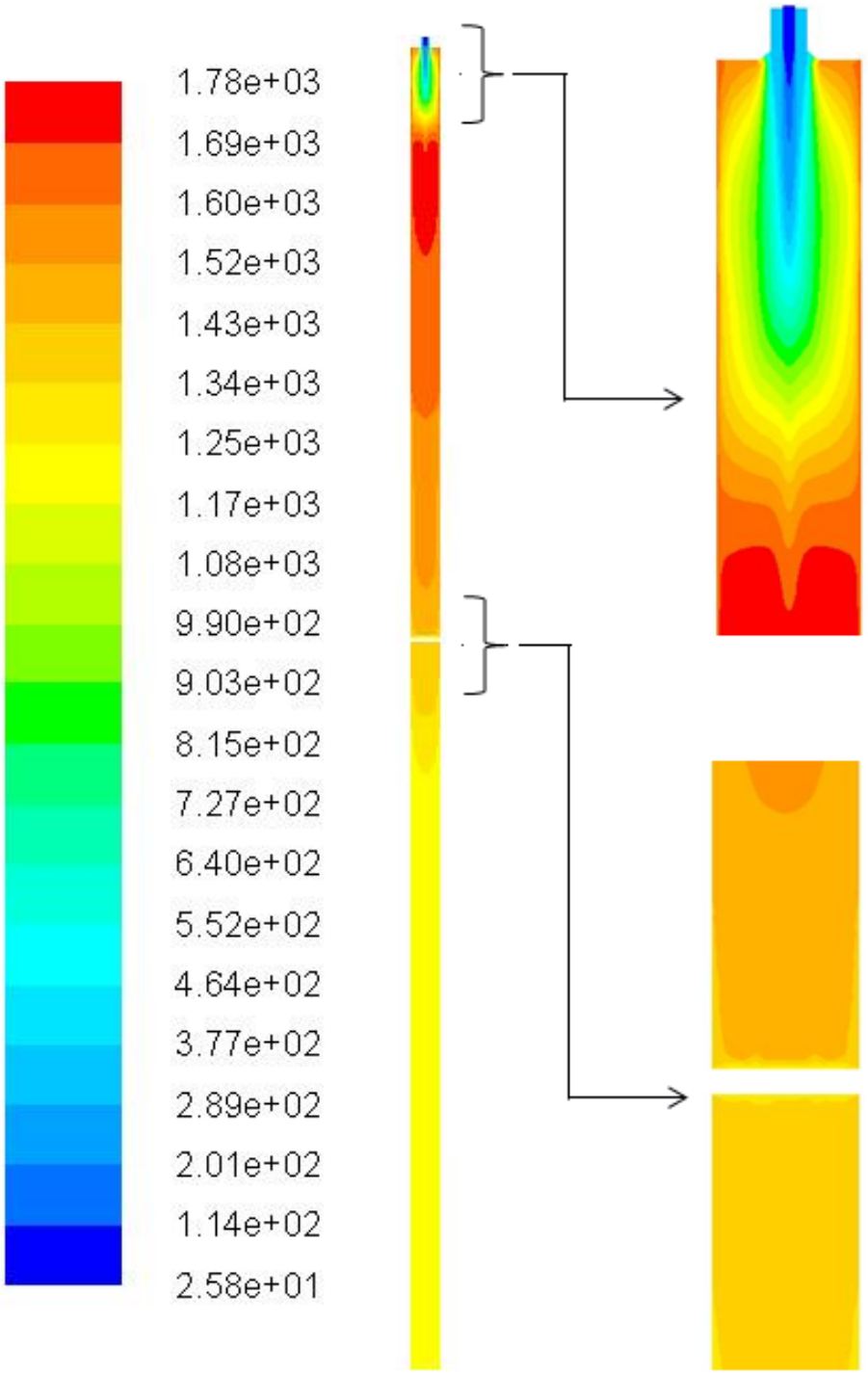

Figure 5.6: Contours of the gas temperature (^{o}C) in the vertical plane of the furnace.

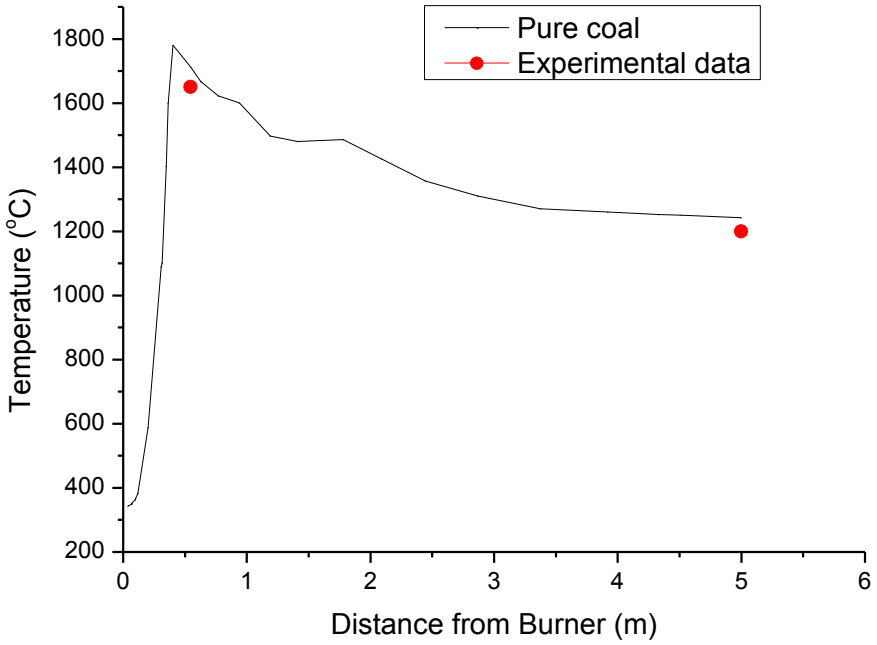

Figure 5.7: Gas temperatures (°C) as a function of the distance from the burner for co-firing of Russian coal with different ratios of SRC.

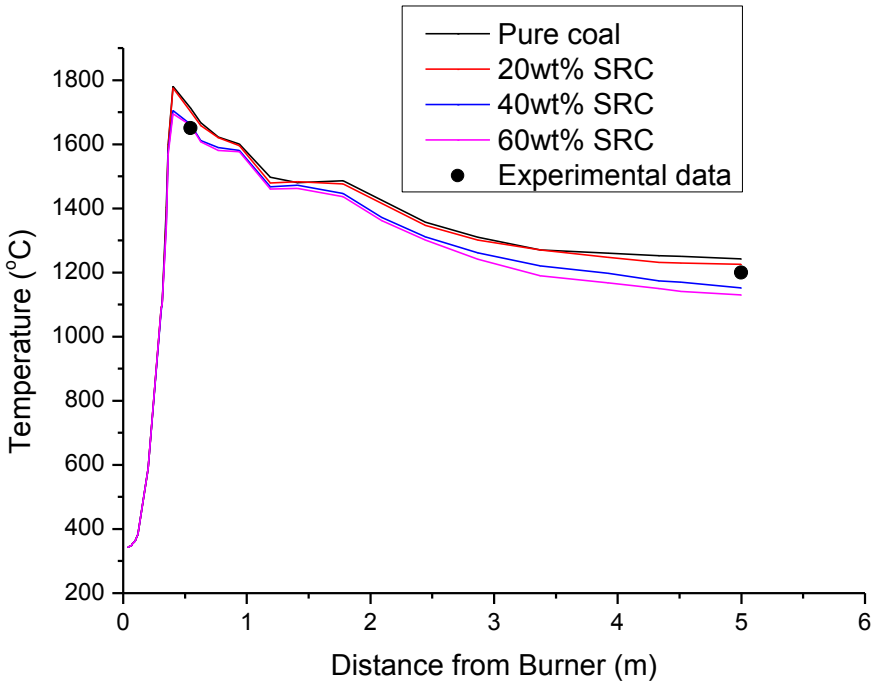

Figure 5.8: Gas temperatures (°C) as a function of the distance from the burner for co-firing of Russian coal with different ratios of SRC.

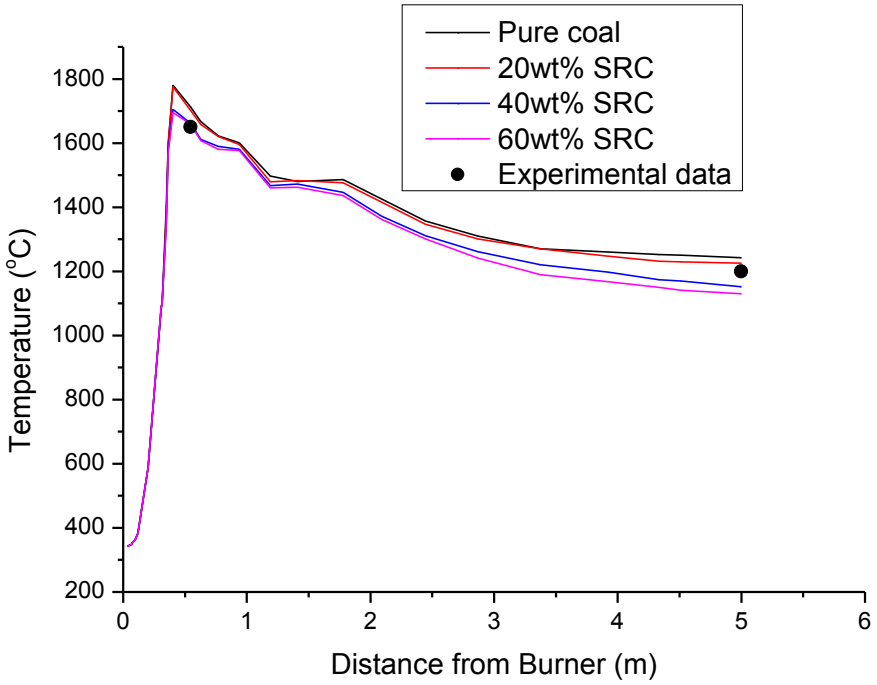

Figure 5.9: Gas temperatures (°C) as a function of the distance from the burner for co-firing of Russian coal with different ratios of SRC.

5.2.2 Gas and Particles Velocities

Figure 5.10 illustrates the stream-wise gas flow velocity on the symmetry plane of the EFR. It can be seen from the figure that the mixing of the air and the fuel near the burner exit is promoted by means of the recirculating flow produced by the motion of the primary air and the strong swirling motion of the secondary air. Since, in the EFR, the particles are entrained into the gas flow, the flow of the gas down the centre of a 0.1 m diameter tube (see Figure 5.10) indicates the absence of any dispersion which causes the particles to experience differing flow velocities and residence times.

Many publications (for example (Hutchings et al., 1995; Manton et al., 1997; Wua et al., 2011) have confirmed that the combusting gas flow produced by the EFR under well-controlled conditions is necessary for the precise determination of the particle heating rates and this is considered as an advantage over large rigs. The velocities introduced at the two secondary air inlets (see Figure 5.10), which evolves into a single peak velocity, has adequately captured this advantage. A peak velocity of about 4.2 ms^{-1} near to the fuel injection is obtained for the hot travelling gas at corresponding temperatures of about 1600 ^{o}C. The gas velocities in the central region of the EFR have been found to be approximately twice the average velocity and this is in good agreement with what has been reported by Hutchings et al. (1995), as shown in Figure 5.11. Further, we have found that the radial velocity profile decreases from the peak values on the centreline, to almost zero on either side of the reactor wall.

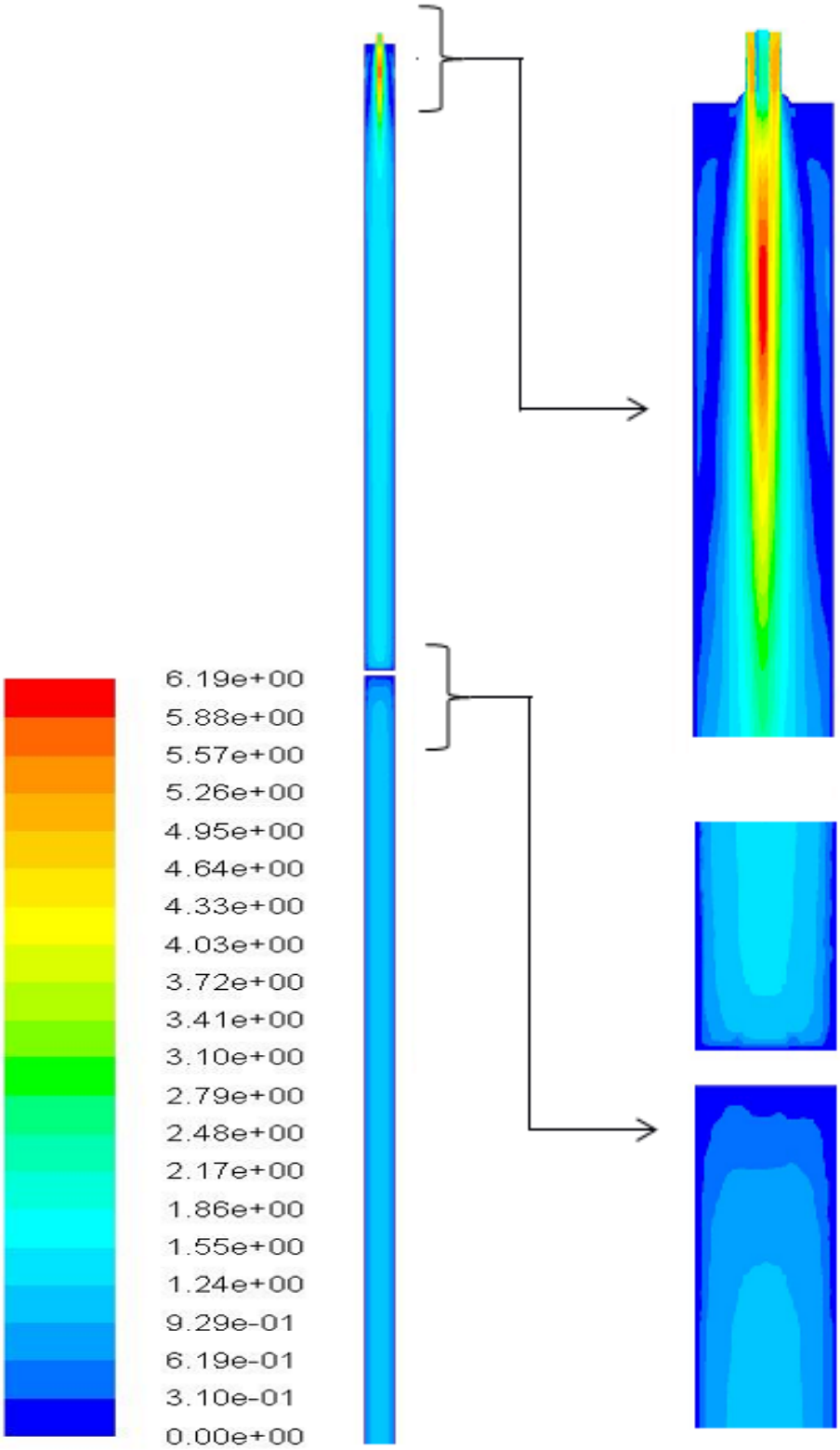

Figure 5.10: Contours of the gas velocity (ms^{-1}) on the symmetry plane of the EFR.

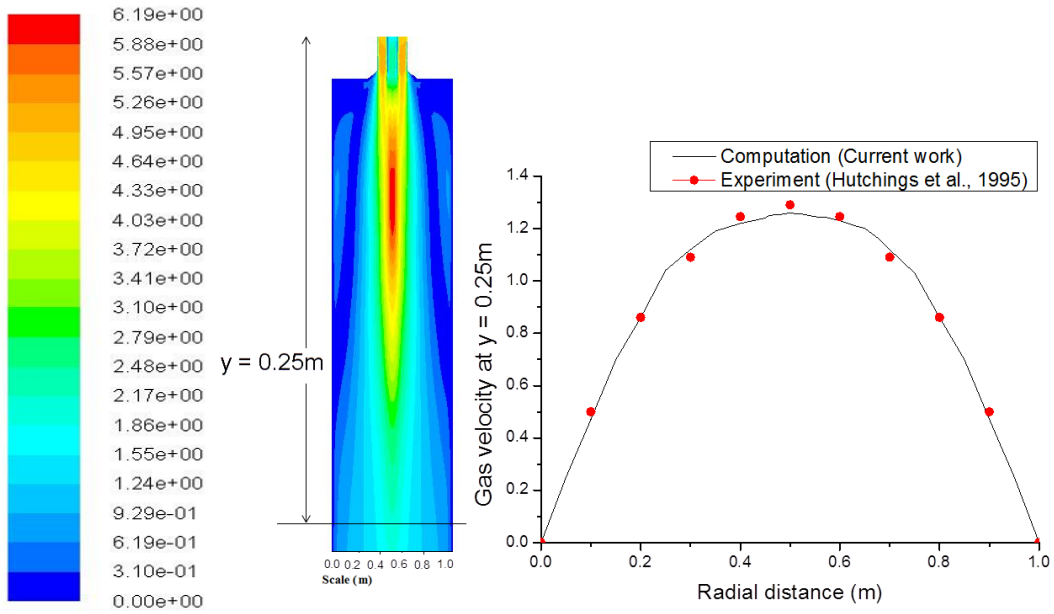

Figure 5.11: Radial gas velocity (ms^{-1}) at y=0.25m from the burner in the EFR.

5.2.3 Particles Residence Time

The results presented in Figure 5.12 show that the residence time of the pulverized coal particles in high temperature fields near the burner is lengthened by the recirculating flow. Also, the result shows that the thermal decomposition of the coal particles is accelerated. Because of the streamline flow, and the same size of the particles used, they have the same residence time.

Generally, particles with smaller diameters instantly vanish due to devolatilisation, and those with larger diameters are not caught by the recirculation flow because of their large inertias. The maximum residence time of about 3.65s predicted agreed with the experimental data of about 3 seconds(Wigley et al., 2007), although slightly overpredicted.

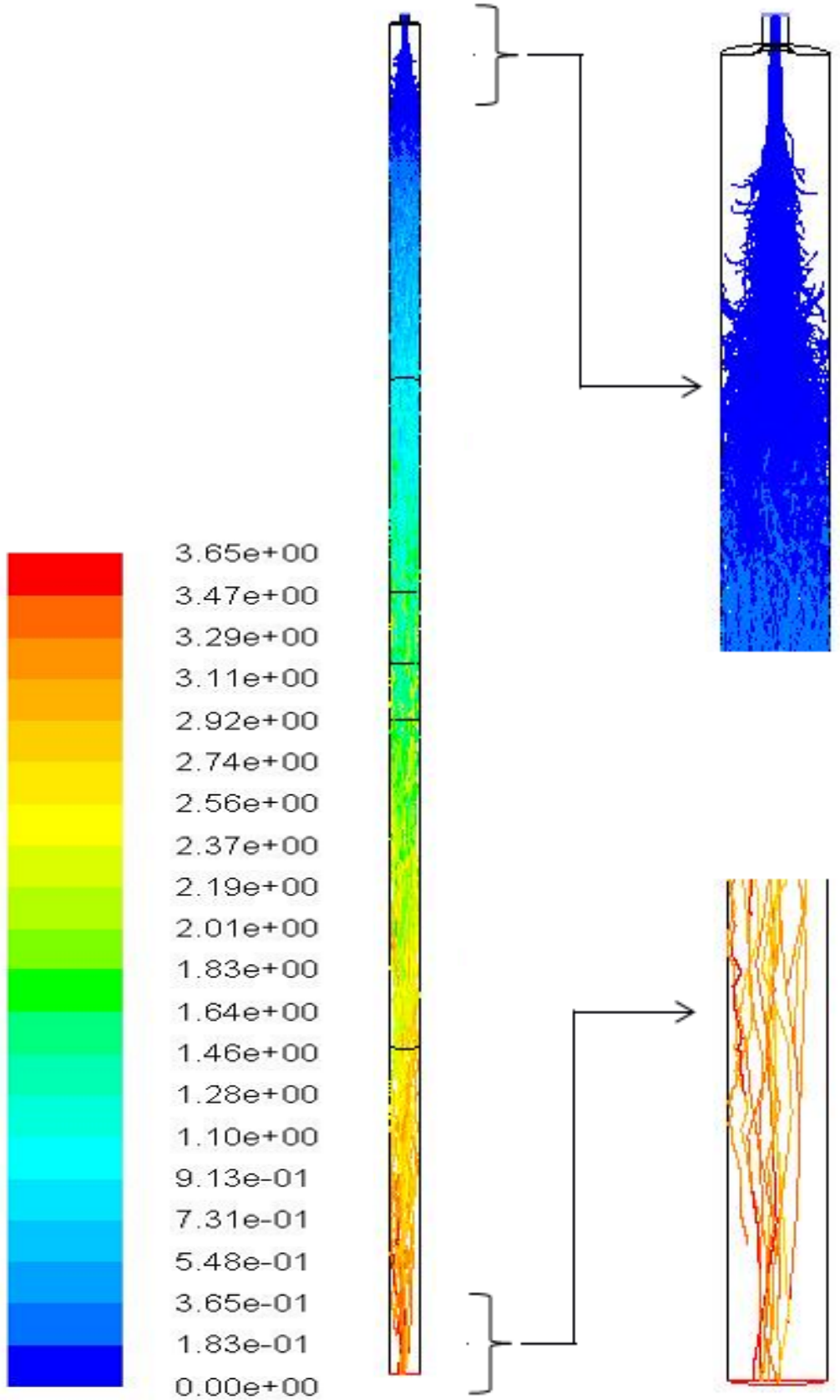

Figure 5.12: Particle traces coloured by residence time (s) on the symmetry plane of the EFR.

The influence of the swirling motion on the overall velocity magnitude is an indication that the strength of the swirling air has on the particle residence time. A strong swirl may lead to a strong recirculation zone in the furnace, and this may increase the particle residence time thereby enhancing the complete burning of the particle. In the other words, particles have relatively longer residence time if they are in higher recirculations flows (Vuthaluru et al., 2006).

5.2.4 Deposition Rate

The use of solid biomass for the production of heat and electricity is at present the most important utilization of this renewable energy resource. However, a technical problem that limits its application is the formation of depositions in the combustion processes which employs the biomass either as a single fuel or in combination with coal.

The deposition formation processes are principally associated with the slagging, sintering and fouling of ash particles on surfaces within the furnace. The mechanisms of ash deposition on the coal ash have been studied extensively (Rushdi et al., 2004; Huang et al., 1996), and much of which is applicable to biomass firing and co-firing.

The main cause for the ash deposition includes the quality of the fuel, boiler designs, and operational conditions, among others (Ma et al., 2006; Degereji et al., 2011). Whatever the system and conditions of the biomass combustion, there will always be problems with the ash. This is because of

the fate of the inorganic materials associated with biomass is not fully understood.

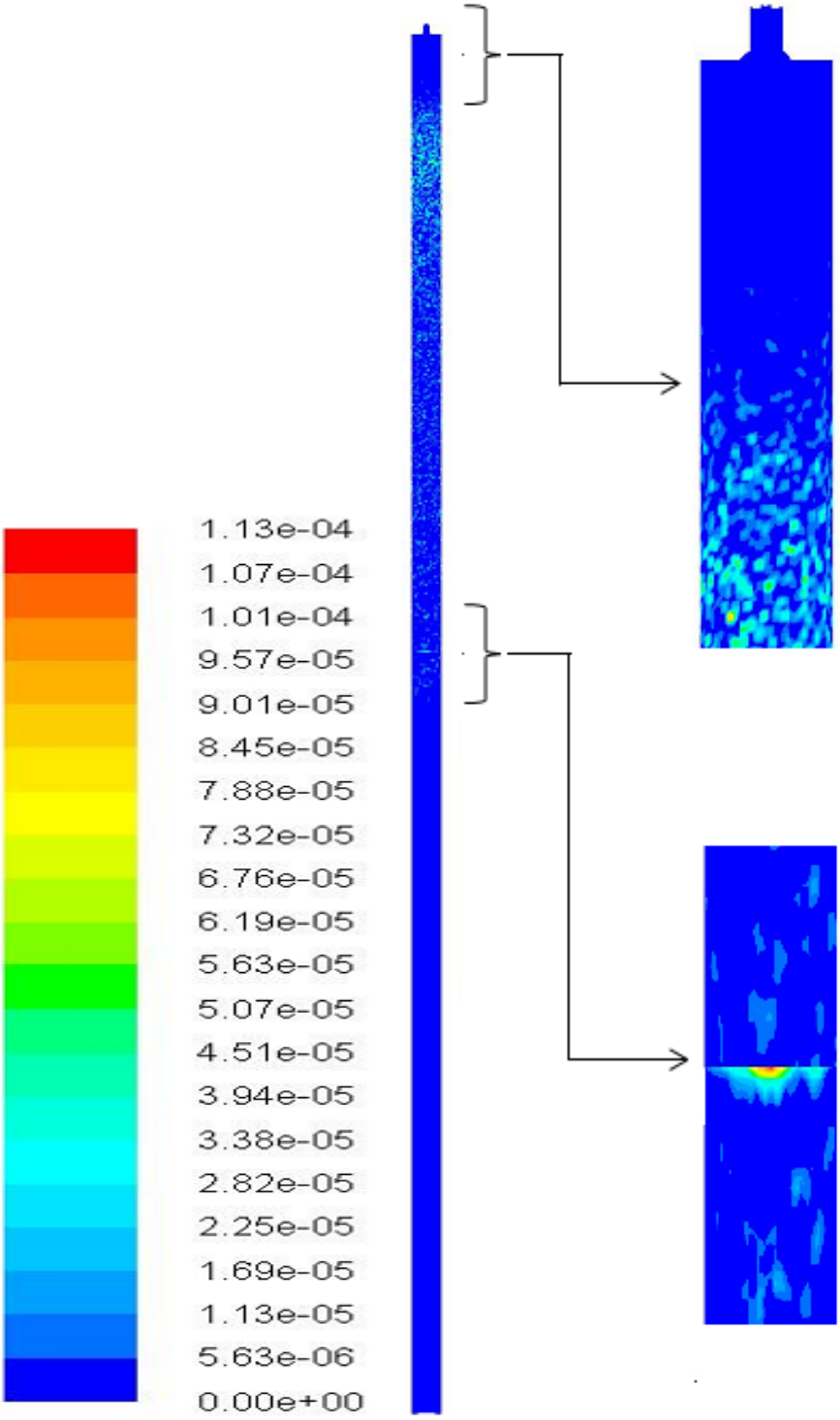

Figure 5.13: Contours of the particle deposition rates ($kgm^{-2}s^{-1}$) on the furnace wall and probe 2 for Russian coal.

Slag, sinter and foul are mainly related to biomass with a high relative content of alkaline compounds in their ashes, such as cereal straws and herbaceous biomasses in general. Some agricultural residues, such as palm kernel cake, have high content of phosphorus oxide, which can lead to various problems during the combustion process.

The specific composition of biomass deposits gives different characteristics if compared to coal ash deposits, i.e. different physical significance of the deposition mechanisms, lower melting temperatures, etc. Low melting temperatures make biomass ash especially troublesome, since their stickiness is higher at lower temperatures, if compared to coal ashes. Increased stickiness will eventually lead to a higher capture efficiency of the large ash particles, meaning that the deposit may grow faster and become thicker (Zbogar et al., 2008).

The ash formation depends on the state of the particle and the surface. For ash deposition to occur, the particle must be molten or partially molten or the surface must be sticky. During the first stage of the deposit formation, sticky condensate appears at low temperatures (below the saturation temperature of the vapour) follow the melting fraction of the biomass particle at low fusion temperatures (Ma et al., 2006, Garba et al., 2012). The composition of the initial deposit consists of loosely sintered fly ash particles bonded together by a small amount of melting phase. As the deposition proceeds, the flow properties increase (become more liquid) with increasing temperature. The deposit surface can now accommodate the incoming particles, and thus the deposition rate increases. In this case, the

chemical composition of the deposits can be approximated from the bulk ash property. In the EFR that was employed as a source of the experimental data, the temperature was set at a higher value (≥1250 ^{o}C) so that the deposition rate does not depend on the metal surface. As pointed out in Chapter 4, the use of mullite instead of metallic probe provides a porous ceramic surface, which is much more similar to a partially fouled wall than a polished metal, and this avoids the long exposure times that might be required for the initial deposit layer to be formed on the steel surfaces.

The ash deposition rate is then a function of (i) the ash flux which is dependent on the ash content of the coal and flow patterns through the furnace, and (ii) the collection efficiency which depends on the stickiness of the substrate (Gibb, 1993). This explains the fact that most bulk deposit composition is invariably very similar to the composition of the coal ash from which it is derived. Therefore the key to furnace slagging is the rate of ash deposition and, most importantly, the longer term behaviour of the deposits, i.e. the consolidation process. It is well know that deposit consolidation occur by a viscous flow sintering mechanism and is dependent on both the temperature and the composition of the individual ash particles that make up the deposits (Gibb, 1996).

The major component present in the two bituminous coals used during EFR trials by Wigley et al. (2007) is aluminosilicate, which behaves like a liquid with an extremely high viscosity. While ash from Russian coal displays a high content of iron, whilst the ash from South Africa coal shows a low content of iron, see Table 5.1. This phenomenon has been reported before by Cunningham et al. (1991) and this is primarily due to the

preferential deposition of low melting, dense iron-rich particles derived from pyrite. The reaction between silica and iron in coal ash is also significant because it influences the way in which deposit is accumulated. Numerous investigators, such as Barroso et al. (2006b), have reported that the reaction between iron and silica have been reported to show evidence of a high slagging potential.

Computational fluid dynamic (CFD) models have been widely used (Ma et al., 2006; Vuthaluru et al., 2006; Garba et al., 2011) but at the present they suffer from a lack in accuracy since the numerical methods rely on the modelling assumptions that have not been validated to a satisfactory level. For the case of coal-biomass co-combustion, additional complexities are introduced such as non-sphericity of the particles(Smith, 1982; Forstner et al., 2006).

Most of the papers that model ash deposition consider the ash particle viscosity under high temperature regions to determine the particle collection efficiency for coal and biomass combustion (Degereji et al., 2011; Forstner et al., 2006). The melting fraction and particle melting temperature in the high temperature region are also essential in determining the sticking probability (Ma et al., 2006). The effects of these criteria have been tested in biomass combustion but for the co-combustion of coal and biomass little has been reported on this effect. Most of the experimental studies on biomass co-firing have suggested that the viscosity and melting fraction are the key components required in the high temperature environment for determining the ash stickiness (Heinzel et al., 1998; Wigley et al., 2007; Watt et al., 1969). However, there have been no modelling investigations that have

taken advantage of combining the effects of these components in determining the particle collection efficiency.

Table 5.2: Input data to the EFR (wt %) (Wigley et al., 2007).

Tube wall	Heating element	Temperature (^{o}C)	Emissivity
Furnace 1	$MoSi_2$	1650	0.82
Furnace 2 Zone 1 Zone 2 Zone 3	SiC SiC SiC	1500 1400 1300	0.83 0.83 0.83
Furnace 3	Kanthal AF wire	1200	0.7
Furnace 4	Kanthal AF wire	1200	0.7
Deposition probe	Mullite	1250	0.5
Primary air flow (kg/s)		0.067	
Secondary gas flow (kg/s)		1.167	
Coal mass flow rate (gs^{-1})		0.014	
Particle size distribution		1 and 95 μm, with a mean particle size of 85 μm and a spread parameter 1.3	

A view of the EFR deposits on a deposition probe for Russian coal can be seen in Figure 5.13 and Figure 5.14 shows the deposition probe for South African coal. The deposition occurs on the furnace walls and on the mullite probe in Figures 5.13 and 5.14. Close to the burner, it can be seen that the reactor walls initially contains no deposits, and then the deposits are formed rapidly at about 0.2 m away from the burner exit by the impacting ash particles. The impacting ash particles that remain on the heat transfer surface have been reported to constitute most of the deposits formed on the pulverized furnace walls (Hutchings et al., 1995). These ash particles may possess sufficient inertia to transverse the boundary layer and impact on the furnace walls. In addition, the intensity of the volatile combustion results in a zone of sharp temperature rise and a significant number of the particles soften, thereby increasing the tendency to stick to the walls. Due to the streamline flow of the combustion particles under the influence of gravity, a high concentration of deposits (slagging intensity) has been found on the centre of the mullite probe.

Another factor that contributes to the high concentration of the deposits on the central region of the mullite probe is due to the high degree of carbon burn out that occurs further downstream where the probe 2 was located. However, at a lower section of the EFR, the ash particles are less sticky, due to the lower temperatures in this region. Among the mechanisms of ash deposition (inertial impaction, including impaction and sticking, thermophoresis, condensation and chemical reaction) inertial impaction is prevailing in reactors such as the EFR, depending on the variations in the physical gas properties, e.g. in the stream wise gas flow.

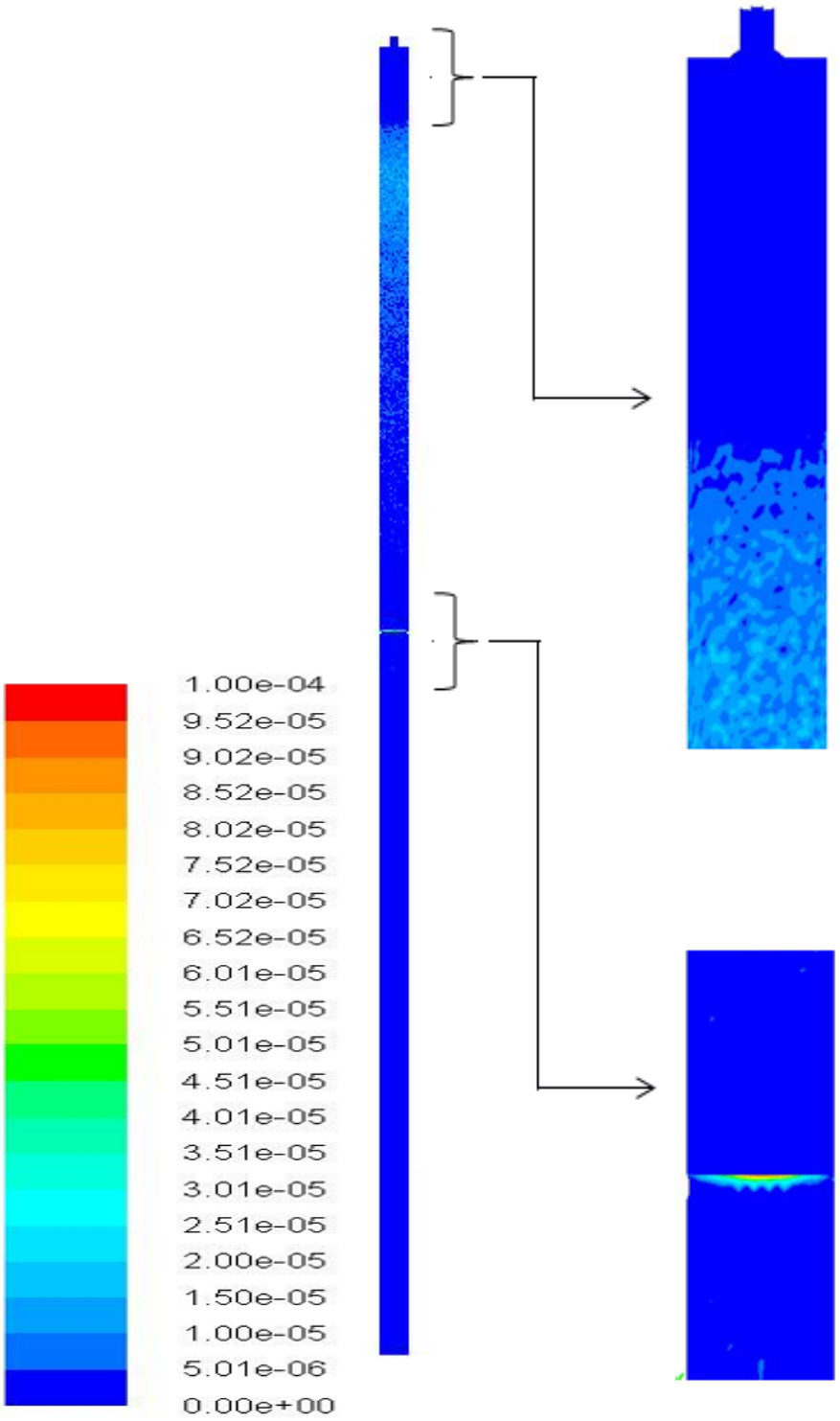

Figure 5.14: Contours of the particle deposition rates ($kgm^{-2}s^{-1}$) on the furnace wall and probe 2 for South African coal.

Another remark concerning the inertial impaction in the EFR is that the deposits were found to be predominantly on the front side of the tube, as

the deposition probe is placed in the cross flow, thus promoting the collision of the particles in the front area of the probe. In addition, there is no deposition built up on the sides of the probe or even less on the downstream side of the probe, except for a thin layer of fine ash on the side of the probe. This justifies the use of a ceramic probe and the presence of other mechanisms in a less dominant form than inertial impaction, e.g. thermophoresis.

A photograph of the ash deposition on the probe after 30 minutes of deposition time for pure coal in (Wigley et al., 2007) is shown in Figure 5.15(a). Although it is difficult to recognize the full details of the ash deposits from this photograph, due to the quality of the image, the dark part in the photograph shows that the deposits are scattered over the probe with most of them concentrated on the central region of the probe. The predicted deposition pattern, see Figure 5.15(b), is reasonably consistent with that observed experimentally, particularly in the central region of the probe. Also, Figure 5.16 shows the top view of the deposit collected from South Africa coal in an EFR reactor. As expected, the deposition pattern for the South Africa coal and Russian coal shows a good resemblance to the photograph illustrated in Figure 5.15(a). This indicates that the model is appropriate and has provided the right qualitative predictions which serves as a basis for quantitative validation. The deposition rates has been calculated using FLUENT 12.1 with a user defined function incorporating the deposition modes developed in this thesis.

This work looked at a steady-state deposition rate. Therefore, the CFD post-processing packages provide imagery of deposition rates after

convergence of the solution has been achieved. As a consequence it is not possible to show deposit development with time. Therefore, the images in Figures 5.15 and 5.16 represent the initial deposition rate (where probe temperature is equal to input probe temperature).

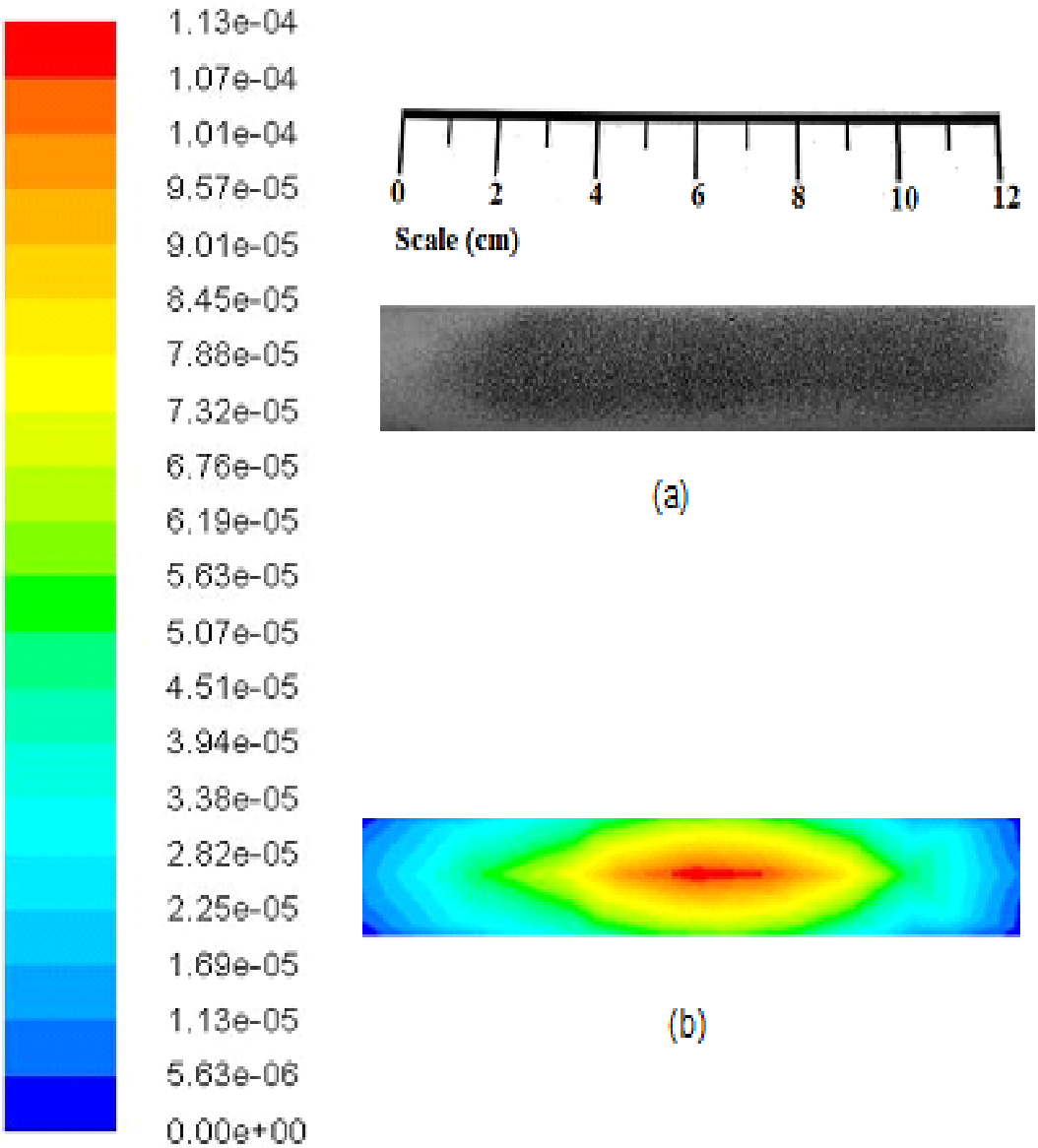

Figure 5.15: (a) Photograph of the deposits from Russian coal on the mullite probe 2 (Wigley et al., 2007), and (b) the corresponding CFD prediction ($kgm^{-2}s^{-1}$).

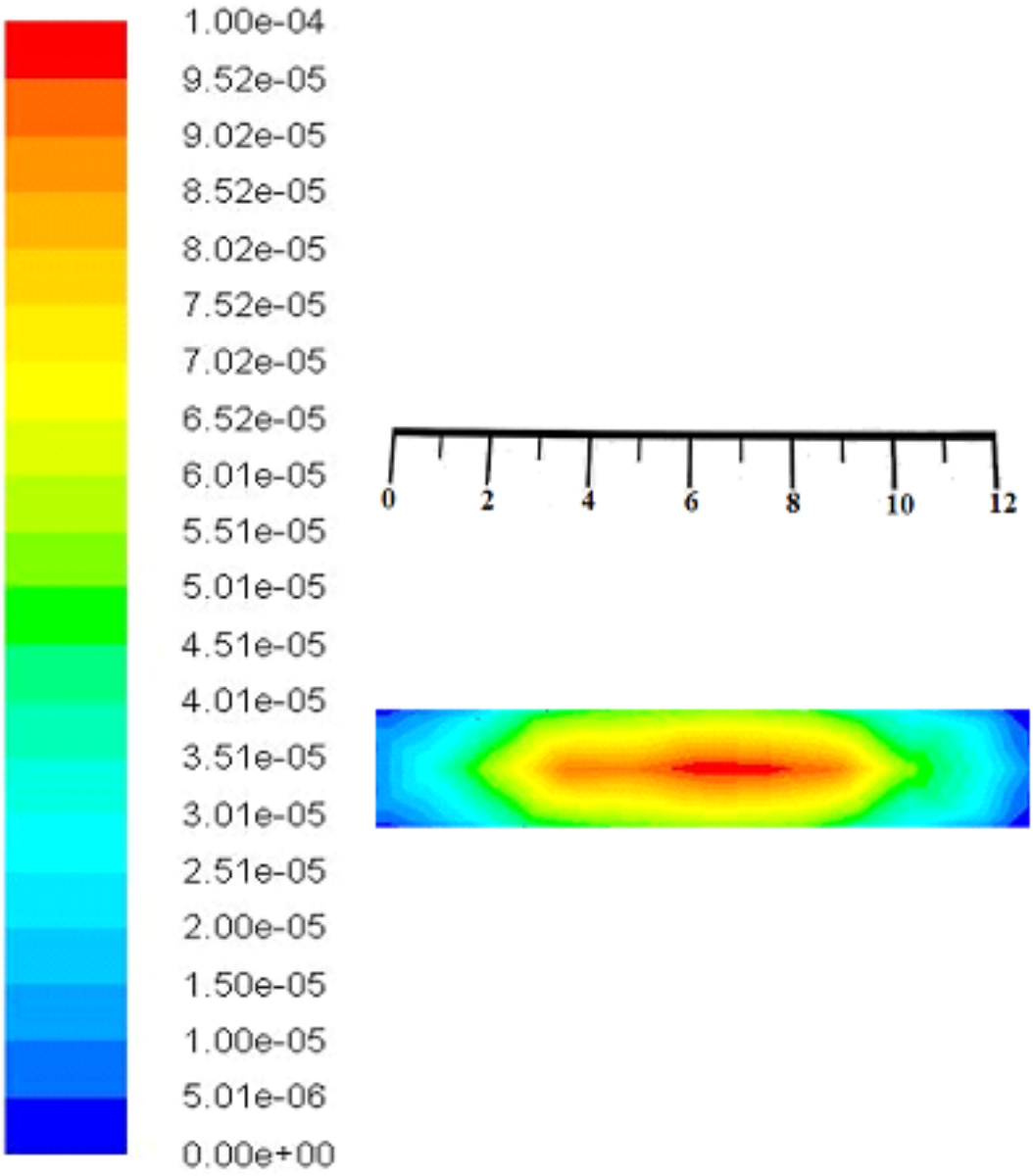

Figure 5.16: CFD prediction of the deposits from South Africa coal on the mullite probe 2 ($kgm^{-2}s^{-1}$).

5.2.5 Deposition Efficiencies

The deposits collected on the mullite probes were first characterised by the deposition efficiency. The deposition efficiency (the proportion of incident ash retained on the probe) on a probe which has been calculated during the co-combustion of coal and different masses of the biomass

materials in the EFR (Wigley et al., 2000). The deposition efficiency was calculated for each EFR run based on the mass percentage of the fuel ash calculated to impact on the projected surface area of the probe that was retained in the collected deposit. The projected surface area is calculated from the probe outer diameter of 20 mm and the EFR inner tube diameter 100 mm. The deposition efficiency was calculated as follows:

$$Deposition\ efficiency = \frac{Incident\ ash\ retained\ on\ the\ probe\ per\ \mathrm{sec}ond}{Total\ ash\ flow} \tag{5.1}$$

$$\times 100 \times \frac{1}{(projected\ area\ of\ the\ probe / surface\ area\ of\ the\ probe)}$$

where

$$Total\ ash\ flow(kg/s) = coal\ flowrate \times ash\ content \tag{5.2}$$

$$\begin{aligned} &The\ projected\ area\ of\ the\ probe(m^2) = length\ of\ probe(l_{probe}) \\ &\times diameter\ of\ the\ probe(d_{probe}) \end{aligned} \tag{5.3}$$

$$Surface\ area\ of\ the\ probe = \pi d_{probe} l_{probe}(m^2) \tag{5.4}$$

The deposition efficiency in equation (5.1) was defined as the total ash passing down the reactor whilst Wigley et al. (2007) defined it as ash impacting on the probe (equation 3.63). There is a difference and the results have to be multiplied by 1/(the projected area of the probe/surface area of the tube). The incident ash retained per second on the probe is obtained directly from the CFD calculations (ANSYS FLUENT 13.0.0) by turning-on the computation of the surface integral $(kg/m^2 s)(m^2)$ of the deposit rates on the probe surface.

It was found that the Russian coal exhibited the highest deposition efficiency, with 11.25 wt.% collection efficiency, while the deposition efficiency for South Africa coal was 10.10 wt.% (see Table 5.3). Although the deposition efficiency provides valuable information on the severity of the deposition problem when the two coals are compared. The detailed chemical analysis of the slagging tendency will be dealt with in the subsequent Chapter 6.

Although the experiment has been performed under identical operating conditions for pure coal, the variability in the deposition efficiency was observed in the experimental data. This variability is reflected by the large deviations of the repetition experiments performed on pure coal, i.e. 0 wt.% biomass. According to Wigley et al. (2000), the source of the variability is associated with the heating conditions to the operational temperature and the final setup.

Figure 5.17 shows the deposition efficiency as a function of the SRC ratio. The deposition efficiency for the co-firing SRC increases as the ratio of SRC addition reaches 40 wt.% and then decreases when up to 60 wt.% was added. The addition of 20 wt.% Miscanthus shows a significant reduction in the deposition efficiency but as the ratio of Miscanthus increases beyond 20 wt.%, the deposition efficiencies increases as shown in Figure 5.18. This is probably because of the higher level of alkali present at higher co-firing ratios. The reaction between silica and alkali, which may result in alkali silicates with a lower melting temperature. According to Hughes et al. (1998), potassium silicate is important at high temperatures, where strong sintering and fusion can occur. In general, the deposition efficiency of

Miscanthus is lower than that of SRC and Olive (see Table 5.3). This may probably be linked to the low ash content in the Miscanthus, which has significantly decreased the ash flux towards the probe. However, the addition of Olive shows an increasing trend in all co-firing ratios, as highlighted in Figure 5.19.

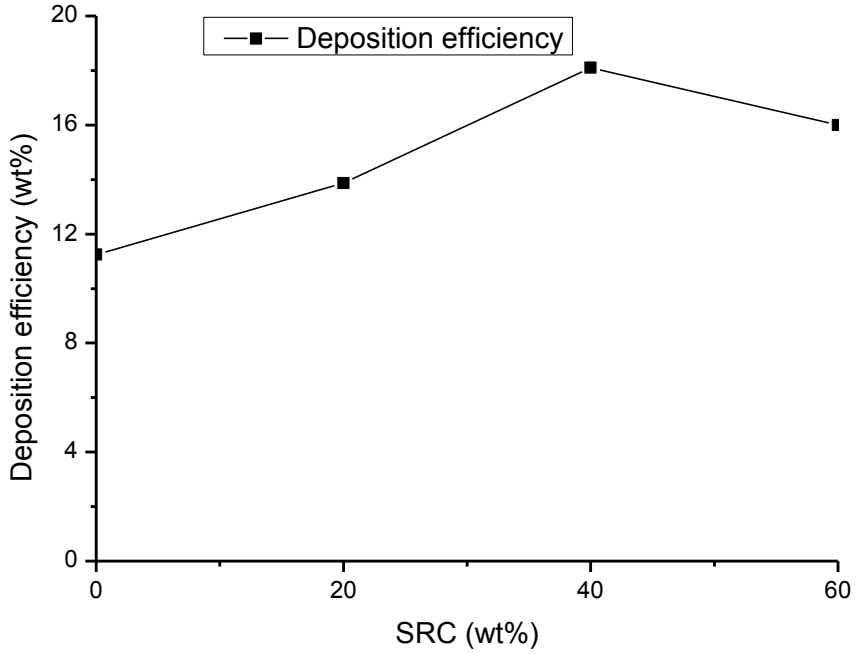

Figure 5.17: The computed deposition efficiency rates obtained from burning mixtures of Russian coal and SRC as a function of the co-firing ratio.

However, experimental investigations show that the deposition efficiency increases when the biomass is co-fired from 0 wt.% to 40 wt.% and then unexpectedly decreases when 60 wt.% biomass is added. This trend is nonlinear and may be presumably caused by many factors, including the significant reduction in the blend ash, the possibility of the erosion effect on the deposits, etc. It should be noted that other authors have observed

similar nonlinear ash deposition behaviours in their experiments (Heinzel et al., 1998; Zheng et al., 2007).

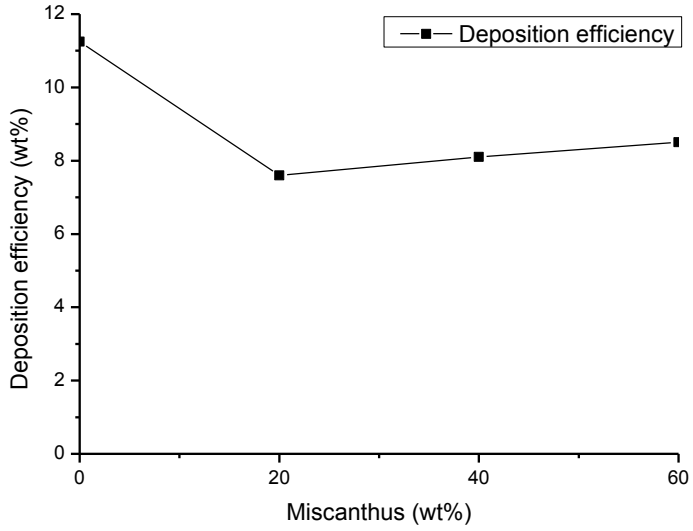

Figure 5.18: The computed deposition efficiency rates obtained from burning mixtures of Russian coal and Miscanthus as a function of the co-firing ratio.

The addition of Olive increases the ash retention index because of the fairly high ash content of 5.7 wt.%, see Figure 5.19, thereby increasing the degree of sintering, and these effects increase with the level of biomass addition. Some of the properties of the biomass also provide valuable information on the sintering tendency. For example, biomasses with high ash content are expected to yield a high degree of sintering. From Table 5.2, it is observed that palm and Olive, with a ash content greater than 4 wt.%, are more likely to cause troublesome deposits than biofuel (Miscanthus, Sawdust S and SRC) whose ash contents are less than 3 wt.%.

Table 5.3: Proximate and Ultimate Analysis of coal and biomass and ash chemical composition (wt.%)(Wigley et al., 2007; Phyllis, 2004).

Component	Russian Coal	South African coal	Miscanthus	Olive	Palm	Short Rotation Crop	Sawmill
Proximate analysis	wt.% on dry basis						
Volatiles	30	36	83.5	79.0	77.1	80.5	81.2
Fixed carbon	76	73	29.3	33.1	34.0	32.1	31.6
Moisture	5.56	5.47	30.7	24.0	23.0	18.5	19.0
Ash	12.6	12.1	2.3	5.7	4.2	2.4	2.5
CV(MJ/kg)	27	26.7	18.5	22.0	21.4	18.7	19.1
Ultimate analysis	wt.% on dry basis						
C	76.5	68.67	48.1	42.2	4.31	50.2	50.1
H	4.5	4.66	5.8	5.1	5.1	5.9	6.2
O	4.9	26.54	41.9	45.6	45.2	42.2	42.4
N	1.9	1.78	0.3	1.62	1.51	0.1	0.5
S	0.4	0.83	0.1	N/A	N/A	N/A	0.05
Cl	0.25	0.00	0.16	N/A	N/A	N/A	0.013
Ash composition	wt.% on dry basis						
SiO_2	60.1	54.1	57.0	32.1	15.1	17.3	40.7
Al_2O_3	24.0	33.5	2.4	6.6	3.2	4.4	8.1
Fe_2O_3	6.0	3.1	3.4	4.9	5.3	3.8	3.8
CaO	4.1	4.1	10.0	12.4	10.7	33.3	28.6
MgO	1.1	1.3	3.1	12.2	12.0	8.6	4.1
K_2O	3.0	0.7	18.2	18.9	9.7	13.8	6.8
Na_2O	0.4	0.1	1.1	0.4	0.3	1.0	1.1
TiO_2	1.2	1.7	0.2	0.2	0.1	0.3	1.1
MnO	0.1	0.0	0.4	0.0	1.0	0.4	3.6
P_2O_5	0.0	1.4	4.2	12.2	42.7	17.0	2.1

N/A = not available.

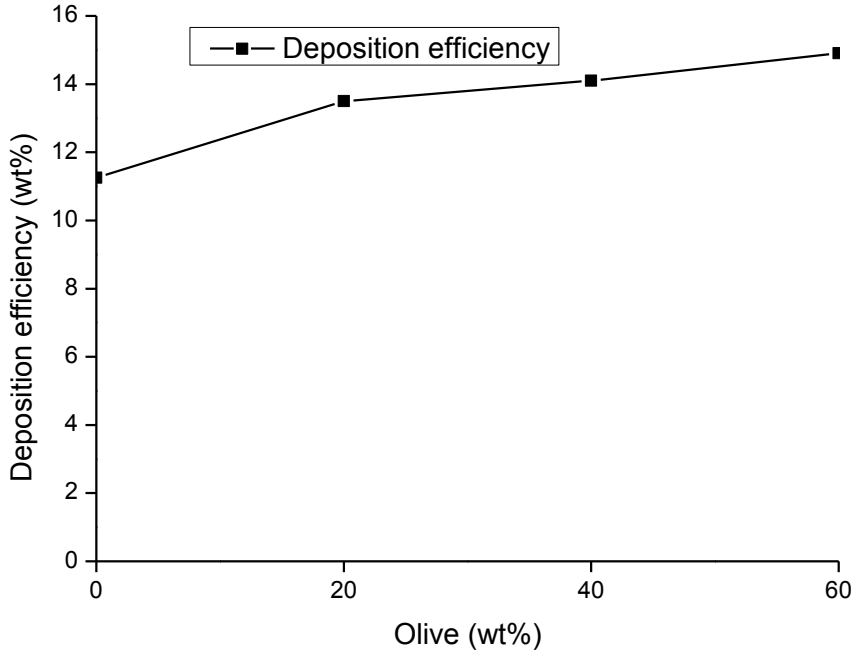

Figure 5.19: The computed deposition efficiency rates obtained from burning mixtures of the Russian coal and Olive.

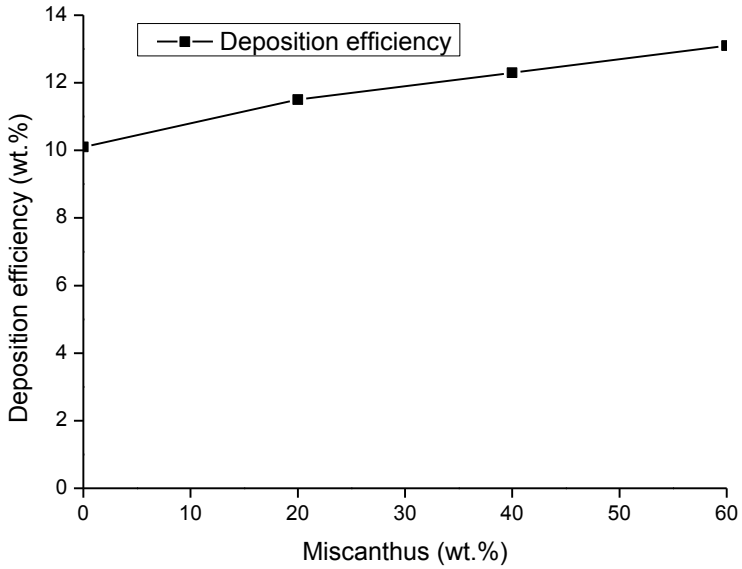

Figure 5.20: The computed deposition efficiency rates obtained from burning mixtures of South Africa coal and Miscanthus as a functions of the co-firing ratio.

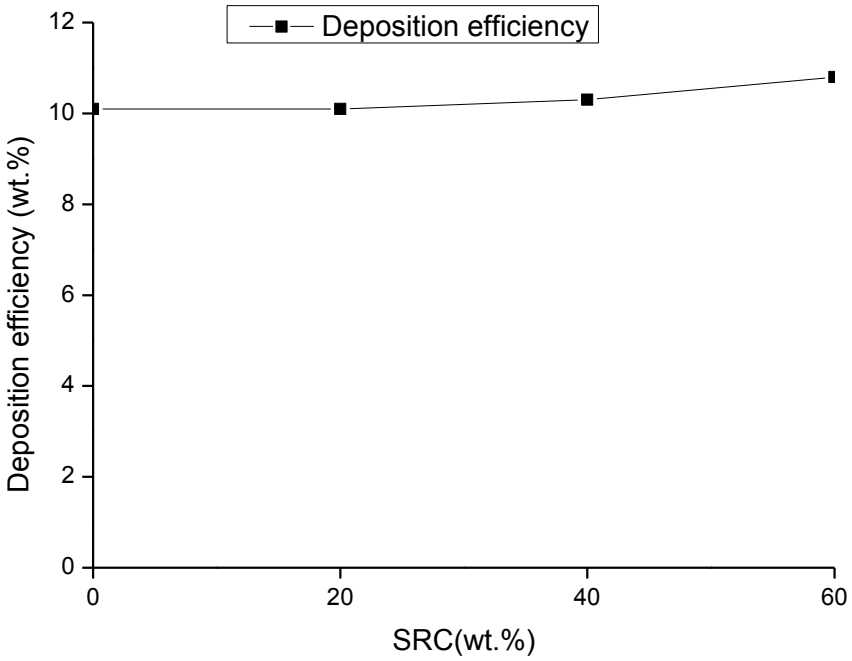

Figure 5.21: The computed deposition efficiency rates obtained from burning mixtures of South Africa coal and SRC as a functions of the co-firing ratio.

Table 5.4: Predicted deposition efficiency (wt.%) for pure Russian coal and South Africa coal.

Russian coal	South Africa
11.25	10.10

Five measurements have been made on Russian coal alone and the deposition efficiencies varied from 4.7 wt.% to 14.4 0 wt.% collection efficiency, with an average of 9.5%. In order to compute the experimental results on an equal basis, all the experimental results were normalized so that the 0 wt.% biomass addition was the mean value. These results are shown in Tables 5.5 and 5.6. The deposition efficiency of 20 wt.% SRC is

lower than that of the 100% coal combustion. A primary reason for this phenomenon is that the coal ash is diluted by the low iron biomass ash during co-combustion, thereby decreasing the amount of iron introduced into the boiler.

Another reason for the deposition efficiency reduction may be related to the relatively high calcium content in the ash of the SRC, which may generate calcium components with high melting points.

Table 5.5: Deposition efficiency (wt.%) for mixtures of Russian coal with SRC, Miscanthus and Olive.

Biomass	Level of biomass addition (wt.%)			
	0	20	40	60
SRC experimental	14.4	11.6	19.7	13.3
SRC normalized to 9.5%	9.5	7.7	13.0	8.6
SRC computed	11.25	13.87	18.1	16.0
Miscanthus experimental	4.7	5.6	6.3	6.1
Miscanthus normalized to 9.5%	9.5	11.3	12.6	12.2
Miscanthus computed	11.25	7.6	8.1	8.5
Olive experimental	13.0	15.2	13.4	9.7
Olive normalized to 9.5%	9.5	11.1	9.8	7.1
Olive computed	11.25	15.2	14.1	14.9

Figures 6.16 and 6.17 show the deposition efficiency obtained from burning mixtures of South Africa coal with Miscanthus and SRC, respectively. It is observed that the deposition efficiency of both Miscanthus and SRC addition increases with the level of biomass addition. While the

addition of Miscanthus slightly overpredicts the experimental measurements at all co-firing ratios, the addition of SRC under predicts the experimental measurements by 9 wt.% and 17 wt.% at 40 wt.% and 60wt.%, respectively, see Table 5.6. The primary reason for the under prediction for the SRC addition of SRC is mainly due to the high content of phosphorus in SRC which has not been taken into account in the deposition model.

Table 5.6: Deposition efficiency (wt.%) for mixtures of South African coal with SRC, Miscanthus and Olive.

Biomass	Level of biomass addition (wt.%)			
	0	20	40	60
SRC experimental	10.2	4.1	12.7	14.6
SRC normalized to 9.1%	9.1	3.7	11.3	13.0
SRC computed	10.1	10.1	10.3	10.8
Miscanthus experimental	8.0	8.2	10.3	12.7
Miscanthus normalized to 9.1%	9.1	9.3	11.7	14.5
Miscanthus computed	10.1	11.5	12.3	13.1
Olive experimental	10.9	11.8	11.5	16.4
Olive normalized to 9.1%	9.1	9.9	9.6	14.6
Olive computed	10.1	11.2	12.7	14.0

5.3 Conclusions

In this chapter, co-combustion of two bituminous coals and biomass materials were carried out in an entrained flow reactor. In the modelling

calculations, the deposition rate is related to the viscous deformation of the coal ash and the liquid content of the biomass ash. The model is suitable for the prediction of the deposition rates of heterogeneous coal/biomass ash slag in a high temperature regions.

The addition of 20% SRC and Olive increases the deposition efficiencies of coal ash deposits, while the addition of 20% Miscanthus decreases the deposition efficiencies of the coal ash deposits. The deposition efficiency increases with the higher levels of the biomass additions (up to 20%), except for SRC whose trend depicted that observed in the experimental data. The reason for this discrepancies is likely to be linked to the high calcium content in the SRC. A conceivable explanation is that the formation of low fusion K-bearing silicate is inhibited by the high calcium content in the SRC, thus resulting in a reduced collection efficiency for the EFR. Further investigations are required in order to support this reasoning.

Chapter 6

Numerical Assessment of Deposit Sintering

The numerical slagging index (NSI), previously developed by Degereji et al. (2011), has been modified to account for the effect of sintering. The model has been tested for coal with five different biomass materials in order to predict their slagging performance. Also, in this chapter, the results obtained for the predictions using the numerical slagging index (NSI) has been presented and discussed.

The chapter is divided into four sections. The first section briefly discusses the frontier literature in deposit sintering. The numerical modelling steps are presented in the second section. The equilibrium calculations used in the prediction of the slag-liquid and it chemical composition has been explained in the third section. In the fourth section, the performance of the NSI has been presented and discussed.

6.1 Introduction

The co-firing of coal with biomass is an attractive option for power generation due to the reductions of carbon dioxide (CO_2), nitric oxide (NO_x) and sulphur dioxide (SO_x) emissions (Williams et al., 2000). Coal may be replaced partially, or entirely, by biomass in power generating plants, the extent depending on the economics and national energy policies that prevail at the time. Co-firing of coal with biomass takes advantage of the high efficiencies obtainable in coal-fired power plants and can be used over a wide range of coals. The biomass can be divided into two-categories: energy

crops and agricultural residues, and their combustion behaviour is dependent on their history and pre-treatment (Williams et al., 2000). In a coal-fired power station, some ash particles impact on the heat transfer surfaces and are retained, forming deposits that cause slagging in the boiler or fouling in the convective pass. The use of biomass in coal fired plants may present additional technical problems. One of these is related to the low melting point of some biomass ash, especially from agricultural residues, which may create deposition problems. Deposits are removed naturally by shedding, or mechanically by soot blowing from a boiler, but because of the strength of certain deposits, boilers may be temporarily shut-down for manual cleaning. Often, the strength of the deposit may be more important than the rate of deposition.

The rate of ash deposition at operating conditions close to those for the real boilers are very difficult to be determined effectively. The major pathways for the ash particle transport to the boiler walls, which are inertial impaction, thermophoresis, heterogeneous reactions and condensation, have been well documented (Huang et al., 1996; Baxter et al., 1993). Despite the details in these reports, the understanding of their pathways and thermal behaviour in terms of the deposit formation and the strength and degree of fusion on the heat transfer surface are still fragmentary.

A number of experimental techniques have been adopted (Huang et al., 1996; Lee et al., 1999; Hutchings et al., 1995; Manton et al., 1997) to study deposition under controlled conditions. The Entrained Flow Reactor (EFR) is often employed because the temperature and reaction times can be controlled (Hutchings et al., 1995; Manton et al., 1997; Wigley et al., 2007;

McLennen et al., 2000). Hutchings et al. (1995) describe the design and operation of an EFR to assess the slagging propensity of a coal ash. Manson et al. (1997) discussed coal ash slags and deposits from both single and blended fuels in an EFR. Borroso et al. (2006) examined the slagging behaviour of coal blends under different operating conditions in an EFR. Wu et al. (2011) have studied the co-combustion of coal with biomass with up to 20 wt% of the total thermal input, and the influence of additives on the co-combustion was investigated. Wigley et al. (2007) have presented experimental data on the deposition efficiency, as well as the extent to which the deposits were sintered for up to 60 wt.% of coal replacement by biomass in an EFR. These results provide an objective assessment of the slagging propensity of coal ash and biomass and they can be run at varying deposition rates as required. The major shortcoming of the EFR is the lack of a standard testing procedure.

As yet, there are no available tools that can predict the slagging and fouling properties of a given fuel unequivocally. The ash fusion temperature, ash viscosity, and ash chemistry are the three basic tools for characterizing coal ash slagging and deposits during combustion (McLennen et al., 2000). Most of the ash deposits are derived from the inorganic components of coal, biomass and their blends. Their consolidation occurs by two main mechanisms: (i) viscous necking (flow sintering) of adjacent particles at a rate determined by viscosity, and (ii) the bonding of particles by melting type or quantity (Backman et al., 1997; Mueller et al., 2005). Sintering between particles enhances the stickiness by increasing the resistance to the thermal shock and erosion. In addition to the stickiness, the tendency of a particle to deposit is also affected by the particle surface energy and its static angle of

impact. The effects of these factors have been tested in both biomass and coal combustion (Degereji et al., 2011; Ma et al., 2006).

The Ash Fusion Test (AFT) and cone deformation are other widely used tools that are required for the progress of the sintering mechanism (Gupta et al., 2006). The AFT, which determines the temperature at which the various stages of the ash softening and flow takes place, is based on the judgment of the analyst as to when the ash reaches and passes through the defined stages of the softening. Since the assessment of this method is subjective rather than objective, the results obtained may be misleading. The most frequently used parameter for correlating fusibility with its composition is the Basic/Acid (B/A) ratio. Because an increase in the percentage of the basic component of the ash lowers the melting-point phases of the ash, the basic components are also known as the fluxing agents (Pronobis et al., 2006). The ratio B/A, which was introduced originally for the assessment of coal ash is restrictive and cannot be applied to certain types of biomass materials, especially those with a high phosphorus content in their ash. Although phosphorus is acidic, many publications, such as Kupka et al. (2008), have confirmed that the presence of phosphorus acts as an additional fluxing agent for the development of the low-melting-point phases in the fly ash. Therefore, in order to account for this influence, the phosphorus contents have been added to the basic oxides (Pronobis et al., 2006 ; Kupka et al., 2008).

Several attempts have been made to find reliable models to accurately predict ash deposition rates in boilers and this has exercised the minds of fuel technologists for many years. Most of these models have used

the particle viscosity as a function of the temperature to determine the capture efficiency of the ash particles on impaction with the boiler walls for coal ash (Huang et al., 1996; Degereji et al., 2010 ; Rushdi et al., 2005). In the case of co-firing, the appearance of the melt phase is thought to increase not only the tendency for the ash particles to adhere to the furnace walls but also the rate at which the strength of the deposits build-up (Heinzel et al., 1998).

6.2 Numerical Modelling

The numerical slagging index (NSI), as previously developed by the group at Leeds University has been implemented and validated successfully for various coals and their blends (Degereji et al., 2012). This was modified to account for the coal/biomass blend. The NSI is generally expressed in terms of the incoming ash, γ and the ash viscosity, μ, as follows (Degereji et al., 2010; Degereji et al., 2012):

$$S_x = \gamma / Log(\mu) \tag{6.1}$$

The incoming ash γ is defined as follows (Lawrence et al., 2008):

$$\gamma = \frac{ash\,content\ per\,kg}{CV\ (MJ/kg)} \tag{6.2}$$

For coal/biomass blends, the effects of the biomass addition can be predicted on the deposit sintering by determining the viscosity of the blend ash from the ash content and the ash chemistry of the individual fuels (Wigley et al., 2007). Thus, the weight of the incoming ash has been defined in terms of the content of the ash and the heating value of the individual fuels as follows:

$$\gamma = x\gamma_c + y\gamma_b \tag{6.3}$$

where γ_c and γ_b are the weight of the coal ash and the weight of the biomass ash, respectively. Also, the modified Watt-Fereday ash viscosity model used previously by some of the authors (Degereji et al., 2010) has been redefined to take into consideration the effect of MgO and blend ash as follows:

$$Log(\mu) = \frac{m.10^7}{T_s{}^2} + c \tag{6.4}$$

$$m = 0.01404294(SiO_2) + 0.0100297(Al_2O_3) \tag{6.5}$$

$$\begin{aligned} c = {} & 0.0154148(SiO_2) - 0.0388047(Al_2O_3) \\ & -0.0167264(SiO_2) - 0.0089096(CaO) \\ & -0.012932(MgO) + 0.004678 \end{aligned} \tag{6.6}$$

where $\alpha = 100 - (SiO_2 + Al_2O_3 + Fe_2O_3 + CaO + MgO).$

In equation (7.4), the term T_s can be postulated as presented below using the softening temperature of the coal (T_c) and that of biomass (T_b), and their respective weight percent in the blend, as follows (Degereji et al., 2011):

$$T_s^2 = xT_c^2 + (y/\kappa_i)T_b^2 \tag{6.7}$$

where the T_s total softening temperature is the sum of the softening temperature of coal, T_c^2 and biomass, T_b^2. While x and y are fraction of coal and biomass in the fuel mix, k_i has been defined only for biomass. Because of the variability of the ash composition of biomass fuel, k_i is defined for two types of biomass materials : those with low phosphorus content, k_1 (such as wood) and high phosphorus content, k_2 (such palm kernel residue).

$$T_c = a(SiO_2) + b(Al_2O_3) + c(Fe_2O_3) + d(CaO) + e(MgO) + f(\alpha) + g + 150^0 C \qquad (6.8)$$

The factor, κ_i (Pronobis, 2006; Kupka et al., 2008) is introduced to take into account the differences in the composition of biomass ash and it is estimated either as

$$\kappa_1 = \frac{Fe_2O_3 + CaO + MgO + Na_2O + K_2O}{SiO_2 + Al_2O_3 + TiO_2} \qquad (6.9)$$

or

$$\kappa_2 = \frac{Fe_2O_3 + CaO + MgO + Na_2O + K_2O + (P_2O_5)}{SiO_2 + Al_2O_3 + TiO_2} \qquad (6.10)$$

The values for the constants (a, b, c, d, e, f and g) are given based on the percentage of SiO_2, Al_2O_3 and Fe_2O_3 available in the ash content (Yin et al., 1998). The slope, m, and intercept, c, in equations (7.5) and (7.6) are recalculated using the Bomkamp-correction in order to account for the content of MgO (Vargas et al., 2001). Bomkamp (1976) attempted the modification of the Watt-Fereday equations for calculating the constants m and c, to account for the MgO-content (Quon et al., 1985). Quon et al. (1985) found the Bomkamp modification provide good estimate for melts from wide range of coals.

6.3 FactSage Results

Coal combustion: Substantial liquid formation requires higher temperatures: for the South Africa and the Russian coals shown in Figures 6.1 and 6.2, respectively, approximately 60% liquid is predicted at 1500 ^oC. Also, the extent of the liquid formation depends on the fuel ash. The larger amount of

slag liquid for the Russian coal in the temperature range 1300 to 1600 ^{o}C may be attributed to the high Fe_2O_3 content which is greater than the sum of CaO and MgO in the fuel ash, see Figure 6.2. Conversely, the low slag liquid predicted in Figure 6.1 is due to the fact that the Fe_2O_3 content in South Africa coal is less than the sum of CaO and MgO in the fuel ash. The slag obtained depends on the gas temperature at the sampling port of the EFR as this will directly affect the degree of the assimilation of the iron phases into the aluminosilicate melt. Previous research, such as McLennen et al. (2000) has shown that the higher content of divalent iron in reduced conditions promotes the formation of the molten phase.

The FactSage results show that mullite ($Al_6Si_2O_{13}$)(s) is the main solid phase in South Africa coal, as shown Figure 6.1, and this persists at a temperature 1600 ^{o}C. In contrast, the main solid at 1000^{o}C in the Russian coal ash is tridymite (SiO_2)(s), see Figure 6.2. From Table 6.1, it is observed that Russian coal has high SiO_2 (60.1 wt.%) (s) and low Al_2O_3 (24 wt.%) (s), while South Africa coal has high SiO_2 (54.1 wt.%) (s) and high Al_2O_3 (33.5 wt.%) (s) in the ash. The difference in the identity of the primary solid phase results from the differences in the composition of the ash. The higher is the SiO_2 in the fuel ash then this favours the tridymite formation, while higher Al_2O_3 levels favours mullite formation. Anorthite ($CaAl_2Si_2O_8$) (s) is formed because of the interaction between of quartz with Al_2O_3 and CaO at about 1000 ^{o}C. Hematite (Fe_2O_3) (s) and leucite ($KAlSi_2O_6$) (s), appear at about 1400 ^{o}C, but leucite ($KAlSi_2O_6$) (s), which has a significant effect on the fusion characteristics, rises sharply and remains fairly constant at 1230 ^{o}C. The slag almost disappears below 1000 ^{o}C for both the South Africa and Russian coals. In Russian coal, the silicate, in particular potassium silicate,

is characterized by large variations, and this is probably due to the periodic formation and dissolution of the crystals in the melt (see Figure 6.2). The high amount of calcium, iron and potassium lead to the formation of the Ca- , K- and Fe- silicates that are crystallized even at temperature of 1500^{o} C. This may simplify the operation of the EFR because the ash will be relatively non-sticky.

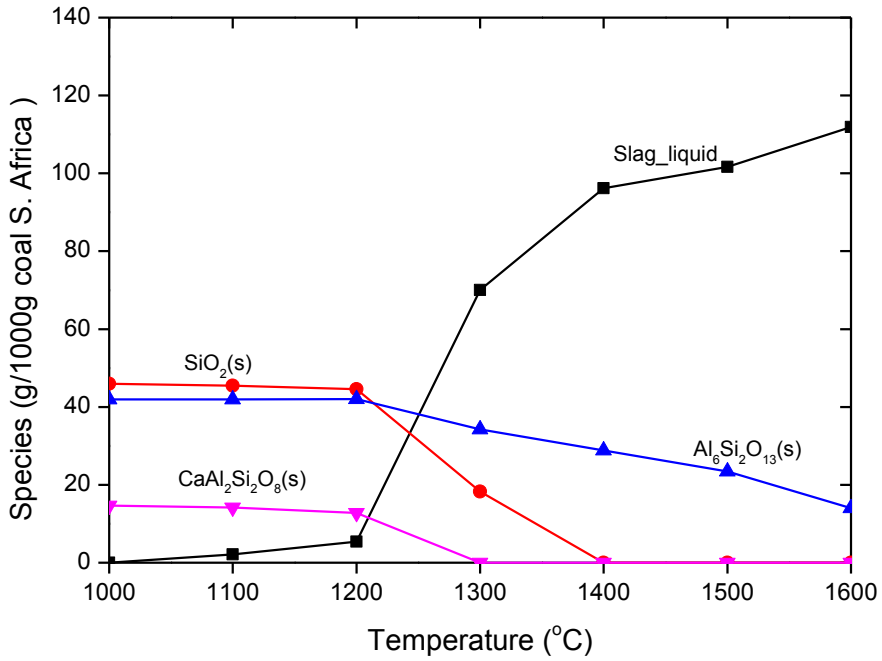

Figure 6.1: Mineral matter output from the South African coal combustion at different temperatures (where s in the figure represent solid). The vertical axis show the mass of relevant species in grams per kg fuel.

Figures 6.3 and 6.4 show the percentage of the basic oxides in the slag liquid for South Africa coal and Russian coal, respectively. 1000 kg fuel is used as a basis (units in the y-axis of Figures 6.1 and 6.2) for the equilibrium calculation**.** The percentage of iron and calcium increase significantly when the combustion temperature is in excess of about 1100 ^{o}C, while potassium and sodium increases when the combustion temperature is less that 1100

^{o}C. As the iron and calcium concentration of aluminosilicate glass increases, up to a certain level, the viscosity will tend to decrease and the rate of deposit sintering is enhanced. However, at higher concentrations of the oxides in the slag, the solubility limit of such oxide is reached and the oxide crystallises out in the form of mullite, tridymite, leucite, cordierite, hematite, anorthite, forsterite and spinel (see Figures 6.1 and 6.2).

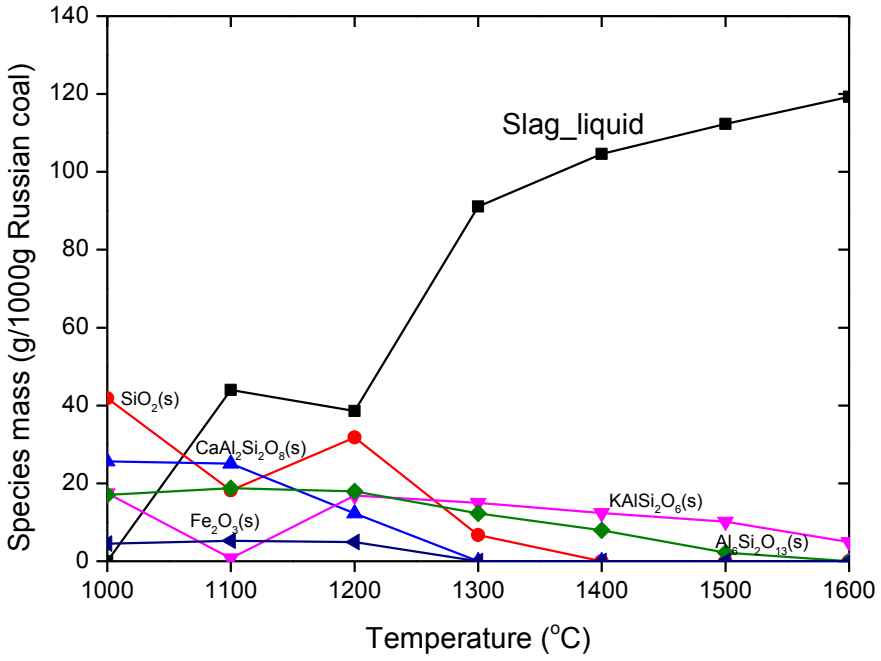

Figure 6.2: Mineral matter output from the Russian coal combustion at different temperatures (where s in the figure represent solid). The vertical axis show the mass of relevant species in grams per kg fuel.

Biomass: Biomass as a natural material has variable characteristics that differ from that of coal. As an example, the principal properties are shown in Table 4.3 for the fuels used in the EFR experiments. In general, the ash content of the biofuels (SRC and Sawdust S) and Miscanthus are in the

range of 2.3-2.5 wt.%. In contrast, the ash content of the Olive and Palm are between 4 wt.% and 6 wt.%.

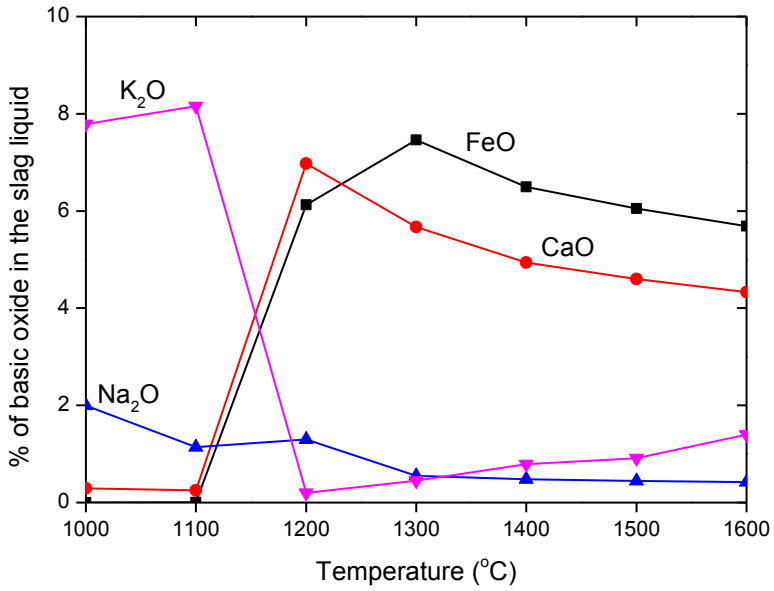

Figure 6.3: The percentage of the basic oxide in the slag liquid for Russian coal combustion at different temperatures.

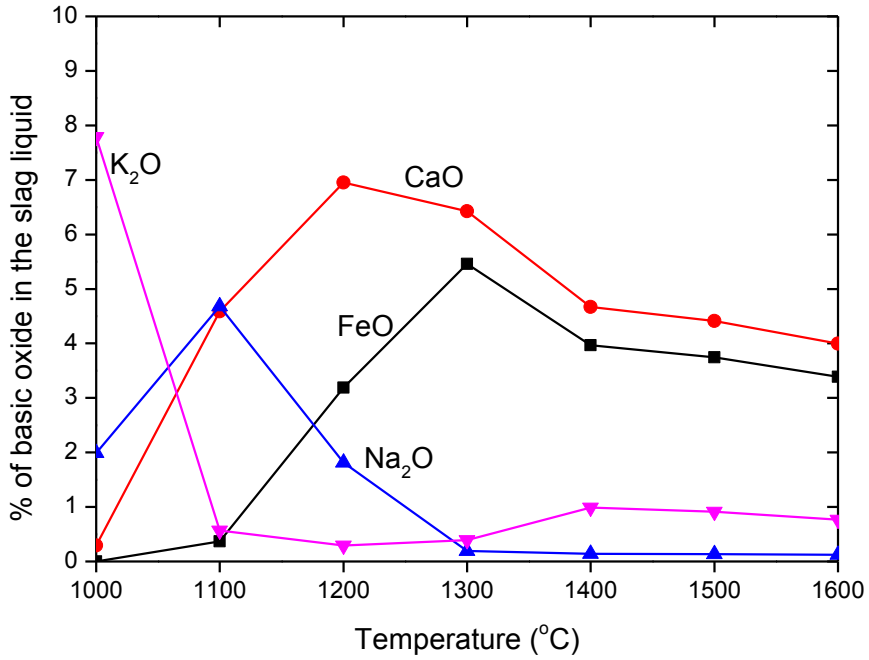

Figure 6.4: The percentage of the basic oxide in the slag liquid for South African coal combustion at different temperatures.

The moisture content of fresh Miscanthus is about 30 wt.% and the moisture content of biofuels (SRC and Sawdust S) are about 18.5 wt.%. Palm and Olive contain about 23 wt.% moisture content. The composition of biomass elements are different from those found in coal, as exemplified by the fuels used in the deposit tests. Table 5.3 shows that the main ash elements (calculated as oxides) found in the Russian and South Africa coals are SiO_2, Al_2O_3 and FeO . A dominance of SiO_2 and Al_2O_3 with fairly large amounts of FeO, K_2O and CaO were found for the Russian coal. Whereas Miscanthus had an unusually high SiO_2 content (>SiO_2), and one of the biofuel fuels (Sawdust S) had about 40 wt.% silica content. Palm and SRC had the lowest SiO_2 content with about 15 wt.% and 17 wt.%, respectively.

The contents of titanium and sodium oxides in the investigated biomass materials are low and, in general, more P_2O_5 is found in the biomass ash than in coal ash. Palm has the highest P_2O_5 content of about 43 wt.%. The content of P_2O_5 in Olive and SRC are moderate with about 17 wt.% and 12 wt.% for SRC and Olive, respectively. However, all the biomass materials content are reasonably high in potassium and the content of potassium decreases in the following order: Olive (18.9 wt.%), Miscanthus (18.2 wt.%), SRC (13.8 wt.%), Palm (9.7 wt.%) and Sawmill S (6.8 wt.%). Further, large amounts of calcium are found for SRC (33.3 wt.%) and Sawmill S (28.6 wt.%) (see Table 4.3).

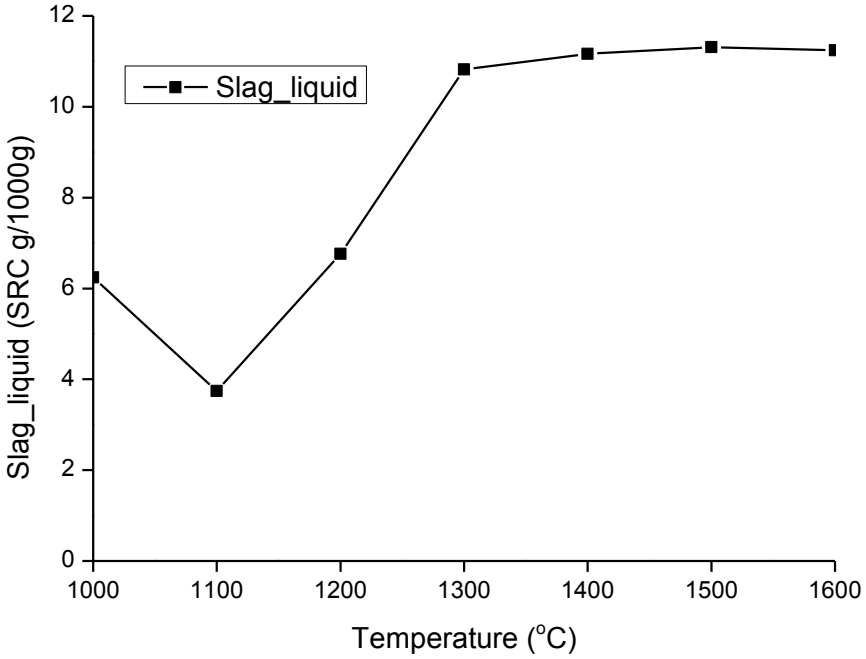

Figure 6.5: Slag liquid (grames per kg fuel) from the SRC combustion at different temperatures.

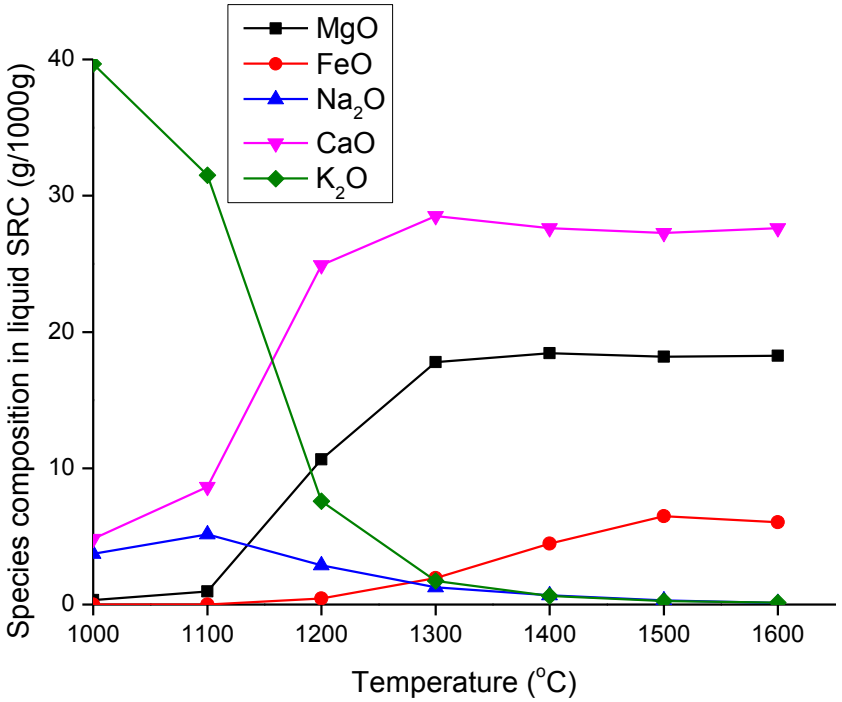

Figure 6.6: Chemical composition of the slag liquid from the SRC combustion at different temperatures.

Figure 6.5 shows the behaviour of slag for SRC at different temperature. It is observed that the slag initially decreases when the temperature increases from 1000 ^{o}C to 1100 ^{o}C and then increases as the temperatures increases. The chemical composition of the slag for SRC, as shown in Figure 6.6, indicates that K_2O decreases while CaO, Na_2O, FeO and MgO increases as the temperature increases.

Figure 6.7 and 6.9 show the slag and chemical composition of Miscanthus at different temperatures, respectively. Figure 6.7 shows that the slag remains fairly constant up to a temperature of about 1400 ^{o}C and then increases as the temperature increases. Further, a substantial amount of K_2O is present in Miscanthus when compared to CaO, Na_2O, FeO and MgO, see Figure 6.6, and the percentage of K_2O decreases significantly when the temperature increases from 1000 ^{o}C to 1600 ^{o}C.

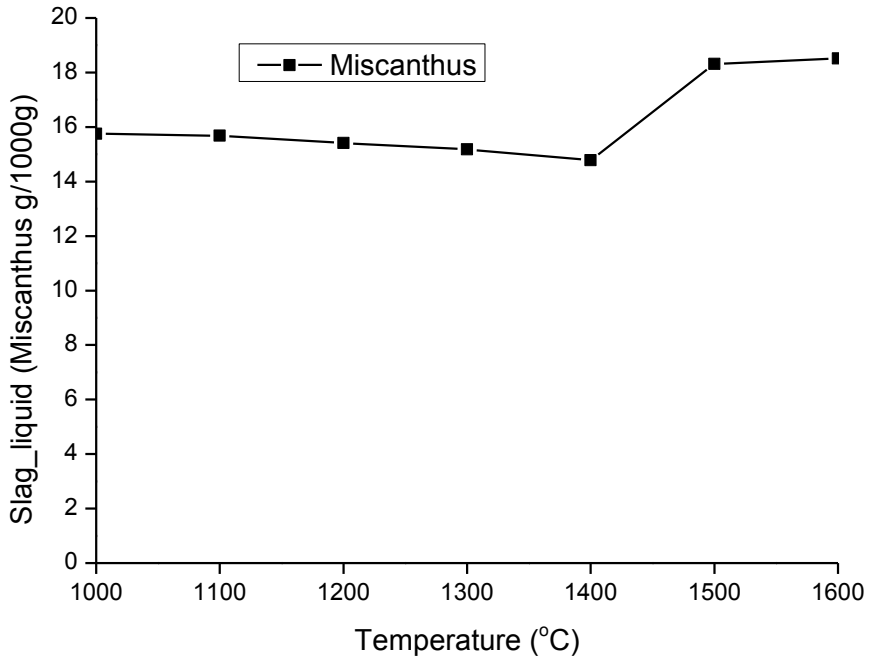

Figure 6.7: Slag liquid (grames per kg fuel) from the Miscanthus combustion at different temperatures.

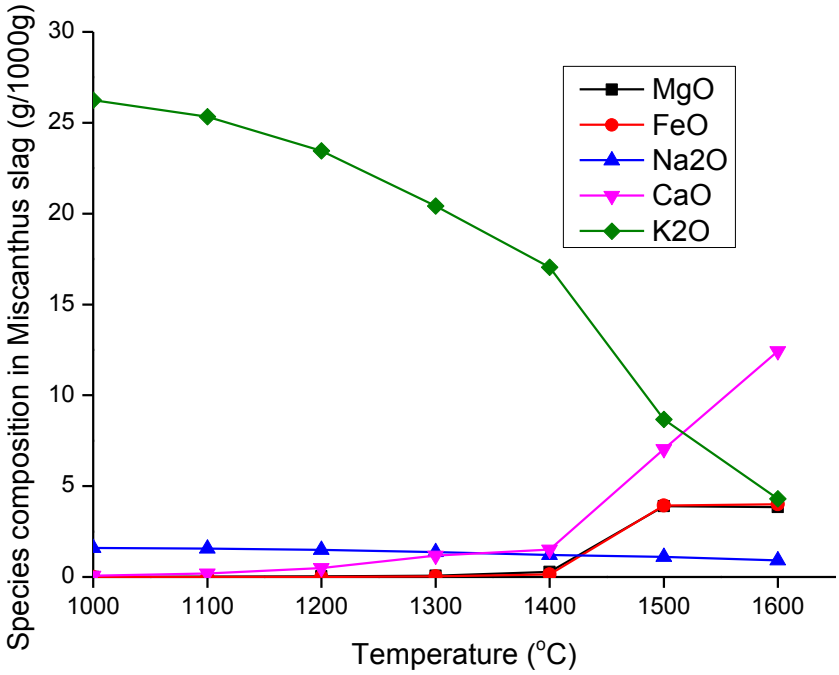

Figure 6.8: Chemical composition of slag liquid (grames per kg fuel) from the Miscanthus combustion at different temperatures.

Figures 6.9 and 6.10 show the slag and chemical composition for Miscanthus at different temperatures, respectively. The behaviour of the slag produced by Olive residue decreases significantly as the temperature increases from 1000 to 1400 ^{o}C and then increases steeply as the temperature rises to 1600 ^{o}C. The trend of the chemical composition of the slag for Olive mixture shows some similarity with the trend obtained with chemical composition of the slag for Miscanthus mixture except the disproportional rises in the MgO content at temperatures greater than 1400 ^{o}C.

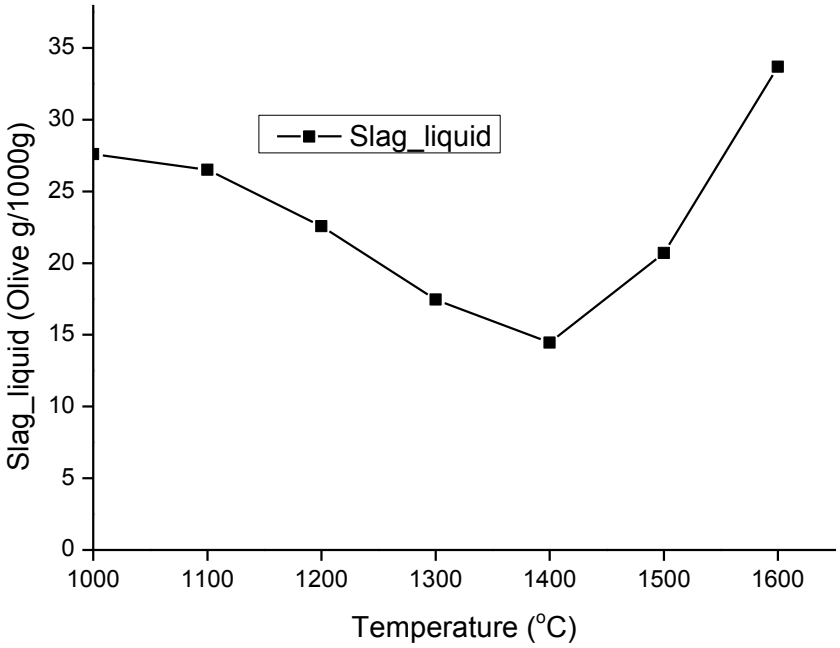

Figure 6.9: Slag liquid (grames per kg fuel) from the Olive residue combustion at different temperatures.

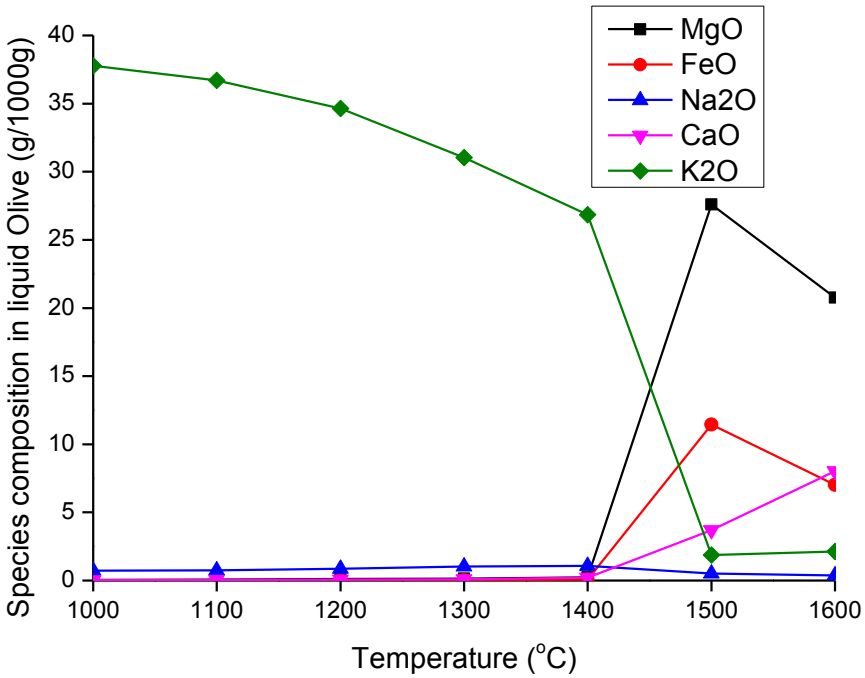

Figure 6.10: Chemical composition of slag liquid (grames per kg fuel) from the Olive residue combustion at different temperatures.

Model prediction versus experimental data: The model prediction of the slag liquid and its composition for co-firing South African coal with SRC and Olive (0 wt%, 20 wt%, 40wt% and 60wt%) are presented in Tables 6.1 and 6.2 respectively. The trend of the model prediction shows that the slag liquid decreases with the level of SRC and Olive addition to the coal. In order to explain the behaviour of the slag system presented in Tables 6.1 and 6.2, the model prediction was compared with the recent experimental investigation carried out by Khodier et al. (2012) in a pilot-scale pulverized fuel combustion rig. The deposits generated on cooled probes in the combustion rig from co-firing miscanthus mixed with coal were monitored at 0 wt%, 20 wt%, 40wt%, 60wt% and 100 wt%. The experimental data from this investigation shows that the amount of the deposit formed on the probe decreases with increases in the level of biomass co-firing (Khodier et al. 2012). The results of the equilibrium calculation in Tables 6.1 and 6.2 also show that the amount of slag liquid decreases with increases in the level of biomass co-firing and this trend matches the experimental data when compared with the work of Khodier et al. (2012). A further explanation of the reduction of the deposits with addition of biomass can be found in the work of Lawrence et al. (2008) who emphasized on the dominance on silica glass in coal slag under high temperatures during coal-biomass combustion. The authors concluded that reducing the amount of coal in the fuel mix resulted in a significant reduction of the deposit formation.

Table 6.1: Chemical composition (wt.%) of EFR deposits from mixtures of South African coal with SRC (Experiment data taken from Wigley et al., 2007).

Biomass	Level of biomass addition (wt.%)			
	0	20	40	60
Slag liquid computed	43.3	42.4	43.1	14.6
SiO_2 experimental	50.4	50.3	48.1	47.4
SiO_2 computed	57.1	56.2	57.4	58.2
Al_2O_3 experimental	29.0	29.8	28.0	26.0
Al_2O_3 computed	20.9	20.7	20.7	24.2
Fe_2O_3 experimental	4.8	3.1	2.9	3.5
Fe_2O_3 computed	7.2	6.8	5.4	5.3
CaO experimental	9.7	9.9	13.6	12.9
CaO computed	6.6	7.1	8.2	8.2
MgO experimental	2.5	1.9	2.3	2.7
MgO computed	3.1	3.2	3.1	4.2
K_2O experimental	0.7	1.3	0.8	1.0
K_2O computed	0.2	0.3	0.3	0.2
Na_2O experimental	0.2	0.4	0.3	0.3
Na_2O computed	0.3	0.2	0.2	1.3
TiO_2 experimental	1.6	1.4	2.0	1.5
TiO_2 computed	4.7	3.9	2.9	6.0

SiO_2, the main component of deposits, shows a heterogeneous behaviour in the deposit data. In coal combustion its share in the deposits make up about 50% of the deposits. SiO_2 in Olive co-combustion is reduced in the deposit at all level of Olive addition as shown by the experimental data and the model prediction. For SRC co-firing experiment, the SiO_2 share slightly decreases in the deposits as the ratio of SRC addition reaches 40 wt.% and then increases when up to 60 wt.% was added. In the case of the model prediction, the share of SiO_2 slightly decreases in the slag up to 20%

SRC addition as in the experimental data and then behaves differently when 40 wt.% and 60 wt.% SRC were added.

Table 6.2: Chemical composition (wt.%) of EFR deposits from mixtures of South African coal with Olive residue (Experiment data taken from Wigley et al., 2007).

Biomass	Level of biomass addition (wt.%)			
	0	20	40	60
Slag liquid computed	43.3	35.5	17.0	3.5
SiO_2 experimental	50.4	47.4	47.0	43.6
SiO_2 computed	57.6	57.1	49.8	42.7
Al_2O_3 experimental	29.0	27.4	26.7	22.9
Al_2O_3 computed	20.8	20.8	23.6	17.4
Fe_2O_3 experimental	4.8	2.5	3.4	3.5
Fe_2O_3 computed	7.2062	6.7559	5.9796	4.5
CaO experimental	9.7	13.5	9.4	12.0
CaO computed	6.6	6.5	7.9	5.4
MgO experimental	2.5	4.0	3.3	4.3
MgO computed	3.1	3.1	4.1	1.3
K_2O experimental	0.7	1.8	6.2	9.2
K_2O computed	0.2	0.6	9.1	23.6
Na_2O experimental	0.2	0.2	0.5	0.5
Na_2O computed	0.3	0.4	1.0	4.7
TiO_2 experimental	1.6	1.1	1.6	1.4
TiO_2 computed	4.7	4.7	7.5	4.9

In co-combustion Al_2O_3 presence in the deposits reduces with the addition of SRC and Olive to the coal while in the model prediction the Al_2O_3 remain fairly constant up to 40wt% SRC and Olive addition but significantly decrease at 60wt%. The model overpredicted SiO_2 and underpredicted Al_2O_3.

For the co-firing of South Africa coal with SRC, the slag decreases when 20 wt.% SRC is co-fired and then increases when 40 wt.% SRC was added and then finally decreases when 60 wt.% SRC is co-fired. When South African coal is co-fired with Olive residue, the slag liquid decreases with the level of Olive addition as shown in Figures 6.10 and 6.11. The quality of the slag produced changes that reflects the oxide components of the biomass ashes. In Table 6.1, SRC additions increase the CaO and K_2O contents of the slag liquid while additions of Palm kernel additions in Table 6.2 increase the K_2O content of the slag liquid.

Further, SRC residue additions in Table 6.1 decrease the Fe_2O_3 and TiO_2 contents of the slag liquid while additions of Palm kernel additions in Table 6.2 also decrease the Fe_2O_3 and TiO_2 content of the slag liquid.

6.4 Viscosity and Sintering

The viscosity calculation is a tool to understand and characterise slag mineral behaviour and it is used as a predicting tool in estimating the ash deposition rate in boilers. According to Gibb et al. (1996), the behaviour of the ash deposits depend on the consolidation by a viscous flow mechanism and the effect of the main fluxing agents on the viscosity of the minerals.

The viscosity of the ashes has thus been calculated on the basis of equation (3.59), which has been chosen between the many available viscosity models since this model provides estimates that are in good agreement with the experimental data in a recent investigation on ash viscosities of co-firing coal with biomass fuels (Degereji et al., 2011). Further, it is relevant to lay special emphasis on the importance of the ash viscosity model. Viscosity is

a complex function of temperature and ash composition (Plaza et al., 2010). Ash deposits can be classified according to their viscosity (log 10 Poise) to be high (>3.8), medium (2.64-3.8) and very low (<2.64) (van Dyk et al., 2009). According to the fluidic state of ash deposit (Couch, 1994), the deposits can be classified as dry deposit, molten with no apparent downward movement, molten and slowly creepy downward, and very liquid and running. The structure of the ash deposits can differ from loose and easy removable through sintered, sintered and lightly melted and completely molten deposits (Hutchings et al., 1996).

The viscosity trend shown in Figure 6.11 at temperatures between 1200 ^{o}C and 1600 ^{o}C follow the different stages of deposit strength when related to the viscosity estimated found in Abbot et al. (1981), van Dyke et al. (2009) and Zhang et al. (2001). At high viscosity, which corresponds to weak, deposit only a small amount of slag is present. As the viscosity decreases with temperature, the mass of the iron increases with increasing slag and iron in the coal ash reaches it peak at temperature 1300 ^{o}C, where the strength of the deposit is assumed to be the strongest. This region corresponds to the region where probe 2 is located in the EFR, as illustrated in Figure 6.12 for Russian coal. Although the mass of CaO decreases at the temperatures increases, the percentage of CaO is fairly high (up 6.5%) in this region. In addition to iron, CaO has been reported to be present in an inner deposit layer in the combustion furnace (Gibb et al., 1996). The slagging behaviour of CaO and FeO in Russian coal (Figure 6.12) shows some level of similarity to that of South African coal (Figure 6.13). This phenomenon has been reported before (Cunningham et al., 1991) and it is

due primarily to the preferential deposition of low melting, dense iron-rich and calcium-rich particles derived from pyrite and calcite, respectively.

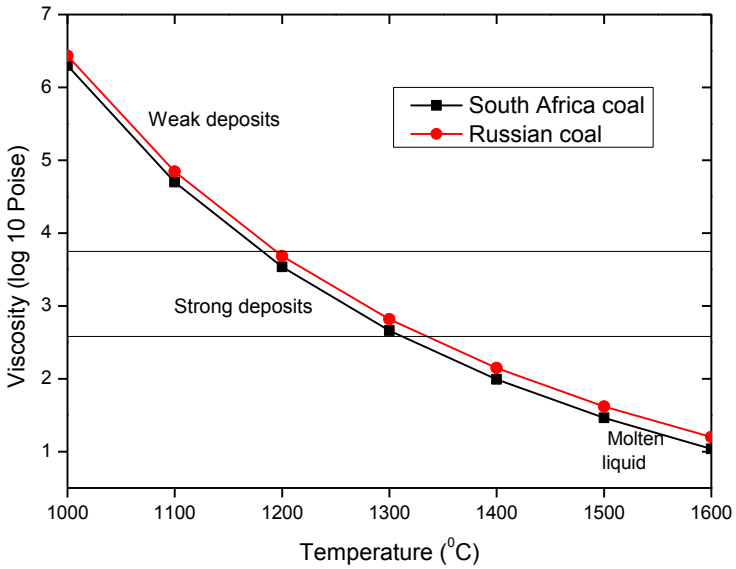

Figure 6.11: The temperature-dependent viscosity for the South Africa and Russian coals as a function of the temperature.

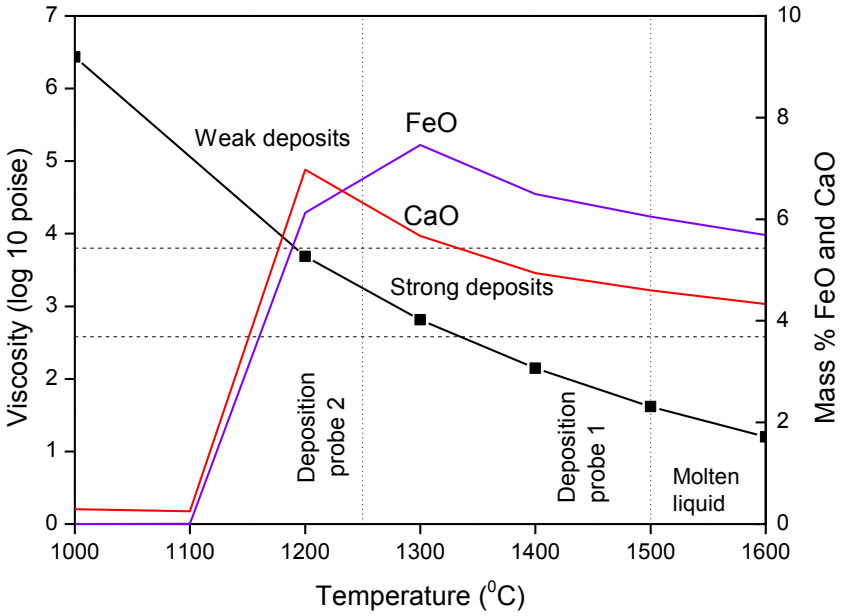

Figure 6.12: The viscosity and composition of the slag liquid for the Russian coal as a function of the temperature.

The concentration of iron and calcium concentration has a direct consequence on the slagging potential. The higher is the concentration of iron and calcium, the lower is the viscosity of the slag and the higher is the extent to which the deposit is sintered, as shown in Figure 6.12 and 6.13.

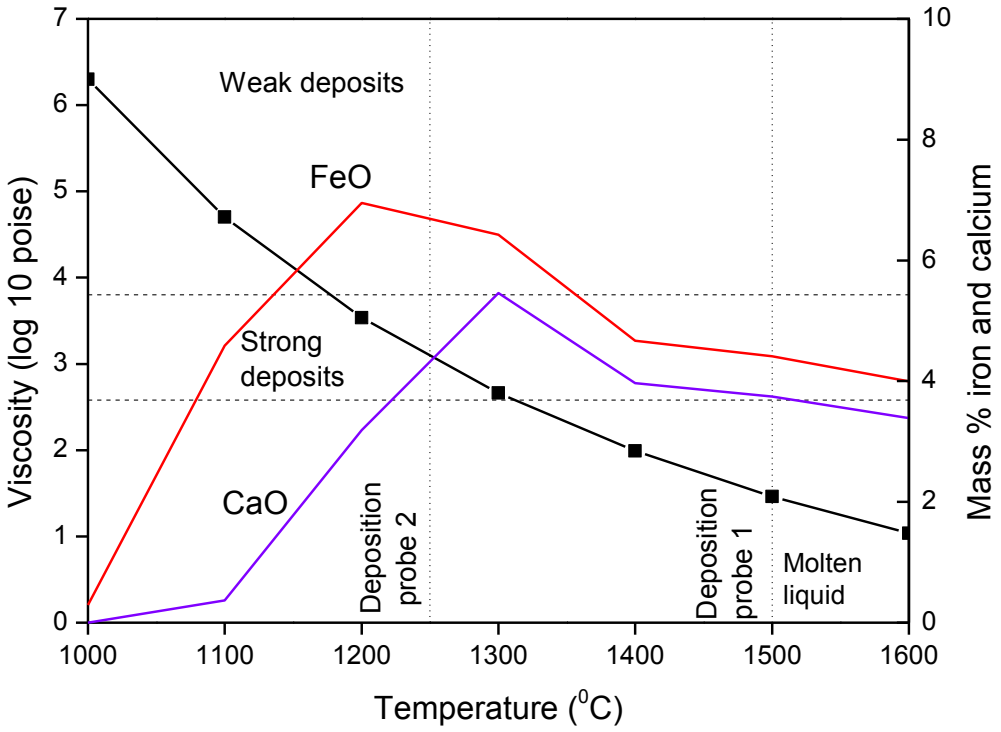

Figure 6.13: The viscosity and composition of the slag liquid for the South Africa coal as a function of the temperature.

6.5 Performance of the Slagging Indices

In this section, the existing slagging indices, namely, AFT, viscosity, B/A and $B/_{A+P}$ have been tested on a single set of two coals and five different biomass materials in order to review and assess the *modi operandi* and the performance of the indices against the reported experimental data.

6.5.1 Ash Fusibility Prediction

The results obtained from of the AFT on the investigated coals and biomass materials are presented in Figures 6.14-6.15 using coal softening temperature (equation 6.8). The coal and biomass with low fusibilities are said to have high slagging potential (McLennan et al., 2000). Figure 6.14 shows that the Russian coal has the highest fusion temperature of about 1375 ^{o}C while South Africa coal has the lowest fusion temperature of about 1280 ^{o}C.

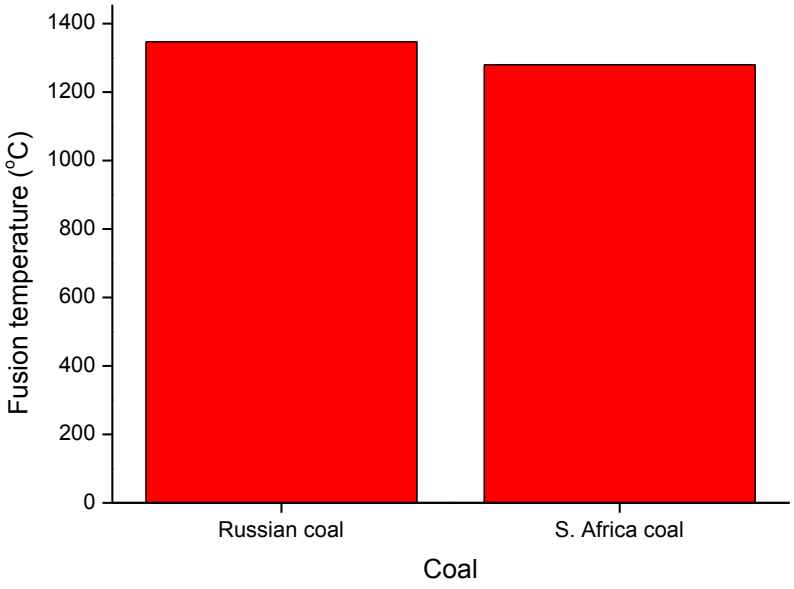

Figure 6.14: The results of the ash fusibility predicted on the Russian and South Africa coals.

Figure 6.15 shows that Palm has the highest fusion temperature of about 1253 ^{o}C, followed by SRC and then sawdust S. Miscanthus has the least value of fusion temperature, about 1024 ^{o}C. Therefore according to the biomass softening temperature (equation 3.61) Miscanthus is expected to have the highest slagging potential, while Palm is expected to have the

lowest slagging potential. It should be noted that low fusibility predicted for Miscanthus may be attributed to its high content of the basic oxides in the ash (Wigley et al., 1990).

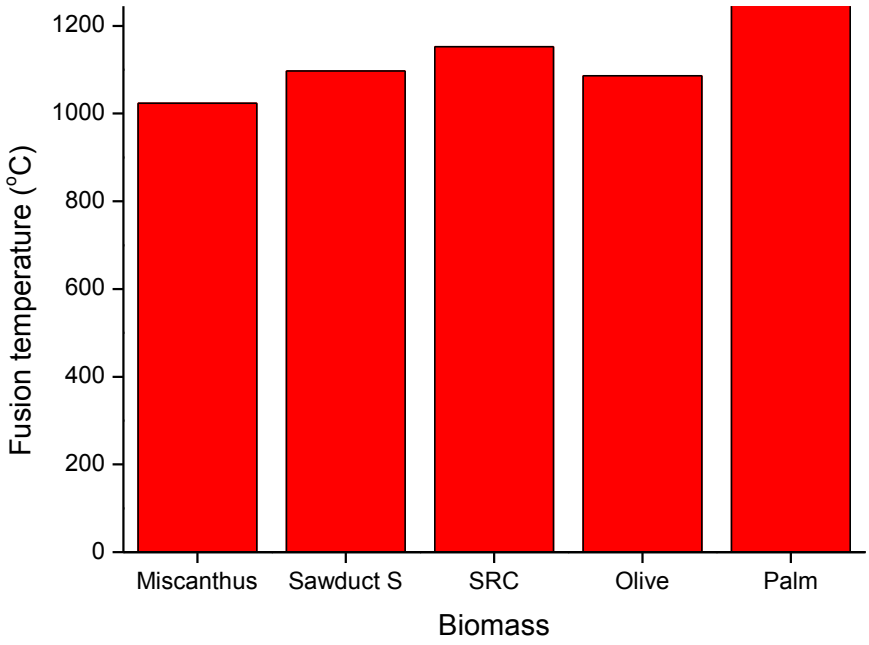

Figure 6.15: The results of the ash fusibility predicted on the Miscanthus, Sawdust S, SRC, Olive residue and Palm.

6.5.2 Slagging Indices Based on the Bulk Ash Chemistry

The performance of the slagging indices that are based on the bulk ash properties, such as the silica ratio (SR), % Fe_2O_3, B/A ratio and B/A_{+P} ratio, have been investigated. Although the indices show similarities in their prediction characteristics, they yield inconsistent results in a some of the cases investigated.

Silica ratio: High silica content in coal increases its fusibility and hence decreases its slagging tendency (Lawrence et al., 2008). The percentage of

silicon oxide in the Russian and South Africa coals, as shown in Figure 6.16, indicates that Russian coal has the highest percentage of silica in the ash (60.1%), while South Africa coal has the lowest percentage of silica in the ash (54.1%). Therefore, according to the silica ratio principles, South Africa coal is expected to have the worst slagging potential and Russian coal to have the least slagging potential.

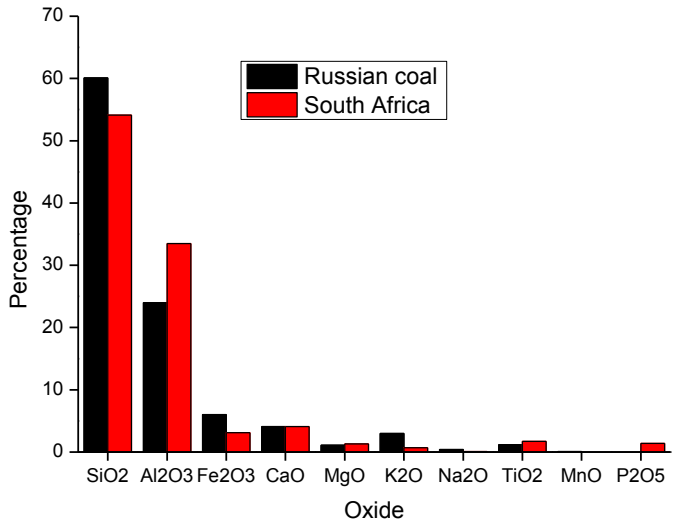

Figure 6.16: The percentage oxides for the Russian and South Africa coals.

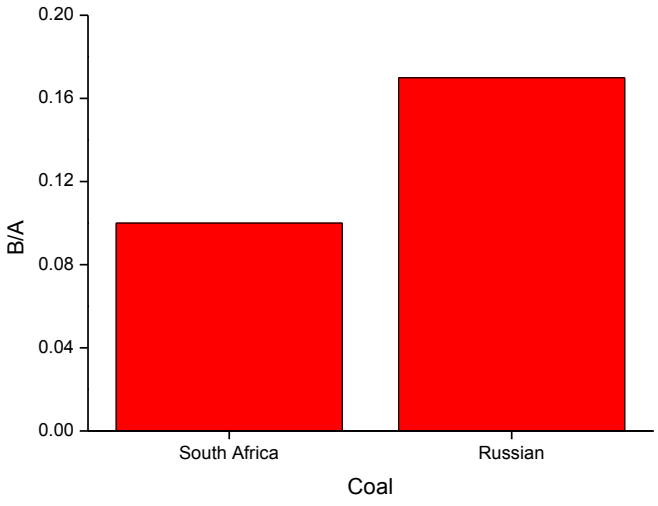

Figure 6.17: The results of the acidic oxide to basic oxide for the South Africa and Russian coals.

Percentage of iron oxide in the ash: Another important parameter in the determination of the ash slagging potential is the percentage of iron oxide available in the ash. Higher iron oxide content usually lowers the slag viscosity (Zhang et al., 2001), and this may result in a high slagging tendency. Coal ash with Fe_2O_3 < 6% in the ash shows a low slagging tendency (Lawrence et al., 2008).

The percentage of iron oxide for South African and Russian coals has been computed and the results are also presented in Figure 6.16. The results shows that Russian coal has the highest Fe_2O_3 (6.0%) content in the ash while South African coal has the lowest Fe_2O_3 (3.1%) content in the ash.

Basic and fluxic to acidic oxide ratio: The ratio basic to acid (B/A), which was introduced originally for the assessment of coal ash is limited and cannot be applied to certain types of biomass materials, especially those with a high phosphorus content in their ash (Kupka et al., 2008). In order to account for the phosphorus content present in some biomass materials, the ratio of the fluxing agent to acidic oxide (B/A_{+P}) has been employed in many recent publications such as Kupka et al. (2008). An increase in B/A and B/A_{+P} lowers its fusion temperature (Wigley et al., 1990). Figure 6.17 shows the ratio B/A for the two bituminous type ashes employed in this investigation. Russian coal has the highest B/A value, while South Africa coal has the lowest B/A value. Therefore it is expected that Russian coal will produce the worst slagging tendency.

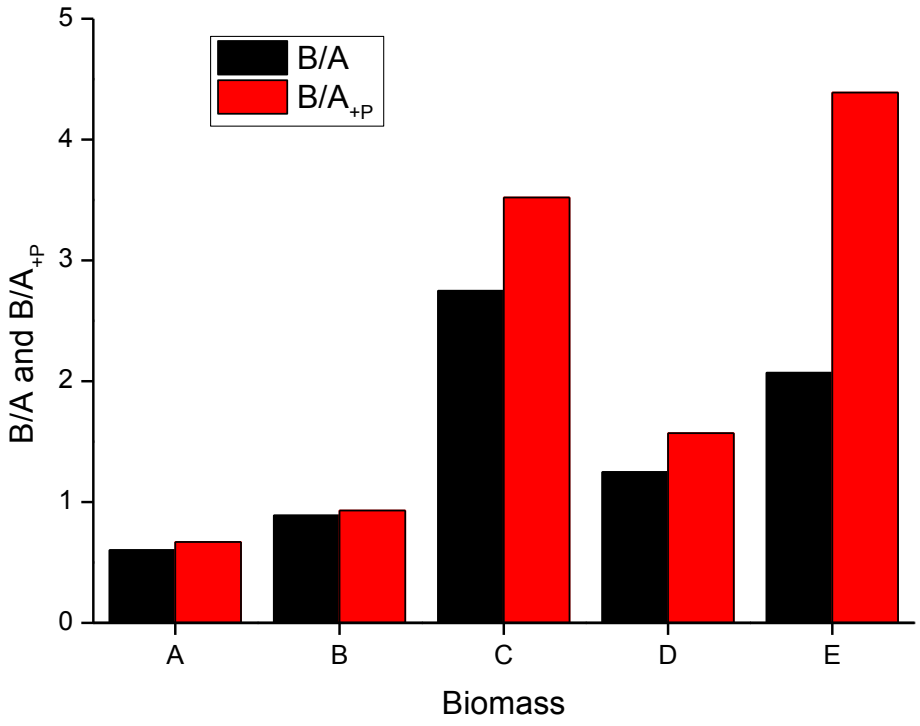

Figure 6.18: The results of the basic and fluxing agent to acidic oxides for Miscanthus (A), Sawdust S (B), SRC (C), Olive residue (D) and Palm (E).

The computed values for the ratio of the B/A oxides for the five biomass materials investigated are shown in Figure 6.18. The results indicate that SRC has the highest B/A value while Palm has the highest B/A_{+P} value. For the B/A ratio, the results indicate that the slagging potential of SRC is expected to be the worst, and this is followed by Palm, Olive, Sawdust and Miscanthus, in decreasing order. In terms of B/A_{+P}, the results indicate that the slagging potential of Palm is expected to be the worst, and then follow by SRC, Olive, Sawdust S and Miscanthus, in decreasing order. When the ratios B/A and B/A_{+P} are compared, the results show some inconsistencies. This suggests that when the slagging indices are based on the bulk ash chemistry then could this give rise to misleading conclusions

because the combustion process is not additive and involves complex transformations.

6.5.3 Sintering Assessment

After characterising the deposit by calculating the deposition efficiency, the deposits were further characterised by the SEM and the extent to which the deposits were sintered was presented in Wigley et al. (2007). The NSI was developed in such a way that all the indicators for the deposit strength and degree of fusion have been combined together. The viscosity is at the root of the deposition problems and consequently it was the first considered by the NSI, equation (6.1). Based on the performance of the NSI in Figure 6.20 and 6.21 (each bar represents the coal-biomass mix) the Miscanthus fuel mix has the highest normalized slagging index and this corresponds to the weakest deposit. The ash property of the Miscanthus is comparable to the coal ash property. For example, the high content of the SiO_2 (>50%) in the solid fuel ash is an attribute well known to coal (Zhang et al., 2001). The SiO_2 possess strong covalent bonds and large amounts of silica in the coal (>50%) and miscanthus (>50%) ash blend (see Table 5.3) may lead to a high viscosity melt and hence a low deposition potential. Al_2O_3 content in miscanthus ash (2.4%) is much lower than Al_2O_3 content Russian coal ash (24.0%) and this may contribute lower deposition potential of miscanthus.

Another indicator for the rate of the deposit sintering, namely NSI has considered, is the melting characteristic of the viscous ash particles. Although the AFT analyses do not indicate exactly at what temperature the first melt / slag occurs, they (AFT and cone deformation) provide an estimate

of the ash melting phase where the fluxing agents can be strongly sticky. While pure compounds of potassium have a melting point of 774^{o}C (KCl) and 1069^{o}C (K_2SO_4) (Cook et al., 1989), pure compounds of the phosphorus melt at 583^{o}C (P_2O_5) (Pronobis et al., 2006). The high content of the phosphorus in palm kernel cake ash (P_2O_5 content >SiO_2 content in the ash) is given in Table 5.3. This indicates the formation of the low melting phase see Figure 6.21, with the coal-palm mix showing the lowest bar in all the co-firing ratios. In addition to the AFT, the effect of the ash chemistry has also been captured by modifying the softening temperature in order to recognize the fluxing/bonding elements to an adequate degree. For dry ash and high melting temperatures, κ_2 in equation (6.10) is low. Generally, as the content of the fluxing agents increase in the fuel mixture, the ash becomes stickier and the ash melting temperature begins to decrease.

The results presented in Figures 6.20-6.21 were obtained after normalization by the corresponding maximum value of the slagging index. Of the two sub-models presented in equations (6.9) to (6.10), sub-model 2, i.e. equation (6.10), produced results that correlate very well with the experimental data. Although the sub-model 1 (equation (6.9)) is able to predict the experimental trend of the degree of sintering up to BR ≤ 40 wt % (Miscanthus<Sawmill<SRC<Olive<Palm), it fails to accurately predict the experimental trend when BR is wt. 60% (Miscanthus<Sawmill<SRC<Palm<Olive). The reason for this failure is because the ratio B/A has been initially introduced for coals with very low phosphorous oxide content, which therefore is not included in equation (6.9). However, for a more accurate prediction of the ash chemistry, the effect of

the phosphor oxide on the ash chemistry has been accounted for in equation (6.10).

The ranking of sintered deposits based on the sub-model 2 is considered more realistic for all levels of biomass addition. This is because the low hemispheric temperature of P_2O_5 significantly increases the melting phase. At low hemispherical temperatures, where the ash stickiness is dependent on the viscosity, the deposition formation and deposit sintering are more efficient. This fact is seen in Figure 6.19 where the palm bar moves from the second highest sintering tendency in Figure 6.19 to the first position in Figure 6.20. This is a consequence of its significantly higher P_2O_5 content (42.7 wt %), which causes a significant deposit sintering and fusion. The order of the sintering tendency predicted by sub-model 2 for the coal/blend is, from highest to lowest, Palm Kernel, Olive, SRC, Sawmill and Miscanthus, i.e. the tests suggest that Palm Kernel ashes are more prone to form a deposit than those from Olive residue.

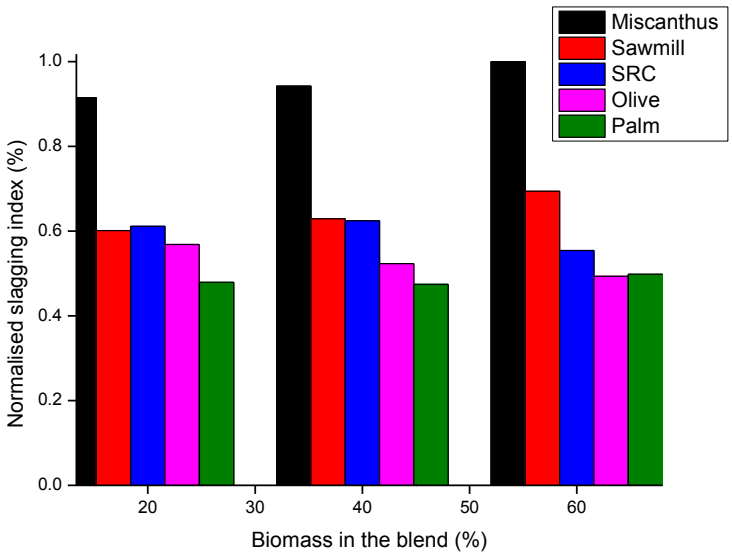

Figure 6.19: Slagging index as a function of the % biomass in the blend considering B/A ratio submodel.

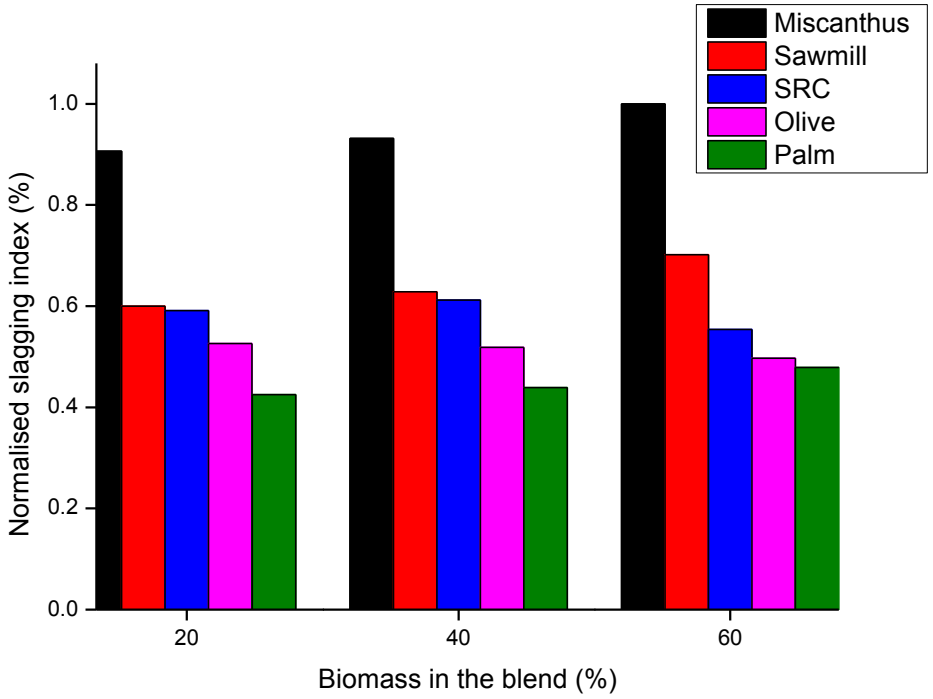

Figure 6.20: Slagging index as a function of the % biomass in the blend considering the ratio B/A_{+P} submodel.

Table 6.3 shows a comparison between the experiment data and the predictions. The degree of the deposit sintering observed in the EFR deposits increase in the order: Miscanthus<Sawmill<SRC<Olive<Palm (see Figure 6.18). The results of the NSI show that the Miscanthus is the least in terms of the slagging, followed by Sawmill, then SRC, followed by Olive and Palm is the highest. This ranking of the NSI agrees with the observations of the EFR deposits, but it does not agree with the slag viscosity index. This is because the model adopted in the calculated viscosity (Kalmanovitch and Frank method (Kalmanovitch et al., 1988)) does not take into account the role of the phosphorus and the prediction may be misleading, especially at higher levels of biomass addition.

Table 6.3: NSI versus the experiment and slag viscosity index.

Sintering behaviour	Ranking of the sintered deposits
Experiment (Wigley et al., 2007)	Miscanthus<Sawmill<SRC<Olive<Palm
Slag viscosity index (Wigley et al., 2007)	Miscanthus<Sawmill<SRC<Palm=Olive
NSI (current work)	Miscanthus<Sawmill<SRC<Olive<Palm

6.6 Conclusions

The results of the NSI are biased towards the higher ash components in the fuel mixture. The results from the equilibrium calculations revealed the presence of a larger quantity of liquid formation in Russian coal compared to South Africa coal due the fact that the composition of Russian coal has more Fe_2O_3 (Fe_2O_3> CaO +MgO) than South African coal (Fe_2O_3<CaO +MgO).

Thermodynamic modelling of the combustion process predicted that the potassium was in the form of potassium oxide when coal is co-fired with biomass.

Experimental data of the degree of sintering were reasonably predicted with the NSI, using both B/A and $B/A_{(+P)}$ sub-models. The ratio B/A predict the experimental trend up to 40 wt %, while $B/A_{(+P)}$ predictes all the experimental trends for all levels of the biomass addition. However, significant differences in sintering with biomass addition has been observed. The differences in the ash chemistry between the parent fuels are responsible.

Chapter 7

General Conclusions and Possible Future Work

In this chapter, the conclusions derived from the research findings are presented. This thesis is considered as a conceptual basis for broader research activities towards the understanding of the ash behaviour for biomass and coal fuels. Therefore, some areas of possible future research work are identified and discussed at the end of this chapter.

7.1 General Conclusions

The increasing demand for energy is apparent in view of the population increase and technological advancements across the globe. The availability of energy in reliable and economical form is considered as a major pre-requisite for national development and it remains a major challenge for energy engineers.

One of the most important ways of generating electricity is the burning of coal to generate the required steam to turn the turbines, and it has been anticipated that coal will remain the major source of energy for electricity generation in the foreseeable future. Coal is one of the most preferred sources of energy due to its high calorific value and the World Coal Institute suggests that coal will fuel about 44% of the world electricity in the year 2030.

However, coal combustion faces a number of challenges; environmental problems, such as CO_2 emissions and operational problems,

such as slagging and fouling. The search for an alternative option to the coal combustion has become imperative.

Utilization of biomass materials in heat and power production has gained substantial interest in recently years and this is primarily due to the demand for reducing the CO_2 emissions originating from fossil fuel consumption. However, biomass contains significant amounts of inorganic species which cause a number of problems. In particular, the presence of potassium can significantly lower the melting temperature of the biomass particles and this increases the tendency of deposition in the combustion system. The deposits on the furnace walls and the superheater tubes can change substantially the heat transfer characteristics of the tube surface and cause damage to the system.

Compared to dedicated biomass plants, the addition of biomass to high efficiency coal-fired power plants can greatly increase the electrical efficiency of utilizing these fuels. In addition, the cost of retrofitting an existing coal-fired power plant to a co-combustion plant can be considerably lower than building a new dedicated biomass plant. Further, co-combustion can be operated in a flexible mode (i.e. with different shares of biomass materials) which can minimize the fluctuating supply of some biomass fuels (such as straw) and secure the constant level of power generation. However, careless co-firing of difficult biomass materials can lead to a reduction in the boiler reliability and availability, and unscheduled plant shut-downs due to excessive slagging or fouling. Additionally, the increased danger of corrosion is often a further consequence of deposits resulting from the slagging and fouling during co-firing of biomass materials.

To overcome the difficulty of the experimental study of the ash deposition processes under combustion conditions, several efforts have been made towards developing acceptable and robust numerical prediction models. Although the problem is still not fully understood, significant advancements have been recorded.

In a high temperature environment, such as a pulverized coal combustor, the behaviour of ash particles is difficult to predict. This is because of the uncertainties caused by the turbulent eddies in the boiler and the changing physical properties of the fuel. Further, in the low temperature environment, the transformation of mineral matter (detailed mechanism) involves many mechanisms, such as condensation (homogeneous and heterogeneous), nucleation, crystallization and agglomeration. Despite several research studies in the field of ash deposition, the ash deposition mechanism is yet to be fully understood.

However, the problems of ash in boilers can be minimized by a careful selection of coal/biomass fuel before combustion. However, most of the existing selection tools (the coal slagging indices) have been established based on coal properties, and more often they yield misleading results, specifically when their use is extended to biomass. Although there are several reports on coal and biomass deposition assessment tools, the research for a generic and more reliable slagging index continues.

In an attempt to contribute towards a better understanding of the boiler slagging problems, CFD techniques are used in the implementation of the ash particles deposition rate model and the numerical slagging index (NSI) that have been proposed in this thesis.

A CFD-based model that simulates the combustion of the biomass-fired grate furnace has been developed and model results for the combustion of a typical straw in a 10 MW_{th} grate-fired furnace have been presented. Also, a CFD-model that simulates the co-combustion of coal with biomass in an EFR has been developed. The effects of five types of biomass have been studied: Miscanthus and short rotation coppice (SRC) are biofuels; Olive residue and Palm kernel expeller cake are by-products of agricultural processing; and Sawmill residue is an industrial by-product. The two coals used, Russian and South African, are typical bituminous UK power station coals with higher and lower slagging potentials, respectively. The two models have been validated using the available experimental data on biomass and biomass/coal co-combustion, and some conclusions are drawn.

To make the description of the combustion system more complete, parallel with the CFD calculations, a set of chemical equilibrium model calculations were performed using the FACTSage computer software. The software incorporates the Chemsage engine for free energy minimization combined with the FACT (Facility for Analysis of Chemical Thermodynamics) database of chemical compounds. The results obtained from the equilibrium calculations were used to explain some of the observations made from the CFD predictions.

7.1.1 Ash Deposition Model for Biomass

The existing models for various phases of solid fuel combustion are used in order to establish the gas phase temperature and velocity field which are necessary for ash deposition studies. The particle trajectories are predicted in a Langrangian reference frame.

Inertial impaction has been considered as the major pathway for the transportation of particles to the boiler walls. The overall sticking tendency of the particle was determined on the basis of its calculated viscosity at impaction on the boiler walls and its tendency to rebound after impaction if it possesses excess energy. Some of the predicted results that have been compared with the measurement data include the following: the flame temperature, the air velocity and most importantly, the ash deposition rates in the superheaters.

The following general conclusions are made based on the investigations performed using the proposed ash particles deposition rates model that is reported in this thesis:

- As a preliminary step, a detailed chemical mechanism for alkali chloride sulphation was identified from the literature. The starting scheme contains 54 species and 220 elementary reactions with elementary rates taken from Hindiyarti et al. (2008).
- Starting with a detailed gas-phase kinetic mechanism for the alkali chemistry, a systematic reduction procedure has been performed using a sensitivity analysis to reduce the reaction mechanism to a level that can be easily implemented into a CFD calculation.

- Examination of the features of the reduced mechanism reveals that the potassium vaporization process is well-predicted by the reduced scheme, where the two full mechanism and reduced mechanism predictions overlap each other. For sulphation process the difference between full mechanism and reduced mechanism were about 2%.
- The agreement between the experimental data and the model results shows that, while the reduced mechanism accurately reproduced the primary features of the detailed mechanism, both mechanisms match the experimental data to up to accuracy of about 5%.
- For the straw-fired grate furnace, the predicted gas temperatures in the region of the three superheaters were compared to measured data. Experimental errors for the temperature measurements are approximately 5%. Therefore, the discrepancies observed in are believed to be reasonably small and satisfactory for the purpose of this investigation.
- To predict the ash deposition, a deposition model has been developed. The model is based on the particle-sticking probability that takes into consideration the size of the ash particles, local vapor, and saturation pressure of the potassium salts, which determine the condensation of the salts on the particle surface.
- The deposition model developed, together with the reduced alkali kinetic mechanism, was implemented into a multi-dimensional CFD model. The integrated model has qualitatively reproduced the key deposit positions as observed experimentally in the large-scale industrial boilers investigated that are firing cotton straw.

- The ash deposition model has not been tested quantitatively due to non-availability of field performance data at the time of this investigation. However, the model prediction on the straw-fired grate furnace shows a good resemblance to the photograph of the deposit formed on the secondary superheater. This indicate that the model is appropriate and has provided the right qualitative predictions which serves as a basis for quantitative validation.
- The performance of the model in the downstream boiler is not guaranteed. This is because at low temperature regions, condensation is considered as a major deposition pathway, and also, ash crystallization may occur, thereby introducing non-homogeneous characteristics in the ash. The effects of these transformations due to the change in temperature gradient are not accounted for in the model.

7.1.2 Ash Deposition Model for Co-firing

The slagging process can be divided into three phases – initial deposit, deposition formation and deposit sintering. This result of this comprehensive study shows how biomass ash affects the strength of deposits or sinter deposits. Sintering occurs by a viscous deformation and the melting of ash particles which is dependent on both the temperature and the composition of the individual ash particles that make up the deposits. Fly ash, and therefore deposits from the co-firing of coal with biomass, are mainly composed of aluminosilicate glass and it is the composition of this glass that determines the viscosity. The aluminosilicate glass is mainly derived from the coal ash, but in blend ash, it may incorporate potassium, calcium and phosphorus

depending on the type of biomass that is being co-fired. These elements are the powerful fluxants for the aluminosilicate system. The concentration and distribution of the fluxing agents in the blend ash determine their degree of assimilation into the glass and, hence, the extent to which the deposit is sintered.

- A computational fluid dynamic (CFD) model to predict the deposition rates in boilers has been developed. This deposition model is based on the combined sticking probabilities of the ash particle viscosity and the melting behaviour of the ash particles.
- The deposition model is suitable for the prediction of the deposition rates of heterogeneous coal/biomass ash slag in a high temperature region.
- For biomass ash, a combination of particle softening temperature and melting fraction has been used to estimate the stickiness of the particle and since both are related to salt material within the biomass particle.
- The thermodynamic equilibrium calculations are used to calculate the amount of the melt fraction considering possible phases of the liquid slag and solid solution. These calculations have been used to provide insight into some of the observations made during the computational fluid dynamics investigations.
- The deposition efficiencies in the EFR were computed for the Russian and South Africa coals with five different biomass materials (Miscanthus, Short Rotation Coppice (SRC), Olive residue, Palm kernel expeller cake and Sawmill residue) using a CFD code. The

trend of the CFD predictions were consistent with the trend of the experimental data.

- The predicted particle temperatures at the burner region and at the exit of the furnace were compared to measured data. Experimental errors for the temperature measurements are approximately 5%.
- The variability in the experimental data obtained for two runs with 100 wt.% coal was not experienced during the CFD model calculation. This is because the CFD calculation has been performed under well-defined and reproducible operating conditions.
- The predicted deposition efficiencies on the deposition probe were compared to measured data. Experimental errors for the temperature measurements are approximately 10%.
- The CFD results were obtained using the EFR that simulate the conditions in the superheater region of a commercial-scale boiler. The CFD results can be extrapolated and therefore it may be easy to form direct conclusions concerning commercial-scale applications.
- In addition to the smaller scale of the EFR, the main obstacle with the EFR is that it is a laminar flow reactor in which the fuel ashes are directed towards the deposition probe and may interact during flight. In a commercial-scale combustor, the situation may be similar only in the pulverized fuel combustors.
- In the EFR, the flue gas temperature was set at 1250 ^{o}C. However, in commercial boilers, the temperature in the combustion zone may be significantly lower, leading to the increased vapourization of alkali compounds.

- The model can identify the type of deposit that is most troublesome. In practice, highly fluid deposits, such as those formed when firing high slagging potential coal (Russian coal), are traditionally thought of as ones to be avoided.
- As a whole, the work carried out in this thesis has provided modelling tools for the ash deposition on heat exchange surfaces.
- The co-firing slagging index has been modified to predict the slagging potential of coal and biomass blends. The softening temperatures, ash composition and the ash content of the individual fuels have been considered in the modelling the co-firing index.
- The proposed co-firing index has been tested on some sets of coal blends with five biomass materials. The results of the prediction, using the co-firing index, correlate very well with the reported experimental data.

7.2 Possible Future Work

In this thesis, two numerical models have been developed: one is to predict the biomass ash particle deposition rates in the freeboard or downstream of the grate furnace, and the other is to predict the deposition rates for the co-firing of coal with biomass in an EFR. The NSI has been modified to predict coal and biomass blends. The successful testing of these models precipitates the need for further investigations along the same lines. Thus, the following investigation can be based on the content of this thesis:

The biomass deposition rate model has not been validated quantitatively because of the lack of measurement data on the industrial

grate furnace. Therefore, there is the need to run the ash deposition model when measurement data is available. Further work should consider the installation of a well-controlled ash deposition probe to obtain the actual deposition flux and to verify the model quantitatively.

The deposition rate model for co-firing of coal with biomass has been tested on a pilot-scale furnace because there was no experimental deposition data on industrial scale boilers that was readily available at the time of this investigation. Therefore, there is a need to run the ash deposition model when full 3D industrial scale boiler data is available.

The use of the ash deposition model can be extended to account for a wide variety of biomass materials. For example, biomass rich in phosphorus content are said to have significant effects on the ash deposition. The stickiness of the ash particles can also be determined based on the softening temperature of the biomass ash particles. In the case where the biomass particle is not completely burnt, the melt fraction of the particle can be used in order to determine its stickiness.

The deposition model is limited to only SRC, Olive and Miscanthus that are fairly rich in alkali contents. However, Palm is not modelled because of the high content of phosphorus. To calculate the deposition rate for the co-firing of coal with palm, the melting curve of phosphorus-rich biomass is required. The relatively large size of biomass pellets is another issue of concern. Owing to its large size, the biomass particles may possess adequate inertial forces to transverse the boundary layer and impact on the boiler walls, and this may result in an increased slagging potential.

A recent investigation (Khodier et al., 2012) in a pilot-scale pulverized fuel combustion rig shows that the amount of the deposit formed on the top and side surfaces (upstream and side surfaces in the gas path) decreases with increases in the level of biomass co-firing. However, the amount of the deposits formed on the underside of the probes (downstream surface in the gas path) increases with increasing levels of biomass co-firing. The results of the equilibrium calculation shows that the amount of slag liquid decreases with increases in the level of biomass co-firing and this is in line with the deposit formed on the top and side surfaces when compared with the Khodier et al. (2012) investigation. However, the deposit formed on the underside of the probes is a relatively new phenomenon. Further work on the CFD approach should focus on the deposit probe to investigate the side-stream and down-stream surfaces of the probes in more detail.

The modified NSI has been tested on Russian and South Africa coals. While the NSI predicted the degree of sintering for co-firing of Russian coal with biomass materials, it did not predict the correct order of sintering for South Africa coal. This suggests that, with more investigations on the biomass ash behaviour and the coal biomass interaction, the features of the NSI can be extended to predict the slagging potential of different coals and biomass. Further work on the CFD approach should focus on phosphorus rich fuels to investigate the effect of fluxant in more detail.

Also it is be of interest to assess the deposit thickness, density and strength in order to develop a comprehensive ash deposition model. It may be worthwhile to change the EFR operating conditions, such as lowering the

probe surface temperature and increasing the flue gas temperature (more alkali vapourization).

For a straw-fired grate furnace, it could be useful to study how the sulphation mechanism lowers the deposition rate in this mixture type. In the study of biomass combustion whose particles are non-spherical, the calculation is needed for the drag forces instead of using a shape factor to modify of the drag law as used for spherical particles. Further, some experimental work could be carried out so that there are some more data available for comparison.

Mineral matter in the fuel particles undergoes complex chemical and physical transformation towards the deposit surface. As a result, the chemical composition and the physical properties of the ash particles have a big influence on the sticking probability as well as the thermal behaviour of the deposit layer. Future work should address mechanistic models to predict these processes.

The formation and coagulation of aerosols near to the superheater with a high temperature gradient has a pronounced effect on the local deposition rates as well as the chemical composition of the deposit. To improve the predicted deposit accumulation rates, this mechanism is suggested to be dealt with in further work.

In case where deposit build-up occurs quickly, the temperature increase on the deposit surface will be relatively high. Furthermore, various layers will be formed with a large difference in the thermal and physical properties. Therefore a model taking into account the effect of the different layers on the heat transfer process should be developed.

In order to validate the prediction model more comprehensively, exploiting the available data bases on full and pilot scale experiments should also be a major issue of future work. More detailed experimental data are required in terms of the temperature increase and the temperature distribution on the deposit surface.

List of References

Abbas, T., Costen, P. G. & Lockwood, F. C. (1996). Solid fuel utilization: from coal to biomass. *Proc. Combustion Inst.*, 26, 3041–3058.

Abbot, M. F., Moza, A. K. & Austin, L. G. (1981). Studies on slag deposit formation in pulverized coal combustors. Result on the wetting and adherence of synthetic coal ash drops on different steel substrates. *Fuel,* 60, 1065-1072.

Akbar, S., Schnell, U. & Scheffknecht, G. (2010). Modelling potassium release and the effect of potassium chloride on deposition mechanisms for coal and biomass-fired boilers. *Combustion Theory & Modelling,* 14(3), 315-329.

Backman, R., Hupa, M., Skrifvars, B-J. (1997). Predicting superheater deposit formation in boilers burning biomass. *Proceeding of the conference on impact of mineral impurities in solid fuel combustion, Hawaii,* 405-416.

Backreedy, R. I., Fletcher, L. M., Jones, J. M., Ma L., Pourkashanian, M. & Williams, A. (2005) Cofiring pulverized coal and biomass: a modelling approach. *Proc Combust Inst*, 30, 2955–64.

Bale, C. W., Chartrand, P., Degterov, S. A., Ericksson, G., Hack, K., Mahfoud, R. B., Melancon, J., Pelton, A. D. & Peterson, S. (2002). FactSage thermochemical software and databases, *Calphad*, 26, 189-228.

Barroso, J., Ballester, J., Ferrer, L.M. & Jiménez, S. (2006a). Study of coal

ash deposition in an entrained flow reactor: Influence of coal type, blend composition and operating conditions. *Fuel Processing Technology,* 87, 737–752.

Barroso, J., Ballester, J., Ferrer, L. M. & Jiménez, S. (2006b). Study of coal ash deposition in an entrained flow reactor: Influence of coal type, blend composition and operating conditions. *Fuel Process Technol,* 87, 737–752.

Baxter, L. L. (1993). Ash deposition during biomass and coal combustion: a mechanistic approach. *Biomass and Bioenergy,* 2, 85-102.

Baxter, L. L. & DeSollar, R. W. (1993). A mechanistic description of ash deposition during pulverized coal combustion: opportunity for affordable renewable energy, *Fuel,* 84, 1295-1303.

Benson, S. A., Steadman, E.N., Zygerlicke, C. J. & Erickson, T. A. (1996). Ash formation, deposition, corrosion and erosion in conventional boilers, Application of advance technology to ash related problems in boilers, Edited by Baxter L.L and DeSollar R. W., *Kluwer Academic*, Prenum Press, New York,1-15.

Boonsongsup, L., Iisa, K. & Frederick, W. J. (1997). Kinetics of the Sulfation of NaCl at Combustion Conditions. *Industrial and Engineering Chemistry Research, 36,* 4212-4216.

Bryers, R. W. (1996). Fireside slagging, fouling, and high-temperature corrosion of heat-transfer surface due to impurities in steam-raising fuels. *Progress in Energy & Combustion Science*, 22(1), 29-120.

Burcat, A. (1984). Thermochemical data for combustion calculations. *In* W.C. Gardiner (ed.) *Combustion Chemistry,* Springer-Verlag, New York, 455-504.

BP, (2012). Statistical review of world energy. BP p.l.c. 1st St Jame's Square, London, SW1Y 4PD, 3-12.

Christensen, K. A., Stenholm, M. & Livbjerg, H. (1998). The formation of submicron aerosol particles, HCl and SO_2 in straw-fired boilers, *Journal of Aerosol Science*, 29(4), 421-444.

Christensen, K. A. & Livbjerg, H. (2000). A plug flow model for chemical reactions and aerosol nucleation and growth in an alkali-containing flue gas. *Aerosol Science and Technology*, 33, 470-89.

Cunningham, A. T. S., Gibb, W. H., Jones, A. R., Wigley, F. & Williamson, J. (1991). The effect of mineral doping of a coal on ash deposition behaviour. *Proceedings of the Engineering Foundation Conference on Inorganic Transformations and Ash Deposition during Combustion*. Palm Coast, Florida, 10-15,.

Davidsson, K. O., Korsgren, J. G., Pettersson, J. B. C. & Jaglid, U. (2002). The effects of fuel washing techniques on alkali release from biomass. *Fuel,* 81, 137-142.

Dayton, D. C. & Milne, T. A. (1996). Laboratory measurements of alkali metal containing vapors released during biomass combustion, *Applications of Advanced Technology to Ash-Related Problems in Boilers: New York: Plenum Press*, 161-179.

Degereji, M. U., Ingham, D. B., Ma, L., Pourkashanian, M. & Williams, A. (2011). Prediction of ash slagging propensity in a pulverized coal combustion furnace, *Fuel*, 101, 171-8.

Degereji, M. U., Ingham, D. B., Ma, L., Pourkashanian, M. & Williams, A. (2012). Numerical assessment of coals/blends slagging potential in pulverized coal boilers. *Fuel*, 102, 345-53.

Degereji, M. U. (2011). Predictive modelling of ash particle deposition in a pf Combustion furnace, *Ph.D. Thesis*, University of Leeds.

Demirbas, A. (2000). Biomass resources for energy and chemical industry. *Energy Edu Sci Technol*, 5, 21-45.

Dhumai, S. S. & Saha, R. K. (2007). A one dimensional model of pulverized coal combustion in a cylindrical furnace and its experimental validation. *Journal of Energy and Environment*, 6, 72-86.

Eghlimi, A., Lu, L., Sahawalla, V. & Harris, D. (1999). Computational modelling of char combustion based on the structure of char particles, 2nd International Conference on CFD in the Mineral and Processing Industries, CSIRO, Melbourne, 781-993..

EC, (2011). A roadmap for moving to a competitive low carbon economy in 2050, Brussels, 5-12.

Favre, A. (1965). Equations de gas turbulent compressibles. *Journal de Mécanique*, 4, 361-421.

Field, M. A. (1969). Rate of combustion of size-graded fraction of char from a low rank coal between 1200K-2000K. *Combustion & Flame*, 13, 237-252.

Frenke, J. (1945). Viscous flow of crystalline bodies under the action of surface tension. Journal of Physics, 9(5), 385-390.

Ferna´ndez Llorentea, M. J. & Carrasco Garcı, J. E. (2005). Comparing methods for predicting the sintering of biomass ash in combustion. *Fuel*, 84 1893–1900.

Flagan, R. C. (1978). Submicron particles from coal combustion, *Proceeding of Combustion Institute*, 17, 97-104.

FE, (2006). FLUENT User's Guide (Version 6.3), Fluent Europe Limited, Sheffield, England, 1-300.

Frandsen, F, Dam-Johansen K, Rasmussen, P. (1994). *Prog Energy Combust Sci*, 20, 115–38.

Forstner, M., Hofmeister, M., Joller, J., Dahl, M., Braun, S., Kleditzsch, R. & Scharler, Oberberger, I. (2006). CFD simulation of ash deposit formation in fixed bed biomass furnaces and boilers, *Progress in Computational Fluid Dynamics*, 6(4/5), 248-261.

Garba, M.U., Ingham, D.B., Ma L., Porter, R. T. J. , Pourkashnian, M, Tan, H. Z., Williams, A. (2012). Prediction of potassium chloride sulfation and its effect on deposition in biomass-fired boilers. *Energy & Fuels* , 26(11):6501-8.

Gibb, W. H., Jones, A. R. & Wigley, F. (1993). The UK collaborative research Programme on slagging in pulverized coal-fired furnaces. Results of full-scale plant trials. *Proceedings of the Engineering Foundation Conference Palm Coast, Florida,* 3-18.

Glarborg, P. & Marshall, P. (2005). Mechanism and modelling of the formation of gaseous alkali sulphates. *Combustion & Flame*, 141, 22-39.

Gibson, J. R. & Livington, W. R (1991). Sintering and fusion of bituminous coal ashes, In: Inorganic transformation and ash deposition during combustion, *Proceedings of the Engineering Foundation Conference Palm Coast, Florida,* 425-447.

Griffiths, J. F. & Barnard, J. A. (1995). *Flame & Combustion, Third Edition.* Blackie Academic and Professional, London, 123-145.

Gupta, S. K., Gupta, R. P., Bryant, G. W. & Wall, T.F. (1998).The effect of potassium on the fusibility of coal ashes with high silica and alumina levels. *Fuel,* 77, 1195-1201.

Heinzel, T., Siegle, V., Spliethoff, H. & Hein, K. R. G. (1998). Investigation of slagging in pulverized fuel co-combustion of biomass and coal at pilot-scale test facility, *Fuel Processing Technology*, 54, 109-125.

Hindiyarti, L., Frandsen, F., Livbjerg, H. & Glarborg, P. (2008). An exploratory study of alkali sulfate aerosol formation during biomass combustion. *Fuel*, 87, 1591–1600.

Honea, F. I. (1983). Studies of ash fouling potential and deposit in the GFETC pilot test furnace, *Proceedings of the 1981 Engineering Foundation Conference on Fouling & Slagging Resulting From Impurities in Combustion Gases*', R. W. Bryers (ed.). 117-141.

Huang, L. Y., Norman, J. S., Pourkashanian, M. & Williams, A. (1996). Prediction of ash deposition on superheater tubes from pulverized coal combustion, *Fuel*, 75(3), 271-279.

Huang, L. Y., Norman, J. S., Pourkashanian, M. & Williams, A. (1996). Prediction of ash deposition on superheater tubes from pulverized coal combustion, *Fuel*, 75(3), 271-279.

Hurely, J. P., Erickson, T.A., Benson, S.A. & Brobjorg, J.N. (1991). Ash deposition at low temperatures in boilers firing western U.S. coals. *Presented at the International Joint Power Generation Conference, San Diego, CA, 245-467.*

Hutchings, I. S., West, S. S. & Williamson, J. (1996). An assessment of coal ash slagging propensity using an entrained flow reactor, in: L.L. Baxter, R. DeSollar (Eds.), *Applications of Advanced Technology to Ash-related Problems in Boilers, Plenum,* NewYork, 201–222.

Iisa, K. & Lu, Y. (1999). Sulfation of potassium chloride at combustion conditions, *Energy & Fuels*, 13, 84-90.

IPCC, (2012). Global warming report. *35th Plenary Section, Geneva, Switzerland,* 2-19.

Jenkins, B. M., Baxter, L. L., Miles Jr., T. R. & Miles, T. R. (1998). Combustion properties of biomass, *Fuel Processing Technology,* 54, 17–46.

Jensen, J. R., Nielsen, L. B., Schultz-Møller, C., Wedel, S. & Livbjerg, H. (2000). *Aerosol Science & Technology*, 33, 490–509.

Jiménez, S. & Ballester, J. (2007). Formation of alkali sulphate aerosols in biomass combustion. *Fuel*, 86, 486-493.

Junfeng, L. (1997). Renewable Energy Development in China: Resource Assessment, Technology Status, and Greenhouse Gas Mitigation Potential *Applied Energy*, 56, 3/4, 381-394.

Jungt, B. & Schobert, H. H. (1991). Viscous sintering of coal Ashes. 1. relationships of point and sinter strength to particle size and composition sinter, *Energy & Fuels,* 5, 555-561.

Kassman, H., Bäfver, L. & Åmand, L.E. (2010).The importance of SO_2 and SO_3 for sulphation of gaseous KCl – An experimental investigation in a biomass fired CFB boiler, *Combustion & Flame*, 157, 1649-1657.

Kaer, S. K. (2004). Numerical investigation of deposit formation in straw-fired boilers. *Fuel*, 83, 1183-1190.

Kaer, S. K. (2001). The impact of deposits on heat transfer during biomass combustion. *Proceedings of the first biennial meeting of the Scandinavian-Nordic Section of Combustion Institute*, Gothernburg, Sweden, 91-96.

Kalmanovitch, D. P., Frank, M. (1988). An effective model of viscosity for Ash deposition phenomena. In: *Engineering foundation conference on mineral matter and Ash deposition from Coal. Santa Barbara,* CA: United Engineering Trustees Inc.; 301-391.

Khodier, A.H.M., Hussain,T., Simms, N. J., Oakey, J. E. & Kilgallon, P.J. (2012). Deposit formation and emissions from co-firing miscanthus with Daw Mill coal: pilot plant experiments, *Fuel,* 101, 53–61.

Kupka, T., Mancini M., Irmer M., & Weber, R. (2008). Investigation of ash deposit formation during co-firing of coal with sewage sludge, saw-dust and refuse derived fuel, *Fuel*, 87, 2824-2837.

Lee, F.C.C, & Lockwood, F.C. (1999). Modelling ash deposition in pulverized coal-fired applications. *Progress in Energy & Combustion Science*, 25, 117-132.

Lignola , P.G. & Reverchon, E. (1987). Cool flames. *Progress in Energy & Combustion Science,* 13, 75-96.

Lokare, S. S., Dunaway, J. D., Moulton, D., Rogers, D., Tree, D. R., & Baxter, L. L. (2006). Investigation of ash deposition rates for a suite of biomass fuels and fuel blends. *Energy & Fuels,* 20(3), 1008-1014.

Hansen, L. A., Nielsen, H. P., Frandsen, Flemming J., Dam-Johansen, K., Hørlyck, S. & Karlsson, A. (2000). Influence of deposit formation on corrosion at a straw-fired boiler. *Fuel Processing Technology*, 64, 189–209.

Ma, L., Pourkashanian, M., Williams, A. & Jones, J. M. (2006). A numerical model for predicting biomass particle deposition in a PF furnace. *Proceeding of ASME Turbo Expo, Barcelona, GT2006-90356,* 333-342

Magnussen, B. F. & Hjertager, B. H. (1979). On mathematical modelling of turbulent combustion with special emphasis on soot formation and

combustion. *In Proceedings from the 16th International Combustion Symposium*, 719-729.

Ma, L., Gharebaghi, M., Porter, R., Pourkashanian, M., Jones, J. M. & Williams, A. (2009). Modelling methods for co-fired fuel furnaces, *Fuel,* 88, 2448-54.

Mao, T., David, C., Kuhn, S. & Tran, H. (1997). Spread and rebound of liquid droplets upon impact on flat surfaces. *AIChE Journal*, 43(9), 2169-2179.

Michal, P. G., Khan, N. A., Jong, W., Spliethoff, H., Schurmann, H. & Monkhouse, P. (2005). Alkali metals in circulating fluidized bed combustion of biomass and coal: measurements and chemical equilibrium analysis, *Energy & Fuels, 19,* 1889-1897.

Miessen, G., Behrendt, F., Deutschmann, O., & Warnatz, J. (2001). Numerical studies of the heterogeneous combustion of char using detailed chemistry. *Chemosphere*, 42, 609-613.

McLennen, A. R., Bryant, G.W., Bailey, C.W., Stanmore, B. R. & Wall, T. F. (2000). Index for iron-based slagging for pulverized coal firing in oxidizing and reducing conditions. *Energy & Fuels,* 14, 349–54.

Manton, N. J., Williamson, J., Riley, G. S. (1997). Changes in slagging behaviour with composition for blended coals. Paper Presented to Engineering Foundation Conference on “Impact of mineral impurities in solid fuel combustion”, Hawaii, 297-303.

McBride, B.J., S. Gordon, & Reno, M. A.. (1993). Coeffiecients for calculating thermodynamic and transprt properties of individual species. *Technical Report* TM-4513, NASA.

Morsi, S. A., Alexander, A. J. (1972). An investigation of particle trajectories in two-phase flow systems. *J Fluid Mech,* 55(2), 193–208.

Moza, A. K. & Austin, L. G. (1981). Studies on slag deposit formation in pulverized coal combustors. 1. Result on the wetting and adherence of synthetic coal ash drops on steel, *Fuel*, 60, 1057-1064.

Molcan, P., Lu, G., Bris, T. L., Yan, Y., Taupin, B. & Caillat, S. (2009). Characterization of biomass and coal co-firing on a 3 MWth combustion test facility using flame imaging and gas/ash sampling techniques, *Fuel*, 88, 2328-2334.

Mueller, C., Selenius, M., Theis, M., Skrifvars, B. J., Backman, R., Hupa, M. & Tran, H. (2005). Deposition behaviour of molten alkali-rich fly ashes-development of a sub model for CFD applications. *Proceedings of the Combustion Institute*, 30, 2991-2998.

Munir, S., Nimmo, W. & Gibbs, B. M. (2010a). Co-combustion of agricultural residues with coal: turning waste into energy, *Energy & Fuel*, 24, 2146- 2153.

Munir, S., Nimmo, W. & Gibbs, B. M. (2010b). Potential slagging and fouling problems associated with biomass-coal blends in coal-fired boilers, *Journal of the Pakistan Institute of Chemical Engineers*, 13, 38-43.

Murphy, J. J., & Shaddix, C. R. (2002). Combustion kinetics of coal chars in oxygen–enriched environments. *Combustion & Flame*, 144, 710-729.

Naganuma, H., Ikeda, N., Kawai, T., Takuma, T., Ito, T., Igarashi, Y., Yoshilie, R. & Naruse, I. (2009). Control of ash deposition in pulverized coal-fired boiler. *Proceedings of the Combustion Institute, 32, 2709-2716.*

Niu,Y., Tan, H., Ma, L., Pourkashanian, M., Liu, Z., Liu, Y., Wang, X., Liu, H., Liu & Xu, T. (2010a). Slagging Characteristics on the Superheaters of a 12 MW Biomass-Fired Boiler. *Energy & Fuel,* 24, 5222-5227.

Niu, Y., Tan, H., Wang, X., Liu, Z., Liu, Y. & Xu, T. (2010b). Study on deposits on the surface, upstream, and downstream of bag filters in a 12MW biomass-fired boiler, *Energy & Fuels*, 24, 2127–2132 : DOI:10.1021/ef901491a

Nowok, J. W., Hurley, J. P. & Benson, S. A. (1998). The role of physical factors in mass transport during sintering of coal ashes and deposit deformation near the temperature of glass transformation. *Fuel Processing Technology*, 56, 89–101.

Obernberger, I, Brunner, T. & Joller, M. (2001). Characterisation and formation of aerosols and fly ashes from fixed-bed biomass combustion. *Aerosols from Biomass Combustion*, Zurich, 1-13.

Oh, M .S., Brookerb, D.D., de Pazb, E.F., Bradyb, J.J. & Deckerb, T.R. (1995). Effect of crystalline phase formation on coal slag viscosity, *Fuel Processing Technology*, 44, 191-199.

Palz, W., Coombs, J. & Hall, D. O. (1985). Energy from biomass: 3rd E.C. Conference Taylor & Francis Group Venice, Italy. 369-375

Phyllis, (2004). Database, Energy Research Centre of the Neitherlands, http://www.ecn.nl/phyllis .

Plaza, P., Griffiths, A. J., Syred, N., & Rees-Gralton, T. (2009). Use of a predictive model for the impact of co-firing coal/biomass blends on slagging and fouling propensity. *Energy & Fuels*, 23, 3437-3445.

Plaza, P., Ferens, W., Griffiths, A. J., Syred, N. & Rybak, W. (2010). Predicting slagging/fouling propensities of solid fuels with the aid of experimental and modelling techniques, Archivum Combustionis, 30, 203-213.

Pohl, J. H. & Juniper, L. A. (1996). Slagging: Problem definition, Applications of advance technology to ash related problems in boilers, Edited by Baxter, L. L. and DeSollar, R.W. *Kluwer Academic, Prenum Press*, New York, 567-577.

Pronobis, M. (2006). The influence of biomass co-combustion on boiler fouling and efficiency. *Fuel*, 85, 474–80.

Quaak, P., Knoef, H., Stassen, H. E. (1999). Energy from Biomass: Review of Combustion and Gasification Technologies. World Bank Technical Paper. *Energy Series*, 22, 10-14.

Quon, D. H. H., Wang, S. S. B., Chen, T. T. J. (1985). Viscosity tests of slags from pulverized western Canadian coals in a pilot scale research boiler. *Fuel*, 63, 939-942.

Raask, E. (1979). Sintering characteristics of coal ashes by simultaneous dilatometry-electrical conductance measurements. *Journal of Thermal Analysis*, 16, 91-102.

Ragland, K. W, Aerts, D. J & Baker, A. J. (1991). Properties of wood for combustion analysis. *Bioresource Technol,* 37, 161–8.

Raj, R. & Lange, F.F. (1981). Crystallization of small quantities of glass or a liquid. segregated in grain boundaries, *Acta Metall*, 29, 1993–2000.

Reid, W. T. (1984). The relation of mineral composition of slagging, fouling and erosion during and after combustion. *Progress in Energy & Combustion Science,* 10, 159-175.

Rushdi, A., Gupta, R., Sharma, A. & Holcombe, D. (2005). Mechanistic prediction of ash deposition of ash description in a pilot-scale test facility. *Fuel*, 84, 1246-1258.

Shao, Y., Xu, C., Zhu, J., Preto, F., Wang, J., Tourigny, G. Badour, C. & Li, H. (2010). Ash deposition during co-firing biomass and coal in a fluidized-bed combustor, *Energy & Fuels*, 24, 4681-4688.

Senior, C. L. & Srinivasachar, S. (1995). Viscosity of ash particles in combustion systems for prediction of particle sticking. *Energy & Fuels,* 9, 277-283.

Sheng, C. D. & Azevedo, J. L. T. (2003). Modeling biomass devolatilization using the chemical percolation devolatilization model for the main components. *Proceedings of the Combustion Institute*, *29*, 407-414.

Sheng, C., Moghataderi, B., Gupta, R., & Wall, T. F. (2004). A CFD based study of combustion characteristics of coal blends in pulverized coal-fired furnace. *Fuel*, 83, 1543-1552.

Shin, D. & Choi, S. (2000). The combustion of simulated waste particles in a fixed bed. *Combust Flame*, 121, 167-80.

Smith, I. W. (1982). The combustion rates of coal chars: a review. *19th Symposium (Int.) on Combustion/the Combustion Institute*, 1045-1065.

Srinivasachar, S., Helble J. J. & Boni, A. A. (1990). An experimental study of the inertial deposition of ash under coal combustion conditions, *Proceeding of Combustion Institute,* 23, 1305-1312.

Stephen, N. (2000). Predicting the rapid devolatilization of diverse forms of biomass with bio-FLASHCHAIN. Proceedings of the Combustion Institute, *Niksa Energy Associates, 1745 Terrace Drive Belmont, CA 94002, USA,* 28, 2727–2733.

Stringer, J. (1995). Practical experience with wastage at elevated temperatures in coal combustion systems, *Wear,* 186-187, 11-27.

Tillman, D., Conn, R. & Duong, D. (2009). Coal characteristics and biomass firing in pulverized coal boilers. *Coal Gen,* Charlotte, North Carolina, USA, 346-897.

Tomeczek, J., Palugniok, H. & Ochman, J. (2004). Modelling of deposits formation on heating tubes in pulverized coal boilers, *Fuel*, 83, 213–221.

Tomeczek, J. & Wacławiak, K. (2009). Two-dimensional modelling of deposits formation on platen superheaters in pulverized coal boilers, *Fuel,* 88, 1466–1471.

Turányi, T., Bérces, T. & Vajda, S. (1989). Reaction rate analysis of complex kinetics systems. *International Journal of Chemical Kinetics,* 21, 83-99.

Turnbull, J, (1993). Strategies for achieving a sustainable, clean, and cost-effective. *Biomass & Bioenergy*, 10, 2, 93-100

Turns, S. R. (2006). An Introduction to Combustion. Singapore: McGraw-Hill, 2nd ed., 352-466

van Dyk, J.C., Waanders, F.B., Benson, S.A. Laumb, M.L. & Hack, K. (2009). Viscosity predictions of the slag composition of gasified coal, utilizing FactSage equilibrium modelling, *Fuel,* 88, 67–74.

Vamvuka, D., & Zografos, D. (2004). Predicting the behaviour of ash from agricultural wastes during combustion, *Fuel*, 83, 2051–2057.

Van Lith, S.C., Alonso-Ramírez, V., Jensen, P.A., Frandsen, F.J., Glarborg, P. (2006). *Energy & Fuels,* 20, 964–978.

Versteeg, H. G. & Malalasekera, W. (2007). An introduction to Computational Fluid Dynamics, Essex: Pearson Educational Limited, 2nd ed., 343-416

Vassilev, S. V., Baxter, D., Anderson, L. K. & Vasseleva, C. G. (2010). An overview of the chemical composition of biomass. *Fuel*, 89, 913-933.

Vargas S., Frandsen F. J., Dam-Johansen K. (2001). Rheological properties of high–temperature melts of coal ashes and other silicates. *Progress in Energy & Combustion Science*, 27, 237–429.

Vuthaluru, R. & Vuthaluru, H. B. (2006). Modelling of a wall fired furnace for different operating conditions using FLUENT. *Fuel Processing Technology*, 87(7), 633–9.

Wall, T. F., Lowe, A., Wibberley, L. J. & Steward, C.I. (1979). Mineral matter in coal in coal and the thermal performance of large boilers, *Progress in Energy & Combustion Science*, 5,1-29.

Walsh, P. M., Sarofim, A.F. & Beer, J. M. (1992). Fouling of convective heat exchangers by lignitic coal ash, *Energy & Fuels,* 6, 709-715.

Walsh, P. M., A. N., Sayre, D. O., Loehden, M. L. S., Beer, J. M. & A. F. (1990). Sarofim. Deposition of bituminous coal ash on an isolated heat exchanger tube: effects of coal properties on deposit growth. *Progress in Energy & Combustion Science*, 16, 327-46.

Watt, J. D., Fereday, F. (1969). The flow properties of slag formed from the ashes of British coals: Part 1: Viscosity of homogenous liquid slag in relation to slag composition. *J. Inst. Fuel,* 42, 99-103.

Westbrook, C.K.,Y. Mizobuchi, T.J., Poinsot, P.J. Smith & Warnatz, J. (2005). *Computational Combustion. Proceedings of the Combustion Institute, 30, 125-132.*

Wibberley, L. J. & Wall, T. F. (1982). Alkali-ash reactions and deposit formation in pulverized-coal-fired boilers: the thermodynamic aspects involving silica, sodium, sulphur and chlorine. *Fuel*, 61, 87-90.

Wigley, F., Williamson, J. & Riley, G. (2007). The effect of mineral additions on coal ash deposition, *Fuel Processing Technology*, 88, 1010–1016.

Wigley, F., Williamson, J., Malmgren, A. & Riley, G. (2007). Ash deposition at higher levels of coal replacement by biomass, *Fuel Processing Technology*, 88, 1148-1154.

Wigley, F., Williamson, J. & Jones, A. R. (1990). Slagging indices for UK coals and their relationship with mineral matter, *Fuel Processing Technology*, 88, 1148-1154.

Williams, A., Backreedy, R., Habib, R., Pourkashanian M. & Jones J. M. (2002). Modelling coal combustion, the current position, *Fuel*, 81, 605-618.

Williams, A., Pourkashanian, M. & Jones, J. M. (2000). The combustion of coal and some other solid fuels. *Proceedings of the Combustion Institute*, 28(2), 2141–62.

Williams, R. H., & Larson, E. D. (1993). Advanced gasification-based power generation. In Renewable Energy: *Sources for Fuel and Electricity*, Island Press, Washington, D.C., 729-786.

World Coal Institute, (2010). Coal information. *Cambridge House, Putney, London,* 1-3.

Wua, H., Glarborg, P., Frandsen, F. J., Dam-Johansen, K., Jensen, P. A. & Sander, B. (2011). Co-combustion of pulverized coal and solid recovered fuel in an entrained flow reactor – General combustion and ash behaviour. *Fuel*, 90, 1980–1991.

Xu, M., He, X., Azevedo, L. T., & Carvalho, M. G. (2002). An advanced model to assess fouling and slagging in coal fired boilers. *Int. J. Energy Res.*, 26, 1221-1236.

Xu, L., Lee, J. & Kim, H. (2007). Comparison of low temperature ash deposition determined by theoretical and experimental method in coal gasifier condition. *World Coal Ash (WOCA)*, Northern Kenturky, USA.

Zhang, L. & Jahanshahi, S. (2001). Modelling viscosity of alumina-containing silicate melts. *Scandinavian Journal of Metallurgy*. 30, 364-369.

Zheng, Y., Jensen, P. A., Jensen, A. D., Sander, B. & Junker, H. (2007). Ash transformation during co-firing coal and straw. *Fuel*, 86, 1008–1020.

Zhou, H.; Jensen, P. & Frandsen, F. (2007). Dynamic mechanistic model of superheater deposit growth and shedding in a biomass fired grate boiler. *Fuel*, 86, 1519–153.

Appendix A Reduced Alkali Mechanism

The reduced alkali mechanism is as follows:

No.	Reaction	A	n	E
1	$2K_2SO_4 = 2K_2SO_4XBX$	1.000E+14	0.0000	0.00
2	$H+O_2 = O+OH$	3.600E+15	-0.4100	16.60
3	$2H+M = H_2+M$	7.000E+17	-1.0000	0.00
4	$2H+N_2 = H_2+N_2$	5.400E+18	-1.3000	0.00
5	$2H+H_2 = 2H_2$	1.000E+17	-0.6000	0.00
6	$2H+H_2O = H_2+H_2O$	1.000E+19	-1.0000	0.00
7	$H+O+M = OH+M$	6.200E+16	-0.6000	0.00
8	$H+O_2(+M) = HO_2(+M)$	1.500E+12	0.6000	0.00
9	$H+O_2(+AR) = HO_2(+AR)$	1.500E+12	0.6000	0.00
10	$H+O_2(+N_2) = HO_2(+N_2)$	1.500E+12	0.6000	0.00
11	$2O+M = O_2+M$	1.900E+13	0.0000	-1.79
12	$O+H_2 = OH+H$	3.800E+12	0.0000	7.95
13	$O+H_2 = OH+H$	8.800E+14	0.0000	19.17
14	$O+H_2O = 2OH$	4.500E+04	2.7000	14.55
15	$H_2+O_2 = HO_2+H$	7.400E+05	2.4330	53.50
16	$OH+H+M = H_2O+M$	4.500E+22	-2.0000	0.00

17	$OH+H_2 = H+H_2O$	2.100E+08	1.5200	3.45
18	$HO_2+H = 2OH$	8.400E+13	0.0000	0.40
19	$HO_2+H = H_2O+O$	1.400E+12	0.0000	0.00
20	$HO_2+O = OH+O2$	1.600E+13	0.0000	-0.44
21	$HO_2+OH = H_2O+O2$	3.600E+21	-2.1000	9.00
22	$HO_2+OH = H_2O+O_2$	2.000E+15	-0.6000	0.00
23	$HO_2+OH = H_2O+O2$	-2.200E+96	-24.0000	49.00
24	$2HO_2 = H_2O_2+O2$	1.900E+11	0.0000	-1.41
25	$2HO_2 = H_2O_2+O_2$	1.000E+14	0.0000	11.03
26	$H2O_2(+M) = 2OH(+M)$	4.000E+11	0.0000	37.14
27	$H_2O_2+H = H_2O+OH$	1.000E+13	0.0000	3.58
28	$H_2O_2+H = HO_2+H2$	1.700E+12	0.0000	3.76
29	$H_2O_2+O = HO_2+OH$	9.600E+06	2.0000	3.97
30	$H_2O_2+OH = H_2O+HO_2$	1.000E+12	0.0000	0.00
31	$H_2O_2+OH = H_2O+HO_2$	5.800E+14	0.0000	9.56
32	$CO+O(+M) = CO_2(+M)$	1.800E+10	0.0000	2.38
33	$CO+OH = CO_2+H$	8.000E+10	0.0000	0.00
34	$CO+OH = CO_2+H$	8.800E+05	1.7700	0.95
35	$CO+HO_2 = CO_2+OH$	1.000E+05	2.1800	17.94
36	$SO_2+OH = HOSO+O$	3.900E+08	1.8900	76.00
37	$SO_2+H(+M) = HOSO(+M)$	2.400E+08	1.6300	7.34

38	$SO_2+O(+M) = SO_3(+M)$	3.700E+11	0.0000	1.69
39	$SO_2+O(+N_2) = SO_3(+N_2)$	3.700E+11	0.0000	1.69
40	$SO_2+OH(+M) = HOSO_2(+M)$	5.700E+12	-0.2700	0.00
41	$SO_3+H = SO_2+OH$	8.400E+09	1.2200	3.32
42	$SO_3+H = HOSO+O$	2.500E+05	2.9200	50.30
43	$SO_3+O = SO_2+O2$	2.800E+04	2.5700	29.20
44	$SO_3+OH = SO_2+HO2$	4.800E+04	2.4600	27.25
45	$HOSO+H = SO_2+H_2$	1.800E+07	1.7200	-1.29
46	$HOSO+OH = SO_2+H_2O$	6.000E+12	0.0000	0.00
47	$HOSO+O_2 = HO_2+SO_2$	9.600E+01	2.3550	-10.13
48	$HOSO_2 = HOSO+O$	5.400E+18	-2.3400	106.30
49	$HOSO_2 = SO_3+H$	1.400E+18	-2.9100	54.90
50	$HOSO_2+H = SO_2+H_2O$	1.000E+12	0.0000	0.00
51	$HOSO_2+O = SO_3+OH$	5.000E+12	0.0000	0.00
52	$HOSO_2+OH = SO_3+H_2O$	1.000E+12	0.0000	0.00
53	$HOSO_2+O_2 = HO_2+SO_3$	7.800E+11	0.0000	0.66
54	$HCl+M = Cl+H+M$	4.400E+13	0.0000	81.75
55	$HCl+H = Cl+H_2$	1.700E+13	0.0000	4.14
56	$HCl+O = Cl+OH$	3.400E+03	2.8700	3.51
57	$HCl+OH = Cl+H_2O$	2.700E+07	1.6500	-0.22
58	$Cl+HO_2 = HCl+O_2$	1.100E+13	0.0000	-0.34

59	$Cl+HO_2 = ClO+OH$	2.500E+13	0.0000	0.90
60	$Cl+O_2+M = ClOO+M$	2.300E+24	-3.9000	0.00
61	$Cl+H_2O_2 = HCl+HO_2$	6.600E+12	0.0000	2.00
62	$2Cl+M = Cl_2+M$	2.200E+14	0.0000	-1.80
63	$Cl+ClOO = Cl_2+O_2$	8.400E+13	0.0000	0.00
64	$Cl+ClOO = 2ClO$	4.800E+12	0.0000	0.00
65	$Cl_2+H = HCl+Cl$	8.600E+13	0.0000	1.17
66	$Cl_2+O = Cl+ClO$	2.500E+12	0.0000	2.72
67	$Cl_2+OH = HOCl+Cl$	8.400E+11	0.0000	1.80
68	$ClO+O = Cl+O_2$	2.300E+13	0.0000	0.00
69	$ClO+HO_2 = HOCl+O_2$	2.900E+11	0.0000	-1.40
70	$HOCl+H = ClO+H_2$	2.100E+12	0.0000	0.00
71	$HOCl+OH = ClO+H_2O$	1.800E+12	0.0000	1.20
72	$ClOO+H = ClO+OH$	3.400E+13	0.0000	0.00
73	$ClOO+O = ClO+O_2$	3.000E+13	0.0000	0.00
74	$K+O+M = KO+M$	1.500E+21	-1.5000	0.00
75	$K+OH+M = KOH+M$	3.800E+19	-0.6500	0.00
76	$K+HO_2 = KOH+O$	1.000E+14	0.0000	0.00
77	$K+O_2(+M) = KO_2(+M)$	3.600E+14	0.0000	0.00
78	$K+H_2O_2 = KOH+OH$	2.500E+13	0.0000	0.00
79	$K+H_2O_2 = KO+H_2O$	1.600E+13	0.0000	0.00

80	KO+H = K+OH	2.000E+14	0.0000	0.00
81	KO+O = K+O_2	2.000E+13	0.0000	0.00
82	KO+OH = KOH+O	2.000E+13	0.0000	0.00
83	KO+HO_2 = KOH+O_2	5.000E+13	0.0000	0.00
84	KO+H_2 = KOH+H	1.600E+13	0.0000	0.00
85	KO+H_2 = K+H_2O	3.100E+12	0.0000	0.00
86	KO+H_2O = KOH+OH	1.300E+14	0.0000	0.00
87	KO+CO = K+CO_2	1.000E+14	0.0000	0.00
88	KOH+H = K+H_2O	5.000E+13	0.0000	0.00
89	2KOH = $K_2O_2H_2$	8.000E+13	0.0000	0.00
90	KO_2+H = K+HO_2	2.000E+14	0.0000	0.00
91	KO_2+H = KO+OH	5.000E+13	0.0000	0.00
92	KO_2+H = KOH+O	1.000E+14	0.0000	0.00
93	KO_2+O = KO+O_2	1.300E+13	0.0000	0.00
94	KO_2+OH = KOH+O_2	2.000E+13	0.0000	0.00
95	KO_2+CO = KO+CO_2	1.000E+14	0.0000	0.00
96	K+Cl+M = KCl+M	1.800E+20	-1.0000	0.00
97	K+HCl = KCl+H	9.100E+12	0.0000	1.18
98	K+HCl = KCL+H	1.000E+14	0.0000	3.63
99	K+Cl_2 = KCl+Cl	4.400E+14	0.0000	0.00
100	KO+HCl = KCl+OH	1.700E+14	0.0000	0.00

101	KOH+HCl = KCl+H2O	1.700E+14	0.0000	0.00
102	KO_2+HCl = KCl+HO2	1.400E+14	0.0000	0.00
103	2KCl = $K2Cl_2$	8.000E+13	0.0000	0.00
104	K+SO_2(+M) = KSO_2(+M)	3.700E+14	0.0000	0.00
105	K+SO_3(+M) = KSO_3(+M)	3.700E+14	0.0000	0.00
106	KO+SO_2 = K+SO_3	1.000E+12	0.0000	0.00
107	KO+SO_2(+M) = KSO_3(+M)	3.700E+14	0.0000	0.00
108	KO+SO_3(+M) = KSO_4(+M)	1.000E+14	0.0000	0.00
109	KOH+SO_2(+M) = $KHSO_3$(+M)	1.000E+14	0.0000	0.00
110	KOH+SO_3(+M) = $KHSO_4$(+M)	1.000E+14	0.0000	0.00
111	KO_2+SO_2 = KO+SO_3	1.000E+14	0.0000	0.00
112	KO_2+SO_2(+M) = KSO_4(+M)	1.000E+14	0.0000	0.00
113	KSO_2+O = KO+SO_2	1.300E+13	0.0000	0.00
114	KSO_2+OH = KOH+SO_2	2.000E+13	0.0000	0.00
115	KSO_2+O_2(+M) = KSO_4(+M)	1.000E+14	0.0000	0.00
116	KSO_2+KO_2 = K_2SO_4	1.000E+14	0.0000	0.00
117	KSO_3+O = KO+SO_3	1.300E+13	0.0000	0.00
118	KSO_3+OH = $KHSO_4$	1.000E+14	0.0000	0.00
119	KSO_3+KO = K_2SO_4	1.000E+14	0.0000	0.00
120	KSO_4+O = KSO_3+O_2	1.000E+14	0.0000	0.00
121	KSO_4+HCl = $KHSO_4$+Cl	1.000E+14	0.0000	0.00

122	$KSO_4+KOH = K_2SO_4+OH$	1.000E+14	0.0000	0.00
123	$KSO_4+KCl = K_2SO_4+Cl$	1.000E+14	0.0000	0.00
124	$KHSO_3+OH = KSO_3+H_2O$	2.000E+13	0.0000	0.00
125	$KHSO_3+OH = KHSO_4+H$	2.000E+13	0.0000	0.00
126	KHSO3+KO = KHSO4+K	1.000E+14	0.0000	0.00
127	$KHSO_3+KO = KHSO_4+K$	1.000E+14	0.0000	0.00
128	$KHSO_3+KO_2 = KHSO_4+KO$	2.000E+13	0.0000	0.00
129	$KHSO_4+H = KSO_3+H2O$	2.000E+13	0.0000	0.00
130	$KHSO_4+KOH = K_2SO_4+H_2O$	1.000E+14	0.0000	0.00
131	$KHSO_4+KCl = K_2SO_4+HCl$	1.000E+14	0.0000	0.00
132	$KCl+SO_3(+M) = KSO_3Cl(+M)$	1.000E+14	0.0000	0.00
133	$KSO_3Cl+H = KSO_3+HCl$	2.000E+13	0.0000	0.00
134	$KSO_3Cl+OH = KHSO_4+Cl$	1.000E+14	0.0000	0.00
135	$KSO_3Cl+H2O = KHSO_4+HCl$	1.000E+14	0.0000	0.00
136	$KSO_3Cl+K = KSO_3+KCl$	2.000E+13	0.0000	0.00
137	$KSO_3Cl+KOH = K_2SO_4+HCl$	1.000E+14	0.0000	0.00